Search for Penguin Decays of B Mesons at CDF

by

Kostas Kordas

Department of Physics
McGill University, Montréal
January 2000

A Thesis submitted to the
Faculty of Graduate Studies and Research
in partial fulfillment of the requirements for the degree of
Doctor of Philosophy

Στους γονείς μου
Σωκράτη και Διαμάντω

To my parents
Socrates and Diamanto

Abstract

Using a data sample of integrated luminosity $\int Ldt = 28.9 \pm 1.2$ pb^{-1} of proton-antiproton collisions at a center-of-mass energy $\sqrt{s} = 1.8$ TeV collected with the CDF detector at the Fermilab Tevatron collider, we searched for "penguin" radiative decays of B_d^0 and B_s^0 mesons which involve the flavor-changing neutral-current transition of a b quark into an s quark with the emission of a photon, $b \to s\gamma$. Specifically, we searched for the decays $B_d^0 \to K^{*0}\gamma$, $K^{*0} \to K^-\pi^-$ and $B_s^0 \to \phi\gamma$, $\phi \to K^-K^-$, as well as for the charge conjugate chains.

In order to collect such decays, we designed a specialized trigger which required information on all the decay products of the B meson decay chain, the first such trigger in a hadron collider environment. This "penguin" trigger collected data during the last quarter of the 1994 – 1996 data-taking period. After all selection criteria, we are left with one candidate $B_d^0 \to K^{*0}\gamma$ decay and no $B_s^0 \to \phi\gamma$ candidates in the entire data sample. We then proceed to set upper limits on the branching fractions of the penguin channels.

We exploit the topological similarity between the $\bar{B} \to e^- D^0 X$, $D^0 \to K^-\pi^-$and the penguin decays, by forming ratios of branching fractions between the penguin and the $\bar{B} \to e^- D^0 X$ channels. Uncertainties associated with the B meson production cross section, common efficiency corrections and other systematic effects are minimal in the ratio of branching fractions. The uncertainty on the $\bar{B} \to e^- D^0 X$ yield is the biggest contribution to the total uncertainty on the penguin branching fraction. We assume equal production rates for B_u^+ and B_d^0 mesons, while the probability of producing B_s^0 mesons relative to B_d^0 mesons, f_s/f_d, is taken to be 1/3. The inferred upper limits on the ratios of branching fractions are

$$\frac{\mathcal{B}(B_s^0 \to \phi\gamma)}{\mathcal{B}(\bar{B} \to e^- D^0 X)} < 3.5 \times 10^{-3} \qquad \text{at 90\% C.L.}$$

$$\frac{\mathcal{B}(B_d^0 \to K^{*0}\gamma)}{\mathcal{B}(\bar{B} \to e^- D^0 X)} < 1.9 \times 10^{-3} \qquad \text{at 90\% C.L.}$$

Relative branching fraction measurements were combined with the branching fraction measurement of the $\bar{B} \to e^- D^0 X$, $D^0 \to K^- \pi^+$ decay chain, $\mathcal{B}(\bar{B} \to e^- D^0 X) \times \mathcal{B}(D^0 \to K^- \pi^+) = (294 \pm 40) \times 10^{-5}$, to extract the following absolute branching fraction limits

$$\mathcal{B}(B_s^0 \to \phi\gamma) < 2.8 \times 10^{-4} \qquad \text{at } 90\% \text{ C.L.}$$

$$\mathcal{B}(B_d^0 \to K^{*0}\gamma) < 1.5 \times 10^{-4} \qquad \text{at } 90\% \text{ C.L.}$$

The upper limit for the $B_d^0 \to K^{*0}\gamma$ decay is consistent with the branching fraction measurement reported by the CLEO collaboration, $\mathcal{B}(B_d^0 \to K^{*0}\gamma) = (4.0 \pm 1.9) \times 10^{-5}$, while the upper limit for the as yet unobserved $B_s^0 \to \phi\gamma$ decay is the most constraining one set to date.

Résumé

Nous utilisons un échantillon de données de $\int Ldt = 28.9 \pm 1.2$ pb^{-1} enregistré par le détecteur CDF au collisionneur proton-antiproton Tevatron du Fermilab à $\sqrt{s} = 1.8$ TeV, pour rechercher les contributions radiatives "pingouin" intervenant dans les désintégrations des mésons B_d^0 et B_s^0. Celles-ci impliquent des courants neutres avec changement de saveur lors de la transition d'un quark b en un quark s avec émission de photon, $b \to s\gamma$. Plus précisément, nous recherchons les désintégrations $B_d^0 \to K^{*0}\gamma$, $K^{*0} \to K^-\pi^-$ et $B_s^0 \to \phi\gamma$, $\phi \to K^+K^-$ (et conjuguées).

Afin de les détecter, nous avons conçu un décleucheur spécial exigeant l'information sur tous les produits de la chaîne de désintégration du méson B. C'est la première fois qu'un tel décleucheur est utilisé dans un collisionneur hadronique. Il a recueilli des données pendant le dernier quart de la période de prise de données 1994-96. Après avoir appliqué tous les critères de sélection, il subsiste un seul candidat de la désintégration $B_d^0 \to K^{*0}\gamma$ et aucun candidat $B_s^0 \to \phi\gamma$. Ceci nous permet d'établir de limites supérieures sur les rapports d'embranchement des chaînes pingouin.

La ressemblance topologique entre $\bar{B} \to e^- D^0 X$, $D^0 \to K^-\pi^+$ et les désintégrations pingouins est exploiteé en formant les rapports de fractions d'embranchement entre le pingouin et les canaux $\bar{B} \to e^- D^0 X$. Les incertitudes associées à la section efficace de production du méson B, aux corrections sur l'efficacité et autres effets systématiques interviennent faiblement dans ce rapport. La plus importante incertitude sur la fraction de branchement pinguin provient de l'incertitude sur la réaction $\bar{B} \to e^- D^0 X$. Nous supposons des taux de production égaux pour les mésons B_u^- et B_d^0. Par contre, la probabilité de production des B_s^0 par rapport à celle des B_d^0, f_s/f_d, est prise égale à 1/3. Les limites supérieures sur les rapports d'embranchement sont:

$$\frac{\mathcal{B}(B_s^0 \to \phi\gamma)}{\mathcal{B}(\bar{B} \to e^- D^0 X)} < 3.5 \times 10^{-3} \qquad \text{à 90\% de niveau de confiance}$$

$$\frac{\mathcal{B}(B_d^0 \to K^{*0}\gamma)}{\mathcal{B}(\bar{B} \to e^- D^0 X)} < 1.9 \times 10^{-3} \qquad \text{à 90\% de niveau de confiance}$$

Les mesures des rapports d'embranchement relatifs ont été combinées avec les

mesures de rapport d'embranchement des canaux de désintégration $\bar{B} \to e^- D^0 X$, $D^0 \to K^- \pi^+$, $\mathcal{B}(\bar{B} \to e^- D^0 X) \times \mathcal{B}(D^0 \to K^- \pi^+) = (294 \pm 40) \times 10^{-5}$. Ceci permet d' extraire les limites sur les rapport d'embranchement absolues:

$$\mathcal{B}(B_s^0 \to \phi\gamma) < 2.8 \times 10^{-4} \qquad \text{à 90\% de niveau de confiance}$$

$$\mathcal{B}(B_d^0 \to K^{*0}\gamma) < 1.5 \times 10^{-4} \qquad \text{à 90\% de niveau de confiance}$$

La limite supérieure pour la désintégration $B_d^0 \to K^{*0}\gamma$ est en accord avec la mesure du rapport d'embranchement annoncé par la collaboration CLEO, $\mathcal{B}(B_d^0 \to K^{*0}\gamma) = (4.0 \pm 1.9) \times 10^{-5}$. Par contre, la limite supérieure pour la désintégration $B_s^0 \to \phi\gamma$, non encore observée, est la plus contraignante connue à ce jour.

Acknowledgments

I would like to thank my supervisor Ken Ragan for his support and encouragement, guidance and patience, and inspirational discussions throughout my Ph.D. It was his enthusiasm that boosted me at times where the light at the end of the tunnel was becoming dim.

Fritz DeJongh is the one who provided invaluable help in all the steps of this work. I am grateful to him for guiding me through the whole process of a self-contained research project, from the proposal of a physics project to the implementation of the necessary tools, and finally to the analysis of the collected data. Many thanks to the trigger experts Kevin Burkett and Soo-Bong Kim for invaluable help with the implementation of "penguin" trigger. Thanks also to Jonathan Lewis for helpful suggestions at the analysis stage. I would also like to thank Klaus Strahl for the helpful and insightful discussions over the last years, where physical intuition was always put ahead of mathematical description.

This work would not have been possible without the hard work of the physicists, engineers and technicians who built and operated the CDF detector and the Fermilab Tevatron collider. A list of the physicists comprising the Run 1 CDF collaboration is given in Appendix A.

Thanks to the officemates at McGill for making our office a real fun place to work. In order of appearance in Room 303, I'd like to say thank you Niri, François, Graham, Yunling, Dean, Marko, Rainer, Ling Wai, Claude, Shem, Sanjay, Michael, Declan and René. I should not of course forget the honorary officemates Ioulia, Imran, Abhijit, Alex and especially Andrew. Thank you Géraldine, for the help with the French version of the abstract. Special thanks to Marko, Declan, Michael, Andrew and Ioulia for the outings of this last, long year.

Thanks to the "Torontonians", especially George, Andreas, Hyunsoo, Wendy and Prof. Pekka Sinervo, for friendship, many helpful physics discussions and for good times at Fermilab. Special thanks to Foti and Maria; without you guys Fermilab would have not been nearly as fun.

Life in Montréal without my other friends outside work would have been dangerously one-dimensional. Thank you guys, especially Georgia, Prokopi, Dimitri, Antoni, Apostolo, Maria, Dionusia, Angeliki, Dimitra, Theodore, Constantine, Jelena and Bridgette. Special thanks to my extended family here; my aunts, uncles, cousins and my girlfriend's parents. I am grateful to you for making me feel at home all these years and providing me with the necessary energy to keep going.

Very special thanks to my better half, Alexandra, whose encouragement and love is priceless throughout these years. *Σ' αγαπώ καρδούλα μου. Χωρίς εσένα ο κόσμος θά 'ταν λιγότερο όμορφος.*

Lastly I thank my parents, Socrates and Diamanto, my brothers, Michael and Vassili, and my sister Vassiliki, back home for their patience and encouragement. *'Ενα μεγάλο ευχαριστώ, αν και κανένα ευχαριστώ δεν θα είναι ποτέ αρκετό για όσα κάνατε για μένα.*

Personal contributions to the CDF experiment

When I joined the CDF experiment as a Master's student in 1991, I participated in the data taking of electron and pion test-beam data. Using these data, I performed a comparison between the response of the central electromagnetic calorimeter to the incident particles and the predictions of the simulation package. I then suggested improvements to the parameterization of the electromagnetic shower development and I documented this work in an internal CDF-Note. The findings of this work are used now to test the new simulations of the calorimeters. The central calorimeter is going to be used again during the next data-taking period commencing in the year 2000 and this work is invaluable, because the 1991 data were the last test-beam data taken for this detector component.

My most important contribution to CDF, the subject of this thesis, was the design, testing and implementation of the "penguin" trigger which required an energetic photon and a pair of oppositely charged energetic tracks. This trigger is a pioneer for a hadron collider environment in the sense that it combines information from all the decay products. Its use was also a proof-of-principle for CDF, which is expected to observe significant signals in penguin channels with a similar trigger during the upcoming data taking period, expected to commence in the year 2000. In fact, most of the triggers to be used in the next data taking period will be looking for exclusive or semi-exclusive decay channels.

When I started my Ph.D, in 1993, the collider and the detector were upgraded for the 1994-1996 data-taking period. I joined the B physics group at CDF and I decided my research topic be the "penguin" decays $B_d^0 \to K^{*0}\gamma$, $K^{*0} \to K^+\pi^-$ and $B_s^0 \to \phi\gamma$, $\phi \to K^+K^-$, which involve the flavour-changing neutral-current transition $b \to s\gamma$. With the use of simulations I predicted the signal yield as a function of the energy and topological requirements on the B decay products. I also used events selected with a low energy threshold requirement on photons to study the trigger rate as a function of the photon energy threshold. The limitations in the trigger bandwidth had dictated the already existing photon triggers to have high energy thresholds,

resulting in trivial penguin signal yields. I then investigated scenarios of trigger logic where information from all the penguin decay products were used. I made predictions about the rate of a trigger that would require information on a photon-like cluster of energy and two tracks as a function of the energy and topology of these three objects. The signal characteristics and the limitations in the trigger bandwidth dictated the penguin trigger requirements. The penguin trigger logic could not be implemented prior to the arrival of the programmable ALPHA processors which gave the trigger system unprecedented flexibility compared to the hardware trigger previously employed.

After numerous presentations to convince the collaboration of the feasibility of the method, I implemented the trigger as a FORTRAN routine at the 3^{rd} (highest) level of the CDF trigger system and, with the help of trigger experts, as assembly code at the 2^{nd} trigger level. The trigger was tested on-line and the rates were as predicted. In April 1995 the penguin trigger became part of the CDF trigger system and until the end of the data taking period (February 1996) it collected $\sim$ 800000 events, corresponding to $\sim$ 30 pb^{-1} of $p\bar{p}$ collisions, of which only $\sim$ 15 events are expected to contain $B_d^0 \to K^{*0}\gamma$ and $\sim$ 5 to contain $B_s^0 \to \phi\gamma$ decays.

In the analysis of the collected data I managed to bring the signal-to-background ratio from $\sim$ 4 in 10000 to almost 8/1 with the use of characteristics of events containing B mesons: I used $B \to eD^0X$, $B \to J/\psi K^{*0}$ and $B \to J/\psi K^+$ events to understand the background and B signal behaviour. Not observing enough signal events, I then set an upper limit on the ratio of branching ratios $\mathcal{B}(B_d^0 \to K^{*0}\gamma)/\mathcal{B}(B \to eD^0X)$ and $\mathcal{B}(B_s^0 \to \phi\gamma)/\mathcal{B}(B \to eD^0X)$; systematic effects common to these topologically similar decays cancel in the ratio and the result has minimal dependence on Monte Carlo predictions.

I have documented my work on the penguin trigger and the analysis of the collected data in several internal CDF notes and I have presented this work at the Canadian Association of Physicists (CAP) meetings in Quebec city (1995) and Ot-

tawa (1996), and at the American Physical Society (APS) meeting in Washington, DC (1997).

During my studies I participated actively in both data-taking periods (1992-93 and 1994-96) of the experiment by monitoring the data-quality with the help of on-line monitor programs and by having responsibilities for the reconstruction of part of the data. I was also responsible for the maintenance of the Monte Carlo generator for b hadrons for several months. This package was used extensively by the B physics group until a new and similar simulation package became available. I have also introduced new M.Sc students to the software and analysis techniques used at CDF and I have guided their work in B physics analyses and provided them with code to start.

During these years I have also reviewed and edited numerous CDF paper drafts through the exchange of ideas with the main authors about physics, analysis methods and presentation issues. My participation in this process was vital in keeping the McGill group as one of the few groups commenting on the vast majority of the intended CDF publications.

Contents

List of Figures

List of Tables

Chapter 1

Introduction

The quest of particle physics is the identification of the elementary building blocks of nature and the description of their interactions. In the road for that search, increasing accelerator energies have enabled particle collisions (usually protons or electrons) which resulted in the birth of hundreds of new particles. This diversity is analogous to the diversity of atoms; some of the particles produced are thought to be elementary, while most of them are explained as combinations of a small number of more fundamental entities. Furthermore, it is now understood that these particles feel each other via a limited number of interaction processes and all known forces in nature can be expressed in terms of these interactions.

1.1 Fundamental particles and interactions

Advances on the experimental and the theoretical fronts have resulted in the current theory of elementary particles and their interactions, which describes very well all known particle physics phenomena. We refer to this theory as the Standard Model.

According to the Standard Model the elementary particles are of two types: the basic building blocks of matter, which are fermions, and the particles that mediate the forces between them, which are bosons. For each particle, there exists an "an-

tiparticle" with the same mass and spin as the corresponding particle, but opposite values of other quantum numbers, such as electric charge.

1.1.1 The fundamental fermions

The fundamental fermions have spin $s = \frac{1}{2}\hbar$ and are classified according to the type of interactions they participate in. The ones that can feel the strong force, which is responsible for holding the atomic nuclei together, are called quarks. The ones that do not feel the strong force are called leptons. Leptons can feel the weak force which is responsible for transformations of one particle type into another, resulting for example in nuclear decays. The fundamental fermions of the Standard Model are shown in Table 1.1.

Six distinct types (called flavours) of leptons have been identified. The electron (e^-), the muon (μ^-) and the tau (τ^-) have electric charge -1, with the charge given in units of the absolute value of the electron charge from here on. For each of these leptons there exists a corresponding neutrino (ν_e, ν_μ and ν_τ respectively) with no charge. The distinctive nature of the neutrino types can be demonstrated in the reaction $n + \nu \rightarrow p + \ell^-$. When the neutrino, ν, is a muon neutrino (e.g., from pion decays), the lepton, ℓ, is a muon, whereas when the neutrino is an electron neutrino (e.g., from β decay), the produced lepton is an electron. The pairing of leptons is indicated by the observation that lepton interactions seem to respect boundaries that classify them in three families: the electron, the muon and the tau family. Each lepton in a given family is then assigned a lepton family number of $+1$. For each of the aforementioned lepton particles, there exists an antiparticle with the same mass and spin, but opposite values of other quantum numbers, such as electric charge and lepton number: the antielectron, also known as positron, (e^+) and its electron antineutrino ($\bar{\nu}_e$), the antimuon (μ^+) and its muon antineutrino ($\bar{\nu}_\mu$), and the antitau (τ^+) and its tau antineutrino ($\bar{\nu}_\tau$). As an example of leptons preserving lepton family boundaries, a muon (μ^-) decays into a muon neutrino (ν_μ), the lepton

Leptons				Quarks			
Name	Symbol	Charge	Mass (MeV/c^2)	Name	Symbol	Charge	Mass (MeV/c^2)
electron neutrino	ν_e	0	$\simeq 0$	up	u	$+\frac{2}{3}$	$1.5 - 5$
electron	e	-1	0.511	down	d	$-\frac{1}{3}$	$3 - 9$
muon neutrino	ν_μ	0	< 0.17	charm	c	$+\frac{2}{3}$	$(1.1 - 1.4) \times 10^3$
muon	μ	-1	105.67	strange	s	$-\frac{1}{3}$	$60 - 170$
tau neutrino	ν_τ	0	< 18.2	top	t	$+\frac{2}{3}$	$(173.8 \pm 5.2) \times 10^3$
tau	τ	-1	1777	bottom	b	$-\frac{1}{3}$	$(4.1 - 4.4) \times 10^3$

Table 1.1: *The fundamental fermions in the Standard Model. The charges are given in units of the absolute electron charge. For each of these particles, there exists an antiparticle with the same mass and opposite charge.*

family partner, and at the same time gives birth to an electron (e^-), to conserve charge, and an electron antineutrino ($\bar{\nu}_e$), so that there is no net presence of the electron family in the decay products, exactly as there is no such presence in the parent state.

Six types (flavours) of quarks, q, are known as well: the up (u), down (d), strange (s), charm (c), bottom or beauty (b) and the top (t) quark. Unlike leptons, quarks have fractional electric charge; the u, c and t quarks have a charge of $+\frac{2}{3}$, and the d, s and b quarks have a charge of $-\frac{1}{3}$. Quarks carry a quantum number called "colour", which comes in three types: "red", "green" and "blue". Each quark flavour comes in any of these "colours". Colour is the "charge" of the strong interactions. As for the leptons, for each one of the quarks there exists an antiparticle, antiquark, with

the same mass and spin, but opposite charge and colour ("anti-red", "anti-green" and "anti-blue"). They are the $\bar{u}$, $\bar{d}$, $\bar{s}$, $\bar{c}$, $\bar{b}$ and $\bar{t}$ (called "u bar", "d bar" and so on). The colour quantum number has nothing to do with the colour experienced in everyday life. Nevertheless, it got its name from the fact that a combination of the three different degrees of freedom, i.e. "red", "green" and "blue", results in no net presence of the "colour" quantum number, in analogy to the mixture of red, green and blue colours resulting in a white colour in everyday life. Since no free quarks have been observed in nature, it is believed that colour is a hidden degree of freedom; only colourless objects can be observed. Therefore quarks must be confined into particles that can interact strongly, yet they are colourless. These composite particles are called hadrons. They can be combinations of a quark of a given colour and an antiquark of the opposite "anticolour" thus resulting in a colourless combination. Such quark-antiquark states are called mesons and they have integer spins. For example a positive pion, π^+, is a combination of an up quark and d-bar antiquark, $u\bar{d}$. The next simplest colourless combinations of quarks are combinations of three quarks each carrying a different colour, one red, one green and one blue. Such states are called baryons and they have half integer spins. Protons and neutrons are examples of baryons, with protons (neutrons) being uud (udd) combinations.

1.1.2 The fundamental forces

Any particle interacts with other particles by exchanging energy carried by discrete quanta, which also carry well defined quantum numbers. These quanta are identified with the particles transmitting the force[1] and they are called gauge bosons. Four forces describe all particle interactions. They are the gravitational, electromagnetic, weak, and strong forces. In Table 1.2 we summarize some of their properties.

The gravitational force is presumed to be mediated by massless bosons with spin $2\hbar$, called gravitons. This force is by far the weakest of all but since it is always

[1]The words "force" and "interaction" are used interchangeably.

Force	Range (m)	Strength at 10^{-15} m	Particles affected	Carrier	Mass GeV/c^2	Spin	Electric charge
Gravity	∞	10^{-38}	All	Graviton	0	2	0
Electro-magnetic	∞	10^{-32}	Charged	Photon	0	1	0
Weak	$\sim 10^{-18}$	10^{-13}	All	W^+	80.41 ± 0.10	1	+1
				W^-	80.41 ± 0.10	1	−1
				Z^0	91.187 ± 0.007	1	0
Strong	$\sim 10^{-15}$	1	Quarks, hadrons, gluons	Gluons	0	1	0

Table 1.2: *The fundamental forces and the mediator bosons in the Standard Model. The charges are given in units of the absolute electron charge. The strength of each force is given relative to the strong force [1].*

attractive and has an infinite range, its cumulative effects become significant for massive bodies (e.g., the earth). For interactions of subatomic particles gravity can be ignored.

The electromagnetic force is felt by all electrically charged particles. The carrier of this force is the photon, γ, which is massless, electrically neutral and has spin $1\hbar$. When a charged particle emits a photon it recoils and when the photon is absorbed by another charged particle the momentum of the latter changes. Thus the two charged particles "feel" each other. The electromagnetic force is proportional to the electric charge of the "source" and "target" particles and it decreases with the distance between them. Electric charges of opposite signs attract and same sign repel. This force is responsible for binding the negatively charged electrons to positively charged nuclei to form atoms. The theory that describes the electromagnetic interaction

is called Quantum Electrodynamics (QED) and it gives by far the most accurate predictions in physics; for example, the calculated magnetic dipole moment of the muon agrees with experiment to 12 significant digits [2].

Even though the electromagnetic force is strong enough to bind the negatively charged electrons to positively charged nuclei to form atoms, it is not strong enough to prohibit protons from being confined in nuclei. The strong force is felt by all particles that carry "colour", which is the "charge" of the strong force. The elementary fermions that feel the strong force are the quarks. The carriers of this "colour" force are eight massless gluons of spin $1\hbar$. Gluons carry a combination of colour with a different anticolour and are consequently coloured. Thus a quark changes colour when it emits or absorbs a gluon. The fact that gluons carry colour means that they can interact with each other. Detailed calculations show that this feature results in a decreasing strength of the strong interactions as the energy of the exchanged gluon increases (see for example, Ref. [3]). This behaviour is the opposite that one would expect if gluons did not interact with each other. In QED, where the photons do not carry electric charge and consequently no direct photon-photon interactions occur, the interaction strength increases as the energy of the exchanged photon increases [3]. The fact that gluons carry colour is also believed to be the cause for colour confinement, even though no rigorous proof exists within the framework of Quantum Chromodynamics (QCD), the theory of strong interactions. A somewhat simplistic argument is that because there is flow of colour between two interacting coloured objects, the force between them does not decrease with distance. Consequently when two quarks separate, the potential energy of the colour field between them increases linearly with distance and it becomes large enough to create a quark-antiquark pair. Then it is energetically favourable to form combinations of quarks and antiquarks into hadrons. This process repeats until all quarks are confined into hadrons, or "hadronized". Only combinations of quarks (and gluons) that are colourless can be separated by more than ~ 1 fm (a typical size for hadrons). Thus the range of the

strong interactions is ~ 1 fm. But colourless hadrons does not mean no strong interactions between them; for example, it is the residual colour field outside protons and neutrons that is responsible for binding them together in nuclei. This is analogous to the electrically neutral atoms combining into molecules.

The weak force is the only one capable of changing the flavour of a particle. It is felt by all leptons and quarks and it is mediated by three types of massive bosons with spin $1\hbar$. Two of these bosons are charged and are a particle-antiparticle pair, the W^+ and W^-, and one is neutral, the Z^0. When a quark or a lepton emits or absorbs a W boson, its charge, and consequently its flavour, changes. The W and Z bosons are heavy with $M_W = (80.41 \pm 0.10)$ GeV/c^2 and $M_Z = (91.187 \pm 0.007)$ GeV/c^2. The range of the weak interactions is about 10^{-3} fm.

Transformations between quarks prefer to respect family boundaries, but inter-generation interactions occur, though with smaller probabilities. Inter-generation interactions can be explained if the quark eigenstates which participate in weak interactions, q', are different from the mass eigenstates, q, where q denotes any of the u, d, c, s, t and b quarks. One set of eigenstates can be expanded in terms of another. It is conventional to "mix" the down-type quarks only, since this is enough to allow inter-generation interactions. This mixing is summarized by the Cabibbo-Kobayashi-Maskawa (CKM) matrix:

$$\begin{pmatrix} d' \\ s' \\ b' \end{pmatrix} = \begin{pmatrix} V_{ud} & V_{us} & V_{ub} \\ V_{cd} & V_{cs} & V_{cb} \\ V_{td} & V_{ts} & V_{tb} \end{pmatrix} \begin{pmatrix} d \\ s \\ b \end{pmatrix} \tag{1.1}$$

where the 90% confidence limits on the magnitudes of the elements of the CKM matrix are [4]:

$$\begin{pmatrix} |V_{ud}| = 0.9745 - 0.9760 & |V_{us}| = 0.217 - 0.224 & |V_{ub}| = 0.0018 - 0.0045 \\ |V_{cd}| = 0.217 - 0.224 & |V_{cs}| = 0.9737 - 0.9753 & |V_{cb}| = 0.036 - 0.042 \\ |V_{td}| = 0.004 - 0.013 & |V_{ts}| = 0.035 - 0.042 & |V_{tb}| = 0.9991 - 0.9994 \end{pmatrix} \tag{1.2}$$

Note that the structure of the CKM matrix is such that the only direct couplings occur between up-type and down-type quarks. Flavour-changing neutral-currents (e.g., $b \rightarrow sZ^0$ transitions) are suppressed by the GIM mechanism [5] of paired weak doublets of quarks: (u, d'), (c, s') and (t, b'). In this scheme, $d'\bar{d}'Z^0$, $s'\bar{s}'Z^0$, and $b'\bar{b}'Z^0$ couplings result in a zero strength for $d\bar{s}Z^0$, $s\bar{b}Z^0$, and $b\bar{d}Z^0$ couplings, through the expression of the mass eigenstates in terms of the weak eigenstates. In 1970, when only the up, down and strange quarks were known, Glashow, Iliopoulos and Maiani [5] postulated the existence a new quark (the "charm") as the weak partner of the strange quark and they wrote: $d' = cos\theta_W\ d + sin\theta_W\ s$ and $s' = -sin\theta_W\ d + cos\theta_W\ s$, where θ_W is the Cabibbo "weak mixing angle" with $sin^2\theta_W \simeq 0.23$ [4]. Thus, the neutral current couplings $d'\bar{d}'Z^0$ and $s'\bar{s}'Z^0$ between the weak eigenstates, result in a zero strength for the flavour-changing neutral current couplings $d\bar{s}Z^0$ and $s\bar{d}Z^0$ between the mass eigenstates of the down and strange quarks. In this manner, the "mixing" of the mass eigenstates of the quarks explained the observed absence of flavour-changing neutral current transitions.

Diagonal elements in the CKM matrix are large, favouring intra-generation transitions. The more family boundaries a transition crosses, the less probable it is. For example, a $b \rightarrow cW^-$ transition is $|V_{cb}|^2/|V_{ub}|^2 \sim 150$ times more probable than a $b \rightarrow uW^-$ transition, neglecting phase space factors.

The CKM matrix is a 3×3 unitary matrix with four independent parameters: three real and one imaginary. Therefore a time reversal operation (T), which introduces complex conjugation, results in violation of time invariance. In quantum field theories, like the Standard Model, the combination of time reversal, charge conjugation (C), which changes particles into their antiparticles, and space reversal, $\vec{r} \rightarrow -\vec{r}$, also known as parity (P), leaves any state invariant. Thus, violation of time reversal invariance implies violation of charge-parity (CP) invariance. It is in this sense that the Standard Model accommodates CP violation. Should there be only two generations of quarks, the CKM mixing matrix would have been a 2×2 matrix

with one real parameter only; and the absence of imaginary parameters means no violation of time reversal invariance, and consequently no CP violation.

Experiments demonstrate that W bosons interact with left-handed fermions, or right-handed antifermions only. The handedness refers to the helicity of the fermions, i.e. the orientation of their spin with respect to their momentum. Thus weak interactions are not invariant under space reversal or charge-conjugation. Nevertheless, they rarely violate the combined CP invariance, even though there are systems where CP violation has been observed (e.g., in the kaon system).

As mentioned above, the existence of an imaginary parameter in the CKM matrix allows for CP violation in the Standard Model. The CKM matrix elements are not predicted by theory, but are fundamental parameters of the theory; measurement of the CKM parameters should determine whether the Standard Model can accommodate the extent of CP violation observed. Measuring all the CKM matrix elements independently can also test the Standard Model by determining whether all couplings are consistent with the unitarity of the matrix and thus checking the three-generation structure of the theory.

For leptons only transformations within the family boundaries have been observed. But if neutrinos have mass, the mass eigenstates could no longer be degenerate and similar behaviour to the quarks might then be anticipated.

1.2 The b quark

In 1977, a fixed target experiment at Fermilab which collided 400 GeV protons on nuclei observed an enhancement in the rate of $\mu^+\mu^-$ production [6]. The enhancement occurred for $\mu^+\mu^-$ pairs with invariant masses ~ 9.5 GeV/c^2 and was interpreted as a $b\bar{b}$ bound state which, in analogy to the $c\bar{c}$ charmonium states (ψ states), was called bottomonium (Υ). The result was confirmed by experiments at DESY and more Υ resonances were subsequently found [7, 8, 9, 10, 11]. Since then, the lowest mass

b-flavoured hadrons (i.e. bound states containing a b quark and a lighter antiquark, or two lighter quarks) have been found[2]: $B_d^0 = \bar{b}d$, $B_u^+ = \bar{b}u$, $B_s^0 = \bar{b}s$, $B_c^+ = \bar{b}c$, and $\Lambda_b^0 = bdu$. Higher mass states decay strongly to these ones, whereas these low mass states decay weakly. Hadrons containing the b quark are the heaviest ones experimentally accessible, because the top quark is so heavy that it decays before it is able to hadronize[3].

Since B mesons decay weakly, they provide opportunities to study the CKM matrix, in particular the elements in the third column and the third row. Elements in the third column (V_{ub}, V_{cb}) can be accessed from $b \to uW^-$ or $b \to cW^-$ transitions with the partner antiquark in the B meson being a mere spectator of the b quark decay; by exchanging a W boson between the b quark and the lighter antiquark partner; or by "fusing" the b quark and the partner up-type antiquark into a W boson.

Elements in the third row (V_{td}, V_{ts} and V_{tb}) can be accessed via "box" diagrams, where $b \to qW^-$ transitions, with q being any of the up-type quarks (i.e. u, c, or t), result in the partner antiquark ($\bar{q}_{partner} = \bar{d}$ or $\bar{s}$) getting involved. The result is that $b \to (u, c, t \text{ or } W^-) \to \bar{b}$ and $\bar{q}_{partner} \to (u, c, t \text{ or } W^-) \to q_{partner}$ transitions occur simultaneously, with the box diagram with the heaviest quark (i.e. the top quark) being the dominant one. Consequently B "mixing" occurs, with neutral B mesons "oscillating" into their antiparticles ($\bar{B}$) and vice versa.

Information about elements in the third row of the CKM matrix can also be obtained from "penguin" diagrams where the partner quark remains a spectator. Emission of a W boson from the b quark ($b \to tW^-$) is followed by the W boson being reabsorbed by the quark line from which it was emitted, thus forming a tW^- loop. Consequently, $tW^- \to s$ or $tW^- \to d$ transitions occur, yielding the effective

[2]Throughout this dissertation reference to a specific charge state implies the charge-conjugate state as well, unless noted otherwise.

[3]Using the typical size of a hadron, $\sim$ 1 fm, as an estimate for the range of the strong interactions, we infer that strong interactions occur within $\sim \frac{1\text{fm}}{c} \sim 10^{-23}$ s, where c denotes the speed of light.

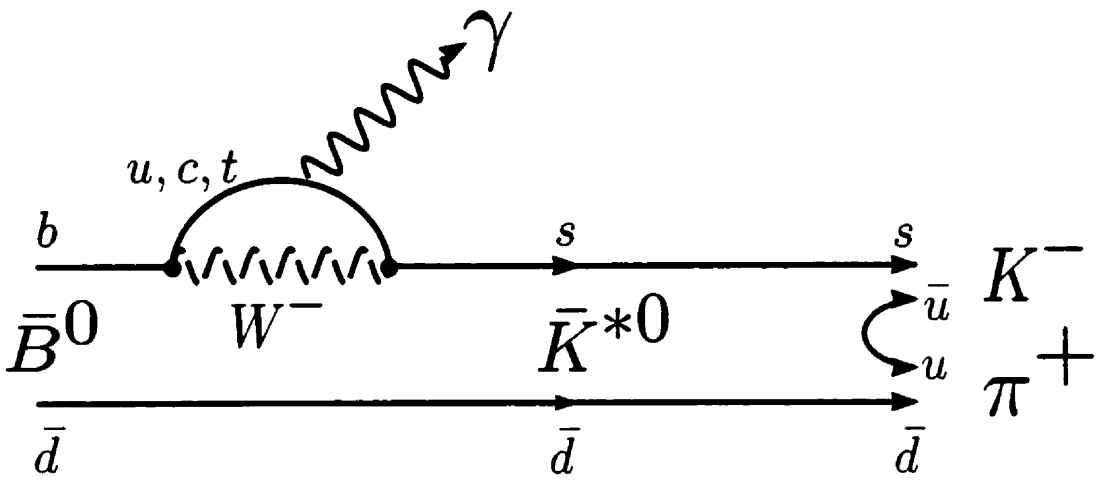

Figure 1.1: $b \to s\gamma$ *transition in the* $\bar{B}^0 \to \bar{K}^{*0}\gamma$, $\bar{K}^{*0} \to K^-\pi^+$ *decay channel.*

flavour-changing neutral-current transitions $b \to s$ or $b \to d$, with gluon, photon, or Z^0 boson emitted from the loop. In Fig. 1.1 we see an "electromagnetic penguin" process resulting in a $\bar{B}^0_d \to \bar{K}^{*0}\gamma$ decay.

As seen above, the weak force governs the decays of b-flavoured hadrons. It is the strong force though that is responsible for the hadronization of b quarks into colour-singlet hadrons, while in hadronic collisions, it is also responsible for the b quark production in the first place. The b quark is heavy compared to the scale parameter of QCD, Λ_{QCD}, which is of the order of 200 MeV. Roughly speaking, at energy scales higher than Λ_{QCD} one can expand a transition amplitude in powers of the QCD coupling strength in a perturbation series, and this allows for calculations for production and decays of b-flavoured hadrons to be performed perturbatively. The coupling strength of the strong interactions becomes smaller as the energy scale of a process increases, so that it is more reliable to apply perturbative QCD calculations in the B system than in lighter mesons. Consequently, experimental measurements on the B system should provide a more stringent test of the theory. Furthermore, the heaviness of the b quark facilitates experimental work, because there is significant energy given to its decay products, which are significantly lighter than the b quark.

Another feature of the b quark that facilitates experimental work with B mesons is its long lifetime which is long enough to be directly observed as a displacement of the B meson's production and decay points. Given the fact that the ratio of b-to-c quark masses is ~ 3, one would expect the ratio of b-to-c quark lifetimes to be $\sim (1/3)^5 = 4 \times 10^{-3}$. The fact that the lifetimes are comparable, is a demonstration of the difficulty the b quark has in crossing a family boundary in order to decay to a c quark, as opposed to the "easiness" of the intra-family $c \to s$ transition. The factor that "restores" the b lifetime to be comparable to the c lifetime is mostly the CKM factor $|V_{cs}|^2/|V_{cb}|^2 \sim 600$.

The distance L a B meson travels before it decays is proportional to its momentum: $L = ct_B \cdot \beta\gamma = ct_B \cdot p_B/m_B$, where t_B is the decay time of the B meson in its rest frame, p_B is its momentum, and m_B is its mass. Thus, more energetic B mesons travel further in the laboratory frame. However, the resolution of the B flight distance worsens with energy, due to the B decay products traveling at smaller angles relative to each other. Nonetheless, the signal-to-background ratio can then be enhanced significantly by requiring that the candidate decay products not originate from the B production point.

The subject of this dissertation is $b \to s\gamma$ transitions, studied via the decays $B_d^0 \to K^*(892)^0\gamma$ and $B_s^0 \to \phi(1020)\gamma$ reconstructed with the Collider Detector at Fermilab (CDF). The primary motivation for doing b physics at a hadron collider is that the cross section for producing b quarks is very large. At the Fermilab Tevatron collider $p\bar{p}$ collisions at $\sqrt{s} = 1.8$ TeV yield the b quark production cross section of $\sigma_b \simeq 50$ μb, which is enormous compared to the b production cross section in e^+e^- collisions; this is ~ 1 nb at the CESR ($e^+e^- \to \Upsilon(4S)$) and ~ 6 nb at the LEP ($e^+e^- \to Z^0$) colliders. Thus the yield of $b\bar{b}$ pairs at the Tevatron is $\sim 10^4$ times higher than at e^+e^- colliders. However, less than one out of a thousand inelastic $p\bar{p}$ collisions result in b quark production at the Tevatron, whereas this fraction is $\sim 1/4$ for the e^+e^- colliders (see Table 1.3 [12]). The low signal-to-background ratio for b

Collider type	$p\bar{p}$	e^+e^-	
Accelerator	Tevatron	CESR, PEP II, KEKB	LEP
$\sqrt{s}$ (GeV)	1800	10.58	91.2
$\sigma_{b\bar{b}}$	$\sim 50\ \mu$b	~ 1 nb	~ 6 nb
σ_b/σ_{total}	$\sim 10^{-3}$	~ 0.26	~ 0.22
b-flavoured hadrons produced	all	B_u^+ and B_d^0 only	all
Average $\beta\gamma$ boost	$\sim 2-4$	~ 0 (same beam energy)	~ 6
		~ 0.6 (asymmetric beams)	

Table 1.3: *Comparison of parameters important for B physics for existing $p\bar{p}$ and e^-e^- colliders.*

quark production at a hadron collider poses significant experimental challenges.

The fact that the transverse momentum[4] of the quarks produced at $p\bar{p}$ collisions scales with the quark mass, results in higher average transverse momenta for heavy quarks than for light quarks. As a result, B mesons have an average transverse momentum of $4-5$ GeV/c. Kinematic requirements can improve the signal-to-background ratio for event containing b quarks; when we consider all momenta, b production is $\sim 0.2\%$ of the total $p\bar{p}$ cross section, while for high momenta, jets of hadrons originating from the hadronization of b quarks comprise almost 2% of the total jet production. Consequently, the kinematic requirements at the trigger level are geared towards selecting events with energetic b quarks, typically with momenta above 8 GeV/c at CDF. Moreover, the long lifetime of B mesons allow for further improvement of the signal-to-background ratio for energetic B mesons.

The CDF collaboration has taken full advantage of the high b production cross section at the Tevatron to carry out a rich B physics program. The installation of

[4]Whenever the characterization "transverse" characterizes a quantity, it refers to the plane transverse to the proton and antiproton beams.

the silicon vertex detector in 1992 improved the B physics capabilities of the CDF detector significantly, due to its ability to measure the distance of closest approach of a charged particle to the $p\bar{p}$ collision point with a precision of ~ 15 μm. The CDF collaboration has performed measurements of b production cross sections, determination of the fragmentation fractions of b quarks into B_u^+, B_d^0, B_s^0 and Λ_b hadrons, and measurements of the lifetimes and branching fractions of b-flavoured hadrons. It has established the existence of the B_c meson, pursued searches for rare B decays as hints for new physics, and measured the time-integrated B_d^0 mixing parameter, χ_d, allowing an extraction of the mass difference, Δm_d, between the two mass eigenstates which are mixed to occur as the CP-conjugate B_d^0 and $\bar{B}_d^0$ mesons. Recently it presented the first direct hint for CP violation in the B system. For a summary of measurements of b-flavoured hadron lifetimes, mixing parameters and CP violation at CDF, see Ref. [12]. In brief, in the 1990's CDF has established hadron collider experiments as important players in the field of B physics.

1.3 Production of b hadrons in $p\bar{p}$ collisions

1.3.1 Production of b quarks

The colliding beams of protons and antiprotons at the Tevatron can be thought as beams of partons: the uud ($\bar{u}\bar{u}\bar{d}$) "valence" quarks, gluons and various "sea" quark-antiquark pairs. The collision of a proton and antiproton can then be thought as the collision between one parton from the proton and one parton from the antiproton. We are interested in collisions that result in the production of b quarks:

$$p + \bar{p} \rightarrow bX \tag{1.3}$$

where X denotes the $\bar{b}$ quark produced in association with the b quark and the "underlying event" resulting from lower-energy interactions between the proton and antiproton partons which did not participate in the "hard" scattering resulting in

the $b\bar{b}$ production.

In QCD the "partonic" cross section $\hat{\sigma}_{ij}$ for a parton i with momentum $x_i p_p$ to interact with a parton j with momentum $x_j p_{\bar{p}}$ and create a b quark with momentum p_b, is calculable as a perturbation series in powers of the strong coupling strength, α_s. The momentum of the proton (antiproton) is denoted by p_p ($p_{\bar{p}}$) and x_i is the fraction of the hadron momentum carried by parton i. The energy scale of the process, μ, is usually set equal to the four-momentum transfer Q and it is at least equal to the, relatively heavy, mass of the b quark, m_b. Thus, the coupling strength α_s is small enough to allow application of perturbation theory [13]. Apart from the factors mentioned so far, the partonic cross section $\hat{\sigma}_{ij}$ depends also on an experimentally-determined energy scale Λ, because the value of α_s at some energy scale μ cannot be calculated unless its value at some other energy scale, Λ, is known.

For a given b momentum, the calculation of interest is the differential hadronic $p + \bar{p} \rightarrow b + \bar{b} + X$ cross section, $\sigma_{p\bar{p}}$, which can be obtained by integrating the differential partonic cross section for all possible momenta of partons i and j. Integrating again over the momentum of the b quark, p_b, yields the total cross section for the production of a b quark from proton-antiproton collisions at center-of-mass energy $\sqrt{s}$. The momenta of the hadrons (protons and antiprotons) are not necessarily divided equally among the partons. This sharing is described by the parton distribution function $F_i^a(x_i, Q^2)$ which is the number density of parton i carrying a momentum fraction x_i of the hadron a when probed at a momentum transfer Q.

At leading order, $\mathcal{O}(\alpha_s^2)$, b quark production results from "$2 \rightarrow 2$" processes of quark-antiquark annihilation, $q + \bar{q} \rightarrow b + \bar{b}$, and gluon-gluon fusion, $g + g \rightarrow b + \bar{b}$. Such processes result in b quarks with transverse momenta, $p_T(b)$, that are on average of order of their mass, m_b, and have a distribution which falls rapidly for $p_T(b) > m_b$. The average transverse momenta of b quarks is therefore around $4 - 5$ GeV/c. These processes also result in b quarks preferably traveling at large angles with respect to the proton and antiproton beam directions, while the average separation of b and $\bar{b}$

quarks in rapidity is of order unity. The rapidity is a measure of the polar angle of the b quark and it is defined as:

$$y = \frac{1}{2} \ln \left[\frac{E_b + p_z(b)}{E_b - p_z(b)} \right] \tag{1.4}$$

where $p_z(b)$ is the momentum component of the b quark along the proton beam direction (z direction) and E_b is its energy. The rapidity is very useful in descriptions of particle production at high energies, because a boost along the z axis to a different reference frame results in a uniform shift of all the y values in the old reference frame. Thus distributions of particle-multiplicities as a function of rapidity, dN/dy, are invariant under such reference frame transformations [4].

Next-to-leading order, $\mathcal{O}(\alpha_s^3)$, contributions can contribute significantly to the b quark production cross section [14]. For example, the $g + g \rightarrow g + g$ processes occur almost a hundred times more often than $g + g \rightarrow b + \bar{b}$. The fact that a final state gluon can subsequently "split" into $g \rightarrow b + \bar{b}$ with a probability of $\sim \alpha_s$, means that the $\mathcal{O}(\alpha_s^3)$ process $g + g \rightarrow b + \bar{b} + g$ are competitive with the production of b quarks through the $\mathcal{O}(\alpha_s^2)$ $2 \rightarrow 2$ processes. Other $\mathcal{O}(\alpha_s^3)$ processes can result from emission of gluons from one of the final state b quarks in the $2 \rightarrow 2$ process.

In Fig. 1.2 we see the differential hadronic cross section for b quarks with $p_T(b)$ above some minimum $p_{T,min}$ and $|y_b| < 1$. The theoretical prediction shown is based on parton distribution functions by Martin, Roberts and Stirling [15] and the Nason-Dawson-Ellis calculation of the inclusive differential cross section for b quark production as a function of $p_T(b)$ and y_b up to next-to-leading order in α_s [16]. If the cross section calculation had been performed at all orders of α_s, the theoretical prediction would be independent of the energy scale μ chosen to evaluate α_s. Consequently, the large dependence of the theory on the "renormalization scale" μ implies that processes of higher order in α_s are important.

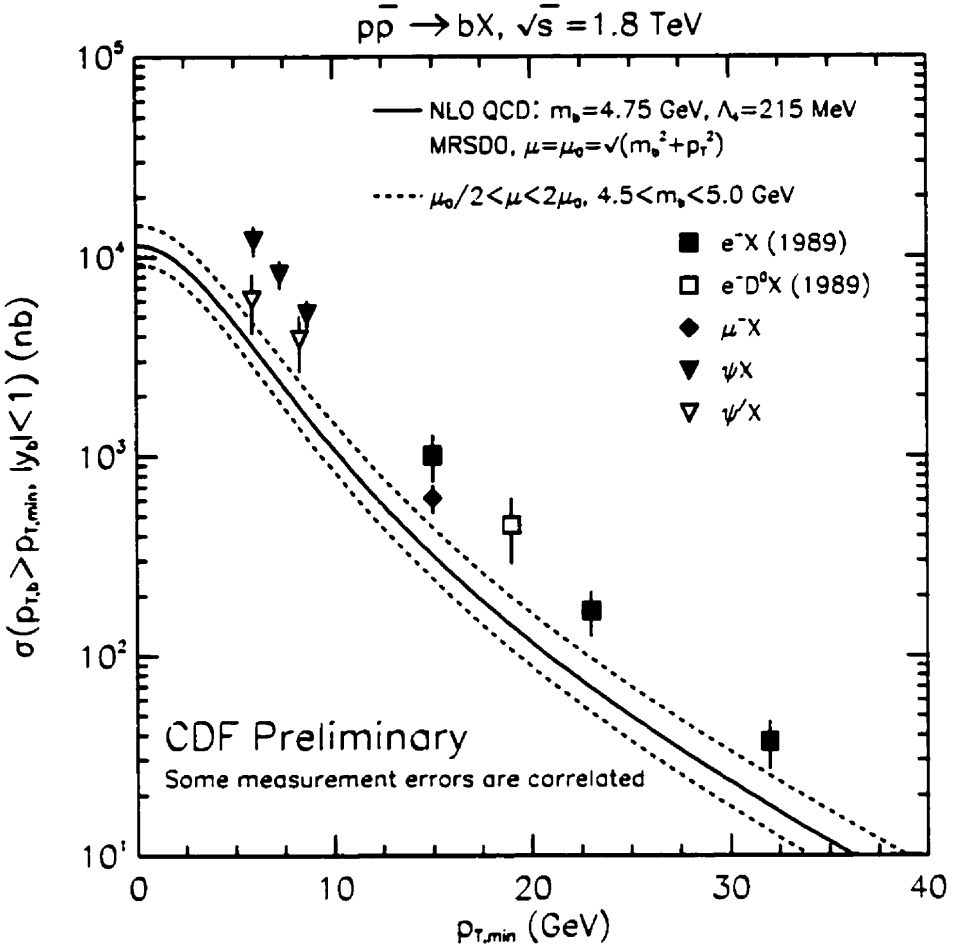

Figure 1.2: *Differential cross section for $p\bar{p} \rightarrow bX$, i.e. production of a b quark plus anything else at $p\bar{p}$ collisions at $\sqrt{s} = 1.8$ TeV.*

1.3.2 Hadronization of b quarks into b-flavoured hadrons

Once b quarks are produced from the initial hard scattering of proton and antiproton partons, they hadronize within a time frame of 10^{-23} sec and appear as colourless hadrons in the CDF detector. This process can not be calculated with perturbative QCD because it is low Q^2 and α_s is large. Semi-empirical arguments like the one made in Section 1.1.2 are used to describe this hadronization (or "fragmentation") process. The particles produced in this process, the b-flavoured hadron included, are usually referred to as fragmentation products. The fraction of the initial b quark

momentum carried by the b-flavoured hadron is described by fragmentation functions, parameterized in terms of the variable $z = \frac{E_B + p_{\parallel}(B)}{E_b + p_b}$, where $p_{\parallel}(B)$ is the projection of the b-hadron momentum on the b quark direction before hadronization; E_B is the energy of the b-hadron; and E_b and p_b are the energy and momentum respectively of the b quark before hadronization. Peterson, Schlatter, Schmitt and Zerwas [17] have provided a fragmentation function for B mesons of the following form:

$$\frac{dN}{dz} \sim \frac{1}{z\left(1 - \frac{1}{z} - \frac{\epsilon_b}{1-z}\right)^2} \tag{1.5}$$

where ϵ_b is the "Peterson parameter" related to the ratio $(m_{\bar{q}}/m_b)^2$, with $m_{\bar{q}}$ denoting the mass of the light antiquark $\bar{q}$ combined with the b quark to form the B meson. The Peterson parameter is an experimentally determined parameter. Chrin has estimated $\epsilon_b = 0.006 \pm 0.002$ based on data from e^+e^- collisions [18]. In Fig. 1.3 we see the differential $p\bar{p}$ cross section for production of a B meson with $p_T(B)$ above some minimum p_T value and $|y_B| < 1$. From such measurements we infer the production cross section of b quarks, which are not observed in the detector. In order to achieve that we rely on fragmentation functions like the one mentioned above. Thus, measurements that improve our understanding of the b quark fragmentation are important to test the perturbative QCD predictions of the b quark productions. CDF has reported measurements on the fraction of the time a b quark hadronizes into a B_u^+, B_d^0, B_s^0 or Λ_b hadron [19, 20].

1.4 Penguin decays of B mesons

As mentioned in Section 1.2, the subject of this dissertation is $b \to s\gamma$ transitions. In Section 1.1.2 we saw that by construction, flavour-changing neutral currents (FCNC) are forbidden in the Standard Model at the tree level; e.g., no $b \to sZ^0$ or $b \to dZ^0$ transitions are allowed. However FCNC transitions can be induced by higher order processes. For example, the so-called "penguin" processes result in effective

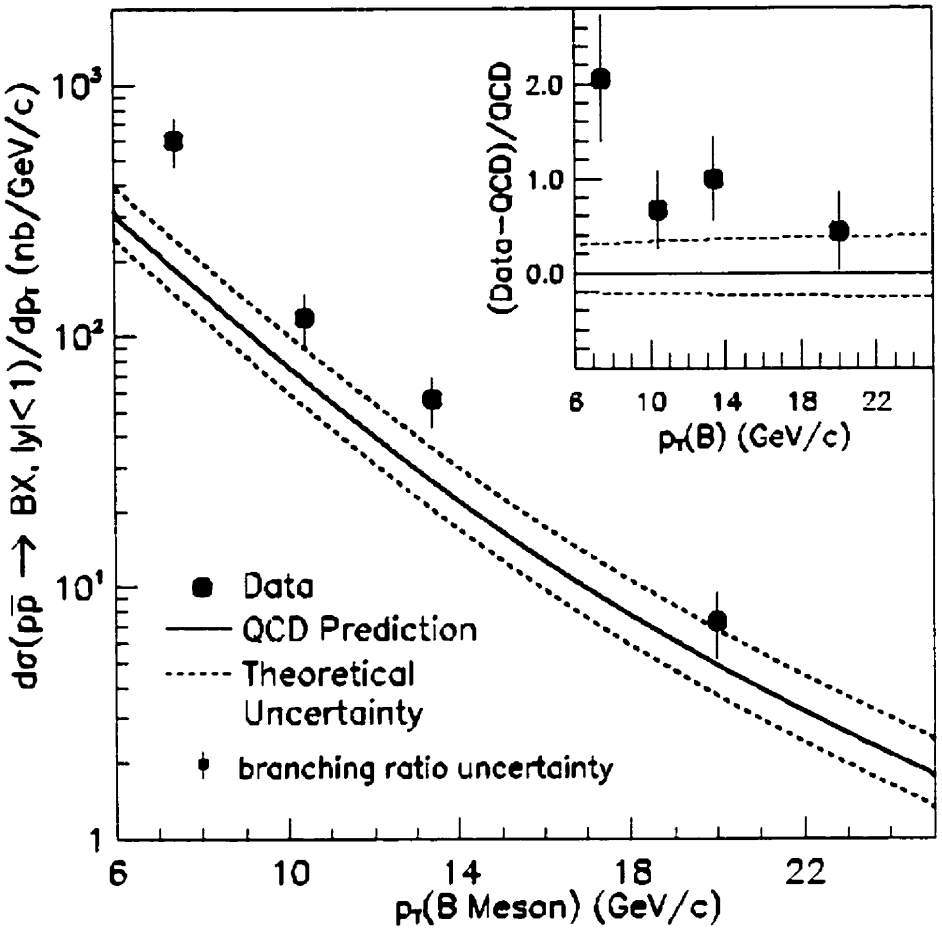

Figure 1.3: *Differential cross section for $p\bar{p} \rightarrow BX$, i.e. production of a B meson plus anything else at $p\bar{p}$ collisions at $\sqrt{s} = 1.8$ TeV.*

flavour-changing neutral current $b \rightarrow s$ or $b \rightarrow d$ transitions with the emission and reabsorption of a W boson from the b quark line, as shown in Fig. 1.1. When such a transition is accompanied by the emission of a photon (gluon), we refer to it as an "electromagnetic" ("gluonic") penguin decay. Since the CKM-favoured[5] b quark transition $b \rightarrow t$ is not kinematically allowed, penguin decays are a relatively important option for the b quark decays. Penguin processes are also possible in decays of the charm and top quarks, but these have CKM-favoured decays $c \rightarrow s$

[5]A CKM-favoured transition has its rate depending on a CKM matrix element with large magnitude (see Eq. 1.1 and 1.2).

and $t \to b$ which are kinematically allowed. Thus the importance of penguin decays for charm and top quarks is suppressed. This work deals with electromagnetic $b \to s\gamma$ transitions.

The lowest order amplitude for $b \to q\gamma$ transitions, with q denoting an s or d quark, is written as a sum of three terms, each describing the involvement of one of the charge $+\frac{2}{3}$ quarks in the penguin loop. Each one of these terms is proportional to $V_{ib}V_{iq}^{*}F_2(x_i)$, where $i = u, c, t$ and x_i is the square of the quark-to-W mass ratio, $x_i = m_i^2/m_W^2$ [21]. The function $F_2(x)$ is:

$$F_2(x) = \frac{x}{24(x-1)^4}[6x(3x-2)\ln x - (x-1)(8x^2+5x-7)] \qquad (1.6)$$

Because the u and c masses are small, $F_2(x_t)$ is much larger than $F_2(x_u)$ and $F_2(x_c)$. Furthermore, $|V_{ib}V_{iq}^{*}|^2$ is large for $i = t, c$ compared to u quarks. Thus the $b \to q\gamma$ amplitude is dominated by the presence of the t quark in the loop. In addition, measurements of the penguin transition rates are sensitive to contributions from heavy non-Standard-Model particles, such as heavy charged Higgs or supersymmetric particles. Therefore, measurements of loop processes constitute the most sensitive low energy probes for such extensions to the Standard Model [22].

Feynman diagrams containing the W and t propagators, like the $b \to s\gamma$ transition depicted in Fig. 1.1, describe the situation at energies of the order of the W mass. For the decays of b-flavoured hadrons the appropriate energy scale is set by the mass of the b quark which corresponds to relatively large wavelengths. The Wt loop of Fig. 1.1 is then replaced by a point-like interaction where the b quark enters an effective vertex from which the s quark and the photon originate. Such vertices are represented by "local operators", each one describing a specific class of interactions (e.g., $b \to s\gamma$, $b \to sZ^0$, etc.). This picture is a generalization of the Fermi theory where the coupling strength of weak interactions mediated by W bosons, g_W, is described by the Fermi constant G_F at low energies, with $G_F = \frac{\sqrt{2}g_W^2}{8m_W^2}$. In the unified electroweak theory $g_W = e/sin\theta_W$, where e is the charge of the positron and θ_W is the Cabibbo angle describing the d and s quark mixing in the case of two quark

generations only. The measurement of $sin^2\theta_W \simeq 0.23$ [4] indicates that the weak interactions are not that "weak" in principle, but that it is the heaviness of the W boson which results in a low effective strength for the weak interactions at low energies.

QCD corrections to the partonic $b \to s\gamma$ picture have to be taken into account, because the b quark decays while being part of a b-flavoured hadron, a system bound by the strong force. These corrections are incorporated in an effective low energy theory with five quarks, where the heavier degrees of freedom, i.e. the top quark and the W bosons, are not explicitly present. The information about these higher degrees of freedom is included implicitly in the effective coupling strengths and the so-called Wilson coefficients describing the effective strength of the operators at a given energy scale μ. In this framework, the amplitude for a $B \to X_s\gamma$ decay, with X_s denoting an s-flavoured hadron resulting from the B meson decay, can be written as [23, 24]

$$A(B \to X_s\gamma) = \langle X_s\gamma|\mathcal{H}_{eff}|B\rangle = \frac{G_F}{\sqrt{2}} \sum_i V^i_{CKM} C_i(\mu) \langle X_s\gamma|Q_i(\mu)|B\rangle \qquad (1.7)$$

where $Q_i(\mu)$ is the relevant local operator describing the interaction type i involved in this decay. The strength with which a given operator enters the effective Hamiltonian $\mathcal{H}_{eff}$ is described by the CKM factor V^i_{CKM} and the Wilson coefficients $C_i(\mu)$. For the case where the top quark is involved $V^i_{CKM} = V_{tb}V^*_{ts}$. The expansion of the Hamiltonian in terms of operator products allows the calculation to be performed into two distinct parts. The calculations of the Wilson coefficients involve the short distance (i.e. high energy) interactions, while the operator matrix elements $\langle X_s\gamma|Q_i(\mu)|B\rangle$ describe the long distance (i.e. low energy) interactions. For example, contributions of the top quark and other heavy particles (W, Z, charged Higgs, supersymmetric particles, and other non-Standard-Model particles) are included in the Wilson coefficients. The dependence on these heavy particles can be evaluated from the appropriate diagrams and the μ-dependence has to be properly estimated. Technically, the Wilson coefficients are calculated at some high energy scale (e.g., $\mu \sim m_W$) and

they are "evolved" to a low energy (e.g., $\mu \sim m_b$) using renormalization equations. These equations essentially transfer the physics information at energies higher than μ from the operator matrix elements into the Wilson coefficients and guarantee that the μ dependence of $C_i(\mu)$ is canceled by the μ dependence of $\langle X_s\gamma|Q_i(\mu)|B\rangle$, leading to observables that do not depend on μ [23]. Therefore, the value of μ separates the physics contributions into short distance and long distance and so it is a matter of choice what belongs to the Wilson coefficients and what belongs to the operator matrix elements. Although the choice of μ is in principle arbitrary, it is usually chosen to be of the order of the mass of the hadron. Since these calculations are performed perturbatively, truncation of the perturbative series results in inexact cancellation of μ dependencies. Inclusion of higher order terms minimizes the μ scale dependence.

1.4.1 Inclusive $B \to X_s\gamma$ decays

The inclusive $B \to X_s\gamma$ branching fraction, where X_s represents a collection of s-flavoured hadrons, is usually expressed in terms of the inclusive semileptonic $B \to X_c e\bar{\nu}_e$ branching fraction [25]:

$$\mathcal{B}(B \to X_s\gamma) = \left[\frac{\Gamma(B \to X_s\gamma)}{\Gamma(B \to X_c e\bar{\nu}_e)}\right]_{theory} \times \mathcal{B}(B \to X_c e\bar{\nu}_e) \tag{1.8}$$

with the theoretical calculation for the rates ($[\ldots]_{theory}$) performed along the lines discussed above. Unlike the Wilson coefficients, the operator matrix elements cannot be obtained perturbatively due to the large value of α_s at low energies. For inclusive transitions though, it has been shown [26] that the branching fraction can be approximated by the branching fraction of the relevant quark transition, which can be calculated easily. The first corrections to this approximation are of order $1/m_b^2$ and are small due to the relatively heavy b quark mass; including or neglecting these corrections makes a difference of only $\sim 1\%$ in $\mathcal{B}(B \to X_s\gamma)$ [21]. However, the evaluation of the Wilson coefficients introduces larger uncertainties. To leading-order all perturbative contributions can be absorbed into a single effective coefficient,

$C_7^{(0)eff}(\mu)$, which allows the inclusive $B \to X_s\gamma$ branching fraction to be written as [27]:

$$\mathcal{B}(B \to X_s\gamma) = \frac{|V_{tb}V_{ts}^*|^2}{|V_{cb}|^2}\frac{6\alpha_{em}}{\pi f(z)}|C_7^{(0)eff}(\mu)|^2\mathcal{B}(B \to X_c e\bar{\nu}_e) \tag{1.9}$$

where α_{em} is the electromagnetic coupling strength and $f(z)$ is a phase space factor for the semileptonic b-decays with $z = \frac{m_c}{m_b}$. For $\mu = 5$ GeV, $m_t = 170$ GeV/c^2 and $\alpha_s(m_Z) = 0.118$, $C_7^{(0)eff}(\mu) = -0.300$, whereas in the absence of QCD corrections $C_7^{(0)eff}(\mu) = C_7^{(0)}(m_W) = -0.193$ [27]. Thus QCD corrections enhance the inclusive $B \to X_s\gamma$ branching fraction by a factor of ~ 2.4. Note that the perturbative evolution of the Wilson coefficients from $\mu \sim m_W$ to $\mu \sim m_b$ results in the effective coefficient $C_7^{(0)eff}(\mu)$ depending on other Wilson coefficients as well, even though the contribution of $C_7^{(0)}$ is still the dominant one. The sensitivity of $\mathcal{B}(B \to X_s\gamma)$ to the mass of the top is not large, but it is present: $C_7^{(0)eff}(5\,\text{GeV}) = 0.254$ (0.313) for $m_t = 100$ (200) GeV/c^2. A 200 GeV/c^2 mass for the top quark would thus result in an inclusive branching fraction 1.5 times higher than for the $m_t = 100$ GeV/c^2 case. Due to the dependence of $C_7^{(0)eff}(\mu)$ on the μ scale, $\mathcal{B}(B \to X_s\gamma)$ estimates change by $\sim 20\%$ when μ is varied by a factor of 2 in both directions around $\mu = 5$ GeV. Inclusion of next-to-leading order terms reduces this uncertainty significantly, yielding a theoretical prediction of [24]

$$\mathcal{B}(B \to X_s\gamma) = (3.30 \pm 0.15 \pm 0.26) \times 10^{-4} \tag{1.10}$$

where the first uncertainty is the result of μ scale dependencies and the second uncertainty is due to uncertainties in the input parameters like $\mathcal{B}(B \to X_c e\bar{\nu}_e)$.

The CLEO [28] and ALEPH [29] collaborations have measured $\mathcal{B}(B \to X_s\gamma)$ to be:

$$\begin{aligned}(3.15 \pm 0.35 \pm 0.41) \times 10^{-4} \quad &\text{(CLEO)} \\ (3.11 \pm 0.80 \pm 0.72) \times 10^{-4} \quad &\text{(ALEPH)}\end{aligned} \tag{1.11}$$

in excellent agreement with the Standard Model prediction given above. The first uncertainties are statistical and the second are systematic. Unless the experimental

and theoretical uncertainties are reduced dramatically, no contributions from new physics can be seen in this decay. In fact, these results have placed significant constraints on non-Standard-Model contributions (see for example, Ref. [30]).

Alternatively, using the measured value of $\mathcal{B}(B \to X_s\gamma)$ and next-to-leading order Standard Model predictions, one can determine the CKM factor $\frac{|V_{tb}V_{ts}^*|^2}{|V_{cb}|^2}$ from Eq. 1.9. For example, Ali [25] uses information available to him at the time to report $\frac{|V_{tb}V_{ts}^*|^2}{|V_{cb}|^2} = 0.84 \pm 0.10$. Using $|V_{tb}| = 0.99 \pm 0.15$ and $|V_{cb}| = 0.0393 \pm 0.0028$ [31], he obtained:

$$|V_{ts}| = 0.033 \pm 0.007 \tag{1.12}$$

It is clear though that determinations of the CKM matrix elements from loop processes are subject to uncertainties due to possible participation of new physics in the loop. The determinations given above assume the Standard Model description only.

In exactly the same manner as described above, $b \to d\gamma$ transitions lead to $B \to X_d\gamma$ decays, where X_d represents any d-flavoured hadron. A measurement of the ratio of the inclusive branching fractions $\mathcal{B}(B \to X_s\gamma)/\mathcal{B}(B \to X_d\gamma)$ will then determine $|V_{td}/V_{ts}|$ with many theoretical uncertainties cancelling in the ratio of branching fractions. The unitarity of the CKM matrix is represented on the complex plane by a "unitary triangle" which results from the orthogonality of the first and third CKM matrix columns. The lengths of the sides of the unitarity triangle are given by the magnitudes of the CKM matrix elements, and one of the sides has a length proportional to $|V_{td}|$ [24]. Penguin decays can therefore be used to extract information about CP violation in the Standard Model. Note though that $b \to d\gamma$ transitions are suppressed by $|V_{td}/V_{ts}|^2$ and rejection of the dominant $b \to s\gamma$ decays requires very good particle identification. The experimental signature of such decays is less ambiguous, when exclusive decays like $B_d^0 \to K^{*0}\gamma$ and $B_d^0 \to \rho^0\gamma$ are considered. When the spectator quark in the B^0 meson of Fig. 1.1 is an $\bar{s}$ instead of a $\bar{d}$, $b \to s\gamma$ transitions lead to $B_s^0 \to \phi\gamma$ decays. We discuss exclusive electromagnetic penguin decays in the following section.

1.4.2 Exclusive $B_d^0 \to K^{*0}\gamma$ and $B_s^0 \to \phi\gamma$ decays

The distinctive signature of a high energy photon and two oppositely charged tracks from exclusive decays like $B_d^0 \to K^{*0}\gamma$, $K^{*0} \to K^+\pi^-$ and $B_s^0 \to \phi\gamma$, $\phi \to K^+K^-$, makes such decays experimentally accessible. Unlike the inclusive decays though, the operator matrix elements cannot be obtained easily. The branching ratios are then written in terms of "form factors" which exhibit strong model dependence. Extraction of CKM parameters from the measured branching fractions in a fashion similar to the one described for the inclusive decays, would require trustworthy determination of these form factors. Consequently, experimental determinations of the rates for exclusive electromagnetic penguin decays will initially be used to select amongst the various theoretical approaches.

A good quantity to test the model dependence of the form factors for the exclusive decay is the ratio of the exclusive-to-inclusive decay widths $R_{K^*} \equiv \mathcal{B}(B_d^0 \to K^{*0}\gamma)/\mathcal{B}(B \to X_s\gamma)$. The CLEO II collaboration has measured $\mathcal{B}(B_d^0 \to K^{*0}\gamma) = (4.0 \pm 1.9) \times 10^{-5}$ and $\mathcal{B}(B \to K^*\gamma) = (4.2 \pm 1.0) \times 10^{-5}$ including both $B_u^+ \to K^{*+}\gamma$ and $B_d^0 \to K^{*0}\gamma$ decays [32]. As always, charge conjugate decay chains are also included. This result in conjunction with the $\mathcal{B}(B \to X_s\gamma) = (3.15 \pm 0.35 \pm 0.41) \times 10^{-4}$ measurement, results in $R_{K^*} = (13.3 \pm 3.9)\%$. It is interesting to note that before the measurements by CLEO, theoretical predictions for R_{K^*} ranged from $5\% - 30\%$ [33, 34], whereas more recent calculations agree well with the CLEO measurement [27]. Therefore, the experimental input has been used to distinguish amongst theoretical models.

The theoretical uncertainties introduced in the form factors can be significantly reduced when considering the ratio $\mathcal{B}(B \to \rho\gamma)/\mathcal{B}(B \to K^*\gamma)$. This ratio is proportional to $|V_{td}/V_{ts}|^2$. Significant long distance effects on these decay channels could result in the proportionality factor not being purely due to phase space and the determination of $|V_{td}/V_{ts}|^2$ could be subject to large uncertainties. Taking account of long and short distance effects, Ali [35] calculates $\mathcal{B}(B_d^0 \to \rho^0\gamma) = (0.65 \pm 0.35) \times 10^{-6}$, where the uncertainty is mainly due to the poor knowledge of the CKM matrix ele-

ments. Therefore experimental measurements of these branching ratios will provide significant information on $|V_{td}/V_{ts}|$.

So far, $b \to d\gamma$ transitions have not been observed and only upper limits on the $B_d^0 \to \rho^0\gamma$, $B_d^0 \to \omega^0\gamma$ and $B_u^+ \to \rho^+\gamma$ branching fractions have been reported [30]. From these limits the CLEO collaboration obtains $0.45 < |V_{td}/V_{ts}| < 0.56$, where the range is mainly due to theoretical uncertainties.

Alternatively, determination of the relevant CKM matrix elements by other means, e.g., from $B^0 - \bar{B}^0$ mixing involving t quarks in "box" diagrams, can be used to guide theoretical approaches for the determination of long distance effects. This information can be applied to other decay modes involving the same theoretical uncertainties. For example, determination of the appropriate model to use in $B_d^0 \to \pi^+\pi^-$ decays, can reduce the uncertainty on the CP asymmetry to be measured with this channel, by providing reliable estimates of penguin contributions to $B_d^0 \to \pi^+\pi^-$ decays [27].

This dissertation describes searches for the decay chains $B_d^0 \to K^{*0}\gamma$, $K^{*0} \to K^+\pi^-$ and $B_s^0 \to \phi\gamma$, $\phi \to K^+K^-$ using a data sample of $\int Ldt = 28.9 \pm 1.2$ pb^{-1} of proton-antiproton collisions at $\sqrt{s} = 1.8$ TeV collected with the CDF detector at the Fermilab Tevatron collider. We attempt to measure the branching fractions of these decays and we exploit the topological similarity between the $\bar{B} \to e^- D^0 X$, $D^0 \to K^-\pi^+$ and these penguin decays, by forming ratios of branching fractions between the penguin and the $\bar{B} \to e^- D^0 X$ channels. Recall that on the theoretical side, uncertainties on B meson decays were reduced by forming ratios of branching fractions. Similarly on the experimental side, uncertainties associated with the B meson production cross section, common efficiency corrections and other systematic effects are minimal in the ratio of branching fractions.

Chapter 2 describes the accelerator used to produce B mesons and the detector used to record their decay products. Monte Carlo techniques employed in the determination of the efficiency for collecting the decay chains of interest are discussed in Chapter 3. The requirements implemented at the time of the data collection (i.e.

"on-line") in order to collect the penguin decays, are described in Chapter 4. The additional requirements imposed on the data off-line, and the final sample of events satisfying all selection criteria are presented in Chapter 5. The efficiencies of all the on-line and off-line selection requirements imposed on the data, and the effect of systematic uncertainties on them is the topic of Chapter 6. With the information presented in the previous chapters, the calculations of upper limits on the the ratio of branching fractions and on the absolute penguin branching fractions are described in Chapter 7. The last chapter summarizes the results and discusses the prospects for studies of electromagnetic penguin decays in the forthcoming data-taking period in the Tevatron.

Chapter 2

The Experiment

We try to identify events where a B_d^0 (B_s^0) meson decays into $K^{*0}\gamma$ ($\phi\gamma$) from a sample of events produced in proton - antiproton ($p\bar{p}$) collisions at a center-of-mass ($\sqrt{s}$) energy of 1.8 TeV.

The accelerator that brings the protons and antiprotons into such energetic collisions is the Tevatron collider located at the Fermi National Accelerator Laboratory, generally known as Fermilab, located at Batavia, Illinois, USA. The detector that measures properties of the particles that are produced in these collisions is the Collider Detector at Fermilab (CDF).

In this chapter I will describe the basic steps of the acceleration process of the protons and the antiprotons to 900 GeV of energy and the CDF detector, giving more emphasis to the parts and functions of the detector that are important to the topic of this research project.

2.1 The Fermilab Tevatron Collider

The Tevatron collider [36] brings 900 GeV protons into collision with 900 GeV antiprotons. Therefore the center-of-mass energy of a colliding proton-antiproton pair is 1.8 TeV. The acceleration of the protons (antiprotons) to this energy is a process

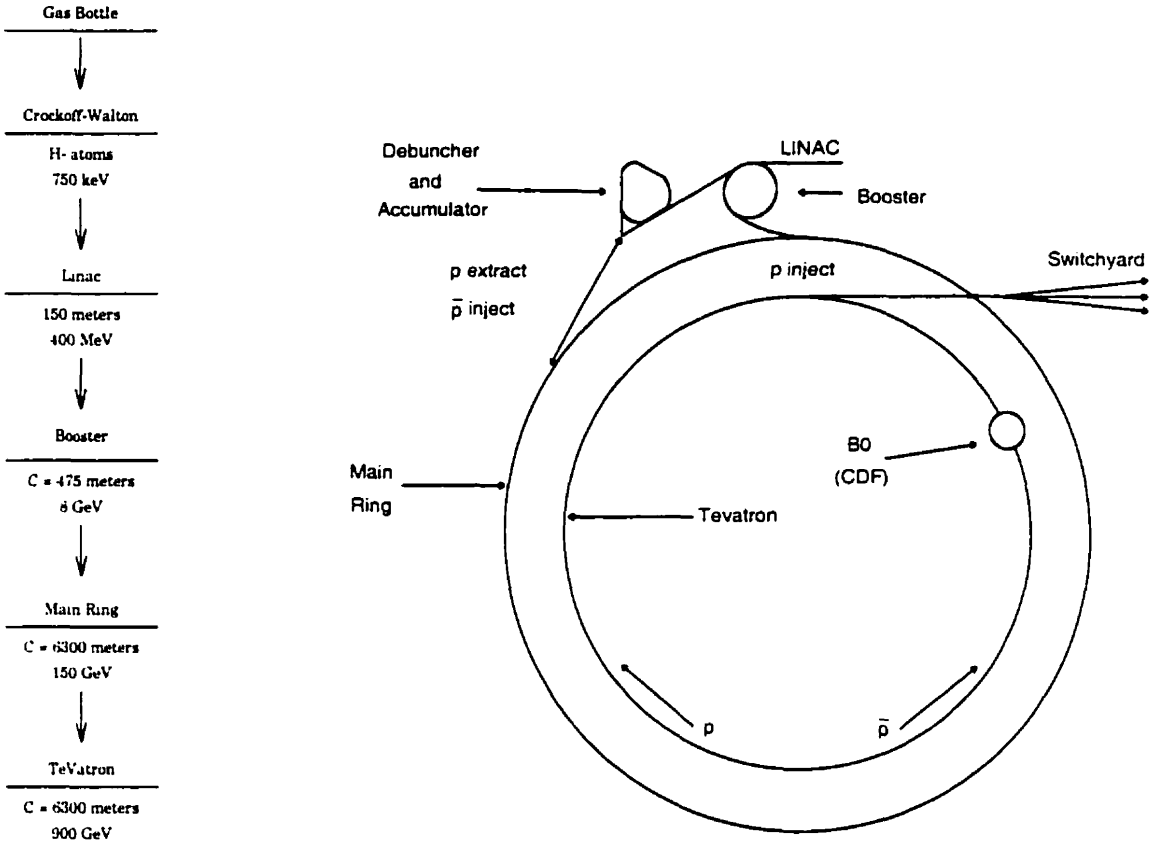

Figure 2.1: Left: *Flow chart of the proton acceleration path.* Right: *The accelerator complex at Fermilab and the location of CDF around the Tevatron ring.*

that involves five (six) accelerators. In Fig. 2.1 a flow chart of the proton acceleration process is given, along with the layout of the Fermilab accelerator complex.

We start by putting an extra electron in the hydrogen atoms and thus having the gaseous H_2 molecules converted into negatively charged hydrogen ions (H^-). We do this inside a Cockcroft-Walton electrostatic accelerator which accelerates the H^- ions across an electric potential difference of 750 kV. Thus the H^- ions obtain an energy of 750 keV.

After leaving the Cockcroft-Walton accelerator, the H^- ions enter a linear accelerator (Linac) which is approximately 500 feet long. The Linac consists of a series of drift tubes spaced further and further apart with the electric field applied to the

tubes repeatedly reversing in direction (i.e. oscillating). The particles travel through the drift tubes when the electric field is in the direction that would slow them down and emerge into the gaps between the drift tubes when the field is in the direction to speed them up. In this fashion the H^- ions are accelerated to energies of 400 MeV in the Linac.

As the beam of H^- ions enters the third accelerator, the circular Booster, it passes through a carbon foil where both electrons of each ion are stripped off leaving a beam of protons. Located nearly 20 feet below ground, the Booster is a rapid cycling synchrotron 500 feet in diameter. As all synchrotrons, it uses magnets to deflect electrically charged particles in a circular path so that they experience the repeated action of accelerating electric fields during each revolution. The protons travel around the Booster about 16000 times and their energy is raised to 8 GeV. The Booster normally cycles twelve times in rapid succession, loading twelve bunches of protons (pulses) into the Main Ring, the next stage of the acceleration process.

The Main Ring is another proton synchrotron which is $\simeq$ 1 km in radius. A tunnel ten feet in diameter, 20 feet underground, houses 1014 conventional copper-coiled dipole and quadrupole magnets which continually bend and focus the protons. Under the operating conditions of the period 1985-1996, the Main Ring accelerated protons to 150 GeV. Work is currently being done to replace the Main Ring with the Main Injector, a synchrotron located tangentially to the Tevatron. The main goal of this new accelerator is to be able to provide the Tevatron with more hefty bunches of protons and antiprotons and to simultaneously provide a beam of protons to the Tevatron collider as well as to the fixed target experiments.

The same tunnel that houses the Main Ring also contains the $\sim$ 1000 superconducting magnets (772 dipole bending magnets and 224 quadrupole focusing magnets) which comprise the proton synchrotron known as the Tevatron because of its ability to accelerate protons to nearly 1 TeV. The superconducting niobium-titanium (Nb-Ti) magnets form a ring directly below the Main Ring magnets and operate

in the temperature range of liquid helium (4.7 degrees Kelvin). Superconducting magnets are used because of their ability to produce larger magnetic fields at a lower operating cost than conventional magnets.

To produce the antiprotons, protons are first accelerated to an energy of 120 GeV in the Main Ring, extracted, transported to a target area, and focused on a 7 cm thick nickel or copper target. Almost 3.3×10^{12} protons every 2.4 seconds are used for antiproton production. The collisions in the target produce a wide range of particles including many antiprotons. Antiprotons of momenta $\sim$ 9 GeV/c are selected and transported to the Debuncher ring where the dimensions and energy spread of the beam are reduced using the debunching technique and a processes known as stochastic cooling. They are then transferred to the Accumulator ring for storage. Finally, when a sufficient number has been accumulated, the antiprotons are reinjected into the Main Ring, they are accelerated to 150 GeV and passed down into the Tevatron, where there is already a counter-rotating beam of 150 GeV protons; both beams are then accelerated simultaneously to an energy of 900 GeV in 86 seconds.

Having an energy of 900 GeV and traveling along a path $\sim$ 60 μm wide, proton and antiproton bunches circulate around the accelerator's $\simeq$ 6.28 km track 45 thousand times every second. Each proton bunch has around 230 billion protons, whereas each antiproton bunch has around 55 billion antiprotons. When all six bunches of protons and 6 bunches of antiprotons are in the Tevatron collider and at maximum energy, we say that the *store* has started.

There are 12 possible regions around the Tevatron where the two beams can be made to collide with each other. Collisions in ten of these regions were avoided in the 1993-96 run by the use of electrostatic separators to keep the proton and antiproton beams apart. The CDF detector surrounded the B0 interaction region and the D0 detector surrounded the D0 interaction region. Due to the large number of particles in the bunches and the large probability of $p\bar{p}$ interaction, there are around 2.5 $p\bar{p}$

interactions per beam crossing at the beginning of a store. In Table 2.1 we show some of the parameters that describe the operational conditions of the Tevatron during the 1993-1996 period.

The number of bunches circulating around the Tevatron along with the number of particles per bunch and the size of each bunch determine how often a particle of one kind "meets" another particle of the oncoming bunch. The parameter that combines this information is the luminosity, L, which is defined as follows:

$$L = \frac{f n_b N_p N_{\bar{p}}}{2\pi\sqrt{\sigma_p^2 + \sigma_{\bar{p}}^2}} F(\frac{\sigma_\ell}{\beta}) \tag{2.1}$$

where f is the revolution frequency of the proton and antiproton bunches, n_b is the number of bunches in each beam, N_p ($N_{\bar{p}}$) is the number of protons (antiprotons) in each bunch, σ_p ($\sigma_{\bar{p}}$) is the proton (antiproton) beam size at the interaction point, and F is a form factor that depends on the ratio of the bunch length, σ_ℓ, to the β function at the interaction point, β^*. The β function describes the amplitude of the beam particle oscillations as a function of their position s around the collider ring. The size of each beam depends on the β function as well as on the emittance, ϵ, which describes the phase-space available to the circulating beam particles; $\sigma(s) = \sqrt{\epsilon\beta(s)}$.

From Eq. 2.1 we see that the units of luminosity are $area^{-1} \times time^{-1}$, the common units being $cm^{-2}s^{-1}$. If we multiply the luminosity with a cross section σ (units of area) which describes the probability to observe a certain outcome of the $p\bar{p}$ collision, we can calculate the rate R at which this outcome occurs. Therefore:

$$R = \sigma L \tag{2.2}$$

Using the total $p\bar{p}$ cross section of $\sigma_{total} = 80.03 \pm 2.24$ mb [1] at $\sqrt{s} = 1.8$ TeV [37], we find that the rate of $p\bar{p}$ interactions is ~ 1.3 MHz at the beginning of a store [2].

[1] One barn, b, is a unit of area equal to 10^{-24} cm^2.

[2] The rate of inelastic $p\bar{p}$ interactions is around 800 kHz, since the cross section for inelastic $p\bar{p}$

Parameter	1993 - 1996 Run	Units
RF frequency	53	MHz
Peak magnetic field in sc. magnets	4.4	Tesla
Acceleration period	86	s
Maximum beam energy	900	GeV
Proton and antiproton bunches	p: 6 $\bar{p}$: 6	
Protons/bunch	23×10^{10}	
Antiprotons/bunch	5.5×10^{10}	
Antiproton production rate	6.0×10^{10}	hr^{-1}
Max. number of $\bar{p}$ in accumulation ring	2×10^{12}	
Injection time	2.5	hr
Duration of a store	12	hr
Percentage of antiprotons at end of store	73%	
Percentage of luminosity at end of store	$1/e$	
Beam radius	~ 30	μm
Proton transverse emittance	23π	mm mrad
Antiproton transverse emittance	13π	mm mrad
β^* (at interaction point)	35	cm
Bunch length (rms)	60	cm
Bunch spacing (time)	~ 3.5	μs
Typical initial instantaneous luminosity	1.6×10^{31}	$cm^{-2}sec^{-1}$
Luminosity lifetime	7 – 30	hr
Integrated luminosity	~ 3.2	pb^{-1}/week
Inelastic interactions/crossing	~ 2.5	

Table 2.1: *Parameters for the Fermilab Tevatron during the 1993-1996 run period.*

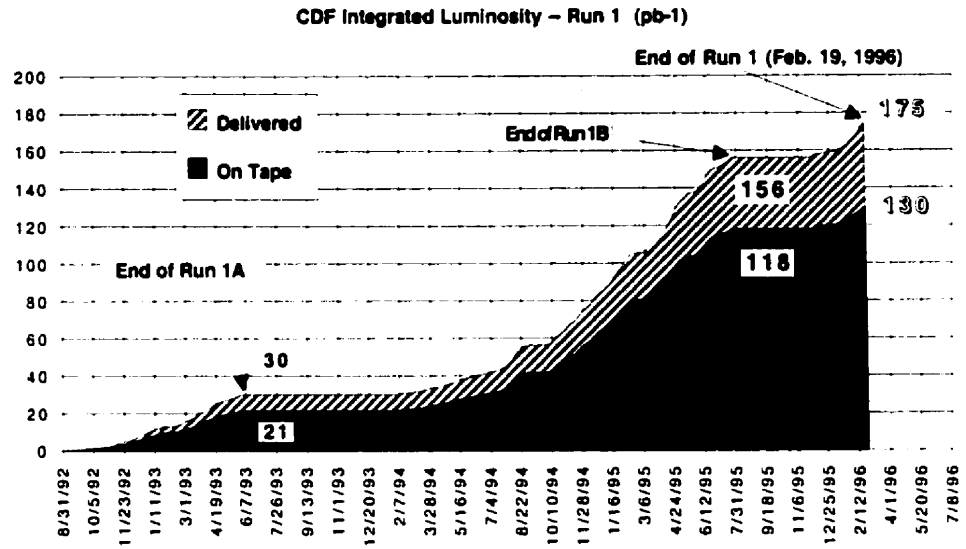

Figure 2.2: *The integrated luminosity delivered to the B0 collision point by the Tevatron collider and the corresponding luminosity that was actually "seen" by CDF.*

The rate of $p\bar{p}$ interactions, and thus of any specific class of events that comes out of a $p\bar{p}$ interaction with a given probability (e.g., production of B mesons or top quarks), increases proportionally with luminosity. As we can see from Eq. 2.1, the more populated the proton and antiproton bunches and the smaller the beam sizes are, the higher the luminosity of the $p\bar{p}$ collider is. The main limiting factor to increased luminosity in the 1993-96 run was the number of available antiprotons in the collider. The luminosity of any store continually decreases from its initial value as protons and antiprotons take part in $p\bar{p}$ interactions or are lost to beam-gas interactions and as the size of the beams increases because of the beam-beam scatterings; typically it drops to half after 7 hours and to $1/e$ of it original value after about 12 hours.

The total number of $p\bar{p}$ interactions is given by the time integration of the rate given in the above formula; therefore the integrated luminosity $\int Ldt$ multiplied by the cross section for any process gives us the number of times this process should have

collisions is $\sigma_{inel} \simeq 50$ mb [38].

occurred during the data-taking period. In Fig. 2.2 we see the data taking periods and integrated luminosity delivered to and accumulated by the CDF detector during the years 1992 – 1996, a data taking period labeled "Run 1". The difference results from the non data-taking periods for the detector while the beams were colliding at the Tevatron (technical problems, etc.). During 1992 – 1996 CDF collected data within three sub-periods that are evident in Fig. 2.2; Run 1A, Run 1B and Run1C. The data used in this thesis were collected during the last quarter of Run 1B and the last half of Run 1C.

2.2 The Collider Detector at Fermilab (CDF)

The Collider Detector at Fermilab (CDF) surrounds the B0 collision point of the Tevatron collider. It is a complex detector made up from many subsystems, each having a complementary role in the detection of the particles emerging from the $p\bar{p}$ collision. Being in the complex yet very rich $p\bar{p}$ physics environment, the CDF detector was designed to be a "general purpose" detector able to trigger on [3] and measure as many individual elements of each event as possible. The main goal of the CDF detector is to trigger on, identify and reconstruct the kinematics (and charge where applicable) of electrons, muons, photons and jets. Emphasis is also placed on the precise reconstruction of charged particle trajectories (usually called "tracks") and measurement of their momenta.

Since the particles produced at the high energy $p\bar{p}$ collisions are uniformly distributed in the space described by the rapidity (see Chapter 1) and azimuthal angle, CDF has a cylindrical geometry with the beam-line being the axis of the cylindrical symmetry and it has a uniform segmentation in the pseudorapidity – azimuthal angle space. In the CDF coordinate system, θ is the polar and ϕ is the azimuthal

[3] As we saw above, the rate of $p\bar{p}$ interactions is around 1 MHz at the beginning of a store. Since it is impossible to record them all, the detector's first task is to decide which collisions are worth recording. Therefore, it has to "trigger" only on the events that look interesting.

angle, with respect to the proton beam direction, which is the z direction. The radial distance from the z axis is denoted by r. The coordinate system is right-handed with the x axis pointing radially outwards in the plane of the Tevatron ring and the y axis vertically upwards. The pseudorapidity η is defined as $-\ln[\tan(\theta/2)]$. When we describe the direction of a particle its pseudorapidity approximates its rapidity to the extent that the mass of the particle is negligible with respect to its energy. The transverse momentum of a particle is $p_T = p \cdot \sin\theta$, where p is its momentum. The analogous quantity using calorimeter energies, defined as $E_T = E \cdot \sin\theta$, is called transverse energy, where E is the energy of the particle or the jet that is measured in the calorimeters. Missing transverse energy $\not\!\!E_T$ is defined as $-\sum E_T^i \cdot \hat{n}_i$, where $\hat{n}_i$ are the unit vectors (in the transverse, i.e. $r-\phi$, plane) pointing from the interaction point to the energy deposition in the i^{th} calorimeter cell. A large $\not\!\!E_T$ indicates undetected energy in the transverse plane mainly due to energetic neutrinos escaping the detector volume undetected.

2.2.1 Overview

The CDF detector [39] is a magnetic spectrometer which covers up to 98% of the solid angle. An isometric view of the CDF detector is shown in Fig. 2.3; a cross sectional view of one quadrant of the detector is shown in Fig. 2.4. Moving radially outwards from the beam line, the basic units of the CDF detector are:

At the heart of the detector is a part of the Tevatron; the beryllium beam pipe, where the proton and antiproton bunches collide, with the nominal collision point being at the center of symmetry of the CDF detector. The beryllium beam pipe is 3.8 cm in diameter and 0.5 mm thick and is, by definition, along the z axis of the CDF coordinate system.

A system of tracking detectors, used to measure charged particle trajectories, surrounds the beryllium pipe. The tracking detectors are surrounded by a solenoidal coil of 1164 turns made of superconducting Nd-Ti/Cu material. The coil is 4.8 m

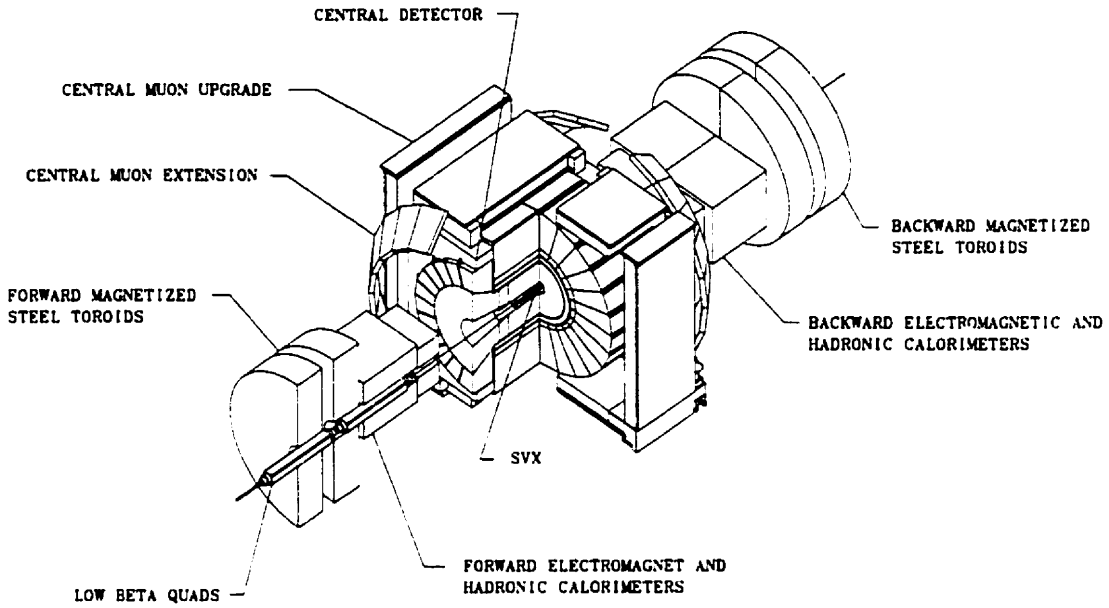

Figure 2.3: *A isometric view of the CDF detector. The $p\bar{p}$ beam axis is the axis of the cylindrical symmetry of the Collider Detector at Fermilab.*

in length, 1.5 m in radius, and produces a $\sim$ 1.4 Tesla magnetic field parallel to the beam-line. The charged particles produced at the $p\bar{p}$ collision point curve as they travel through this magnetic field; the measurement of the curvature of their tracks allows a measurement of their momenta. The tracking detectors are described in Section 2.2.2.

A "preradiator" detector (CPR) made of proportional drift chambers surrounds the solenoid and measures the early part of electromagnetic showers that start when electrons and/or photons pass through the $\sim$ 0.85 radiation lengths of the solenoid.

A system of calorimeters surrounds the tracking volume, the solenoid and the preradiator detector. Their purpose is to measure the energy of electrons and photons as well as of "jets" of particles. Since the electromagnetic showers of particles induced by electrons and photons are contained within a depth of $\sim 20X_0$ [4] in the

[4]The radiation length, X_0, describes the average distance an electron has to travel before losing $1/e$ of its energy.

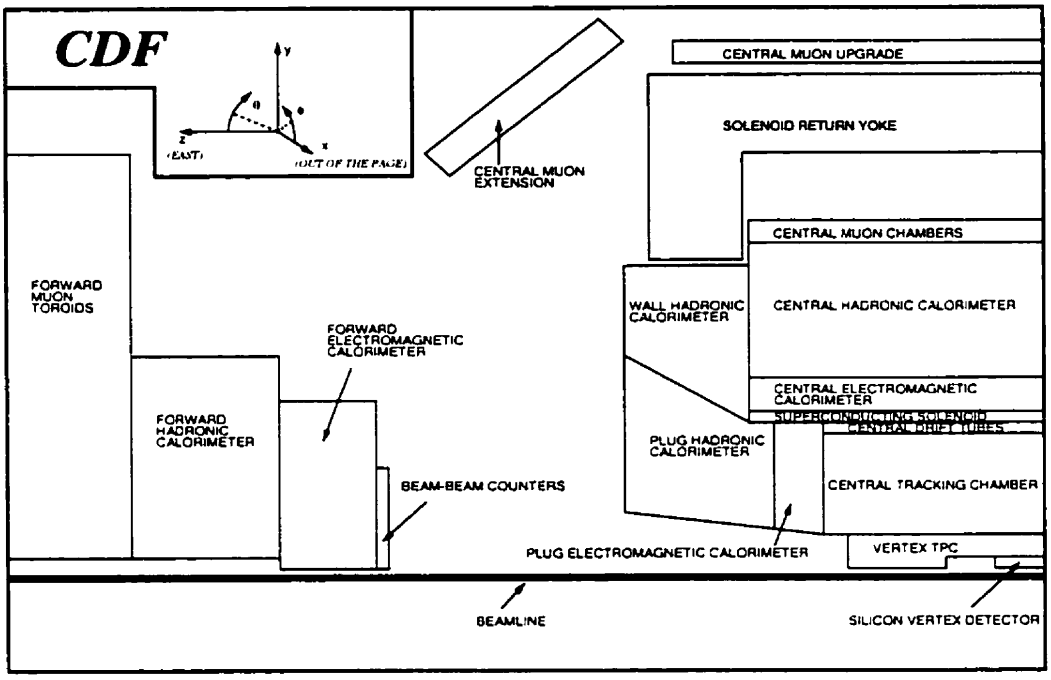

Figure 2.4: *A quadrant view of the CDF detector. The $p\bar{p}$ beam axis is the axis of the cylindrical symmetry of the Collider Detector at Fermilab.*

calorimeter material, whereas the showers induced by hadrons continue deeper in the calorimeter volume, the calorimeters are separated into two main components which can be viewed as hollow cylinders coaxial with the beam line. The components closest to the beam axis are designed to detect photons and electrons by measuring the electromagnetic shower that originates when such a particle enters matter. Such calorimeter devices are called "electromagnetic" calorimeters. The "outer" components, called "hadronic" calorimeters, serve in the detection of hadrons by virtue of their energy deposition due to the strong interaction with the detector material. Since the particles originating from the $p\bar{p}$ collisions are uniformly distributed in $\eta - \phi$ space and it is essential to reconstruct jets in the CDF detector, the calorimeters are segmented into projective divisions (called towers) in $\eta - \phi$ space that point towards the nominal $p\bar{p}$ interaction point.

The CDF detector is divided into a central ($|\eta| < 1.1$), two plug ($1.1 < |\eta| < 2.4$)

Calorim. system	$\|\eta\|$ coverage	Granularity ($\Delta\eta \times \Delta\phi$)	Resolution $\sigma(E)/E$	Thickness	Active material	Absorber material
CEM	$0 - 1.1$	0.11×15^o	$\sqrt{\left(\frac{13.5\%}{\sqrt{E_T}}\right)^2 + (2\%)^2}$	$18\ X_0$	Scint.	Pb
PEM	$1.1 - 2.4$	0.09×5^o	$\sqrt{\left(\frac{22\%}{\sqrt{E}}\right)^2 + (2\%)^2}$	$18 - 21\ X_0$	Gas	Pb
FEM	$2.2 - 4.2$	0.1×5^o	$\sqrt{\left(\frac{26\%}{\sqrt{E}}\right)^2 + (2\%)^2}$	$25\ X_0$	Gas	Pb/Sb
CHA	$0 - 0.9$	0.11×15^o	$\sqrt{\left(\frac{50\%}{\sqrt{E_T}}\right)^2 + (3\%)^2}$	$4.5\ \lambda_0$	Scint.	Fe
WHA	$0.7 - 1.3$	0.11×15^o	$\sqrt{\left(\frac{75\%}{\sqrt{E}}\right)^2 + (4\%)^2}$	$4.5\ \lambda_0$	Scint.	Fe
PHA	$1.3 - 2.4$	0.09×5^o	$\sqrt{\left(\frac{106\%}{\sqrt{E}}\right)^2 + (6\%)^2}$	$5.7\ \lambda_0$	Gas	Fe
FHA	$2.4 - 4.2$	0.1×5^o	$\sqrt{\left(\frac{137\%}{\sqrt{E}}\right)^2 + (3\%)^2}$	$7.7\ \lambda_0$	Gas	Fe

Table 2.2: *Characteristics of the electromagnetic (xEM) and hadronic (xHA) calorimeter systems in CDF. "Scint." ("Gas") indicates the usage of plastic scintillator (gas chambers) to detect the energy deposited in the calorimeter volume.*

and forward-backward ($|\eta| > 2.5$) regions. Each region has an electromagnetic and a hadronic calorimetric component. All the CDF calorimeters are sampling devices with the active material being scintillating plastic for the central electromagnetic (CEM), central hadronic (CHA) and wall hadronic (WHA), while it is gas for the plug electromagnetic (PEM), plug hadronic (PHA), forward electromagnetic (FEM) and the forward hadronic (FHA) calorimeters. The absorbing materials [5] are lead for the electromagnetic and iron for the hadronic calorimeters. Table 2.2 summarizes some characteristics of the CDF calorimeters. Due to its relevance to this thesis, the CEM is described in more detail in Section 2.2.3.

[5] Absorbing material must have small radiation (X_0) and interaction (λ_0) lengths so as to contain the showers in as small a depth as possible. One interaction length is the average distance a charged pion has to travel in a material before losing $1/e$ of its initial energy.

Farthest away from the interaction region, outside of the hadronic calorimeters, are drift chambers dedicated to the detection of muons. Muons are the most penetrating of the massive particles and therefore most of the particles reaching the muon detectors will indeed be muons. There are three subsystems dedicated to muon detection in the central CDF region ($|\eta| < 1$):

(i) The central muon detector (CMU) covers the region $|\eta| < 0.6$ and is located immediately outside the CHA detector (at $r = 347$ cm). There are ~ 5.4 interaction lengths ($5.4\lambda_0$) of material (most of it in the CHA calorimeter) between its face and the $p\bar{p}$ interaction point, which means that only one out of 220 hadrons will make it through the CHA calorimeter and reach the CMU detector. We call such hadrons "punch-through" hadrons and they are present in many samples of "muons" as a background.

(ii) The central muon upgrade detector (CMP) covers the same η region as the CMU, but it is located outside the return yoke of the solenoid which means that particles have to go through an additional ~ 2.4 interaction lengths of material to reach the CMP. Therefore only one out of ~ 2400 hadrons can reach the CMP detector and the purity of the muon samples collected by the CMP is dramatically increased compared to the corresponding CMU samples. The CMP detector does not have the typical cylindrical geometry of the CDF subsystems, but is a "box"-like structure as can be see in Fig. 2.3.

(iii) The central muon extension detector (CMX) covers the region $0.65 < |\eta| < 1.0$. In order for a particle to reach this detector it has to travel at smaller polar angles than when it is heading towards the CMU detector. Therefore, it has to go through ~ 6.2 interaction lengths of material (at $\theta = 55^o$) in order to reach the CMX chambers. The geometry of the CMX detector is a surface slice of a cone that has the beam line as its axis (see Fig. 2.3).

For the reconstruction of the $B_d^0 \to K^{*0}\gamma$, $K^{*0} \to K^+\pi^-$ and $B_s^0 \to \phi\gamma$, $\phi \to K^+K^-$ decay channels we clearly need good tracking and calorimetry in order to reconstruct

the two charged particles and the photon that are the final decay products. Only photons that were detected in the CEM calorimeter are of concern in this analysis, therefore only the CEM calorimeter and the tracking systems are described below.

2.2.2 The Tracking Devices

The CDF detector has four main tracking devices that are cylindrical in geometry with the beam axis being their main symmetry axis. In increasing order of radius, they are: the silicon vertex detector (SVX), the vertex time projection chamber (VTX), the central tracking chamber (CTC), and the central drift tube array (CDT) which is not described here, since it is not used in this analysis.

The Silicon Vertex Detector (SVX)

The main goal of the SVX detector [40, 41] is the identification of the decay points of the long lived b quarks traveling away from the $p\bar{p}$ collision. This detector provides information about the travel path of charged particles but only in the $x - y$ (i.e. "transverse") plane. It is essential in this analysis since its precise tracking close to the beam line can help us distinguish the tracks from the B decay products from the plethora of tracks originating from the $p\bar{p}$ interaction point.

The SVX detector consists of two barrels (Fig. 2.5) that are made of four concentric cylindrical layers located at radii 2.9, 4.3, 5.7 and 7.9 cm. The SVX covers the region $0.5 < |z| < 25.55$ cm, with one barrel covering the positive and the other the negative z side. Since the $p\bar{p}$ collisions are distributed in a rather long region (Gaussian distribution with $\sigma \simeq 30$ cm; see also Table 2.1), only around 60% occur in the SVX fiducial volume.

Each layer is segmented into twelve flat ladders that cover 30^o in azimuth (see Fig. 2.6). Each ladder has three single sided silicon wafers that are electrically bonded together and lie on a light-weight (Rohacell foam) substrate. Thus each ladder has 25.5 cm of silicon as an active detector region. The silicon wafers are 300 μm thick

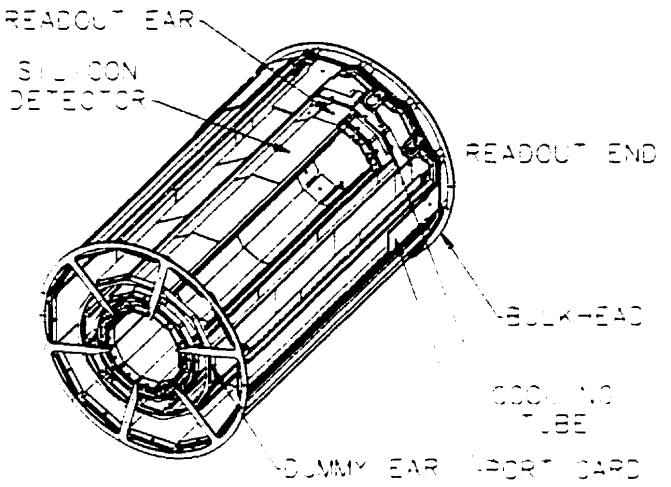

Figure 2.5: *One of the two identical barrels of the SVX detector. The two barrels are connected to the "dummy ears" of each ladder and they leave a gap of* $\simeq 0.5$ *cm on each side of the* $x - y$ *plane that passes through* $z = 0$.

n-type semiconductors that have p-type strips on one side (thus we talk about "single sided silicon detectors"). The strips are 60 μm apart in the inner three layers and 55 μm apart in the outer layer. When a charged particle passes through the silicon, it releases electron-hole pairs via ionization of the material. The electrons and holes travel towards the positive and negative electrodes respectively and the electronic signal caused by them gives information on the position where the traveling charged particle hit the silicon. The average position resolution is around 12 μm and the average impact parameter (distance of closest approach to the beam line) resolution for high p_T tracks is 13 μm.

The electric signal generated in the strips are read by 128 channel chips which are mounted on the "readout ear" of each ladder (see Fig. 2.6). Each chip can read 128 channels and since the width of the ladders increases as we move from the inner to the outer layer (each ladder covers 30^o in ϕ), there are two chips per ladder in the inner layer compared to six chips for each of the outer layer ladders. The total number of channels read out of the SVX detector is 46080. The readout chips of the

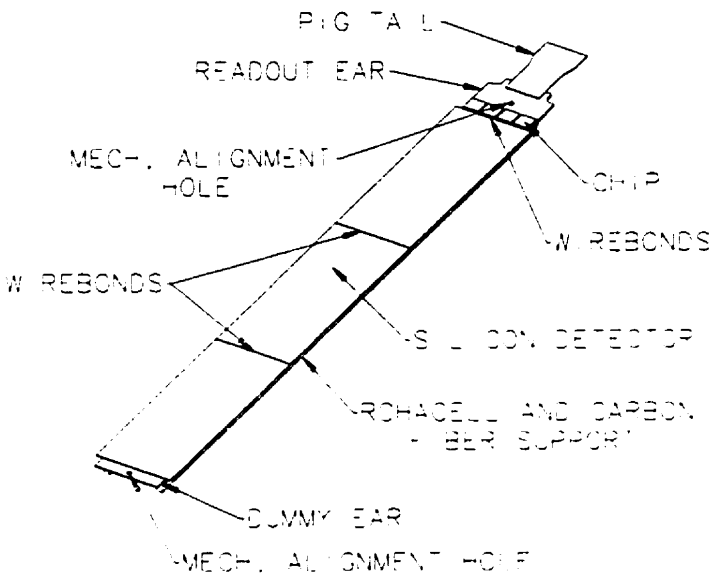

Figure 2.6: *A typical ladder module of the SVX made of three single sided silicon microstrip detectors bonded together. The dummy ear of each ladder is connected to the corresponding ear of the ladder that is part of the opposite z SVX barrel.*

SVX detector are manufactured using radiation-hard 1.2 μm CMOS technology and they have an absorption dose limit of $\sim$ 10 kGy.

The Vertex Time Projection Chamber (VTX)

The VTX detector [42] reconstructs the tracks of charged particles in the $r-z$ plane up to $|\eta| < 3.25$. Its primary task in this analysis is to locate the $p\bar{p}$ interaction point along the z axis. This is essential in order to calculate the kinematics of the reconstructed B decay. The resolution of the determination of the $p\bar{p}$ interaction point is around $1-2$ mm, depending on the number of charged tracks going through the VTX [6].

This time projection chamber covers the region $-136 < z < 132$ cm with 28 drift modules that have an outer radius of 22 cm and are connected together along the z axis. In Fig. 2.7 we see two halves of two drift modules, with their end-caps

[6]Recall that the $p\bar{p}$ interactions are distributed normally with a standard deviation of 30 cm.

connected along the z axis. Each drift module is divided into two drift regions; the electrons resulting from the ionization caused when a charged particle traverses the gas of the chamber drift away from the high negative voltage aluminum grid in the center of the module ("H.V. grid" in Fig. 2.7) until they pass through a cathode grid not shown[7]. Subsequently, the electrons enter the proportional chamber region where they move towards the anode sense wires at the end-cap of the drift module.

The end-plates of each module are segmented in octants that have 16 anode sense wires in the $r-\phi$ direction (see Fig. 2.7). The modules that are in the extreme z positions have 24 sense wires on each octant, since they have a smaller inner radius (see Fig. 2.4).

The electronic signal induced in the sense wires by the arriving electrons provides r information about the track that caused the ionization of the gas. Knowing the time of the $p\bar{p}$ interaction and the time of the arrival of the ions at the end-plates provides the z information as well. The electric field is around 1.6 kV/cm and the gas used is 50% argon and 50% ethane.

The signals in the VTX sense wires are read with a preamplifier mounted on the detector itself with the strategy being similar to that of the central tracking chamber read-out system (see below).

The Central Drift Chamber (CTC)

The central drift chamber is the main tracking device of the CDF detector [43]. It is the only tracking device that can perform three dimensional reconstruction of the tracks of charged particles and thus it is the only CDF tracking system that can perform stand-alone tracking. It is absolutely essential in this analysis since some of the decay products of the penguin decays are charged particles.

The CTC is a drift chamber which has a cylindrical geometry with an inner

[7]This grid has a higher algebraic voltage than the central H.V. grid, but less than the anode sense wires.

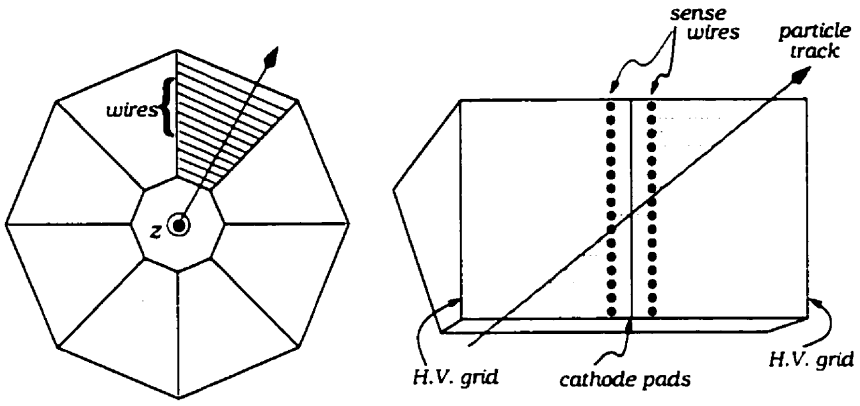

Figure 2.7: *Cross section view of the VTX detector and its operation principle.*

(outer) radius of 27.7 (138) cm and a length of 320 cm. It contains 84 concentric layers of gold-plated Tungsten sense wires with a diameter of 40 μm, with a total of 6156 sense wires. These 84 layers are grouped together into 9 "superlayers" as shown in Fig. 2.8. Five of these superlayers are made of twelve layers that have their wires parallel to the z axis (so-called "axial superlayers"). The remaining four superlayers have their wires tilted at a 3^o angle with respect to the z axis ("stereo superlayers"). Moving radially away from the VTX we meet alternating axial and stereo CTC superlayers with the inner superlayer being an axial one at a radius of 30.9 cm. The outermost superlayer extends to a radius of 132 cm. As a charged particle deflects in ϕ in its passage through the axial magnetic field, the axial layers provide position information in the $r-\phi$ view, whereas the stereo layers can provide information in the $r-z$ view as well. Thus we can reconstruct the path of a charged particle through the CTC in all three dimensions.

The superlayers are arranged in such a way that they form open drift cells with 12 (6) anode sense wires alternating with 13 (7) potential wires in the axial (stereo) superlayers. The use of multiple sense wires in a single cell allows us to look for correlated information in neighboring sense wires in order to take care of corrupted or ambiguous information. Each cell is bounded on both sides of the sense wires by steel field wires, which along with field shaper wires keep the $\sim$ 1350 V/cm electric

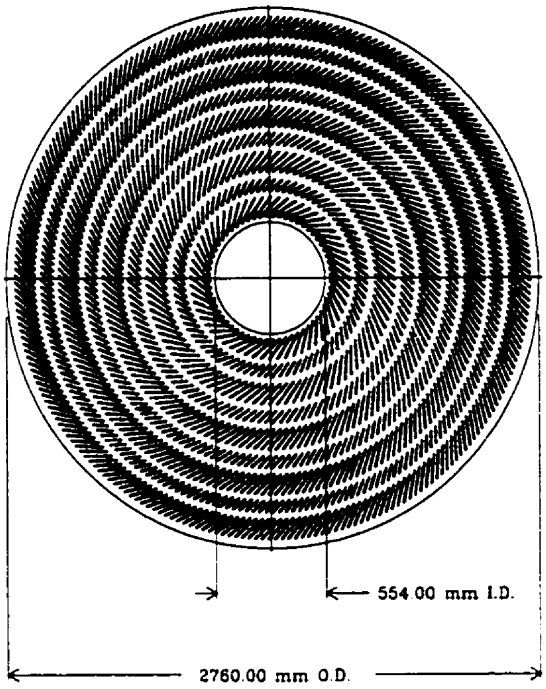

Figure 2.8: *One end-plate of the CTC. The grouping of the sense wires into 9 "superlayers" is apparent. The chamber is placed such that the magnetic field is perpendicular to this end-plate and points inwards.*

field uniform at the 1.5% level.

The size of each cell is large enough to minimize the number of wires required, yet small enough to have a maximum drift distance of less than 40 mm, corresponding to about 800 ns of drift time [8]. Including the sense, potential, field and field shaper wires, we have a total of 36504 wires in the CTC which translates to a total wire tension of 25 tons.

Drift electrons travel at an angle with respect to the electric field, because they move in the region of the axial magnetic field. This "Lorentz angle" depends on the strength of the electric and magnetic fields, as well as the choice of gas for the drift chamber. For the choice of gas (49.6% argon, 49.6% ethane and 0.8% alcohol), electric (1350 V/cm) and magnetic field ($\sim$ 1.4 T), the Lorentz angle is 45°. The

[8] Recall that $p\bar{p}$ collisions occur every 3.5 μs.

drift cells are thus tilted 45° with respect to the radial direction, as can be seen in Fig. 2.8, achieving an azimuthal travel path for the drift electrons. The tilted drift cells facilitate the resolution of the left-right ambiguity problem [9] and they provide large overlap (20%) between the superlayers for redundancy.

The signals from the sense wires are read with preamplifiers mounted at the end-caps of the CTC. The analog pulse is then transmitted to an intermediate circuit (mounted on the solenoid return yoke) that shapes and amplifies it and produces a time over threshold logic signal. It is then transmitted to the counting room where it goes through time-to-digital-coverters (TDC) that have an accuracy of < 1 ns and are able to record more that 7 hits per wire per event. The resolution of the CTC for a single hit is ≤ 200 μm per wire in the azimuthal direction, whereas the double track resolution is less than 5 mm (i.e. 100 ns) and the resolution in the z direction is $\simeq 4$ mm. [10] The momentum resolution of a charged particle measured in both the SVX and the CTC is $\sigma(p_T)/p_T = \sqrt{(0.0009p_T)^2 + (0.0066)^2}$, with p_T in GeV/c.

2.2.3 The Central Electromagnetic Calorimeter (CEM)

Since neutral particles can not be detected with the tracking devices, situated at the heart of the CDF detector, the calorimeters are the only means of measuring their energy and getting information about their direction. The central electromagnetic calorimeter in particular is of great importance in this analysis, since it is the tool used to look for photons from the penguin decays.

The CEM calorimeter [44] has a cylindrical geometry with an inner radius of $\simeq$ 173 cm and a radial depth of 32 cm ($\simeq 18X_0$), enough to contain the showers of electrons and photons ("electromagnetic showers") created by virtue of the bremsstrahlung and pair production processes when an energetic photon or electron

[9] Whenever there is a pulse on a sense wire, we do not know if the avalanche that induced it, approached from the "left" or the "right" of the sense wire.

[10] 200 μm/$sin(3°)$.

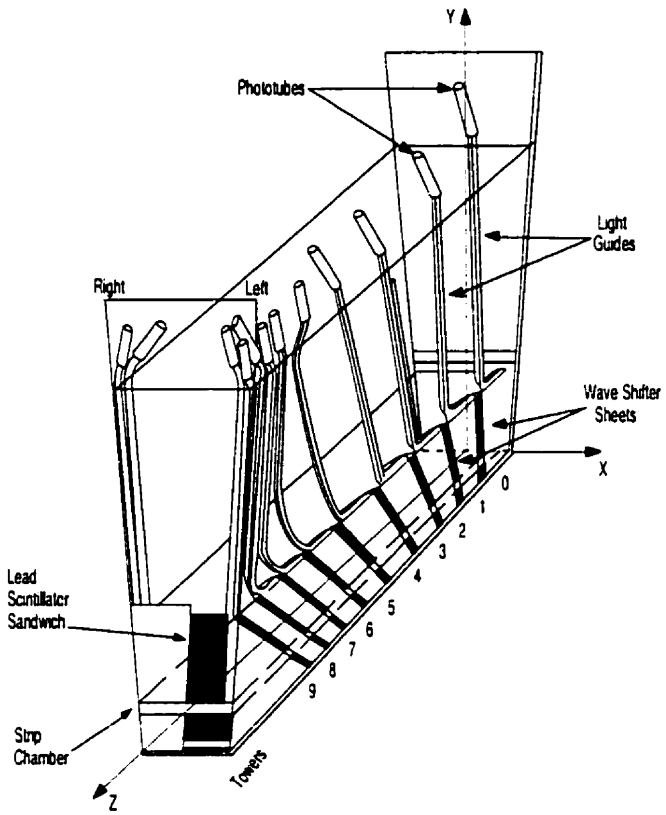

Figure 2.9: *One of the wedges of the CEM calorimeter with the towers that form it. Also shown are the wavelength shifter and the light guides that carry to the photomultipliers the photons produced in the plastic scintillators.*

enters the CEM volume. The CEM provides full azimuthal coverage and, in order to make mechanical construction easier and to be able to roughly locate incoming particles, it is divided into 48 wedges, each covering 15° in ϕ. The wedges are grouped into four arches; two arches of 12 wedges each cover the positive z region, with the remaining two arches covering the negative z region. Each wedge is segmented in ten towers, each extending ~ 0.11 units in η and 15° in ϕ, as can be seen in Fig. 2.9 [11]. The towers have a projective geometry pointing back to the nominal interaction region, since we want to contain the energy deposition of photons and jets flying out

[11] Each wedge houses a CEM component, which is closer to the beam line, and a CHA (central hadronic calorimeter) component.

of the $p\bar{p}$ collision point in as few towers as possible and avoid losing energy in the tower-boundary regions. As seen in Fig. 2.10, due to the same projective geometry, the central hadronic calorimeter (CHA), which is located behind the CEM, has 8 towers per wedge. Therefore there is a need for a "wall" hadronic calorimeter (WHA) to cover the region behind the CEM towers at $\eta > 0.8$. The CEM towers connect smoothly to the towers of the plug electromagnetic (PEM) calorimeter and so there is no need for a "wall" electromagnetic calorimeter.

The central electromagnetic calorimeter is a sampling calorimeter (like all the CDF calorimeters) , which means that it does not measure all the energy of the electromagnetic shower as it develops through the volume of the CEM, but it rather samples it periodically with plastic scintillators. The towers are sandwich structures of 31 layers of 5 mm thick polystyrene scintillator interleaved with 30 layers of 0.318 cm thick lead. Lead is chosen for its high density and atomic number, which ensures that the radiation length in the CEM is small (around 1.8 cm) and therefore results in a reasonable size calorimeter. In order to maintain a constant radiation length thickness as polar angle varies, acrylic is substituted for lead in certain layers of the $\eta > 0.2$ towers.

The electrons of an electromagnetic shower excite molecules in the scintillator material which consequently emit blue light that is collected in 3 mm thick acrylic wavelength shifter (WLS) sheets. There is one WLS sheet at each ϕ side of a tower, collecting light from all 31 scintillator layers in that tower and transporting it through light-guides into the two photomultiplier tubes per tower (see Fig. 2.9). The (total of 956) photomultipliers operate at 1 kV giving a gain of about 10^5. Twelve-channel charge-integrating amplifier modules are used to read out the photomultipliers; they saturate at about 350 GeV and have a high gain for good pedestal systematics for minimum ionizing particles (muons deposit about 300 MeV of their energy in the CEM). Requirements to accurately measure energy losses of minimum ionizing particles at the 0.5 to 5 MeV range force the readout electronics to have a dynamic

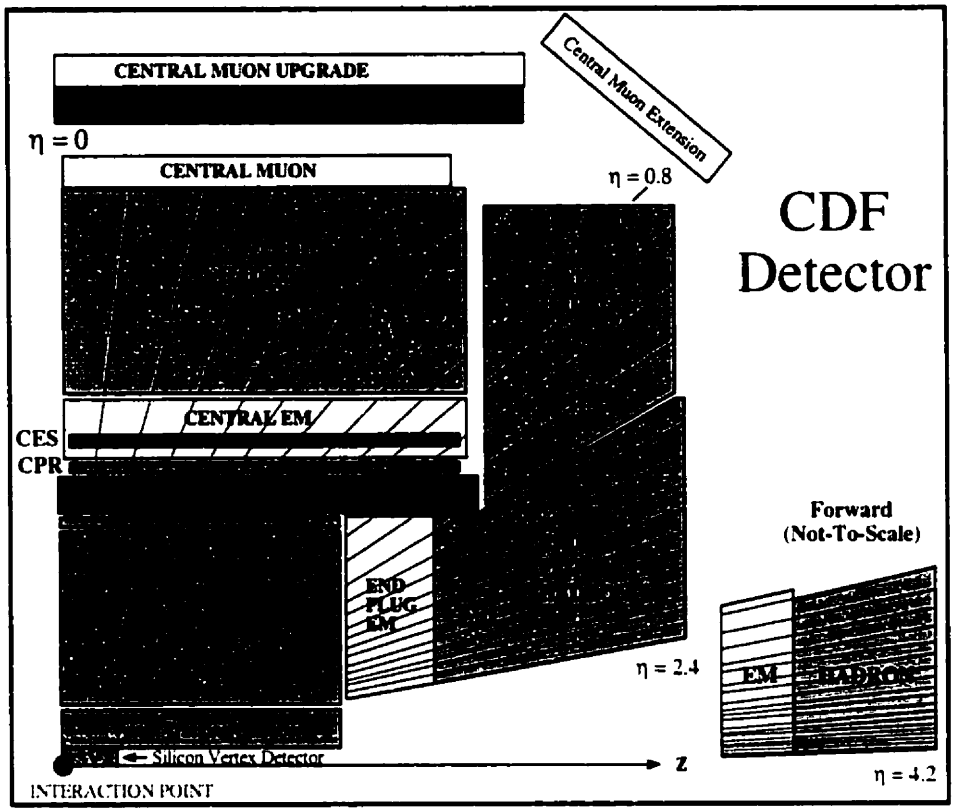

Figure 2.10: *A quadrant view of the CDF detector with the η segmentation of calorimeters shown. The $p\bar{p}$ beam axis is the axis of the cylindrical symmetry of the Collider Detector at Fermilab.*

range of 20 bits, with 16 bits resolution.

Each ϕ side of a wedge is covered by 4.76 mm of steel skin and between the wedges there are gaps of 6.4 mm in ϕ. WLS sheets, steel skins and gaps represent 4.8% of the azimuth. In order to avoid having photons and electrons traverse the ϕ gaps escaping detection, there are "crack detectors" in front of the ϕ boundaries, each consisting of a preradiator (9 radiation lengths thick uranium bar which forces the incoming particles to shower) and a proportional chamber which detects particles going through the cracks. The information from the crack detectors is used for veto purposes.

Note that the CEM design, with the steel skins and ϕ gaps between wedges,

does not allow electromagnetic showers to have a significant fraction of their energy shared between neighboring wedges. The transverse development of electromagnetic showers is characterized by the "Molière radius" R_M, with 95% of the shower energy contained within a radius of $2R_M$. For the CEM material $R_M \simeq 3.53$ cm, resulting in electromagnetic showers mostly contained in a single CEM tower [12]. This fact, along with the very good CEM hermeticity for the longitudinal development of the showers (depth of 18 X_0) and the good scintillator and WLS characteristics, results in the CEM measuring the energy of electromagnetic showers with a resolution of

$$\frac{\sigma(E)}{E} = \sqrt{\left(\frac{13.5\%}{\sqrt{E \cdot \sin\theta}}\right)^2 + (2\%)^2} \tag{2.3}$$

2.2.4 The Central Strip Chambers (CES)

Proportional strip chambers are inserted inside the CEM wedges between the eighth lead layer and the ninth scintillator layer; a depth corresponding to the maximum average transverse development of electromagnetic showers ($5X_0$ from the CEM face or $6X_0$ from the $p\bar{p}$ interaction point). The task of the CES [44] is to determine the shower position and the shower transverse development as a means to distinguish electromagnetic showers induced by electrons or photons from neutral pions. Therefore the CES chambers are essential to the reconstruction of photons and electrons for this analysis.

The CES chambers are proportional chambers with wires running along the z direction and strips along the ϕ direction, i.e. perpendicular to the wires, thus enabling the CES to locate an electromagnetic shower along both the ϕ (from wire information) and z (from strip information) coordinates. The gas used is 95% Ar and 5% CO_2 and the high voltage (1420 V corresponding to a prompt gain of 10^3)

[12] Test beam studies lead to the determination of the appropriate "response maps" for the CEM towers; they are used to estimate the energy of the incoming electron/photon as a function of the detected energy and the location of the shower in the tower.

is set up to give an occasional (few %) channel saturation for 150 GeV/c test beam electrons near normal incidence.

A right-handed local coordinate system ($x_{CES}, y_{CES}, z_{CES}$) is defined for each CEM wedge as follows (see also Fig. 2.9). The z_{CES} axis is parallel to the global CDF z axis with points on the $z < 0$ wedges having $z_{CES} < 0$ as well. The $z_{CES} = 0$ point is at $\eta = 0$, exactly as the $z = 0$ point. The x_{CES} axis is parallel to the face of the CES, perpendicular to the z_{CES} axis and has the $x_{CES} = 0$ point such that half of the wedge has $x_{CES} > 0$ and the other half has $x_{CES} < 0$.

The CES chambers are segmented in z into two pieces per wedge, one at $6.2 < |z_{CES}| < 121.2$ cm (i.e. towers 0 to 4) and the other at $121.2 < |z_{CES}| < 239.6$ cm (towers 5 to 9). Each CES segment has 32 wires spaced 1.45 cm apart, covering the region $-22.5 < x_{CES} < 22.5$ cm. There are 128 strips per wedge, each of width $\simeq 0.159$ cm; 69 (59) of them are in the $|z_{CES}| < 121.2$ cm ($|z_{CES}| > 121.2$ cm) CES segment, spaced 1.67 (2.01) cm apart.

The response of the CES as a function of the incident energy is not linear, since the depth at which the transverse development of an electromagnetic shower reaches its maximum increases with the energy of the incident photon or electron. The shower position measurement in the strip view has a resolution of 3 mm for 10 GeV photons/electrons and reaches a plateau of 2 mm at 50 GeV. The response of the CES (both in energy and in position) is also a function of $\sin\theta$ due to the widening of the showers in the strip view, as can be seen in Fig. 2.11. Applying systematic corrections based on test beam and cosmic ray measurements result in a resolution of $\pm 10\%$ or better in strip to wire pulse height correlation.

The shape of the transverse development of the electromagnetic shower can be used to distinguish between showers induced by a single electron/photon or a neutral pion. Since π^0s predominantly decay to two photons, there should be two separate electromagnetic showers developed for each π^0. The more energetic the π^0 is though, the closer the daughter photons are, resulting in two overlapping electromagnetic

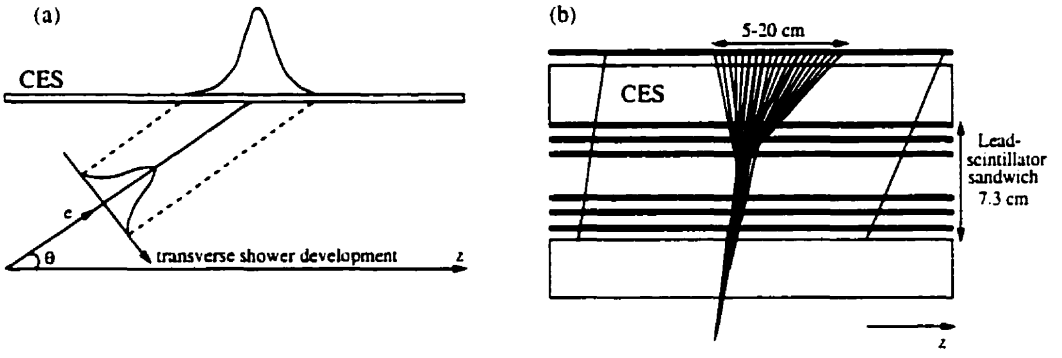

Figure 2.11: *a) The* $1/\sin\theta$ *widening of the showers in the strip view. b) The origin of the asymmetry in the strip profile is schematically illustrated.*

showers, which makes the electron/photon vs. π^0 distinction very difficult.

2.2.5 Beam-Beam Counters (BBC)

A plane of scintillator counters on the front face of the forward (and backward) electromagnetic calorimeters, called the beam-beam counters (BBC), signals the collision of proton and antiproton beams. The counters are arranged in a rectangle around the beam pipe covering angles 0.32^o to 4.47^o in both the x and y directions, corresponding to the region $3.24 < |\eta| < 5.88$. The BBCs have excellent timing properties ($\sigma < 200$ ps), providing the best measurement of the time of the $p\bar{p}$ interaction. Coincident hits in both the $z > 0$ and $z < 0$ BBCs serve as a "minimum-biased" trigger, as well as the luminosity monitor for CDF. The rate of the coincidences in these counters, divided by the effective cross section to which the counters are sensitive, provide the instantaneous luminosity. The number of these coincidences (which is actually the time integration of the rate) leads to the integrated luminosity. The cross section to which the BBC counters are sensitive is measured to be $\sigma_{BBC} = 51.2 \pm 1.6$ mb, and, after accounting for background processes, we get a total uncertainty of 4.1% on the integrated luminosity.

2.3 Triggering at CDF

The proton and antiproton bunches collide every 3.5 μs, corresponding to a crossing frequency of 286 kHz, with more than one $p\bar{p}$ interactions per beam crossing, as Eq. 2.2 and the subsequent discussion indicate. The amount of information the CDF detector collects to describe the result of a single beam crossing (usually called an "event") is typically around 170k bytes. Therefore there is an enormous amount of data to be read and stored properly each second, and writing the data reliably on 8 mm tapes could be done at a rate of $\sim$ 10 Hz only. This means that we have to pick one out of $\sim$ 30000 events to write on tape. Which ones should we pick? Since only one out of 40000 $p\bar{p}$ interactions results in b quark production at $\sqrt{s} = 1.8$ TeV [4], not all beam crossings give interesting processes for investigation (at least not interesting enough for this thesis). Clearly then, we should not pick randomly; we should "trigger" on interesting events and write *them* on tape. If we were to implement a naïve trigger where the decision would be made in one step only, more than 1 ms would be spent to write the interesting event on tape, during which time the detector could not gather information from any of the subsequent 285 $p\bar{p}$ crossings [13]. In order for the detector to be able to consider as many beam crossings as possible, we have to decide on accepting or rejecting the event in more than one step. Thus each "trigger level" deals with lower and lower event rates, allowing the last trigger levels to perform more sophisticated (and thus more time consuming) analysis without introducing significant dead-time.

At CDF we have a three level trigger system [39, 45]. Each successive layer uses more detailed requirements and consequently takes more time to decide. At each level the decision is based on a logical "OR" of these requirements, which are designed to select different physics processes. In the second and third level of the trigger these requirements are programmable, which allows control of the output

[13] This means that the detector would operate with 99.65% "dead-time" if no trigger was present.

rates of each trigger level in the course of different running conditions.

Preamplifiers on some of the detector readout channels provide two outputs: a "fast output" for use by the first two levels of the trigger system and the other for temporary data storage at the front-end electronics to be used for the third level of the trigger and to eventually put the event on tape.

2.3.1 Level 1

The first level trigger ("Level 1") makes a decision within the 3.5 μs between beam crossings, thus introducing no dead-time. It achieves this speed by basing its decision on the fast analog outputs from the calorimeters and the three central muon detectors.

The calorimeter information is summed, separately for the electromagnetic and hadronic parts, into logical "trigger towers", each encompassing enough physical towers to extend to 0.2 units in η and 15° in ϕ. Thus the entire detector is represented as a 42 (in η) by 24 (in ϕ) array of calorimetric "trigger towers" with an electromagnetic and a hadronic component each.

The fast outputs of the photomultipliers that read out the central electromagnetic (CEM) and the central and wall hadronic (CHA and WHA) calorimeters, or the pads that read out the plug and forward calorimeters, are brought to the "trigger counting room" individually, through dedicated cables. These signals are summed and weighted by $\sin\theta$ to form the electromagnetic and hadronic transverse energy ($E_T = E \cdot \sin\theta$) deposited in each of the trigger towers. The transverse energy of each trigger tower is then compared to a programmable minimum-energy threshold (e.g., 1 GeV). The energies of all trigger towers above threshold are summed to form the grand total sums of electromagnetic, hadronic and total (i.e. the sum of electromagnetic and hadronic) transverse energy in the detector, as well as the corresponding sums for each of the calorimeter subsystems (i.e. CEM, CHA, etc.).

The Level 1 trigger accepts an event if there is any trigger tower with energy above

the preset programmable threshold, different for each of the calorimeter subsystems (for the CEM it was set to 8 GeV during Run 1B, and to 5 GeV for Run 1C). Lower thresholds were set for a similar Level 1 calorimetry trigger that was "prescaled" by a factor of 40 [14], collecting events that could be used to study the efficiencies of higher-threshold triggers.

The Level 1 trigger components that look for muons require the presence of "track segments" in the CMU and/or CMX chambers. A track segment is a pair of hits on the radially aligned wires of the CMU or CMX drift cells. The arrival times of the drift electrons on these two sense wires determine the deflection angle of the traversing charged particle due to the magnetic field and thus provide an estimate of its p_T.

Level 1 muon triggers can require any combination of such track segments that makes sense. For example, one could require a track segment in the CMU with $p_T > 6$ GeV/c with coincident hits in the CMP; or two track segments in the CMU system with $p_T > 3.3$ GeV/c each; or a track segment in the CMX with $p_T > 10$ GeV/c with coincident hits in the scintillators placed on both sides of the chambers, etc.

At an instantaneous luminosity of $L = 5 \times 10^{30}$ cm^{-2} s^{-1}, the Level 1 trigger had an acceptance rate of approximately 1 kHz [46]. This means that only $\sim 0.5\%$ of the events were considered interesting enough for further investigation.

2.3.2 Level 2

Once Level 1 signals an accept, the second level trigger ("Level 2") deals with the event. Otherwise, the signals stored in the CDF components are cleared and the detector is ready to consider the next $p\bar{p}$ crossing. The Level 2 takes around $20 - 30$ μs to decide if the event should be considered further or not, and the detector is

[14] In other words, this component of the trigger was accepted for the Level 1 decision only one out of 40 times that the condition was actually satisfied.

"blind" to the outcome of the $6 - 9$ beam crossings happening meanwhile. Thus Level 2 introduces $\sim$ 10% dead-time.

The information obtained at Level 1 is passed to Level 2, which has more time to deal with it in a more sophisticated manner, thus looking for topological features of the event, such as clusters of electromagnetic or hadronic energy, tracks in the CTC, which can be associated with energy depositions in the CEM or track segments in the muon detectors, missing transverse energy, $\not\!\!E_T$, indicative of undetected neutrinos, etc.

Level 1 hands the list of trigger towers above threshold, along with the corresponding energy depositions, to Level 2. A dedicated board (called the "Cluster Finder") looks for towers above some "seed tower" threshold (typically 5 or 8 GeV) and makes a list of "seed towers". Trigger towers that are above a lower "shoulder tower" threshold (typically 1 GeV less than the seed tower threshold) are kept in a separate list. Starting from the seed tower with the smallest η and ϕ, the Cluster Finder checks which of the four nearest neighbors (the "diagonal" neighbors with different η and ϕ are not considered) are in the "shoulder tower" list and includes them in the cluster. The nearest neighbors of each of the newly included towers are checked and so on, until no more contiguous towers are found. Once a tower is included in a cluster it is not considered for any of the subsequent clusters. The process is repeated until no new seed towers exist. The energies of all the towers in a cluster are summed to form the total E_T and the E_T-weighted η and ϕ position, as well as σ_η and σ_ϕ, of the cluster. Separate sums are kept for electromagnetic and total (electromagnetic plus hadronic) energies. The time needed for the energy clustering process is $\sim$ 200 ns per cluster. Finally the Cluster Finder treats the whole detector as one cluster and calculates the global sum of energies for all towers above threshold, exactly as Level 1 did. This gives a more accurate measurement of missing transverse energy than Level 1, which is used by components of the Level 2 trigger looking for neutrinos.

The tilted drift cells in the CTC guarantee that every high p_T track (moving almost along the radial direction) passes through at least one sense wire plane in every superlayer. This fact is exploited by the hardware central fast track processor (CFT), a track-finder [47] that checks the axial CTC superlayers for fast ("prompt") signals, within a time gate of < 80 ns after the $p\bar{p}$ interaction. The CFT also looks for two "delayed" hits (within a time gate of $500 - 650$ ns after the $p\bar{p}$ interaction), in the same axial superlayers, on either ϕ side of the prompt hit. The drift times of the electrons towards the sense wires provide information about the direction and curvature (hence the p_T) of the track. Different time gates for the delayed hits allow the CFT to select tracks above various minimum-p_T thresholds. The CFT uses the recorded prompt and delayed hits to reconstruct tracks in the CTC, classifying them in different p_T bins. It starts from prompt hits in the outer axial superlayer and works its way towards the interaction point at $r = 0$, looking for hits within the limits of a "road" defined by the geometrical acceptance of the prompt and delayed hits expected by a track in the desired p_T range. For each sense wire in the outer axial superlayer there is a total of 32 such roads defined in a look-up table. These are divided into eight p_T bins and two ϕ bins, one for each sign of curvature, covering the entire $p_T > 2$ GeV/c range. The resolution achieved by the CFT is $\sigma(p_T)/p_T \simeq 0.035 \cdot p_T$, with p_T in units of GeV/c. The time needed for the CFT to find tracks in the CTC is ~ 10 μs.

The list of calorimetric energy clusters and muon track segments is handled by the commercially available programmable Alpha processors, that look for an associated track found by the CFT. The muon track segments in the CMU, CMP and CMX detectors must be matched by an extrapolated "CFT track" within $\Delta\phi \leq 5^o$. The parts of Level 2 that look for electrons require that the CEM cluster is also matched by an extrapolated CFT track. Since the CFT reconstructs tracks in the $r - \phi$ plane only, this matching can lead to the association of a CFT track with an electromagnetic cluster in the same ϕ but in a completely different η region, thus

making the trigger decision generous.

At an instantaneous luminosity of $L = 5 \times 10^{30}$ cm^{-2} s^{-1}, the Level 2 trigger had an acceptance rate of approximately 12 Hz [46]; only $\sim 1.5\%$ of the events checked by Level 2 were then considered further.

2.3.3 Level 3

Once an event is accepted by Level 2, the data acquisition system (see Section 2.4) digitizes the signals obtained from all the detector channels and feeds them to the next trigger level ("Level 3"). This takes more than 1 ms, resulting in more than 285 subsequent $p\bar{p}$ beam crossings to go by undetected.

The event is read into 64 commercially available processing units (Silicon Graphics machines running under a UNIX operating system trade-marked as IRIX by the company) with a combined processing power of approximately two billion instructions per second. The processors reconstruct the event using algorithms identical to the ones used in the "off-line" reconstruction, i.e. after the finally accepted event is written on the magnetic tape. Most of the execution time is used to reconstruct three dimensional tracks in the CTC.

The algorithms that look for electrons demand that the electromagnetic energy cluster be matched within a few centimeters in both the $r - \phi$ and $r - z$ view to a three dimensional track found in the CTC and extrapolated to the face of the calorimeter. The p_T of the track should also match the electromagnetic E_T of the cluster. For both electrons and photons, the algorithms further demand that the fraction of energy deposited in the neighboring physical calorimeter towers be consistent with that expected for electrons/photons. The same is true for the fraction of energy deposited in the hadronic towers behind the electromagnetic ones. Finally, the energy profile of the transverse development of the shower, measured in the CES, should also be consistent with the assumption that the shower was induced by an electron or a photon.

The algorithms that look for muons require that a track segment in the muon chambers be matched, in both the $r-\phi$ and $r-z$ planes, to a three dimensional track reconstructed in the CTC and extrapolated to the muon detectors. The difference between the position of the muon track segment and extrapolated track must be smaller than a few standard deviations, taking into account multiple scattering and measurement uncertainties.

Some of the algorithms combine information from such "physics objects" as the electrons, photons and muons mentioned above, to calculate invariant masses, relative directions, etc. This ability of the Level 3 (and to some extent of the Level 2) system is exploited in the design of the specialized "penguin trigger" discussed in Chapter 4.

At an instantaneous luminosity of $L = 5 \times 10^{30}$ cm^{-2} s^{-1}, the Level 3 trigger had an acceptance rate of approximately 5 Hz [46], rejecting about half of the events it considered.

2.4 Data Acquisition (DAQ)

The CDF detector has around 150k channels recording an event. Around 46k of those read out the signals created in the silicon vertex detector, $\sim$ 60k deal with the calorimeters, and the bulk of the remainder deal with the drift chambers. These channels have their analog signals in the "front-end" (i.e. detector mounted) electronics preamplified, transmitted to intermediate circuits that shape and further amplify them, and finally brought up from the collision hall to the counting room to digitize them with analog-to-digital or time-to-digital converters, depending on the origin of the analog signal.

A schematic drawing of the CDF data acquisition system is given in Fig. 2.12. Level 1 and Level 2 use a subset of the event information, sent to them through dedicated cables. Once Level 2 accepts an event, it communicates its decision to a

Fastbus module called the "trigger supervisor". The communication is done through another Fastbus device, known as FRED. Fastbus readout controllers (FRCs), signaled from the trigger supervisor, read out the data from the front-end electronics and guide them to six scanner CPUs (SCPUs), which are VME-based Motorola 68030 processors. The SCPUs, running the VxWorks operating system, "build" the received information into data banks which are organized by detector component and have the same format expected by the tape logger and the consumer processes. Another VME-based Motorola 68030 processor, called the "scanner manger", controls the flow of data through a commercially available Ultranet distributor to the Level 3 system, making sure that all information from a given event is handed to one Level 3 node, with the help of a reflective memory network (Scramnet). A "trigger supervisor interface" was necessary to establish communication between the Fastbus based trigger supervisor and the scanner manager.

Ultranet is also used to transfer the information of events accepted by Level 3 to the consumer server. This is a dedicated Silicon Graphics machine that run data logger programs to write events on local disk and subsequently to tape. In parallel, the consumer server provides event information to consumer processes for on-line diagnostic applications; monitoring of luminosity conditions, trigger rates, detector performance, rates of well established physics processes (e.g., J/ψ production), graphical representation of the current event, etc.

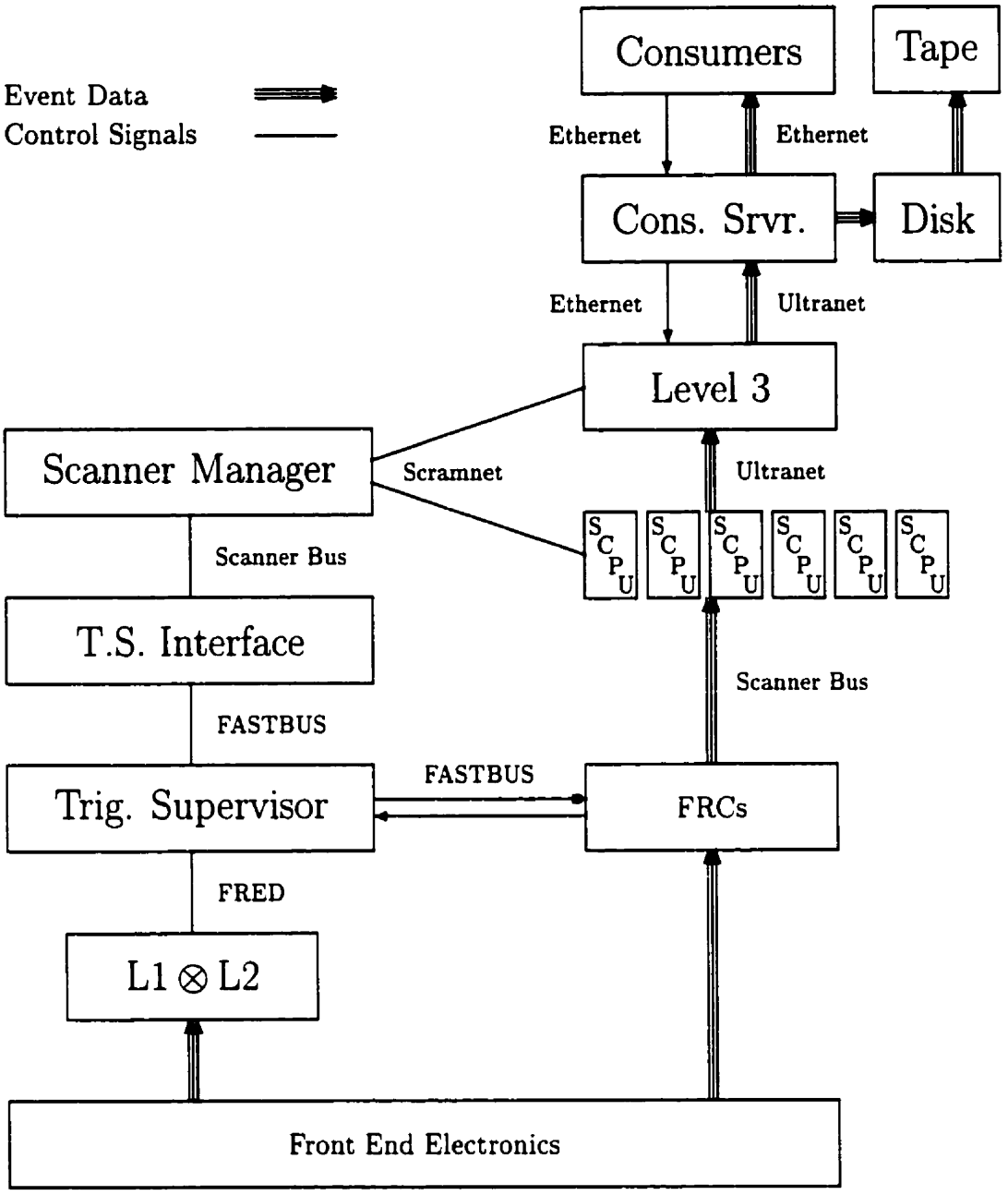

Figure 2.12: *Flow chart of the CDF data acquisition system, along with some of its key elements.*

Chapter 3

Monte Carlo Simulations

In order to devise the necessary strategy to extract the $B_d^0 \to K^{*0}\gamma$, $K^{*0} \to K^-\pi^-$ and $B_s^0 \to \phi\gamma$, $\phi \to K^+K^-$ decays from the large number of events that were accumulated by the CDF detector, we simulate these processes. The use of random numbers to simulate stochastic (statistical) processes, results in calling them Monte Carlo (MC) simulations.

This chapter describes the simulation procedure, which involves several stages: the generation of b quarks, their hadronization into B mesons, the decay of these B mesons into the final state particles, the response of the detector to these particles traversing its volume, and finally the reconstruction of the event along with the information relevant to the trigger.

In this analysis, the design of the specialized trigger (see Chapter 4) to search for penguin decays, relied heavily on such simulations. For the estimation of the fraction of the penguin decays that survived the various selection criteria, we relied on both Monte Carlo simulations as well as data.

3.1 Production and decay of the B mesons

We start by generating single b quarks with a rapidity and momentum distribution based on a next-to-leading order QCD calculation by Nason, Dawson and Ellis [16] that used the MRSD0 parton distribution functions [15] and a renormalization scale of $\mu = \mu_0 \equiv \sqrt{m_b^2 + p_T^2}$, with $m_b = 4.75$ GeV/c^2 for the mass of the b quark and p_T for its transverse momentum.

We generate b quarks with $p_T > 5.5$ GeV/c in the rapidity range $-1.4 < y < 1.4$. In Fig. 3.1 we see the transverse momentum and rapidity distributions of b quarks generated with $p_T > 4$ GeV/c and $-4 < y < 4$ in the Monte Carlo. We note that the resulting B mesons tend to have lower transverse momenta (the B mesons carry on average 80% of the transverse momentum of the b quarks) and are more "central" in rapidity than the parent b quarks; 44% of the B mesons with $-4 < y < 4$ are contained in the $-1 < y < 1$ region. The corresponding fraction for the b quarks is 40%.

These b quarks were subsequently hadronized into B mesons using the Peterson fragmentation function [17] with a fragmentation parameter $\epsilon_b = 0.006$. The hadronization process is $b \rightarrow Bq$, where q is the light quark created from the vacuum in a pair with the $\bar{q}$ that combined with the b quark to form the B meson. The energy transfer $\Delta E \equiv E_B + E_q - E_b$ of the hadronization process is described in terms of the fraction of the b quark energy carried by the B meson and the fragmentation parameter ϵ_b that describes the ratio m_q/m_b, i.e. the ratio of the q to b quark masses. Fits to experimental observations in e^+e^- collisions have resulted in the estimate $\epsilon_b = 0.006 \pm 0.002$ [18].

The Nason-Dawson-Ellis calculation used in conjunction with the Peterson fragmentation model, is found to describe the shape of the differential cross section for B meson production (see Fig. 1.3 and Ref. [48]). This is especially true for B mesons with $p_T > 10$ GeV/c which are of interest to us in the search for penguin decays in the Run1B data (see Section 4.3.1).

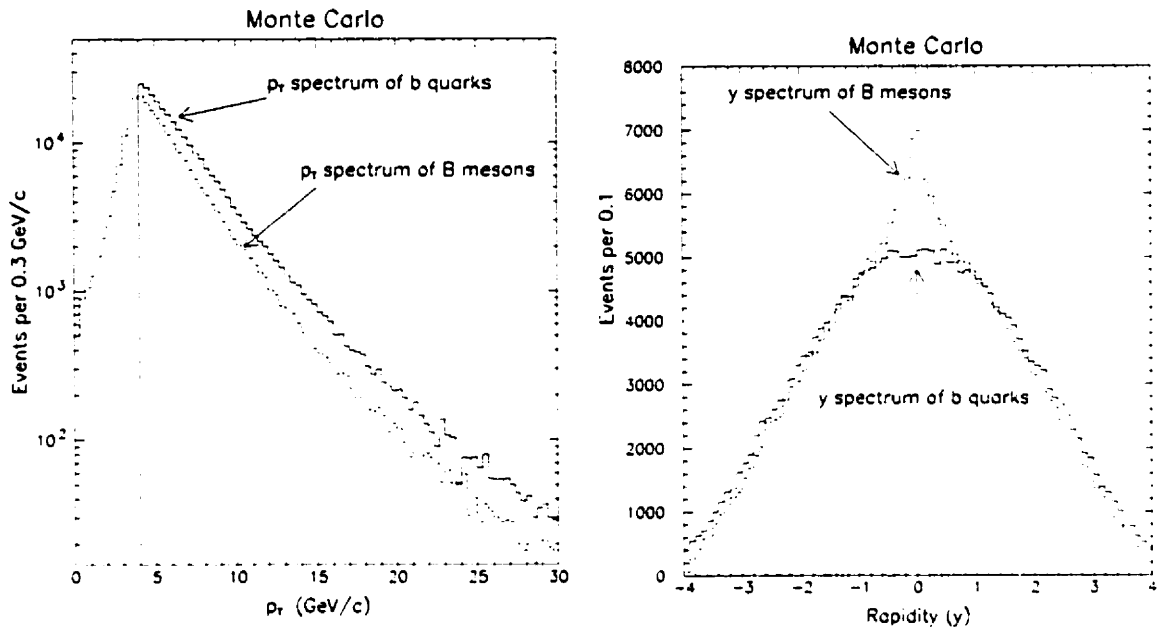

Figure 3.1: *Left: Transverse momentum (p_T) distribution of b quarks generated with $p_T > 4$ GeV/c and $-4 < y < 4$ in the Monte Carlo, as well as the p_T distribution of the resulting B mesons. Right: Rapidity (y) distributions of those b quarks and B mesons.*

The resulting B mesons are then decayed to a photon and a strange meson (K^{*0} or ϕ) according to the CLEO Monte Carlo program, QQ [49], in order to model the phase-space, helicity and angular distributions of the decay products. The penguin processes were included into the QQ decay options, without allowing them any longitudinal polarization, since the photon is massless. The masses, widths and lifetimes of the generated particles match the world average values [4]. This way we generated the penguin ($B^0_d \to K^{*0}\gamma$, $K^{*0} \to K^+\pi^-$ and $B^0_s \to \phi\gamma$, $\phi \to K^+K^-$) decay chains. Similarly we generated the $\bar{B} \to e^- D^0 X$, $D^0 \to K^-\pi^+$ decay chain.

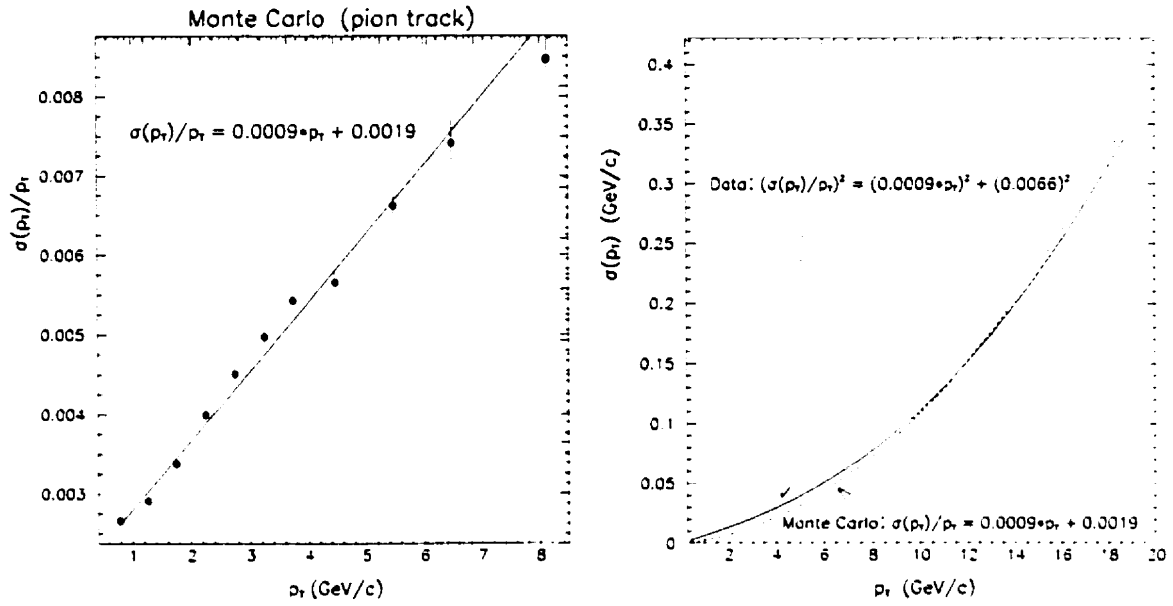

Figure 3.2: *Left: Momentum resolution for Monte Carlo tracks. Right: Comparison of momentum resolution between data [46] and Monte Carlo tracks.*

3.2 Detector simulation

The response of the CDF detector to the final decay products ($\gamma K^- \pi^-$ and $\gamma K^- \pi^-$) traversing its volume is handled by another Monte Carlo program, which uses a parameterized model of the detector response tuned on data. The response of the calorimeter and the strip chambers, for example, has been parameterized based on electron test beam data. This Monte Carlo simulation only produces the final objects. For example, given a charged particle, the Monte Carlo simulation does not generate the electronic signals in the tracking detectors, but rather skips this step and generates the parameters of the particle's track.

The p_T resolution for pion tracks and the energy resolution for electrons measured in the CEM compare well between data [46] and Monte Carlo simulations. This is demonstrated in Figures 3.2 and 3.3 and in Equations 3.1 and 3.2.

We compare the generated momentum of the pion in the $\bar{B} \rightarrow e^- D^0 X$, $D^0 \rightarrow K^- \pi^-$ decay chain, with its momentum after the simulation of the detector response and

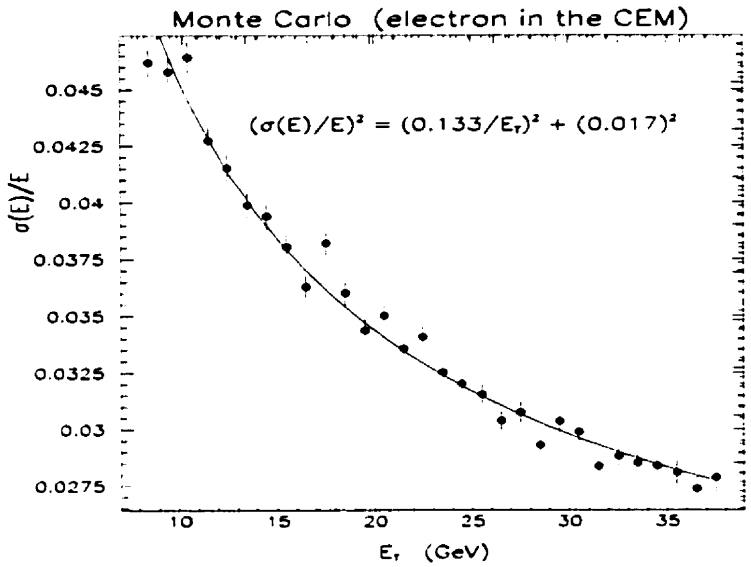

Figure 3.3: *Energy resolution (measured in the CEM) for Monte Carlo electrons.*

after the decay was reconstructed. The pion and kaon tracks were constrained to pass through a common point (presumably the D^0 decay vertex), something that improves the resolution by almost a factor of two. In data, the track resolution is measured with cosmic ray muons that traverse the tracking volume leaving two track segments separated by $\sim 180^o$ in ϕ. The comparison of the momenta obtained from the two different ϕ sides leads to the momentum resolution. The resolution improves considerably when the two track segments are constrained to meet each other[1]. The resolution quoted for tracks in data refers to such "constrained" tracks. The relevant momentum range is up to ~ 8 GeV/c for the kaons and pions in the penguin and the $\bar{B} \to e^- D^0 X$, $D^0 \to K^- \pi^+$ channels. The resolutions (with p_T in units of GeV/c) are found to be:

$$\begin{aligned} \sigma(p_T)/p_T &= \sqrt{(0.0009 \cdot p_T)^2 + (0.0066)^2} \quad (tracks\ \ in\ \ Data) \\ \sigma(p_T)/p_T &= 0.0009 \cdot p_T + 0.0019 \qquad (Monte\ \ Carlo\ \ tracks) \end{aligned} \tag{3.1}$$

[1]This requirement reflects the fact that both track segments are due to the passage of a single particle through the tracking volume.

For the energy resolution of the CEM, we compare the energy of the electrons as generated, with the energy deposited in the CEM, after the detector response is simulated. In data, the energy deposition in the CEM is compared with the momentum of the track, found in the CTC and SVX, that points towards the calorimetric energy cluster. The relevant energy range is from 8 GeV up to $\sim$ 30 GeV for the photons and electrons of the penguin and the $\bar{B} \to e^- D^0 X$ channels. The resolutions for electrons (with E_T in units of GeV) are found to be:

$$\begin{aligned} \sigma(E)/E = & \sqrt{(0.135/E_T)^2 + (0.020)^2} \quad (electrons \ \ in \ \ Data) \\ \sigma(E)/E = & \sqrt{(0.133/E_T)^2 + (0.017)^2} \quad (Monte \ \ Carlo \ \ electrons) \end{aligned} \tag{3.2}$$

Furthermore, we firmly establish our faith to the detector simulation for the energy and the momentum measurements, by verifying that the E/p distribution for electrons reconstructed in the $\bar{B} \to e^- D^0 X$, $D^0 \to K^- \pi^+$ channel compares well between data and Monte Carlo events, which are signal only (see Fig. 3.4 and Eq. 3.3). E is the energy of the electron measured in the CEM in units of GeV and p its momentum measured in the CTC and the SVX in units of GeV/c. The E/p distribution from data corresponds to signal only (i.e. $e^{\pm}$ only); the possible non-$e^{\pm}$ background contribution was subtracted using the events that have a $K^- \pi^+$ mass in the sidebands of the reconstructed D^0 mass peak. The average E_T for the Monte Carlo electrons matches that of the signal electrons in the data (12.89 and 13.05 GeV respectively). Fitting the E/p distributions with Gaussian shapes we get:

$$\begin{aligned} & < E/p >= 1.0102 \pm 0.0056 \ \ and \ \ \sigma(E/p) = 0.0677 \pm 0.0051 \quad (electrons \ \ in \ \ Data) \\ & < E/p >= 1.0132 \pm 0.0012 \ \ and \ \ \sigma(E/p) = 0.0652 \pm 0.0012 \quad (MC \ \ electrons) \end{aligned} \tag{3.3}$$

The z and the transverse $(x - y)$ positions of the $p\bar{p}$ interaction point are also parameterized as Gaussian distributions that approximately match the distribution observed in the data. A Gaussian of width 30 cm was used for the z location of the $p\bar{p}$ interaction. The x and y location of the $p\bar{p}$ interaction was fixed to $(0, 0)$ in the

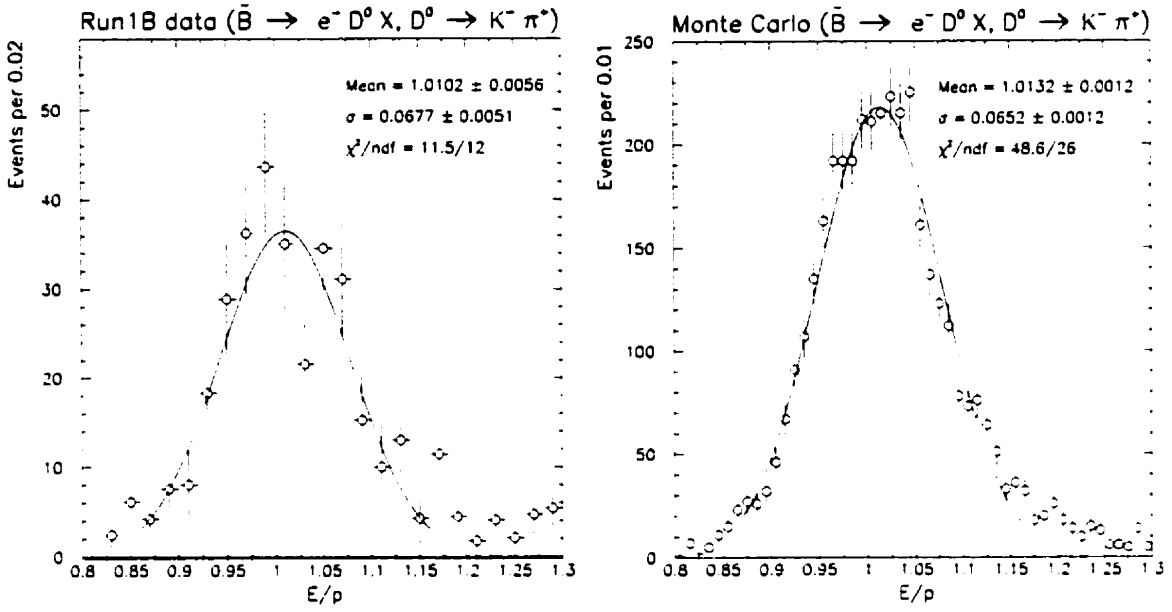

Figure 3.4: *Left: E/p distribution, i.e. energy (measured in the CEM in units of GeV) over momentum (measured in the CTC and SVX in units of GeV/c), for electrons in the Run1B data. The electrons used here are from the* $\bar{B} \rightarrow e^- D^0 X$, $D^0 \rightarrow K^- \pi^+$ *channel. The distribution shown has possible non-*$e^{\pm}$ *background contributions removed by using the sidebands of the* $K^- \pi^+$ *mass around the* D^0 *mass peak. The superimposed fit is a Gaussian distribution. Right: E/p for electrons from the* $\bar{B} \rightarrow e^- D^0 X$, $D^0 \rightarrow K^- \pi^+$ *Monte Carlo sample, which is signal only.*

Monte Carlo, since the $x - y$ distribution in data is a perfect line for each of the $p\bar{p}$ beam stores, a demonstration of the accurately known "beam optics".

The simulation produces data structures almost identical to the ones produced by an event resulting from a $p\bar{p}$ collision. This allows us to follow nearly[2] the same procedure in the processing and analysis of real data and Monte Carlo events. Thus both Monte Carlo and data events are subject to the same reconstruction biases.

[2]E.g The corrections for non-uniformities of the magnetic field are not applied in the Monte Carlo case.

3.3 Trigger simulation

3.3.1 Electromagnetic energy clustering in the CEM

Having simulated the response of the CDF detector, the simulation of trigger decisions that are based on energy depositions in the calorimeters uses algorithms similar to the ones used on data. The clustering of the energy into trigger towers and the application of lower energy thresholds in the first and second levels of the trigger (see Sections 2.3.1 and 2.3.2) are performed by such algorithms. Note though that the Level 1 trigger efficiency for energy deposition in the CEM is not explicitly simulated in either the penguin or the $\bar{B} \to e^- D^0 X$ channels, because the Level 1 requirement is reasserted again at Level 2. Any remaining inefficiency due to the Level 1 trigger will cancel when we consider the ratio of the penguin vs. the $\bar{B} \to e^- D^0 X$ branching fractions (see Chapter 6).

3.3.2 CES information in Level 2

Information from the CES strip chambers was available at Level 2 in Run 1B. This was accomplished with the use of the "XCES bit",which was set for the entire calorimeter wedge whenever there were more than $\sim$ 3500 ADC counts in four adjacent CES wires, corresponding to more than $\sim$ 4.5 GeV of energy in the electromagnetic shower[3]. This means that the trigger was generous in the sense of accepting events where the XCES bit was set by an unrelated energy cluster, as long as it was in the same CEM wedge. Thus the trigger accepted events that should have failed, but it tried to not reject events that should be accepted. Nevertheless, this requirement reduced the Level 2 electron trigger rate by a factor of two, while retaining high efficiency for real electrons[4] and photons: as it is shown in Fig. 3.5, the efficiency

[3]In Run1C the threshold was lowered to $\sim$ 2335 ADC counts .

[4]For electrons it was also required that a track found by the CFT points to the energy deposition in the CEM.

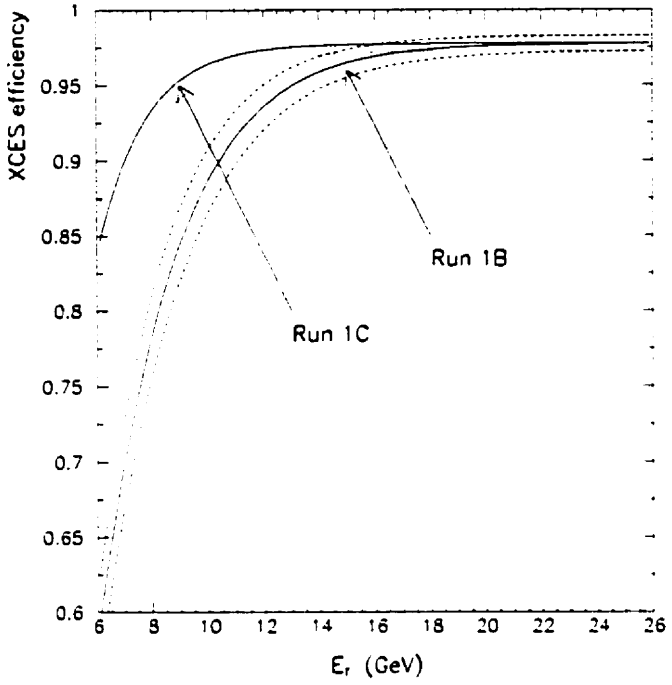

Figure 3.5: *Efficiency of the XCES bit requirement for $E_T > 6$ GeV electrons. The efficiency was studied with electrons from photon conversions ($\gamma \rightarrow e^+e^-$), which yielded a high purity electron sample. The solid curves are the central values and the dashed curves represent shifts of the function parameters by one standard deviation (determined from fitting the functional form to the electron data). For electrons in Run 1B (Run 1C) of $E_T = 10.5$ (7) GeV the efficiency is 90%, reaching the plateau value of $(97.7 \pm 0.5)\%$ at ~ 22 (~ 15) GeV.*

of the XCES bit requirement in Run 1B was $\sim 80\%$ at $E_T \simeq 8$ GeV, rising to 90% for electrons with $E_T \simeq 10.5$ GeV [50]. Before the use of the XCES bit requirement, the electron trigger looking for electrons with $E_T > 8$ GeV had to be prescaled in order to keep the trigger rate within the Level 2 budget. The use of the XCES bit requirement in Run 1B and Run 1C allowed the experiment to collect more than one million additional electrons from b quark decays.

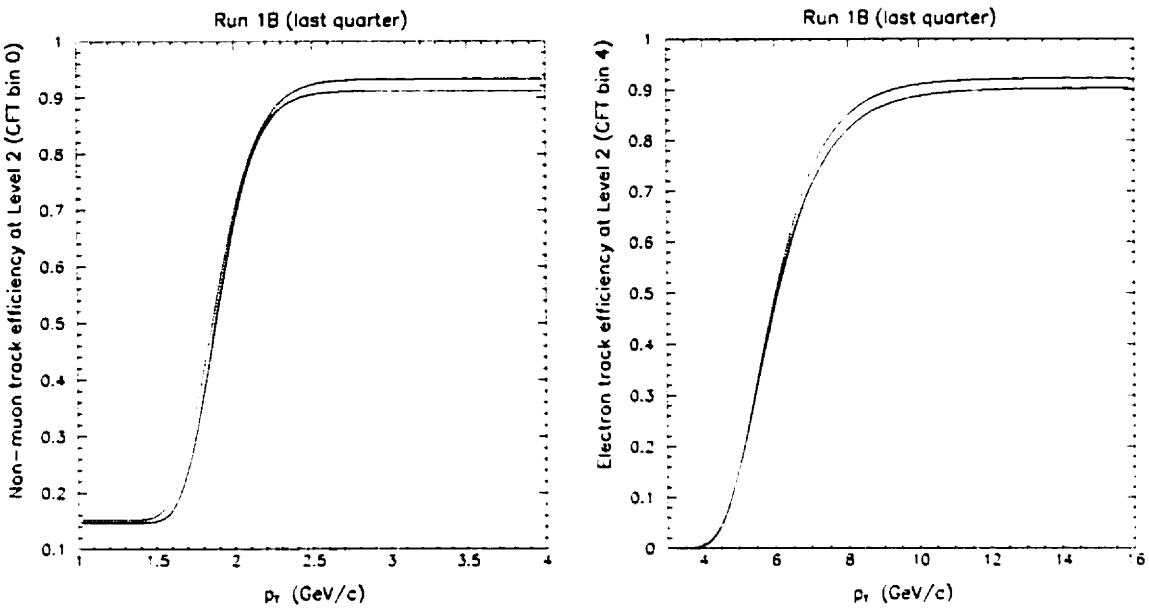

Figure 3.6: *Left: Efficiency of finding a non-muon track with the Level 2 CFT processor as a function of the p_T of the considered track for the lowest-p_T CFT bin (bin 0). The 50% (90%) efficiency point is at 1.9 (2.4) GeV/c. The dotted curve is the central value of the efficiency and the solid curves represent shifts of the function parameters by one standard deviation (determined from fitting the functional form to the data). Right: Same efficiency but for electrons in the fifth CFT bin (bin 4). The 50% (90%) efficiency point is at 6.0 (10.0) GeV/c. For the determination of these efficiencies see discussion in the text (Section 3.3.3).*

3.3.3 Tracks in Level 2

The part of the Level 2 trigger that dealt with tracks in the CTC (i.e. the CFT) is simulated using parameterizations of the measured efficiency with which the CFT detected tracks. In Fig. 3.6 we see the efficiency of finding a track in the lowest-p_T CFT bin (bin 0). This efficiency was determined as a function of the track p_T using non-muon tracks in the vicinity of "non-conversion" electrons (i.e. electrons not from $\gamma \rightarrow e^+e^-$ conversions) reconstructed in the SVX [51]. For each CFT bin there exists a different efficiency curve, due to the different p_T threshold.

The specialized trigger that looks for penguin decays (see Chapter 4) required two tracks in the lowest-p_T CFT bin. The main trigger that looks for electrons (used later to reconstruct the $\bar{B} \to e^- D^0 X$ decay) required the energy deposited in the CEM to be more than 8 GeV and to be matched by a track found in the fifth CFT bin (bin 4). This efficiency, shown in Fig. 3.6, was determined with electrons collected with a lower energy trigger that did not require CFT information. The efficiency of the CFT did not only depend on the transverse momentum of a track. It also depended on its charge, its pseudorapidity (η) and azimuth (ϕ), as well as on the integrated and instantaneous luminosities. Positively charged particles were detected more efficiently by the CFT, since they bent in such a way that they "hit" more wires in each CTC superlayer as they traversed the CTC volume (see Fig. 2.8 for the orientation of the CTC superlayers and the direction of the magnetic field). The efficiency of the lowest CFT bin was found to plateau at a value of $(92.2 \pm 1.2)\%$. This efficiency represents the average value for positive and negative tracks. Since these tracks were reconstructed in data collected in parallel with the Run 1B penguin data (refer to Section 4.2.3), and since most of the non-conversion electrons collected by the trigger come from b quark decays [52], these tracks were embedded in similar environments as the daughter tracks of the penguin decays; this means that the efficiency determined from such tracks can be applied to the penguin daughters with confidence. The CFT efficiency decreased during the data taking period, mainly due to aging of the CTC[5] and increased instantaneous luminosities achieved as the run progressed[6]. The CFT algorithm was changed towards the end of Run 1B, by relaxing the requirement on the number of hits in the inner CTC axial superlayers (i.e. superlayers 0, 2 and 4) associated with a candidate track. This

[5]The aging of the CTC, described in terms of the accumulated integrated luminosity, led to a drop in the CTC single hit efficiency, especially in the inner superlayers.

[6]This caused an increase in the number of hit CTC wires. The presence of extra hits increased the rate at which the CFT accepted "fake" tracks, but it also led to a loss in real track finding efficiency due to unrelated hits assigned to the real track (thus altering its p_T, for example).

change compensated for some of the inefficiency due to CTC aging and increased instantaneous luminosities. Using the same method as for Run 1B, we determine the efficiency of the lowest CFT bin to be $(92.2 \pm 1.6)\%$ during Run 1C. The efficiency of finding electrons in the fifth CFT bin (bin 4), shown in Fig. 3.6, plateaus at $(91.3 \pm 1.0)\%$ for the last quarter of Run 1B and $(92.3 \pm 1.0)\%$ for Run 1C. The efficiency for tracks at high $|\eta|$ was observed to be higher than for tracks at low $|\eta|$, due to the fact that high-$|\eta|$ tracks had longer traveling paths through the CTC gas, depositing more charge on the CTC wires and increasing the efficiency to detect the resulting pulses. The ϕ dependence was not uniform either; it was observed to have a sinusoidal pattern, due to the fact that the CTC assumed that the $p\bar{p}$ collisions happened at $(0,0)$ in the $x-y$ plane, something that was not generally the case since the beam axis did not coincide with the z axis of the detector. This resulted in the CFT assigning a false curvature to the tracks, which introduced an inefficiency that depended on the ϕ of the track. In this analysis we use the p_T-dependent efficiency curves taking into account the corrections for the aging of the CTC and increased instantaneous luminosities, but we treat the other "non-p_T" dependencies of the CFT efficiency as sources of systematic uncertainty in the final result.

3.3.4 Level 3

Since the information arriving at Level 3 was organized in terms of "objects" (e.g., tracks, photons, electrons) for both the data and the Monte Carlo events, we use the same algorithms to simulate the Level 3 trigger decision as the ones used on-line during the course of the data collection period. Thus any biases introduced by these algorithms are common to data and Monte Carlo events.

3.4 Reconstruction efficiencies

The resolutions of the detector response are reproduced adequately in the Monte Carlo, as was demonstrated in Section 3.2. However, the Monte Carlo simulation only produces the final objects without reconstructing them from the electronic signals in the detector channels; this means that the Monte Carlo does not take into account the inefficiencies in the track reconstruction, for example. Such inefficiencies arise from the non-100% efficiency for the hits in the CTC wires to be detected and the inefficiencies in correctly reconstructing the track, given the many hits in the CTC wires ("pattern recognition" problems). The efficiency of reconstructing tracks in the CTC has been estimated by embedding Monte Carlo generated tracks into real J/ψ events. The average efficiency for positive and negative tracks was found to be $(92.8 \pm 2.6)\%$ and the efficiency for reconstructing two oppositely charged tracks was $(88.1 \pm 4.3)\%$ [53]. We apply the efficiencies for reconstructing one or two tracks as a correction factor at the end, after the detector simulation and all selection criteria. This approach is followed in other places as well. For a full account of the efficiencies refer to Chapter 6.

Chapter 4

The "penguin" Trigger

In this chapter we investigate the way penguin events can be selected by the CDF trigger system and the need for a specific "penguin trigger" will become clear. We then present the design of this trigger with the help of Monte Carlo simulations (see Chapter 3). Finally, we describe the implemented penguin trigger and its performance, and the expected event yield.

4.1 The need for a specialized "penguin trigger"

4.1.1 Number of penguin events expected to be produced

From CDF measurements we know the cross section for the process $p\bar{p} \to B_d^0 X$ to be $\sigma(p\bar{p} \to B_d^0 X;\, p_T(B_d^0) > 6 \text{ GeV/c},\, |y(B_d^0)| < 1) = (2.392 \pm 0.544)$ mb [48]. Given the integrated luminosity, we can calculate the number of $p\bar{p}$ collisions that are expected to lead to events containing B_d^0 mesons.

The branching fraction for $B_d^0 \to K^{*0}\gamma$ was measured by the CLEO collaboration to be $\mathcal{B}(B_d^0 \to K^{*0}\gamma) = (4.0 \pm 1.9) \cdot 10^{-5}$ [32], using data collected in the CESR e^+e^- collider [1]. The number of $B_d^0 \to K^{*0}\gamma$ events produced at the $B0$ collision point

[1] Any branching fractions used hereafter are taken from Ref. [4], unless specified otherwise.

of the Tevatron for a given integrated luminosity, can then be estimated with the straight-forward calculation:

$$N(B_d^0 \to K^{*0}\gamma) = \int Ldt \cdot \sigma(p\bar{p} \to B_d^0 X) \cdot \mathcal{B}(B_d^0 \to K^{*0}\gamma) \tag{4.1}$$

where $N(B_d^0 \to K^{*0}\gamma)$ is the number $B_d^0 \to K^{*0}\gamma$ events produced; $\int Ldt$ is the integrated luminosity; $\sigma(p\bar{p} \to B_d^0 X)$ is the cross section for producing a B_d^0 meson plus anything else; and $\mathcal{B}(B_d^0 \to K^{*0}\gamma)$ is the branching fraction of the penguin process.

When we account for both B_d^0 and $\bar{B}_d^0$ production[2] (multiply the quoted production cross section by 2) and use the fact that the K^{*0} meson decays to charged kaon and pions two thirds of the time (i.e. $\mathcal{B}(K^{*0} \to K^+\pi^-) = 2/3$), we estimate the number of $B_d^0 \to K^{*0}\gamma$, $K^{*0} \to K^+\pi^-$ events produced from B mesons with $p_T > 6$ GeV/c and $|y| < 1$, to be:

$$N(B_d^0 \to K^{*0}\gamma, K^{*0} \to K^+\pi^-) = 12757 \pm 6718 \text{ events per } \int Ldt = 100\,\text{pb}^{-1} \tag{4.2}$$

Only a small fraction of these decays are observable though; in Fig. 4.1 we see how the number of "detectable" $B_d^0 \to K^{*0}\gamma$, $K^{*0} \to K^+\pi^-$ decreases as the requirements on the transverse momentum of the decay products increase. The Monte Carlo samples of $B_d^0 \to K^{*0}\gamma$, $K^{*0} \to K^+\pi^-$ events were generated as described in Chapter 3.

4.1.2 Photon triggers

The CDF trigger system accepts events with an energetic cluster in the calorimeters (see Sections 2.3.1 and 2.3.2). Therefore it is able to trigger on the photon from a penguin decay.

In Run 1B the lowest energy "photon trigger" (called `CEM_10_XCES`) required the event to have an electromagnetic energy cluster in the CEM ($|\eta| < 1.1$) with $E_T > 10$ GeV measured by the calorimeter, and more than ~ 4.5 GeV of energy in

[2]In what follows reference to one state or decay chain implies the charge conjugate as well.

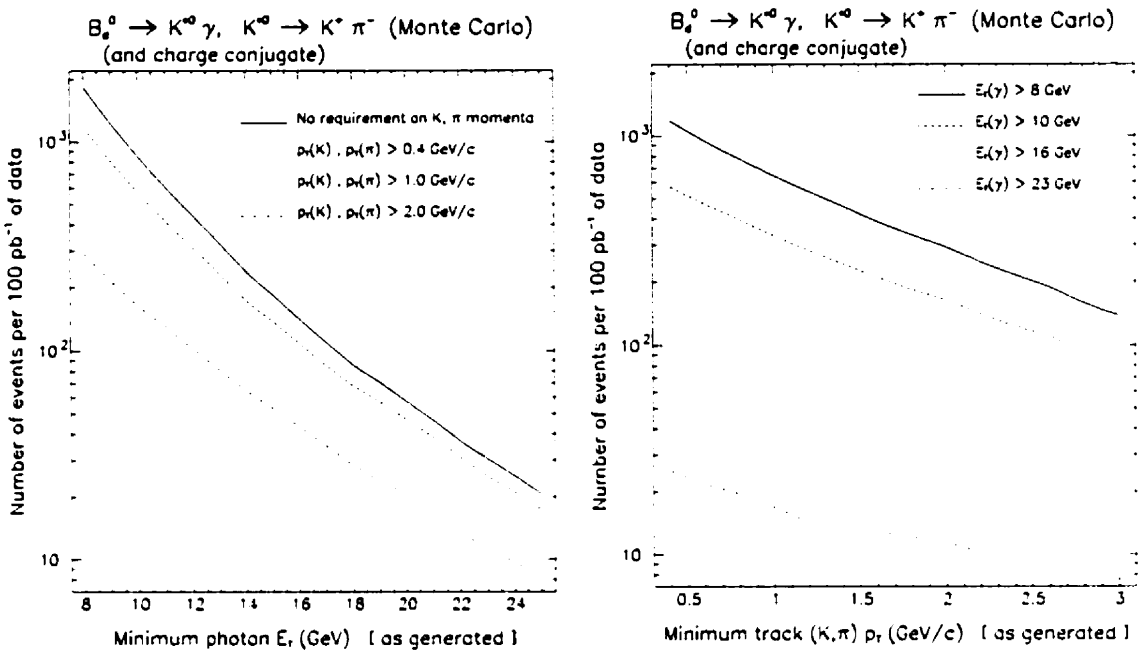

Figure 4.1: *Left: Number of penguin decays per* 100 pb^{-1} *of data as a function of the minimum* E_T *of the photon, starting with* B *mesons having* $p_T > 6$ GeV/c, $|y| < 1$. *Notice that the expected number of penguins has a* $\sim 50\%$ *uncertainty mainly due to the uncertainty in the CLEO measurement of the* $\mathcal{B}(B_d^0 \to K^{*0}\gamma)$. *Right: As before, but as a function of a minimum* p_T *requirement on the kaon and the pion.*

the shower, measured in the CES (XCES bit requirement, see Section 3.3.2). From the $B_d^0 \to K^{*0}\gamma$, $K^{*0} \to K^+\pi^-$ Monte Carlo we expect ~ 460 penguin events per 100 pb^{-1} with the photon having $E_T > 10$ GeV, $|\eta| < 1.1$ and the kaon and pion tracks having $p_T > 0.4$ GeV/c and $|\eta| < 1.1$ when generated. The $|\eta| < 1.1$ requirement on those tracks restricts them to the CTC fiducial volume. Nevertheless, the high rate of such events forced a big prescale factor (~ 200) for this trigger which implies that we expect only ~ 2 such events in the whole Run 1B data sample ($\simeq 100$ pb^{-1}), even before we consider any detector, trigger or off-line reconstruction efficiencies.

The 16 GeV photon triggers (called `CEM_16_ISO` and `CEM_16_ISO_XCES`) require isolated photons (i.e. no CFT track should point to the same wedge as the photon[3])

[3]Keep in mind though that the more energetic the photon, the more energetic the parent B

and they were also prescaled in Run 1B, by factors varying from 8 to 256 depending on the instantaneous luminosity[4]. Most of the time the prescale factors were 8 (for CEM_16_ISO_XCES) and 16 (for CEM_16_ISO). If we require the photon from the penguin decay to have $E_T > 16$ GeV, $|\eta| < 1.1$ and the kaon and pion tracks to have $p_T > 0.4$ GeV/c and $|\eta| < 1.1$ when generated, we expect ~ 12 penguin events in 100 pb^{-1} of data, assuming the lowest prescale factor of 8. This is the estimate before applying the requirement that the energy deposition in the CEM is isolated and the XCES requirement on the photon and without taking into account any detector or trigger efficiencies.

The 23 GeV photon trigger (called CEM_23) was prescaled by 20 most of the time, and by 40 at high instantaneous luminosities. The number of penguin decays expected in this sample is ~ 1 event in 100 pb^{-1} of data, if we were to require the photon from the penguin decay to have $E_T > 23$ GeV, $|\eta| < 1.1$ and the kaon and pion tracks to have $p_T > 0.4$ GeV/c and $|\eta| < 1.1$ at the generator level, assuming a prescale factor of 20.

The lowest energy unprescaled photon trigger (called CEM_23_ISO_XCES) required an isolated photon in the CEM with $E_T > 23$ GeV. If we require the photon from the penguin decay to have $E_T > 23$ GeV, $|\eta| < 1.1$ and the kaon and pion tracks to have $p_T > 0.4$ GeV/c and $|\eta| < 1.1$ at the generator level, we expect ~ 24 penguin events in 100 pb^{-1} of data, before applying the isolation and the XCES requirement on the photon and even before any detector or trigger efficiencies are taken into account. The efficiency of this trigger is 0 for $E_T < 23$ GeV photons, 50% around 25.5 GeV and it reaches its plateau value for $E_T > 30$ GeV photons. This, in conjunction with the fact that the number of penguins expected drops rapidly with photon E_T (see Fig. 4.1), means that we do not expect this trigger to have collected any significant

meson is expected to be and so the more collimated the B decay products and the smaller the chance of the photon to be isolated.

[4]There are three luminosity regions that can be assigned different prescale factors for each trigger: $< 11 \cdot 10^{30}\ cm^{-2}s^{-1}$, $(11-21) \cdot 10^{30}\ cm^{-2}s^{-1}$, and $> 21 \cdot 10^{30}\ cm^{-2}s^{-1}$

number of penguin events.

The integrated luminosity collected during Run 1C is too small ($\sim$ 6 pb^{-1}) for the photon triggers to collect any significant number of penguin events.

4.2 The dedicated Penguin trigger

4.2.1 Available information at the trigger level

Since existing photon triggers were not able to select enough penguin events, our strategy was to have the trigger use information about the kaon and the pion as well. This approach attempts to avoid high prescale factors by designing a specialized trigger to select penguin-like events.

At Level 1, the trigger `L1_CALORIMETER` accepted an event if there was a CEM trigger tower[5] with energy above 8 GeV (5 GeV) in Run 1B (Run 1C), resulting in an acceptance rate that corresponds to a cross section (see Eq. 2.2 and Fig. 4.3) of $\sim$ 20 ($\sim$ 30) μb in Run 1B (Run 1C)[6].

There were two clustering algorithms used at Level 2; the first required that the seed tower have more than 5 GeV of energy and the shoulder towers more than 4 GeV to be considered part of the cluster; the second required a seed tower above 8 GeV and shoulder towers above 7 GeV. There were four available energy thresholds for photons in the trigger. The two lowest in energy (10 and 16 GeV for Run 1B, 6 and 10 GeV for Run 1C) were formed using the first clustering algorithm. All

[5] A CEM trigger tower consists of two adjacent physical CEM towers (see Section 2.3.1). Whenever we talk about a calorimeter "tower" at Level 1 or Level 2, we mean a trigger tower.

[6] Expressing a trigger rate as a cross section, makes it, in principle, independent of the instantaneous luminosity since it is related to the probability to get a specific kind of event out of a $p\bar{p}$ collision: one that satisfies the trigger requirements. The trigger cross section multiplied by the integrated luminosity, gives the number of events that satisfied the specific trigger criteria. Therefore, collecting $\sim$ 90 pb^{-1} during the course of Run 1B means that this trigger accepted $\sim$ 90 pb^{-1} $\cdot$20 μb = $1.8 \cdot 10^9$ events for further consideration.

the electromagnetic clusters at Level 2 were put in the *photon list.* If there was any CFT track pointing to the same ϕ-slice as the wedge of the photon cluster, then the "stiff-track" bit was set and the associated cluster was characterized as an electron candidate and it was put in the *electron list* as well. Since the CFT dealt with the axial CTC superlayers only, it had no information on the η of the track it considers. Thus, a cluster of energy in the CEM could be located at $\eta > 0$ and put in the electron list due to a CFT track that points at $\eta < 0$, but in the same ϕ slice as the CEM wedge of the cluster. Again the trigger was generous in this respect, making the electron list longer than it should be. The lists of electromagnetic clusters contain the following information:

i) the transverse energy (E_T), measured in bins of 0.5 GeV assuming a $p\bar{p}$ collision point at $(x, y, z) = (0, 0, 0)$,

ii) the η and ϕ of the seed tower,

iii) the energy fraction leaking into the hadronic calorimeter (E_{HAD}/E_{TOT}),

iv) the XCES bit, and

v) the "stiff-track" bit.

Level 2 also holds a list of tracks found by the CFT with the following information:

i) the p_T in CFT p_T bins,

ii) the charge (assumed to be either $+1$ or -1), and

iii) the ϕ at the outer superlayer ("superlayer 8") of the CTC.

Knowing the energy spectra and the topology of the decay products from our Monte Carlo, we can use the available information to build a penguin trigger for Level 2. At Level 3 we can form quantities like the ones used off-line, since all the information is available and there is enough time to completely "reconstruct" the

event. Among others, we can then reinforce the Level 2 requirements and apply loose invariant mass cuts for the $K\pi$ and the $\gamma K\pi$ candidate combinations.

4.2.2 The penguin trigger requirements

We used a $B_d^0 \to K^{*0}\gamma$, $K^{*0} \to K^+\pi^-$ Monte Carlo sample to investigate the cuts for quantities that could be formed with the available information at Level 2. In Fig. 4.2 we see distributions of some of these quantities, at the generator level, for the signal events. We then devised requirements that kept as much of the signal as possible, while keeping the acceptance rate for this trigger at reasonable levels.

The resulting Level 2 trigger (named **KSTAR_GAMMA**) required[7]:

I. A photon cluster in the CEM with $E_T > 10$ GeV (> 6 GeV) in Run 1B (Run 1C). These were the lowest photon thresholds available at Level 2. The cluster was required to have less than 12.5% of its energy deposited in the CHA.

II. The XCES bit must be set for this cluster.

III. The stiff-track bit must be off for this cluster in order to reject electromagnetic clusters from electrons. This was also the easiest way to reduce the acceptance rate of the trigger dramatically without sacrificing too many signal events.

IV. At least two oppositely charged tracks, found in the lowest p_T CFT bin ($p_T \gtrsim 2$ GeV/c).

V. The two CFT tracks should point one or two wedges away from the seed wedge of the photon cluster (the ϕ of the tracks at superlayer 8 of the CTC, their charge and their momentum, were used to extrapolate them to the face of the strip chambers with the help of look-up tables).

[7]The sophisticated physics cuts at Level 2 would not be possible without the Alpha processors (see Section 2.3.2), which were installed in the last half of the Run 1B period. Therefore, the penguin trigger started collecting data towards the end of Run 1B.

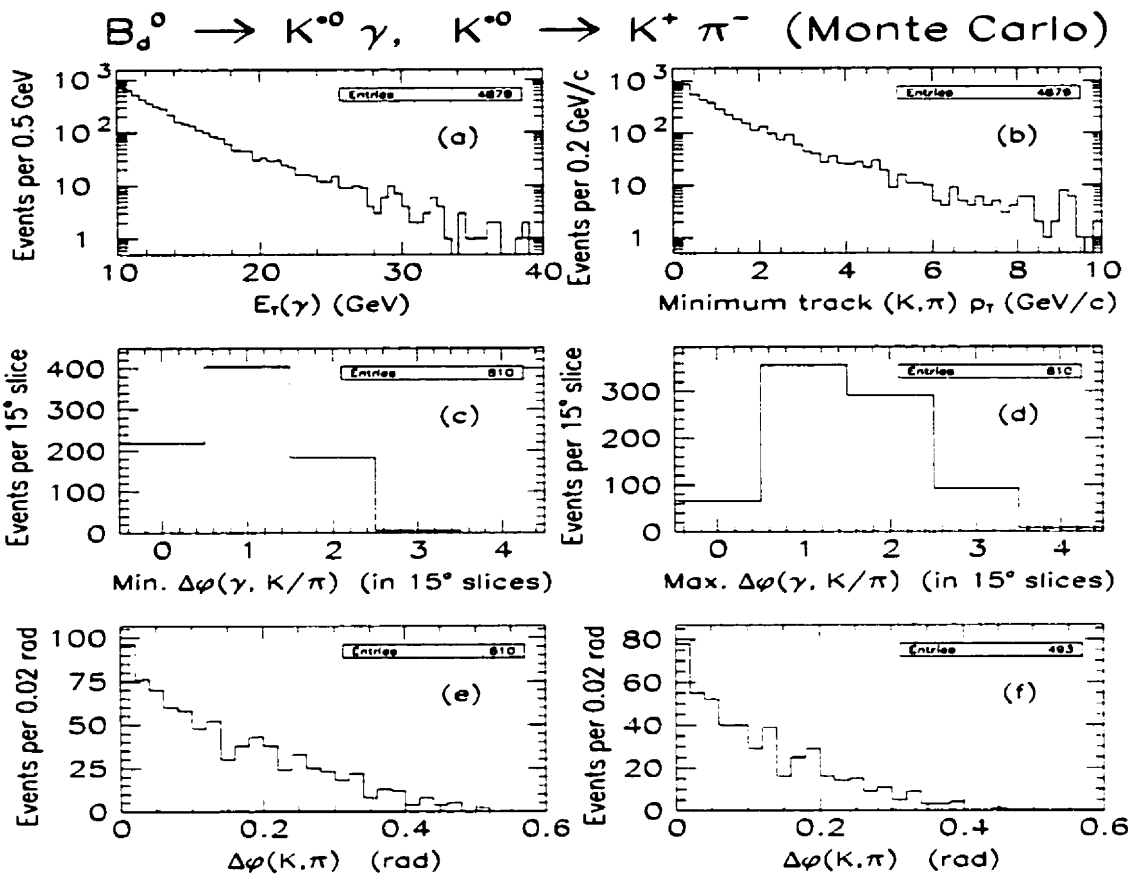

Figure 4.2: *Monte Carlo signal quantities relevant at Level 2 for B mesons with* $p_T > 6$ *GeV/c,* $|y| < 1.25$, *and photons in the CEM* ($|\eta| < 1.1$) *with* $E_T > 10$ *GeV. All quantities shown are formed from generator level information (before the detector and trigger simulation). (a)* $E_T(\gamma)$ *distribution; (b) Minimum track* (K, π) p_T *distribution; (c)/(d) The distance between the photon and the kaon/pion tracks, in slices of* 15^0 *in* ϕ *for tracks with* $p_T > 2.0$ *GeV/c,* $|\eta| < 1.1$. *If the kaon/pion points towards the CEM wedge of the photon (covering* 15^0 *in* ϕ*), then* $\Delta\phi(\gamma, K/\pi) = 0$. *In (c) we plot the* $\Delta\phi(\gamma, K/\pi)$ *for the track (kaon or pion) that is closest in* ϕ *to the photon, whereas in (d) we consider the track that is furthest away from the photon in* ϕ. *The* ϕ *of the tracks has been calculated at superlayer 8; (e)* ϕ *separation* ($\Delta\phi$) *between the kaon and the pion at superlayer 8 with the same cuts as for insets (c) and (d); and (f)* $\Delta\phi$ *between the kaon and the pion at superlayer 8 with the extra requirement that the kaon and the pion point 1 or 2 wedges away from the seed wedge of the photon, i.e.* $\Delta\phi(\gamma, K/\pi) = 1$ *or* 2 *(in units of* 15^0 *in* ϕ*).*

VI. The two CFT tracks should be within 18° in ϕ from each other at superlayer 8.

At Level 3, we implemented a trigger (named **ELEB_KSTAR_GAMMA**) which required the event to have passed the **KSTAR_GAMMA** trigger at Level 2. This trigger also required:

VII. A cluster in the CEM with $E > 7$ GeV (> 5 GeV) in Run 1B (Run 1C).

VIII. Knowing that the CEM has a sufficient depth (18 X_0) to contain most of the longitudinal development of an electromagnetic shower, we require the energy deposited in the CHA (E_{HAD}) to be less than 15% of the energy deposited in the CEM (E_{EM}).

IX. The lateral profile of the energy spread of the cluster should be consistent with expectations based on test beam results for electrons. This was accomplished using both the calorimeter and the strip chambers. The comparison based on the energy measurements in the CEM is expressed in terms of the variable L_{SHR}. This is the excess of the measured compared to the expected energy in the two "shoulder" CEM towers adjacent to the seed, over the characteristic energy fluctuation, which is partly due to the finite resolution of the CEM energy measurement (see Eq. 3.2) and partly due to the uncertainty on the expected fraction of energy to be deposited in the shoulder towers. At the trigger level we required $L_{SHR} < 0.6$, which was satisfied by almost all electrons and photons. The comparison that was based on the CES is expressed in terms of two χ^2's; χ^2_{strips} and χ^2_{wires}, corresponding to the measurements performed by the strips and wires of the CES. Each of these χ^2's characterize the fit of a parameterization of the energy profiles obtained in test beam data, to the measured energy profile along 11 strips or wires. At the trigger level we required $\chi^2_{strips} < 40$ and $\chi^2_{wires} < 45$. More than 97% of electrons and photons satisfied the requirements on χ^2_{strips} and χ^2_{wires}.

X. At least two oppositely charged tracks measured in the CTC with:

- $p_T > 1.6$ GeV/c for each track,
- at least one hit in superlayer 8 for each track,
- matching CFT tracks for the two charged CTC tracks; the extrapolated CTC track to superlayer 8 (at radius $r = 128.1$ cm) should be no more than 0.02 rad ($\sim 1.15^o$) away in ϕ from the closest CFT track,
- The ϕ separation between the two matching CFT tracks at superlayer 8 should be $\Delta\phi < 0.35$ rad, and
- The two tracks should point one or two wedges away from the seed wedge of the photon cluster (the ϕ of the tracks at superlayer 8 of the CTC are used).

XI. Calling z_0 the z position of a track at the point of closest approach to the z-axis, we required the arithmetic mean of the z_0's of the two tracks to be within 70 cm from the nominal interaction point at $z = 0$.

XII. Assigning kaon and pion masses to the two candidate tracks, we imposed two loose invariant mass cuts: $M(K\pi) < 3.5$ GeV/c^2 and $M(\gamma K\pi) < 10$ GeV/c^2. The event was also accepted if $M(KK) < 3.5$ GeV/c^2 and $M(\gamma KK) < 10$ GeV/c^2 in order to accept $B_s^0 \to \phi\gamma$ events.

4.2.3 Trigger tests and performance

The Run 1B set of requirements were tested on data (taken at luminosity $\sim 3 \cdot 10^{30}$ $cm^{-2}s^{-1}$) that had the Level 2 and Level 3 triggers reporting their decision without actually applying it. This gave a sample of events that had all the quantities formed at Level 2 for the usual triggers, including the photon and CFT track lists that were of interest to us. The fraction of events satisfying the penguin trigger requirements indicated that the expected cross section of this trigger was ~ 65 nb (corresponding

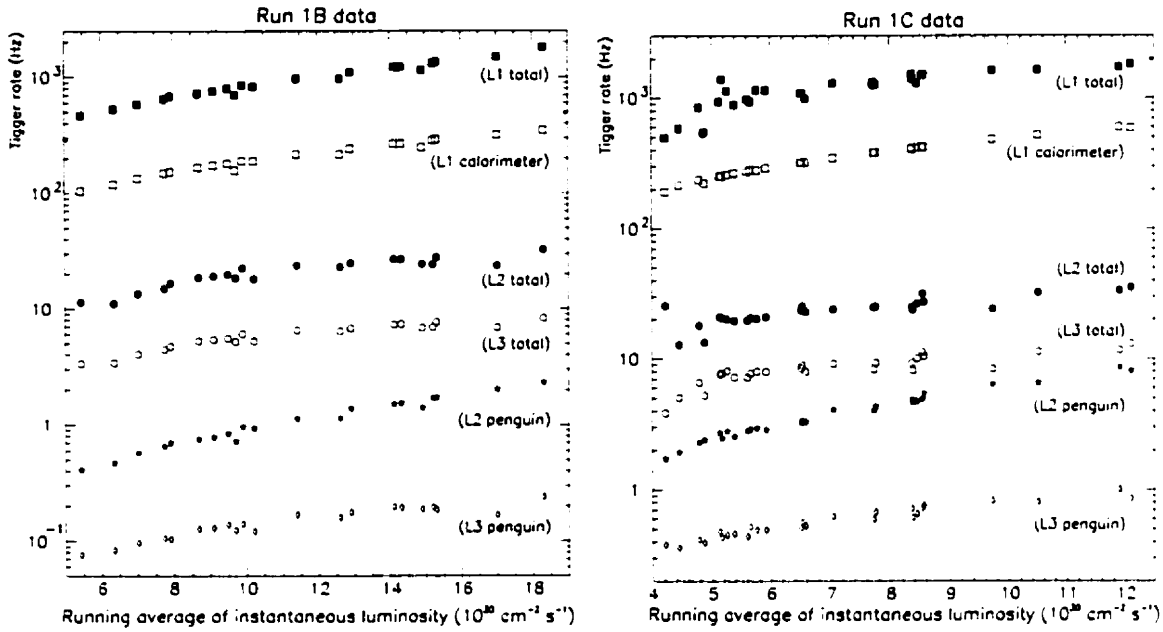

Figure 4.3: *Left: Trigger rates as a function of instantaneous luminosity (running average) for the requirements used in Run 1B. Right: Same, but for Run 1C.*

to a rate of $\sim$ 0.2 Hz at an instantaneous luminosity of $3 \cdot 10^{30}\ cm^{-2}s^{-1}$) at Level 2 and $\sim$ 14 nb (a rate of $\sim$ 0.04 Hz) at Level 3, within the total budget of the Level 2 and Level 3 trigger rates, as seen in Fig. 4.3. This prediction was verified when the penguin trigger algorithms were built and tested as autonomous blocks of the trigger logic (see Fig. 4.3 and 4.4).

The complete penguin trigger was installed on April 13, 1995 under the names **KSTAR_GAMMA** (Level 2) and **ELEB_KSTAR_GAMMA** (Level 3). As we see in Fig. 4.4, the Level 2 penguin trigger cross section was a stronger function of the instantaneous luminosity than the Level 3 penguin trigger cross section. Since the trigger tried to find the elements of the event that satisfied its criteria without "knowing" if the event was the outcome of a multiple $p\bar{p}$ collision in the given beam crossing, its acceptance rate was not really independent of the instantaneous luminosity. Having more strict requirements at Level 3 decreased the probability for unrelated elements originating from different $p\bar{p}$ collisions to satisfy the Level 3 requirements. Thus all

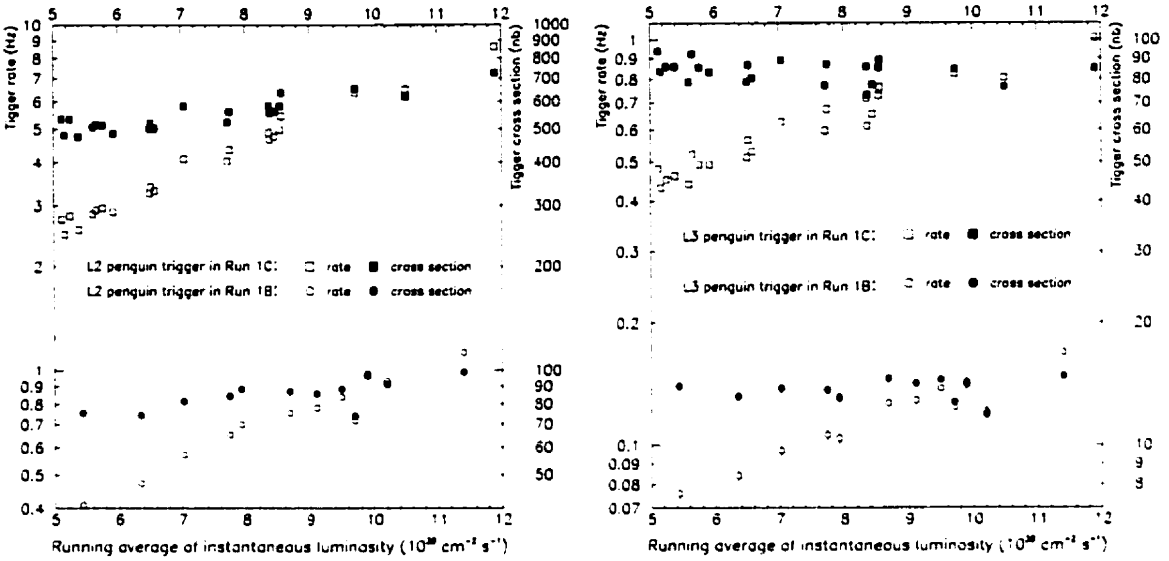

Figure 4.4: *Left: Trigger rates and cross sections as a function of instantaneous luminosity (running average) for the Run 1B and 1C level 2 penguin triggers. Notice that the trigger cross section has a weaker dependence on the instantaneous luminosity, compared to the trigger rate. Right: Same, but for the level 3 penguin triggers.*

the elements (i.e. the photon and two oppositely charged tracks) that satisfied the Level 3 requirements usually came from the same $p\bar{p}$ collision. This fact made the Level 3 cross section weakly dependent on the instantaneous luminosity.

Because of the high acceptance rates at Level 2 the trigger was prescaled by a factor of two whenever the luminosity was above $\sim 21 \cdot 10^{30}\ cm^{-2}s^{-1}$. However, the data loss due to the prescale was minimal; this trigger considered $\sim 22.3\ \mathrm{pb}^{-1}$ out of the $\sim 23.0\ \mathrm{pb}^{-1}$ of data available.

The lowering of the electromagnetic energy threshold in Run 1C, increased the trigger cross section as a consequence. The Level 2 and Level 3 rates for the Run 1C trigger were ~ 8 times higher than the ones for the Run 1B trigger, as can be seen in Fig. 4.4. The penguin trigger collected $22.3 \pm 0.9\ \mathrm{pb}^{-1}$ of data in Run 1B and $6.6 \pm 0.3\ \mathrm{pb}^{-1}$ in Run 1C.

4.3 Trigger efficiency

The number of signal events satisfying the penguin trigger is equal to the number of such events produced at the B0 collision point of the Tevatron, scaled down by the efficiency to retain these events in our sample:

$$N_{recorded} = N_{produced} \cdot \epsilon_{trigger} \tag{4.3}$$

We can classify the trigger requirements such that its efficiency, $\epsilon_{trigger}$, includes:

Topology and kinematics: Efficiency of topology and kinematic cuts (e.g., the requirement that the photon enters the CEM volume and the requirements on the proximity of the penguin decay products),

EM: Electromagnetic clustering efficiency for a photon in the CEM with $E_T > 10$ GeV (> 6 GeV for Run 1C),

XCES: XCES bit efficiency for such a photon,

CFT: CFT efficiency for the two tracks, and

L2 isolation: Efficiency of the requirement that there be no CFT track pointing to the seed wedge of the photon. From here on we refer to this as the "L2 isolation" requirement .

4.3.1 Efficiencies derived from Monte Carlo

The kinematics and topology of the event are believed to be described adequately by the Monte Carlo. For the simulation of the electromagnetic energy clustering (both on the trigger level and off-line) we used algorithms similar to the ones used on data. Since the simulation has been tuned on the response of the detector to real test-beam electrons, we believe that the simulation models the electromagnetic energy clustering reliably (see also Sections 3.2 and 3.3.1).

We generated and simulated $B_d^0 \to K^{*0}\gamma, K^{*0} \to K^+\pi^-$ and $B_s^0 \to \phi\gamma, \phi \to K^+K^-$ events with $p_T(B) > 12$ GeV/c (> 6 GeV/c) and $|y(B)| < 1.25$ in order to study the Run 1B (Run 1C) sample. The thresholds on the momenta and rapidity of the B mesons were imposed in order to avoid simulating events that had no chance meeting the trigger requirements.

4.3.2 Efficiencies measured with data

For the efficiency of the CFT requirements on the two charged daughter particles ($K^+\pi^-$ or K^+K^-) we use the parametric forms derived for non-muon tracks in Run 1B and Run 1C (see Section 3.3.3 and Fig. 3.6). We simulate the CFT requirement for each track by generating a random number between zero and one and, given the p_T of the track we consider, we compare the random number with the CFT efficiency for this track. If the random number is lower, the track is said to meet the CFT requirement.

Considering all the Level 2 and Level 3 efficiencies, except the XCES and the L2 isolation requirements on the photon at Level 2, we see in Fig. 4.5 and 4.6 how this part of the trigger efficiency depends on the transverse momentum of the B meson and the photon, for $B_d^0 \to K^{*0}\gamma$, $K^{*0} \to K^+\pi^-$ events.

In Fig. 4.7 we see how the lower energy threshold for photons in Run 1C, allows the penguin trigger to increase the signal yield substantially. In Table 4.1 we see the decrease in the number of Monte Carlo penguin events as a result of the trigger requirements.

The effect of the XCES requirement is determined with the use of the parameterization of this efficiency as a function of E_T derived from electrons in Run 1B (see Fig. 3.5). Given the E_T spectra of the photons in the penguin channels, we obtain the XCES efficiencies shown in Table 4.1.

The fact that any CFT track in the event could cause the stiff-track bit to be set for the wedge of the photon, makes our signal-only Monte Carlo inappropriate

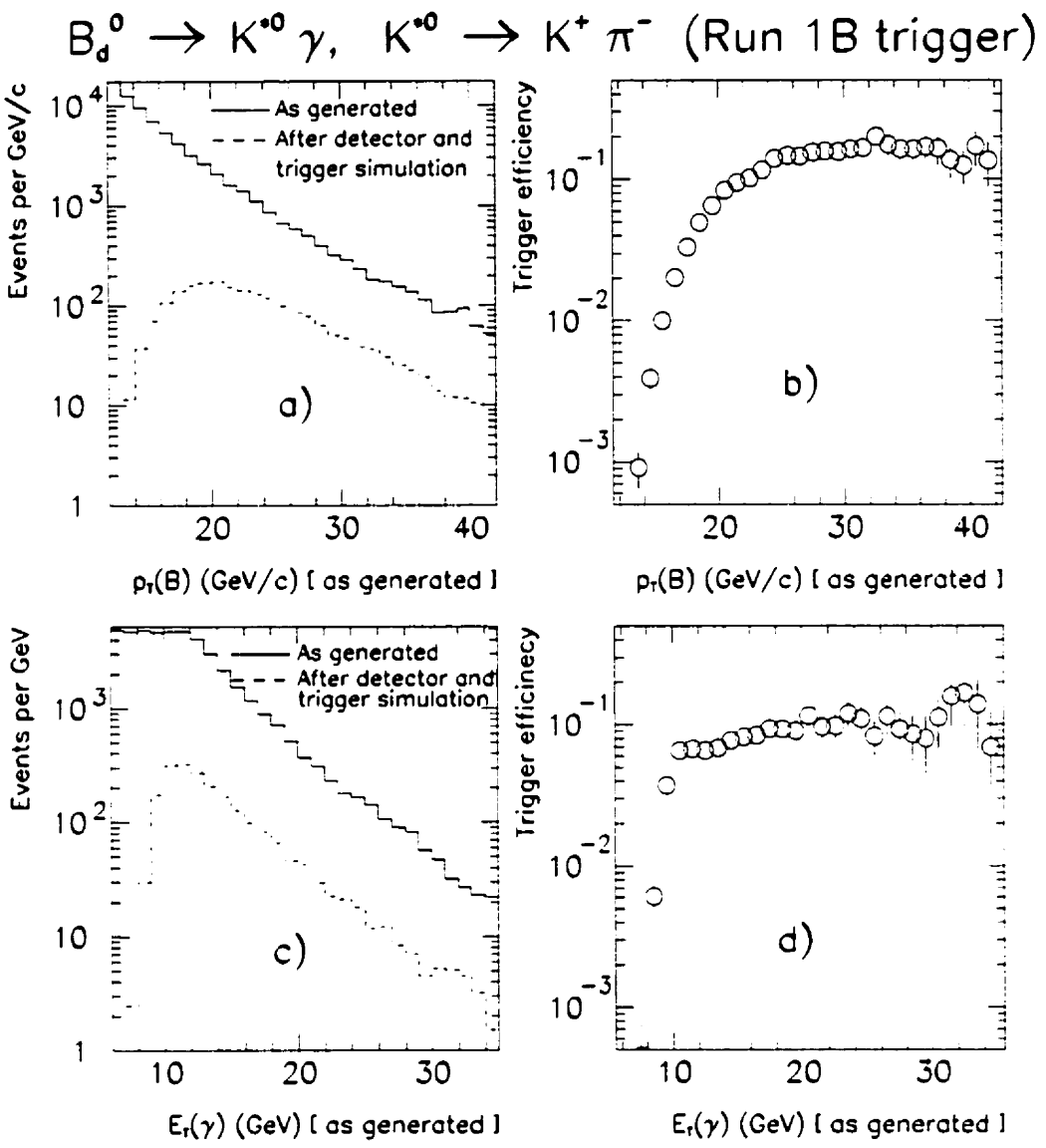

Figure 4.5: *a) Monte Carlo events as generated (solid histogram) and after detector and Run 1B trigger simulation (dashed histogram) as a function of generator level $p_T(B)$. The detector and trigger simulation used here do not include the XCES and the L2 isolation (i.e. no CFT track at the same wedge as the photon) requirements. Therefore the trigger efficiencies shown here are missing these two elements. b) Partial trigger efficiency vs. generator level $p_T(B)$. c) Monte Carlo events as generated (solid histogram) and after detector and trigger simulation (dashed histogram) as a function of generator level $E_T(\gamma)$. d) Partial trigger efficiency vs. generator level $E_T(\gamma)$.*

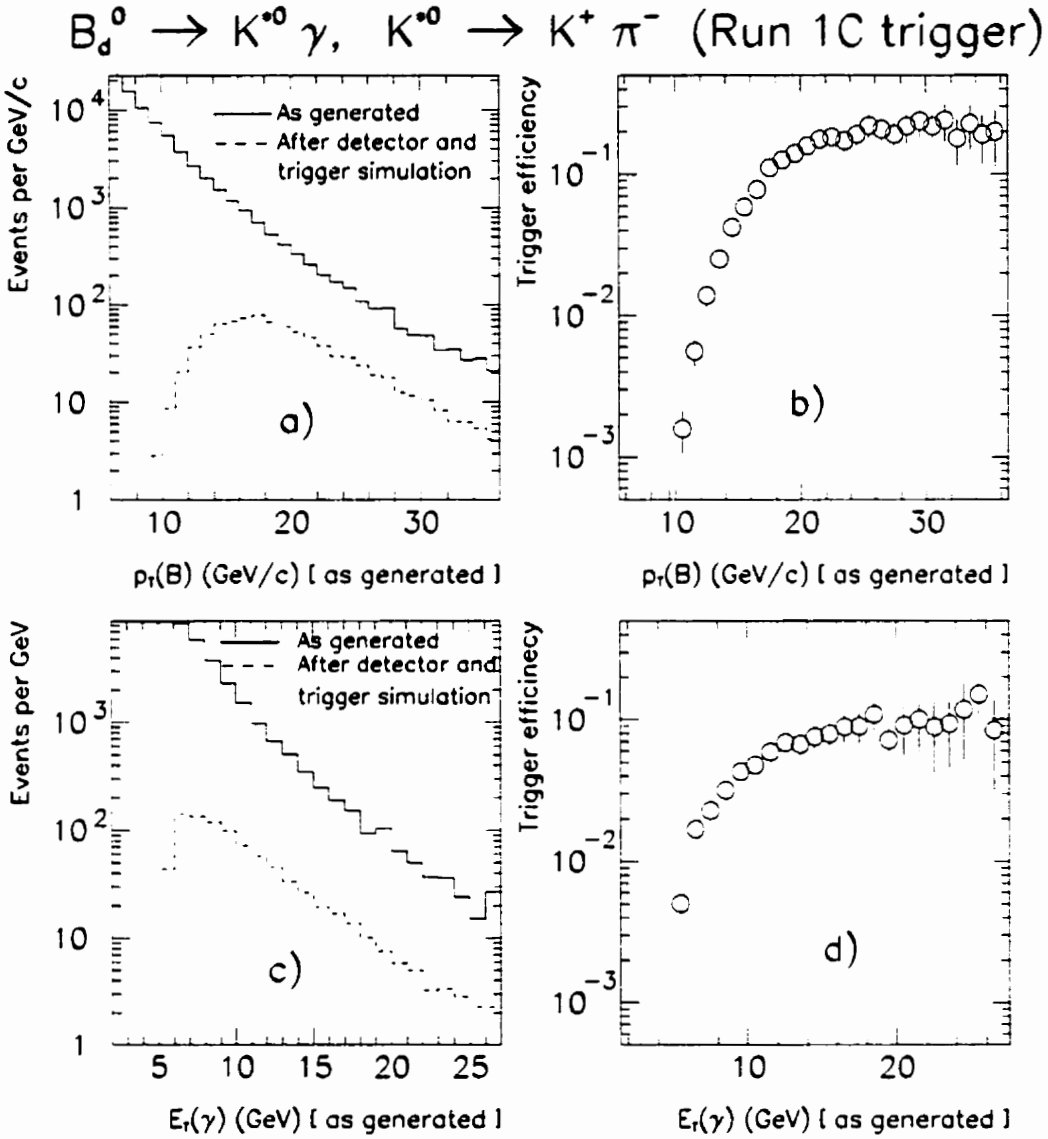

Figure 4.6: *a) Monte Carlo events as generated (solid histogram) and after detector and Run 1C trigger simulation (dashed histogram) as a function of generator level $p_T(B)$. The detector and trigger simulation used here, does not include the XCES and the L2 isolation requirements on the photon. Therefore the trigger efficiencies shown here are missing these two elements. b) Partial trigger efficiency vs. generator level $p_T(B)$. c) Monte Carlo events as generated (solid histogram) and after detector and trigger simulation (dashed histogram) as a function of generator level $E_T(\gamma)$. d) Partial trigger efficiency vs. generator level $E_T(\gamma)$.*

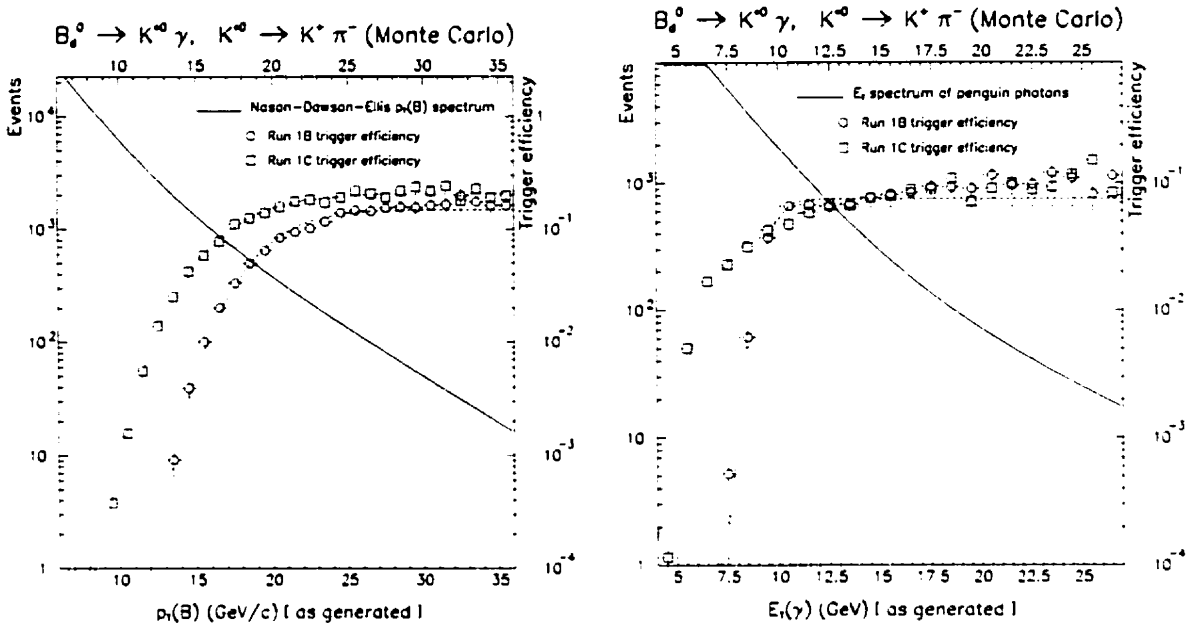

Figure 4.7: *Left: The trigger efficiencies for the Run 1B and Run 1C implementations as a function of the p_T of the B meson. The trigger efficiencies shown do not include the XCES and the L2 isolation (i.e. no CFT track at the same wedge as the photon) requirements. The spectrum of the transverse momentum of the B mesons as calculated by Nason, Dawson and Ellis [16] is shown as a solid line. Right: The (partial) trigger efficiencies for the Run 1B and Run 1C implementations as a function of the transverse energy of the penguin photon. The ability to collect lower energy photons in Run 1C allows the trigger to reach B mesons at lower momenta and thus increase its signal yield substantially due to the rapidly falling $p_T(B)$ spectrum.*

to estimate the efficiency of the L2 isolation requirement on the photon. We then estimate the efficiency of this requirement using the decay $\bar{B} \to e^- D^0 X$, $D^0 \to K^-\pi^+$ observed in a sample of events containing electron candidates with $E_T > 8$ GeV. We reconstruct this decay with the cuts mentioned in Section 6.3, making sure that the momentum spectra of the B mesons in this channel, match the corresponding spectra for the penguin channels. This guarantees that the environment around the B mesons is similar between these channels and thus the efficiency for the L2 isolation

	$B_d^0 \to K^{*0}\gamma$		$B_s^0 \to \phi\gamma$	
Monte Carlo events	Run 1B	Run 1C	Run 1B	Run 1C
$\|y(B)\| < 1.25$ and $p_T(B) > 12$ GeV/c or $p_T(B) > 6$ GeV/c	737303	1942314	550968	1523628
After partial trigger simulation (Topol. & kin., EM, CFT)	21716	21964	23954	24425
Trigger efficiencies (in %)				
Partial trigger simulation	2.95 ± 0.02	1.13 ± 0.01	4.35 ± 0.03	1.60 ± 0.01
XCES	93.9 ± 1.4	93.6 ± 3.2	94.0 ± 1.3	93.8 ± 3.1
L2 isolation	62.0 ± 7.8	$88.6^{+11.4}_{-12.9}$	63.2 ± 8.0	$90.4^{+9.6}_{-13.2}$
Total trigger efficiency (%)	1.72 ± 0.22	$0.94^{+0.13}_{-0.14}$	2.58 ± 0.33	$1.36^{+0.15}_{-0.20}$
$\int Ldt$ (pb^{-1})	22.3 ± 0.9	6.6 ± 0.3	22.3 ± 0.9	6.6 ± 0.3
$2 \cdot \sigma(p\bar{p} \to BX)$ (μb)	0.622 ± 0.144	5.816 ± 1.322	$\frac{1}{3} \cdot \sigma(p\bar{p} \to B_d^0 X)$	
$\mathcal{B}(K^{*0} \to K^+\pi^-)$	2/3			
$\mathcal{B}(\phi \to K^+K^-)$			0.491 ± 0.008	
If: $\mathcal{B}(B_d^0 \to K^{*0}\gamma) =$ $\mathcal{B}(B_s^0 \to \phi\gamma)$	$(4.0 \pm 1.9) \times 10^{-5}$			
Then: Expected signal out of trigger (events)	6.4 ± 3.5	9.6 ± 5.3	2.3 ± 1.3	$3.4^{+1.8}_{-1.9}$

Table 4.1: *Trigger efficiency for the $B_d^0 \to K^{*0}\gamma$ and the $B_s^0 \to \phi\gamma$ decays in Run 1B (Run 1C) are quoted starting with B mesons of $p_T > 12$ (> 6) GeV/c and $|y| < 1.25$ and applying the trigger cuts (see Section 4.2.2).*

requirement can be derived from $\bar{B} \to e^- D^0 X$, $D^0 \to K^-\pi^+$ decays and applied to the penguin channels. Furthermore we reconstruct the $\bar{B} \to e^- D^0 X$, $D^0 \to K^-\pi^+$ decays for events collected in the same time span that the penguin trigger collected

data. This guarantees that the same luminosity, detector, etc. biases are present in both samples.

We look for any CFT track (other than the electron and the possible kaon and pion CFT tracks) that falls on the seed wedge of the electron and thus would have set the stiff-track bit to be on. Comparing the resulting number of events with the number of events before the L2 isolation requirement, we estimate the efficiency of the L2 isolation requirement to be $(59.2 \pm 7.4)\%$ in Run 1B and $(84.6 \pm 12.2)\%$ in Run 1C for $\bar{B} \to e^- D^0 X$, $D^0 \to K^- \pi^+$ decays. (see Fig. 4.8 and 4.9). The reconstructed events from this decay chain result mostly from B_u^+ mesons, whereas the penguin decays originate from B_d^0 and B_s^0 mesons. These B mesons result from the hadronization of b quarks, which at the fragmentation process combine with u, d or s quarks respectively. Differences in the fragmentation processes could result in different isolation efficiencies between the $\bar{B} \to e^- D^0 X$, $D^0 \to K^- \pi^+$ and the penguin channels. Furthermore, contrary to the penguin channels, $\bar{B} \to e^- D^0 X$, $D^0 \to K^- \pi^+$ is not a fully reconstructed decay and the extra particles could result in lower L2 isolation efficiency compared to the penguin channels. We use the PYTHIA Monte Carlo program [54] to generate these decays along with the rest of the $p\bar{p}$ collision outcome. The resulting particles are then fed through the detector and trigger simulation (see Sections 3.2 and 3.3) and the L2 isolation efficiencies are found to be higher for the B_d^0 and B_s^0 penguin channels by $(4.7 \pm 2.0)\%$ and $(6.8 \pm 2.1)\%$ respectively. From the L2 isolation efficiencies measured with the $\bar{B} \to e^- D^0 X$, $D^0 \to K^- \pi^+$ channel, mentioned above, we infer the ones appropriate for the penguin channels, shown in Table 4.1.

Including the efficiencies for the XCES and the L2 isolation requirements, we estimate the combined efficiency for the Level 2 and Level 3 Run 1B penguin trigger to be $(1.72 \pm 0.22)\%$ for B_d^0 mesons of $p_T > 12$ GeV/c and $|y| < 1.25$ subsequently decaying to $K^{*0}\gamma$. The corresponding efficiency for Run 1C is $(0.94^{+0.13}_{-0.14})\%$ for B_d^0 mesons of $p_T > 6$ GeV/c and $|y| < 1.25$.

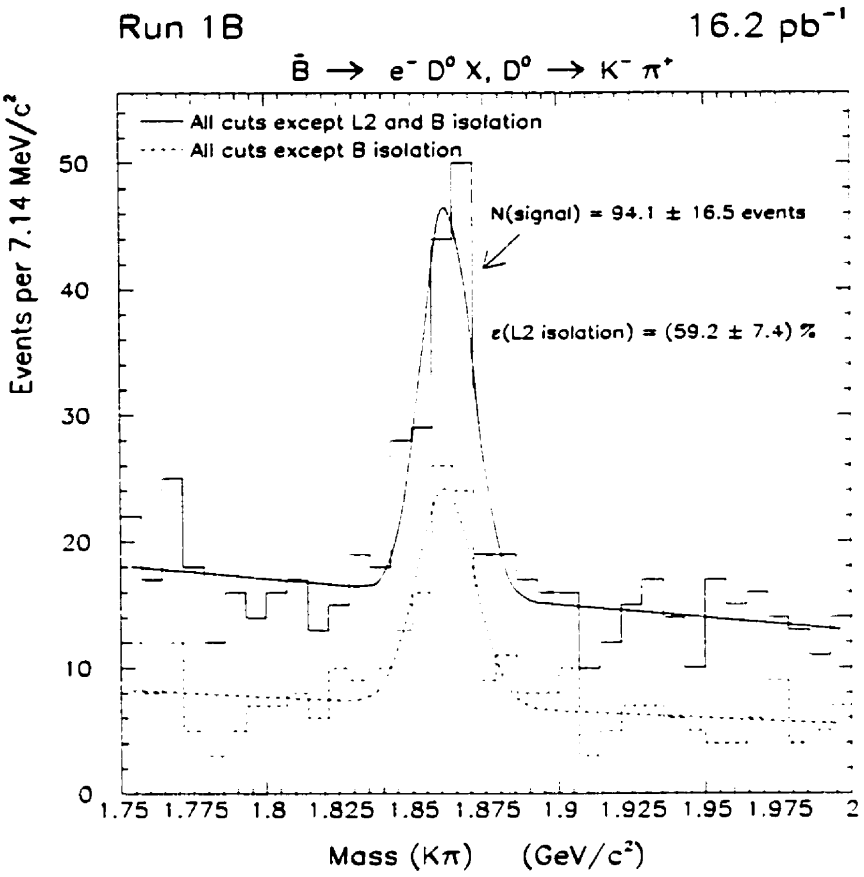

Figure 4.8: *Run 1B $M(K\pi)$ distribution with the kaon having the same charge as the electron, indicating the reconstruction of the $\bar{B} \to e^- D^0 X, D^0 \to K^-\pi^+$ decay chain. The solid histogram shows the events that satisfy all the cuts mentioned in Section 6.3, before the application of the requirements (m) and (p) in that section (i.e. the isolation requirement on the electron at L2 and the B isolation requirements). The dashed histogram shows the events that survive the L2 isolation requirement. The signal was reconstructed with data that required an electron with $E_T > 8$ GeV at the trigger level. Due to different prescale factors, the trigger that looked for such electrons collected a smaller fraction of the available events, than the penguin trigger did; the penguin trigger collected ~ 22 pb^{-1} of data in Run 1B, while the $E_T > 8$ GeV electron trigger collected ~ 16 pb^{-1} during the same time period.*

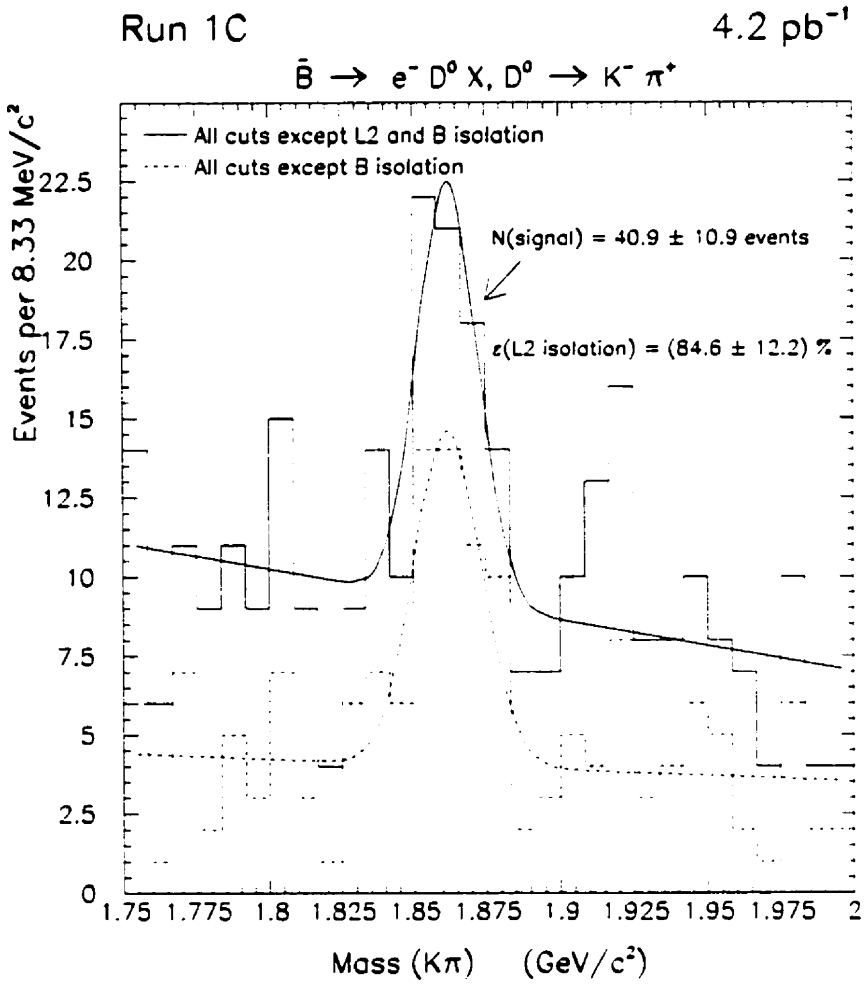

Figure 4.9: *As in Figure 4.8, but for Run 1C data.*

In exactly the same way, the combined efficiency of the Level 2 and Level 3 Run 1B penguin trigger is found to be $(2.58 \pm 0.33)\%$ for B_s^0 mesons of $p_T > 12$ GeV/c and $|y| < 1.25$ subsequently decaying to $\phi\gamma$. For Run 1C the trigger efficiency is $(1.36^{+0.15}_{-0.20})\%$ for B_s^0 mesons of $p_T > 6$ GeV/c and $|y| < 1.25$.

The trigger efficiencies as well as the number of signal events expected to meet the trigger requirements are summarized in Table 4.1.

4.4 Expected signal yield of the penguin trigger

In order to get a feeling for how many penguin events are expected to be recorded by this trigger we first calculate the number of penguin decays expected to have been produced with $p_T(B) > 12$ GeV/c (> 6 GeV/c) and $|y(B)| < 1.25$ during the data collection in Run 1B (Run 1C). We first get the measured cross section of [48]:

$$\sigma(p\bar{p} \to B_d^0 X; p_T(B_d^0) > \mathbf{12}\ \text{GeV/c},\ |y(B_d^0)| < \mathbf{1}) = (0.256 \pm 0.059)\ \mu\text{b}$$

$$\sigma(p\bar{p} \to B_d^0 X; p_T(B_d^0) > \mathbf{6}\ \text{GeV/c},\ |y(B_d^0)| < \mathbf{1}) = (2.392 \pm 0.544)\ \mu\text{b}$$

Then, we use the rapidity spectrum of B mesons as calculated by Nason, Dawson and Ellis [16] (see Fig. 3.1) to obtain the fraction of B mesons with $1 < |y| < 1.25$ and we calculate:

$$\sigma(p\bar{p} \to B_d^0 X; p_T(B_d^0) > \mathbf{12}\ \text{GeV/c},\ |y(B_d^0)| < \mathbf{1.25}) = (0.311 \pm 0.072)\ \mu\text{b}$$

$$\sigma(p\bar{p} \to B_d^0 X; p_T(B_d^0) > \mathbf{6}\ \text{GeV/c},\ |y(B_d^0)| < \mathbf{1.25}) = (2.908 \pm 0.661)\ \mu\text{b}$$

The number of penguin events expected to be produced from both B_d^0 and $\bar{B}_d^0$ decays, assuming the CLEO branching ratio of $(4.0 \pm 1.9) \cdot 10^{-5}$ for $B_d^0 \to K^{*0}\gamma$ [32] and $\mathcal{B}(K^{*0} \to K^+\pi^-) = 2/3$, is then estimated to be:

$$\begin{aligned}
&N_{produced}(B_d^0 \to K^{*0}\gamma, K^{*0} \to K^+\pi^-) = \\
&\quad 2 \cdot \int Ldt \cdot \sigma(p\bar{p} \to B_d^0 X) \cdot \mathcal{B}(B_d^0 \to K^{*0}\gamma) \cdot \mathcal{B}(K^{*0} \to K^+\pi^-) = \\
&\quad \simeq 370 \pm 196 \ \text{ events per } \ 22.3 \pm 0.9\,\text{pb}^{-1} \ \text{ of Run 1B data} \\
&\qquad \text{(originating from } B_d^0 \text{ and } \bar{B}_d^0 \text{ mesons with } p_T > \mathbf{12}\ \text{GeV/c}, |y| < 1.25), \\
&\quad \text{and} \\
&\quad \simeq 1024 \pm 541 \ \text{ events per } \ 6.6 \pm 0.3\,\text{pb}^{-1} \ \text{ of Run 1C data} \\
&\qquad \text{(originating from } B_d^0 \text{ and } \bar{B}_d^0 \text{ mesons with } p_T > \mathbf{6}\ \text{GeV/c}, |y| < 1.25) \quad (4.4)
\end{aligned}$$

Assuming the production cross section of B_s^0 mesons to be 1/3 of that for the production of B_d^0 mesons [48], the unmeasured branching fraction $\mathcal{B}(B_s^0 \to \phi\gamma)$ to be

equal to the branching fraction $\mathcal{B}(B_d^0 \to K^{*0}\gamma)$, and $\mathcal{B}(\phi \to K^+K^-) = (49.1 \pm 0.8)\%$ [4], we estimate:

$$
\begin{aligned}
&N_{produced}(B_s^0 \to \phi\gamma, \phi \to K^+K^-) = \\
&\quad 2 \cdot \int Ldt \cdot \sigma(p\bar{p} \to B_s^0 X) \cdot \mathcal{B}(B_s^0 \to \phi\gamma) \cdot \mathcal{B}(\phi \to K^+K^-) = \\
&\quad \simeq 91 \pm 48 \text{ events per } 22.3 \pm 0.9\,\text{pb}^{-1} \text{ of Run 1B data} \\
&\qquad \text{(originating from } B_s^0 \text{ and } \bar{B}_s^0 \text{ mesons with } p_T > \mathbf{12}\,\text{GeV/c}, |y| < 1.25), \\
&\quad \text{and} \\
&\quad \simeq 251 \pm 133 \text{ events per } 6.6 \pm 0.3\,\text{pb}^{-1} \text{ of Run 1C data} \\
&\qquad \text{(originating from } B_s^0 \text{ and } \bar{B}_s^0 \text{ mesons with } p_T > \mathbf{6}\,\text{GeV/c}, |y| < 1.25) \quad (4.5)
\end{aligned}
$$

Combining the number of penguin events expected to be produced with $p_T > 12$ (> 6) GeV/c and $|y| < 1.25$ and the efficiencies calculated in the previous section (see also Table 4.1), we expect that the 22.3 (6.6) pb^{-1} of data collected during Run 1B (Run 1C), should contain 6.4 ± 3.5 (9.6 ± 5.3) $B_d^0 \to K^{*0}\gamma$, $K^{*0} \to K^+\pi^-$ events. The number of $B_s^0 \to \phi\gamma$, $\phi \to K^+K^-$ events is expected to be 2.3 ± 1.3 ($3.4^{+1.8}_{-1.9}$) in the 22.3 (6.6) pb^{-1} of data collected during Run 1B (Run 1C).

The number of signal events expected to meet the trigger requirements are summarized in Table 4.1.

Chapter 5

Data Selection

In the previous chapter we described the specialized trigger that collected "penguin-like" events. We concluded that we expect around 6 $B^0_d \to K^{*0}\gamma$ events and ~ 2 $B^0_s \to \phi\gamma$ events in the Run 1B sample of 22.3 pb^{-1} of integrated luminosity. In the 6.6 pb^{-1} of data collected during Run 1C we expect that the penguin trigger collected ~ 10 $B^0_d \to K^{*0}\gamma$ events and ~ 3 $B^0_s \to \phi\gamma$ events. These signal events are a very small fraction of the events collected by the penguin trigger though; almost $\sim 3 \times 10^5$ ($\sim 5 \times 10^5$) events were collected by the penguin trigger in Run 1B (Run 1C). Recall that the Level 3 penguin trigger accepted events at a cross section of ~ 13 nb (~ 85 nb) in Run 1B (Run 1C).

In this chapter we will first describe briefly the standard manipulation of data after they were stored on tape. Subsequently we will describe in detail the requirements imposed on the data in the effort to extract the events containing penguin decays from the plethora of non-signal ("background") events. The ability of the requirements to enhance the signal-to-background ratio will be demonstrated with the invariant mass plots of the B meson candidates.

5.1 "Production and splitting" of data

Following an acceptance signal from the third level of the trigger (Level 3), the data acquisition system writes the data on 8mm tape. The data were then processed by "production" programs that reconstructed physics objects (electrons, photons, etc.) from the electronic signals of the detector in a way similar to Level 3. The production stage was initiated some time after the event was written to tape. Therefore it is an "off-line" process, as opposed to the "on-line" manipulation of data from the trigger. At the production stage the information about the condition of the detector (calibration and alignment constants) was more precise than the information available at Level 3. Furthermore, since the processing time was not as big a constraint at the production stage as it was at the trigger level, the time-demanding tracking algorithms used at the production stage were more sophisticated than the Level 3 ones.

The production programs were executed on a "farm" of Silicon Graphics Inc. and IBM computers that also ran "splitting" programs which classified and stored the events into different, but not mutually exclusive, data sets, according to different analysis criteria (e.g., events that contain at least one high energy electron, events that contain high energy jets, etc.). Usually these criteria were the logical "OR" of the decisions of a subset of the Level 3 triggers. The production and splitting farm processed events at a rate of approximately 1.3 million per week.

The events that satisfied the penguin trigger were put on a separate data set named KSGB, derived from KStar Gamma at stream B. There are three "streams" of data at CDF, indicating the priority at which events were put through the production and splitting procedure. Stream A marks events that were processed shortly after they were collected because of their high priority, such as the events that had a high energy electron or muon, missing energy and jets; these events were used to look for production of top quarks. There are around 3.3 million events in stream A. Stream C contains almost 27 million events that were collected with low energy thresholds

and high prescale factors. These events had the least priority and were processed several months after they were collected. Stream B contain most of the events ($\sim$ 65 million) and were processed typically about a month after they were collected. Most of the analyses done on B mesons use stream B data. The KSGB data set is part of the stream B data set.

5.2 General strategy for signal reconstruction

Clearly the signal events are a very small fraction of the total number of events collected by the penguin trigger. Nevertheless, there are some characteristics of the signal events that can be exploited in our effort to identify them and reject most of the other (i.e. "background") events.

We start by selecting reasonable photon candidates and good quality tracks reconstructed in the SVX and the CTC. We also make sure that the photon candidate and the two tracks meet the penguin trigger criteria. In Section 5.4 we discuss the means for discriminating signle photons in the calorimeter against multi-photon showers, mainly from $\pi^0 \to \gamma\gamma$ decays.

We then require the tracks to be consistent with the hypothesis of originating from a common point (called "secondary vertex"), which should be the case for tracks originating from a common parent particle (e.g., K^{*0} or ϕ). In addition, the mass of the combination of these two charged particles is required to be close to the mass of the hypothesized parent particle (e.g., the mass of the K^+K^- pair must be close to the mass of ϕ meson).

If the photon and the two charged particles selected so far are indeed the penguin decay products of a B meson, the mass of this three body system should be close to the B meson mass. We ask for this to be the case for the three body system selected so far.

Apart from the requirements on the masses of the two-body and three-body com-

binations we have some extra handles to reduce the background. The long lifetime of a B meson[1] gives it a good chance to travel away from its production point before it decays. This means that its decay products originate from a "secondary" vertex which is separated from the "primary" $p\bar{p}$ interaction vertex (in the vicinity of which the B meson was created). On the other hand most of the particles traveling through the detector volume originate from the "primary" $p\bar{p}$ interaction vertex. We therefore place some requirements that select events where the decay point of the B meson is detached from the $p\bar{p}$ interaction point.

Since we reconstruct all the B decay products, it is expected that the momentum of the three-body system points along the B flight path, from the primary and the secondary vertices. On the contrary, the combinatoric background should show no such "alignment", and should be easily discriminated from the signal events.

Furthermore, it is expected that b quarks fragment in a way that the resulting B mesons carry most of the available energy ([55]). Therefore a B meson is isolated from activity around it and we exploit this fact in order to further reduce the background.

5.3 Backgrounds

The general strategy outlined above is designed to select B-like events. Nevertheless, apart from the non-B events and the combinatoric background, there are some B decay modes which can fake the penguin signals and it is more difficult to discriminate against them.

However, the lack of significant number of penguin candidates in the present analysis (see end of this chapter) dictates the extraction of upper limits for the penguin branching fractions. In this case the conservative approach is to assume that the observed events be due to the signal process only. I.e., no background subtraction is necessary. Nevertheless, we briefly discuss six sources of background

[1] $\tau(B_d^0) = (1.56 \pm 0.04)$ ps and $\tau(B_s^0) = (1.54 \pm 0.07)$ ps [4]

to the $B_d^0 \to K^{*0}\gamma$ decays for completeness: namely, $B_d^0 \to K_1(1270)^0\gamma$, $B_d^0 \to K^{*0}\pi^0$, $B_d^0 \to \rho\pi^0$, $B_s^0 \to K^{*0}\gamma$, $B_s^0 \to K^{*0}\pi^0$, and $B_d^0 \to \rho\gamma$ decays.

For $B_s^0 \to \phi\gamma$ decays a similar discussion can be held, but the level of background after all selection criteria is so small, that we do not go into details for this channel.

B decays which result partly in $\gamma K^*(892)^0$ combinations (i.e., higher multiplicity modes) can fake $B_d^0 \to K^{*0}\gamma$ decays, if we only reconstruct the $\gamma K^*(892)^0$ part. Naturally then, the reconstructed $\gamma K^*(892)^0$ mass will be lower than the B_d^0 mass. Decays like $B_d^0 \to K_1(1270)^0\gamma, K_1(1270)^0 \to K^*(892)^0\pi^0$ are difficult to distinguish, if we fail to detect the π^0. However, simulations of such decays show that the $\gamma K^*(892)^0$ mass resolution is adequate to reject this background; less than 15% of these events fall in a two sigma window around the B mass [56]. Furthermore, the branching fraction for $B_d^0 \to K_1(1270)^0\gamma$ is expected to be less than that for $B_d^0 \to K^{*0}\gamma$, and $\mathcal{B}(K_1(1270)^0 \to K^*(892)^0\pi^0) \sim 10\%$. Therefore, the contribution from this kind of background is expected to be small.

$B_d^0 \to K^{*0}\pi^0$ and $B_d^0 \to \rho\pi^0$ decays occur less often than $B_d^0 \to K^{*0}\gamma$ decays: $\mathcal{B}(B_d^0 \to K^{*0}\gamma) \sim 4 \times 10^{-5}$, while $\mathcal{B}(B_d^0 \to K^{*0}\pi^0) < 2.8 \times 10^{-5}$ and $\mathcal{B}(B_d^0 \to \rho\pi^0) < 2.4 \times 10^{-5}$ [4], so these decays do not dominate the electromagnetic penguins. The neutral pion tends to be reconstructed as a single energy cluster in the CEM calorimeter, but, as explained in the next section, the CES chambers measure the shower profile and they can be used to discriminate single photons from multi-photon showers. Because of the low level of signal and background, we impose loose requirements on the shower shape variables. However, should there be a substantial signal and background level observed, we can suppress the fraction of multi-photon showers satisfying the selection criteria by imposing tighter requirements on these variables.

There are several reasons why $B_s^0 \to K^{*0}\pi^0$ and $B_s^0 \to K^{*0}\gamma$ decays should not be a considerable background in the present analysis; (i) B_s^0 mesons are produced approximately three times less often than B_d^0 mesons [4, 20], (ii) such decays result from $b \to t \to d$, instead of $b \to t \to s$ transitions and they are suppressed by the

CKM matrix element ratio $(|V_{td}|/|V_{ts}|)^2 < 14\%$ (see Eq. 1.2, and (iii) the $K^{*0}\gamma$ and $K^{*0}\pi^0$ combinations will yield the B_s^0 mass, which is $\simeq 90$ MeV/c^2 higher than the B_d^0 mass [4]. Even if the mass resolution of ~ 100 MeV/c^2 in this analysis is not adequate for an event-by-event separation, a statistical separation can be performed. Furthermore, the shower shape variables can be used to suppress a large fraction of $B_s^0 \to K^{*0}\pi^0$ decays, as discussed in the next section.

$B_d^0 \to \rho^0\gamma$ followed by $\rho^0 \to \pi^+\pi^-$ decays, result in $K\pi$ and $\gamma K\pi$ mass distributions resembling the corresponding distributions from $B_d^0 \to K^{*0}\gamma$ decays, when one of the pions from the ρ^0 decay is misidentified as a kaon: the $K\pi$ mass peaks ~ 100 MeV/c^2 higher than the $K^*(892)^0$ mass with a sigma of ~ 50 MeV/c^2 and the $\gamma K\pi$ mass peaks ~ 100 MeV/c^2 higher than the B_d^0 mass with a sigma of ~ 100 MeV/c^2. Furthermore, the dE/dx energy loss in the drift chamber can provide separation between kaon and pions at the 1σ level in the momentum range we are triggering on. Therefore, a statistical separation can be performed between the $B_d^0 \to K^{*0}\gamma$ and $B_d^0 \to \rho^0\gamma$ decay modes, i.e., the relative contributions can be extracted. In addition, since $B_d^0 \to \rho^0\gamma$ decays result from $b \to t \to d$, instead of $b \to t \to s$ transitions, they are suppressed by the CKM matrix element ratio $(|V_{td}|/|V_{ts}|)^2 < 14\%$. Thus, they are not expected to dominate the $B_d^0 \to K^{*0}\gamma$ decays.

5.4 Photon criteria

Out of all the energy clusters in the central calorimeter we select the ones that are consistent with being electromagnetic showers. Since electrons and neutral pions produce electromagnetic showers as well, we require that the candidate clusters are inconsistent with being electrons and we apply cuts which are as efficient as possible and also enhance the fraction of single photons in the sample of selected photon

candidates[2]. The requirements to select single-photon candidates follow the standard CDF photon selection criteria [57] and are listed in detail below for completeness:

1. We first reinforce the penguin trigger requirements on the candidate photon clusters: e.g., requirements on minimum cluster energy, XCES information, lack of energetic tracks pointing to the same 15° ϕ slice as the calorimeter wedge of the photon candidate etc. (refer to Section 4.2.2). We then discard electron candidates by demanding that there is no three-dimensional track associated with the electromagnetic cluster. Tracks found in the CTC are extrapolated to the face of the CES; if they extrapolate to a cluster of energy in the CEM, this cluster is classified as an electron candidate, otherwise it is called a photon candidate.

2. We correct the energy of the cluster for detector effects according to the response maps of the calorimeter towers [58, 59]. Correction are also applied to compensate for gain variations which could result from changes in the photomultiplier gain or from a decrease in the transparency of the scintillator plates, and thus a deterioration of the light collection efficiency. The transverse energy of the cluster was then required to be $E_T > 10$ GeV in Run 1B data and $E_T > 8$ GeV in Run 1C data. Recall that due to limitations at the trigger bandwidth, we have required the decay products of the B meson to be quite energetic. This means that we collect a reduced number of signal events but this is not necessarily a disadvantage; the charged particles originating from penguin decays are more energetic than the random tracks collected by the trigger (see Fig. 5.1). Thus cutting high on the p_T of the candidate tracks enhances the fraction of signal events among the surviving ones. Nevertheless, even though higher energy requirements on them could get rid of more background events and would probably enhance the signal-to-background ratio on the events that

[2]Electromagnetic showers can also originate from $\pi^0 \to \gamma\gamma$, $\eta \to \gamma\gamma$ or $3\pi^0$, and $K_s^0 \to 2\pi^0$, followed by $\pi^0 \to \gamma\gamma$ decays.

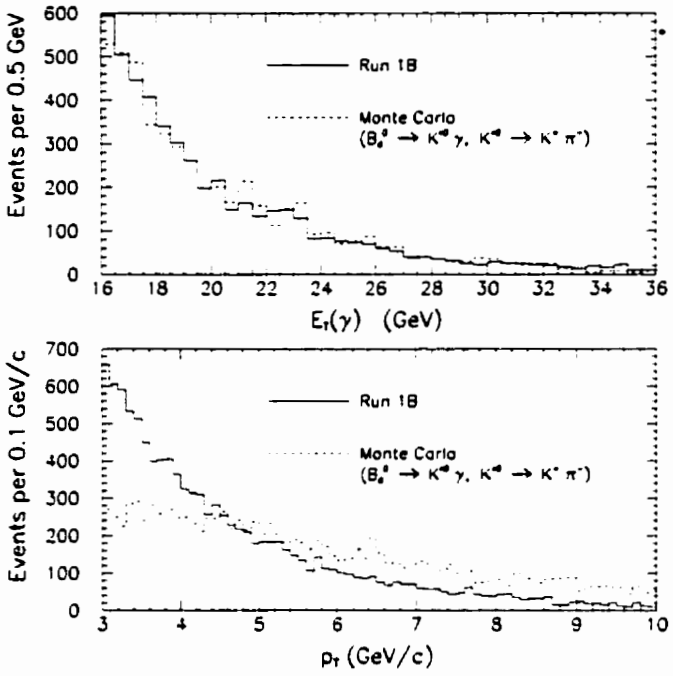

Figure 5.1: *Comparison of p_T and E_T spectra for tracks and photons collected by the penguin trigger in Run 1B (solid histograms) and from simulated penguin decays (dashed histograms). Penguin decays result in photons that are as energetic as the photons collected by the trigger. Charged particles from penguin decays have on average 1 GeV/c higher p_T values than the tracks in data. Over the E_T and p_T values shown, the trigger efficiencies vary only slowly.*

survive, the number of expected signal events would be very small to claim any reliable observation of the penguin decay channel. Therefore we are not keen to raise the energy requirements on the decay products higher than the trigger requirements.

For Run 1C though, we raise the E_T threshold from 6 GeV to 8 GeV. The reason is that in order to reduce the systematic uncertainties in the penguin branching fraction, we will eventually form a ratio of branching fractions between the penguin channel and the $\bar{B} \to e^- D^0 X$, $D^0 \to K^- \pi^+$ channel, which has a similar decay topology. Given the topological similarities between the

penguin and the $\bar{B} \rightarrow e^- D^0 X$ channels, an appropriate choice of the various reconstruction requirements will result in systematic effects affecting the ratio of branching fractions much less than the individual branching fractions. Therefore we require the photon candidate in the penguin decay to have $E_T > 8$ GeV because this is the lowest E_T requirement that can be imposed on the electrons of the $\bar{B} \rightarrow e^- D^0 X$ decays; the energy requirement for electrons at the trigger level was $E_T > 8$ GeV, during both Run 1B and Run 1C.

3. As at Level 3, we place an E_{HAD}/E_{EM} cut (see Section 4.2.2 and Fig. 5.2) by requiring the cluster energy deposited in the CHA (E_{HAD}) to be less than 10% of the energy deposited in the CEM (E_{EM}). This requirement is geared towards rejecting energetic hadrons which usually have a substantial fraction of their energy deposited in the CHA, since hadronic showers develop with a much longer longitudinal scale than electromagnetic showers.

4. The photon candidates face more requirements that select "electromagnetic-like" showers. First we ask that the energy sharing between the towers that contain the cluster be consistent with the expectations for an electromagnetic cluster. We require $L_{SHR} < 0.2$ (see Section 4.2.2 and Fig. 5.2).

5. We also ask that the energy sharing between the wires and strips of the CES be consistent with the expectations for a single-photon shower. The comparison is expressed in terms of two χ^2's; each one corresponding to the measurements performed by the strips (χ^2_{strips}) and the wires (χ^2_{wires}) of the CES (see also Section 4.2.2). Naturally then, single photons yield low χ^2 values (see Fig. 5.2), while hadronic or multi-photon showers yield higher values. We require $\chi^2_{strips} < 10$ and $\chi^2_{wires} < 10$ (see Fig. 5.2).

These requirements have high efficiency in retaining single photons ($\sim 89\%$) and rejecting hadronic showers (e.g., due to charged pions). They also retain a fraction of

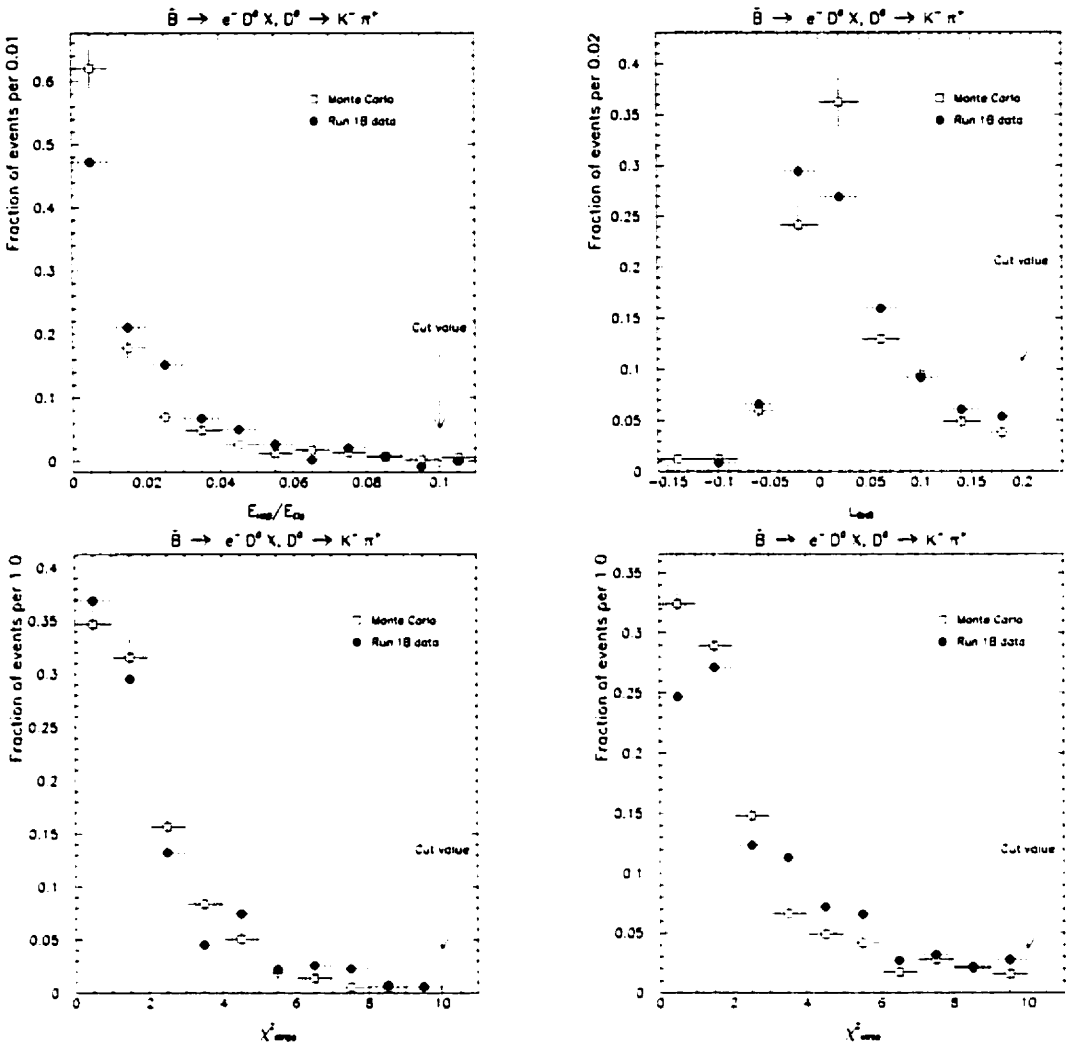

Figure 5.2: *Comparison of calorimeter based (E_{HAD}/E_{EM} and L_{SHR}) and strip chamber based (χ^2_{strips} and χ^2_{wires}) shower shape variables for electrons from $\bar{B} \to e^- D^0 X$, $D^0 \to K^- \pi^+$ decays in Run 1B (open squares) with Monte Carlo (solid circles). The Monte Carlo events ($p\bar{p} \to b\bar{b}$) were generated with the PYTHIA event generator and were subsequently fed through the detector and trigger simulation. Since the electromagnetic showers developed by electrons are very similar to the ones developed by photons, the distributions shown serve as a justification for the cuts chosen for the photons and electrons from the penguin and $\bar{B} \to e^- D^0 X$, $D^0 \to K^- \pi^+$ channels. The arrows indicate the values below which candidate photons and electrons are accepted.*

electromagnetic showers induced by neutral pions from $\pi^0 \to \gamma\gamma$ decays. Such multi-photon showers are the dominant background to single-photon showers, and they have, on average, higher values for the shower-shape variables (χ^2_{strips} and χ^2_{wires}) than showers induced by single photons [57]. However, the fraction of accepted multiple-photon showers from neutral pions increases with the momentum of the pion because the separation of the resulting photons decreases. For example, the efficiency of the $\chi^2_{strips} < 10$ and $\chi^2_{wires} < 10$ requirements for pions relative to that of single photons is $\sim$ 65% for $E_T = 15$ GeV [3] whereas for $E_T > 40$ GeV it is almost 100% [57]. Requiring lower χ^2_{strips} and χ^2_{wires} values provides better discrimination between single- and multi-photon showers; for example, requiring $\chi^2_{strips} < 5$ and $\chi^2_{wires} < 5$ results in the efficiency for pions relative to that of single photons be $\sim$ 35% for $E_T = 15$ GeV [57]. However, the level of background in the present analysis did not require such action to be taken. In Fig. 5.2 we show the comparison between simulated single-electron showers and data from $\bar{B} \to e^- D^0 X$ decays. The plots serve as a justification for the requirements on single photons, because single electron showers resemble those of single photons. In Ref. [57] one can find a comparison of the values of the shower shape variables for single- and multi-photon showers.

6. In order to have a reliable measurement of the photon cluster properties we require it to be located in the "good" fiducial volume of the central calorimeter The seed tower of the cluster should not be the highest $|\eta|$ tower (#9) which has a smaller depth (in radiation lengths) than the rest of the CEM towers and thus contains a smaller fraction of the cluster energy in the CEM. Therefore we only consider towers 0 – 8. We also neglect the cluster if the seed tower is the "chimney" tower which is not fully instrumented, since the cooling system of the solenoid uses part of its volume.

[3] Penguin photons in Run 1B (Run 1C) have an average E_T of $\sim$ 14 (12.5) GeV.

7. We also require the cluster to be away from the edges of the CES fiducial region by requiring 9 cm $< |Z_{CES}| <$ 230 cm and $|X_{CES}| <$ 21 cm (refer to Section 2.2.4 for the CES coordinate system) as the minimal fiducial cuts necessary to get at least half of the photon shower profile measured by the CES and therefore have some confidence in the resulting χ^2's calculated.

These fiducial requirements reject $\sim$ 3% of the photons, and thus the overall efficiency of the photon quality criteria (cuts # 3 to 7) is $\sim$ 86%.

5.5 Track Criteria

The reconstruction of the trajectories of charged particles and a reliable measurement of their momenta, requires a knowledge of the magnetic field inside the tracking volume of the CDF detector. The nominal value of the magnetic field used for Run 1B and Run 1C is 1.4116 T. This value was corrected with more than a thousand measurements of the magnetic field in the central detector during the course of data taking. The corrections were typically less than 0.17% [60] and each measurement had an uncertainty of 2×10^{-4} T [61].

We ask for two tracks which meet the standard CDF charged-particle reconstruction criteria [53] and also satisfy the topology imposed at the trigger level. The quality criteria on the tracks reduce the cases where a poor track measurement misleads us to consider an irrelevant track as a candidate penguin decay product. The criteria imposed on the tracks are listed below in detail for completeness:

8. Each candidate track should be measured by at least two of the five axial CTC superlayers with at least four hits each. It should also be measured by at least two of the four stereo CTC superlayers with at least two hits each.

9. In order to have all candidate tracks going through all of the CTC layers and thus being considered on equal footing, as far as the previous requirement is

concerned, we require that the radius at which each track crosses the end-plate planes of the CTC be more than 130.0 cm. Recall that the outermost sense wire is at a radius of 132.0 cm and the mean radius of the last CTC superlayer layer is 128.1 cm.

10. We then make sure that the candidate tracks have the characteristics required by the penguin trigger. Each track reconstructed so far (found "off-line" in the penguin data set) should have a matching track found on-line by the CFT; extrapolating the off-line track to superlayer 8 there should be a matching CFT track within $\Delta\phi < 0.008$ rad ($\sim 0.45^o$), i.e. the track should extrapolate no further than the immediate neighbors of the CFT seed wire.

11. We require the matching CFT tracks to point towards the immediate or the next to the immediate neighbor of the seed wedge of the photon cluster. The ϕ distance is calculated in 15^o bins and the ϕ of the CFT track (at superlayer 8) is required to be one or two bins away from the ϕ of the seed wedge of the photon cluster.

12. We then check the tracks selected so far in pairs and we require the matching CFT tracks to have $\Delta\phi(track1, track2) < 0.31$ rad at superlayer 8.

13. Each pair of tracks considered should consist of oppositely charged tracks. The charge of a track is assumed to be either $+1$ or -1 depending on the direction the track bends in the magnetic field of the solenoid.

14. Knowing the magnetic field in the tracking volume, we deduce the thee-momenta of the tracks from the parameters of their helical trajectories. The transverse momentum of each track is required to be above 2.0 GeV/c. This is around the 50% efficiency point for a track to be reconstructed at Level 2 by the CFT (see Fig. 3.6).

15. By default all the tracks are reconstructed using information in the CTC and the VTX. Their helical trajectories are then extrapolated back into the SVX and a road algorithm identifies hits in the SVX that are associated with the track. If more than two associated hits are found in the SVX, the track path is re-fit using the information available from all tracking detectors (SVX, VTX and CTC). The increase in the χ^2 of the track fit due to the inclusion of the SVX information is then calculated, and we call it the SVX χ^2. Each track used in this analysis is required to have at least two SVX hits and SVX χ^2/hit < 6.0. The SVX facilitates the reconstruction of tracks close to the beam line and we can thus tell if a track came from the beam line or not with an uncertainty of a few tens of micrometers (refer to Section 2.2.2). Due to the long lifetime of B mesons, the decay products of energetic B mesons have a high probability to not originate from the beam line. Later on we will use this fact to significantly reduce the background and the precision of the SVX information is essential for that.

The efficiency to reconstruct a track in the SVX, meeting the quality criteria described above, is $\sim$ 62%, mainly due to the incomplete coverge of the luminous proton-antiproton collision region ($\sigma \simeq 30$ cm) by the sillicon vertex detector. Once one of the two penguin tracks is reconstructed, the second one meets the same quality criteria with 90% efficiency. The combined efficiency for both tracks is thus $\sim$ 56%, and on top of this we have to consider the $\sim$ 88% CTC pattern recognition efficiency [53], which is included in the efficiencies quoted above.

Apart from the quality criteria imposed on the photon and the tracks, the off-line kinematic requirements[4] are not satisfied by all photons and tracks surviving the trigger selection, because of the non-zero trigger efficiency for objects below the off-line energy cuts. For example, $B_d^0 \to K^{*0}\gamma$ events survivng the off-line kinematic requirements with a $\sim$ 92% efficiency in Run 1B.

[4] $p_T > 2$ GeV/c for the kaon and pion and $E_T(\gamma) > 10$ (> 8) GeV in Run 1B (Run 1C).

5.6 $K^{*0} \to K^+\pi^-$ and $\phi \to K^+K^-$ reconstruction

The CDF detector does not provide sufficient information to identify a track as a pion or a kaon. Therefore we consider all candidate tracks and we assign the mass of a charged kaon (493.65 MeV/c^2) or a charged pion (139.57 MeV/c^2) [4] to them.

We then combine the four-momenta corresponding to each pair of tracks. In cases where the two charged particles are the only daughters of a common parent and the mass assignments are correct, the mass of the combination should be near the mass of the parent particle. If the two tracks were unrelated, the mass of the combination is a random number within the constraints of the kinematics of the combined tracks. Since we do not consider all tracks as possible candidates, but only the ones with $p_T > 2$ GeV/c, the fraction of signal to random combinatorial background is enhanced (refer to Section 5.4 and Fig. 5.1).

In addition to this combinatorial background, the random mass assignment to each track, can result in significant increase of the combinatorial background. In our case, the $\phi \to K^+K^-$ decay is reconstructed using all track pairs of opposite charge using only the K^+K^- mass assignment. We thus have one possible assumption per track pair and just the random combinatorial background. On the other hand, we reconstruct the $K^{*0} \to K^+\pi^-$ decay using all track pairs of opposite charge with both the $K^+\pi^-$ and the π^+K^- assumptions, resulting in two possible combinations per track pair. In order to reduce the combinatorial background due to this K/π mass assignment ambiguity, we select the hypothesis that results in a combination mass $M(K^+\pi^-)$ nearest the $K^*(892)^0$ world average mass [4]. We thus avoid increasing the combinatorial background by a factor of two, while we guess right for 83% of $K^{*0} \to K^+\pi^-$ decays. The success rate increases to 88% once we consider the track pairs with a combined $K^+\pi^-$ or π^+K^- mass within 75 MeV/c^2 of the world average $K^*(892)^0$ mass.

In Fig. 5.3 we see the mass of the $K^+\pi^-$ and K^+K^- combinations after the track quality criteria were imposed on the penguin trigger data (KSGB data set). We

display both the $K^+\pi^-$ and π^+K^- assignments per two-track combination, since a selection such as the one described above would create an enhancement around the $K^*(892)^0$ world average mass even if there was no $K^*(892)^0 \rightarrow K^+\pi^-$ decays in the data. The $K^*(892)^0$ resonance is quite visible in these plots, exactly where it is expected (see Fig. 5.4).

In order to further reduce the combinatorial background, we constrain the two tracks to meet at a common point at which a possible parent particle decayed into the two charged particles under consideration. We call this point the "secondary vertex", in contrast to the "primary vertex" which is the point where the parent $p\bar{p}$ interaction occurred. The track parameters are varied around their central values, within their uncertainties, in order to fit the common vertex hypothesis; the vertex with the lowest χ^2 is considered to be the secondary vertex of the two tracks. Combinations of tracks that are far away from each other are thus discarded and only combinations of two tracks that satisfy the secondary vertex hypothesis are retained. Furthermore we calculate the confidence level of the vertex constraint, $C.L.(\chi^2)$. Combinations of tracks that originate from a common parent should have the confidence levels of the fit distributed evenly between zero and one, if their χ^2 are distributed according to a true χ^2 distribution. On the other hand, combinations of tracks that have bad χ^2's for the common vertex hypothesis, have low confidence levels for the fit. We therefore require $C.L.(\chi^2) > 0.01$ as a mean to get rid of most of the combinations of random tracks.

In Fig. 5.3 we see that the vertex constraint and the $C.L.(\chi^2) > 0.01$ requirement improve the signal-to-background ratio for $K^{*0} \rightarrow K^+\pi^-$ and $\phi \rightarrow K^+K^-$ decays. In Fig. 5.5 we see the distribution of masses for $\pi^+\pi^-$ combinations and the $C.L.(\chi^2)$ distributions for background, signal-plus-background, and signal-only $\pi^+\pi^-$ vertex constraint fit.

Since we look for the decays $K^{*0} \rightarrow K^+\pi^-$ and $\phi \rightarrow K^+K^-$, we retain two-track combinations with masses in the vicinity of the hypothesized parent meson mass.

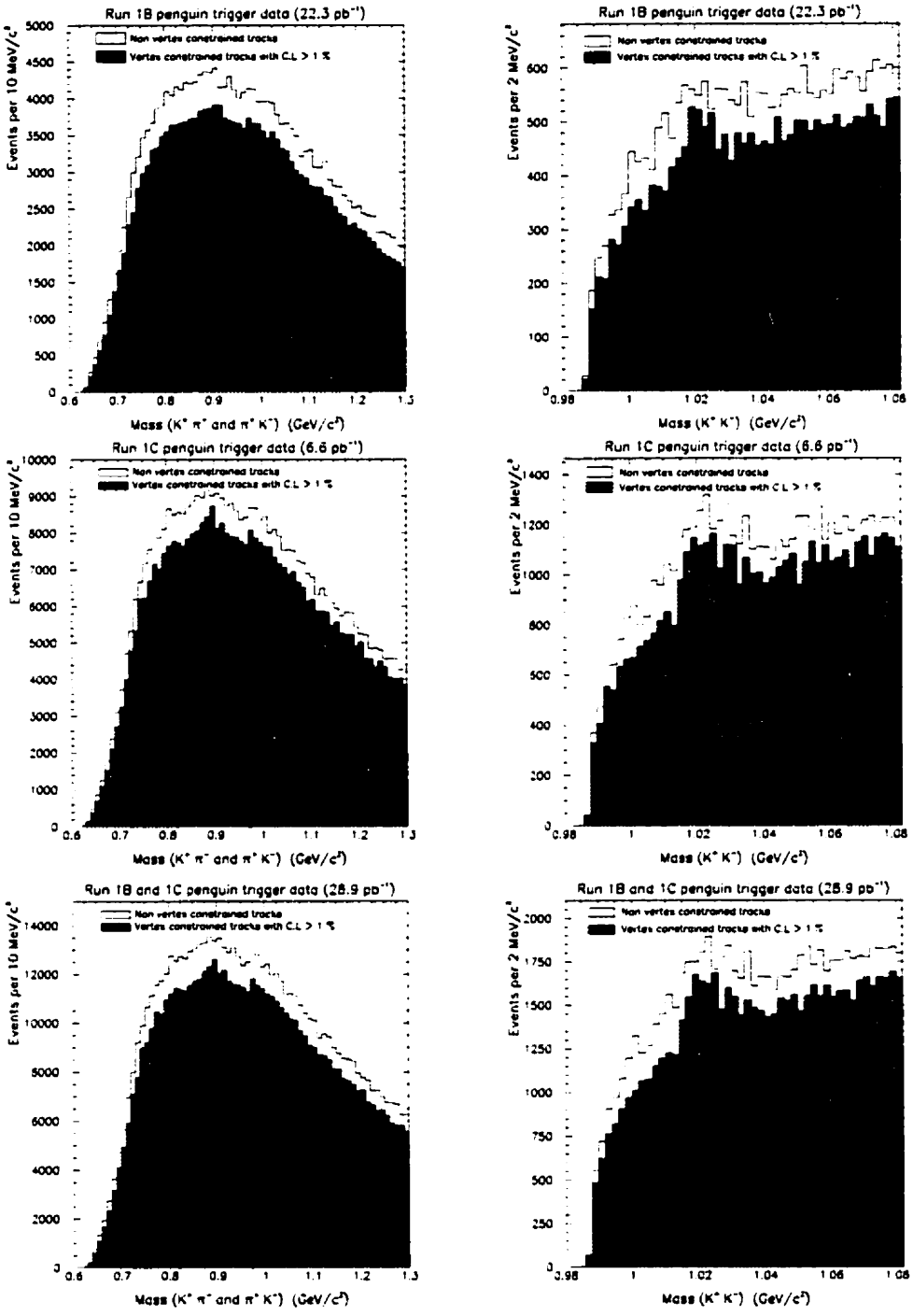

Figure 5.3: *Mass of $K^+\pi^-$ (left) and K^+K^- (right) combinations for tracks meeting the track quality criteria in the KSGB data set. The enhancements around 1 GeV/c^2 in the Mass($K^+\pi^-$) distributions are due to $\pi^+\pi^-$ pairs from $\rho(770) \to \pi^+\pi^-$ decays, where one of the pions was assigned the kaon mass. The arrows indicate the mass windows used for the identification of $\phi(1020)$ or $K^*(892)^0$ decays.*

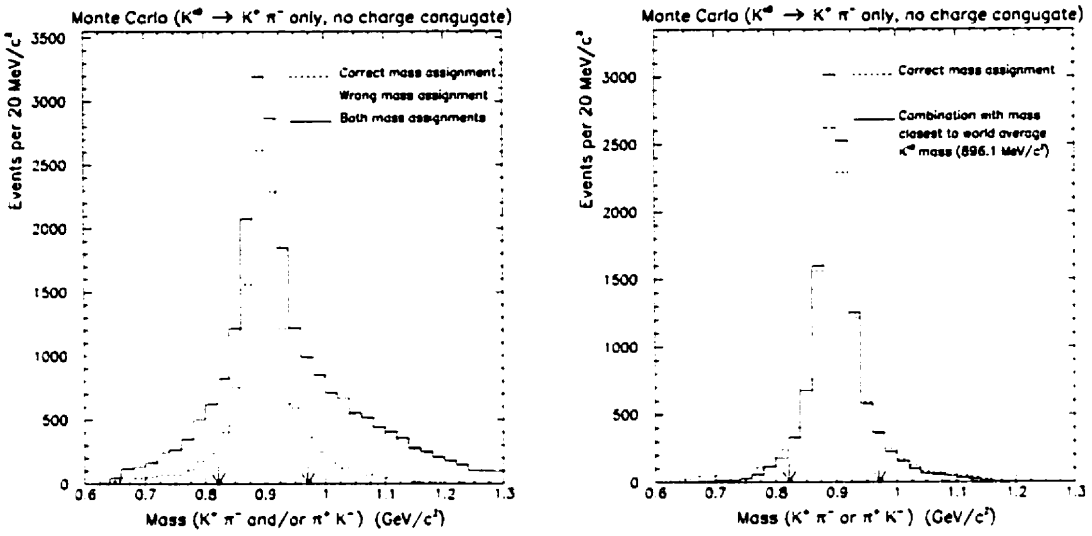

Figure 5.4: *Mass of $K^+\pi^-$ and/or π^+K^- combinations combinations for tracks meeting the track quality criteria in Monte Carlo events. The arrows indicate the mass window used to identify $K^*(892)^0 \rightarrow K^+\pi^-$ decays.*

Specifically, we require $M(K^+K^-)$ to be within a 20 MeV/c^2 window centered at the world average $\phi(1020)$ mass of 1019.4 MeV/c^2 and $M(K^+\pi^-)$ to fall within an 150 MeV/c^2 window centered at the world average $K^*(892)^0$ mass of 896.1 MeV/c^2 [4]. These mass windows were found to be 86.5% efficient for $\phi \rightarrow K^+K^-$ decays and 84.3% efficient for $K^{*0} \rightarrow K^+\pi^-$ decays. Given the inefficiency of assigning the kaon and pion masses correctly to the $K^*(892)^0$ decay products, 74.2% of the $K^{*0} \rightarrow K^+\pi^-$ decays are reconstructed with masses within ± 75 MeV/c^2 from the world average $K^*(892)^0$ mass. The intrinsic width, $\Gamma = 50.5$ MeV [4], dominates the line shape of the $K^*(892)^0$ resonance, giving it a characteristic Breit-Wigner shape, with the experimental resolution being significantly less. The $\phi(1020)$ resonance has also a Breit-Wigner shape, since the experimental resolution is comparable with its intrinsic width of $\Gamma = 4.4$ MeV [4].

Apart from retaining only combinations that are consistent with the $K^*(892)^0$ and $\phi(1020)$ parent hypothesis, we reject combinations which are consistent with the more populous $K^0 \rightarrow \pi^+\pi^-$ decay and contribute some of the background in the $K^*(892)^0$

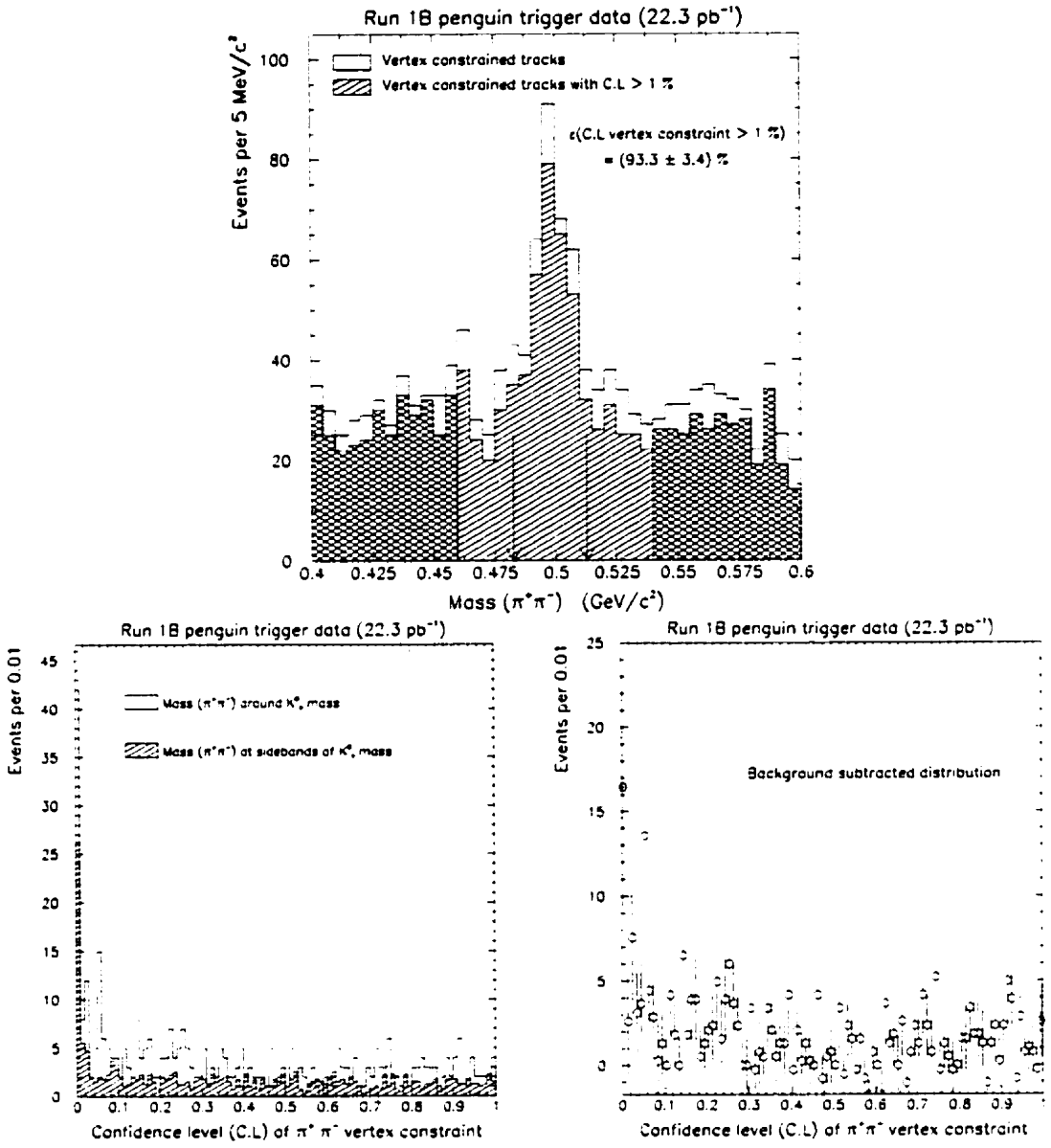

Figure 5.5: *Top: Distribution of $\pi^+\pi^-$ masses for vertex constrained tracks not originating from the primary $p\bar{p}$ vertex, before (clear histogram) and after (shaded histogram) the confidence level requirement for the common vertex hypothesis. The arrows indicate a ± 15 MeV/c^2 window around the world average K^0 mass. The checkered regions are the sidebands used to get background $\pi^+\pi^-$ combinations that do not originate from a K^0_s parent. Bottom: Confidence level of the vertex constrained fit for $\pi^+\pi^-$ combinations. The background subtracted distribution takes care of the different widths between the signal and sideband mass windows.*

case. The reason is that a $K^0 \to \pi^+\pi^-$ decay can have the two track combination resulting in $K^+\pi^-$ or π^+K^- masses inside the window used to select $K^{*0} \to K^+\pi^-$ decays, whereas all K^+K^- combinations result in masses outside the $\phi(1020)$ mass search window. We therefore retain only combinations with $M(\pi^+\pi^-)$ outside an approximately four sigma window (± 15 MeV/c^2) centered at the world average K^0 mass of 497.67 MeV/c^2 [4]. This requirement rejects 4.6% of the $K^{*0} \to K^+\pi^-$ decays and none of the $\phi \to K^+K^-$ decays.

In summary then, we reconstruct $K^{*0} \to K^+\pi^-$ and $\phi \to K^+K^-$ decays using tracks that meet the track quality criteria described in the previous section and we enhance the signal-to-background ratio by the following means:

16. We constrain each pair of candidate tracks to intersect at a common vertex and require the confidence level of the constrained fit to be $C.L.(\chi^2) > 1\%$.

17. We retain only two-track combinations that are consistent with $K^{*0} \to K^+\pi^-$ and $\phi \to K^+K^-$ decays by requiring $|M(K^+\pi^-) - M_{PDG}(K^*(892)^0)| < 75$ MeV/c^2 or $|M(K^+K^-) - M_{PDG}(\phi(1020))| < 10$ MeV/c^2, with M_{PDG} indicating the world average masses according to Ref. [4]. Given two oppositely charged tracks, we consider as correct the mass assignment ($K^+\pi^-$ or π^+K^-) which results in a two-track mass closer to the world average $K^*(892)^0$ mass.

18. $K^*(892)^0$ candidates are considered the two-track combinations that are inconsistent with the $K^0 \to \pi^+\pi^-$ decay, because such decays "reflect" in the $K^*(892)^0$ mass window specified above, when one of the tracks is assigned the kaon mass. We require $|M(\pi^+\pi^-) - M_{PDG}(K^0)| > 15$ MeV/c^2. When both tracks of the $K^0 \to \pi^+\pi^-$ decays are assigned kaon masses, the $K^0 \to \pi^+\pi^-$ decays "reflect" at masses above 1.06 GeV/c^2, well outside the aforementioned $\phi(1020)$ mass window; in this case we do not reject two-track combinations with $|M(\pi^+\pi^-) - M_{PDG}(K^0)| < 15$ MeV/c^2.

5.7 B meson reconstruction

We reconstruct B meson candidates by forming combinations of the photon candidates with either $K^*(892)^0$ or $\phi(1020)$ candidates.

In Fig. 5.6 we show the mass distributions for the three body combinations $\gamma K^+\pi^-$ and γK^+K^- after the selection of photon, $K^*(892)^0$ and $\phi(1020)$ candidates in the KSGB data set, according to the criteria described in the previous Sections (5.4, 5.5, and 5.6). It is clear that there is no apparent clustering of events around the B_d^0 or B_s^0 meson masses of 5.2792 GeV/c^2 and 5.3693 GeV/c^2 respectively [4]. We therefore have to use some characteristic features of the B mesons in order to reduce the background and enhance the signal-to-background ratio.

As outlined in Section 5.2, we make use of the long lifetime of B mesons, $\tau(B_d^0) = 1.56$ ps and $\tau(B_s^0) = 1.54$ [4]. In Fig. 5.7 we see the expected distributions of the "flight distances" of simulated B_d^0 mesons, i.e. the distances traveled by B_d^0 mesons before they decay[5].

Because the lifetimes of the ϕ and K^{*0} mesons are almost a factor of 10^{10} smaller than the lifetime of the B mesons [4], their flight distances are negligible compared to the flight distances of B mesons. Thus we claim that the secondary vertex found by vertexing the two tracks, indicates the point where the parent B meson decayed as well. The secondary vertex resolution is around 100 μm in the x and y directions and about 5 mm in the z direction.

For the determination of the primary vertex, which will indicate the generation point of candidate B mesons, we use two different sources of information. The z position of the primary vertices in a given event were reconstructed using information from the VTX detector. The quality of the vertex was determined based on the number of hits in the VTX that were used to identify the vertex. The (x, y) position of the primary vertices were calculated using the average beam-line measured on

[5]The distributions for B_s^0 mesons are very similar, due to the almost identical lifetimes of the two B meson species.

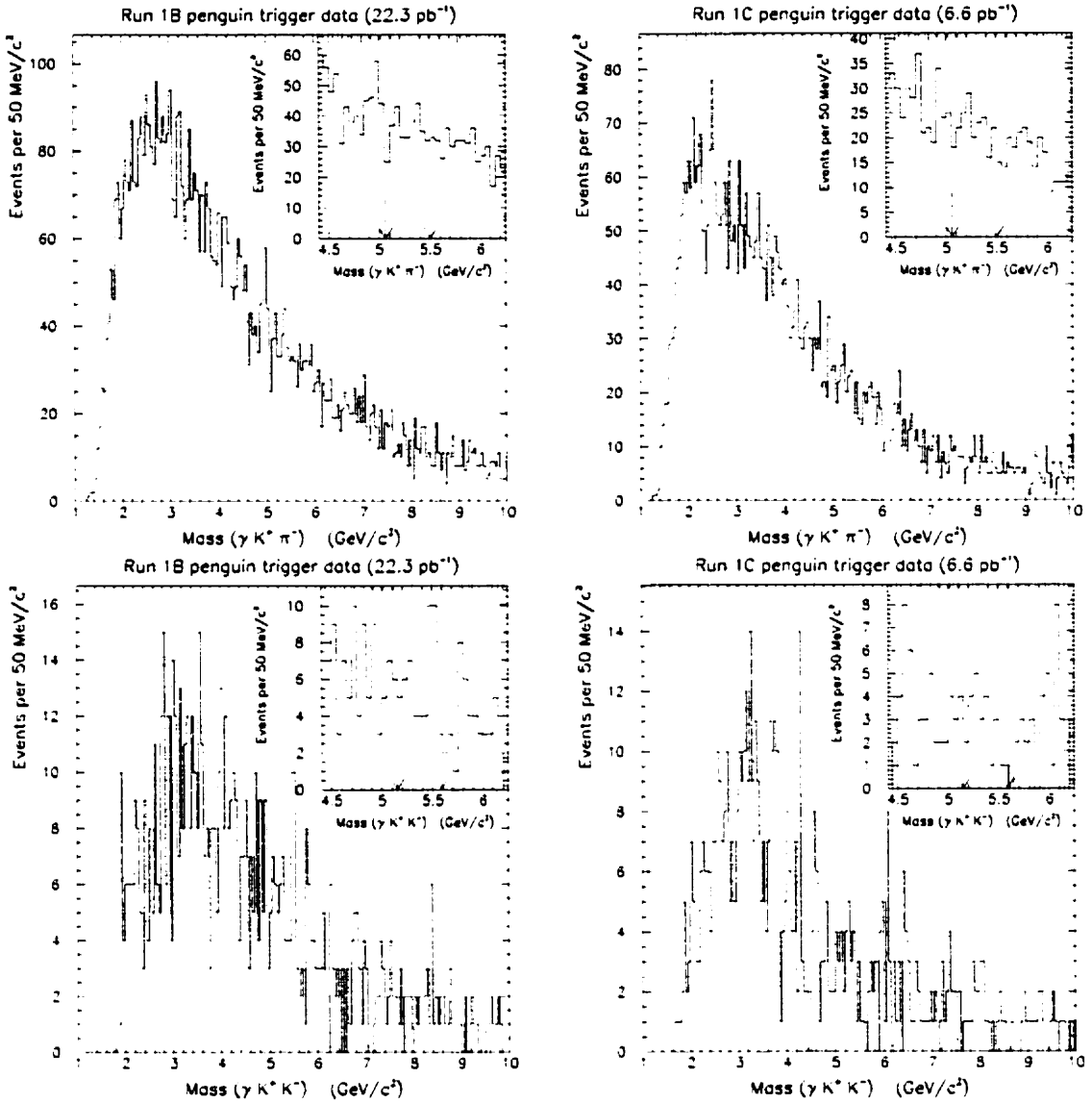

Figure 5.6: *Mass of the $\gamma K^+\pi^-$ (or $\gamma\pi^+K^-$) and γK^+K^- combinations, for photon, K^{*0} and ϕ candidates selected in the penguin trigger data set according to the criteria described in Sections 5.4 - 5.6. The arrows in the inset figures indicate the search windows for penguin events. They span ± 220 MeV/c^2 ($\sim \pm 2\sigma$) around the world average B_d^0 and B_s^0 masses of* 5.2792 GeV/c^2 *and* 5.3693 GeV/c^2 *respectively [4].*

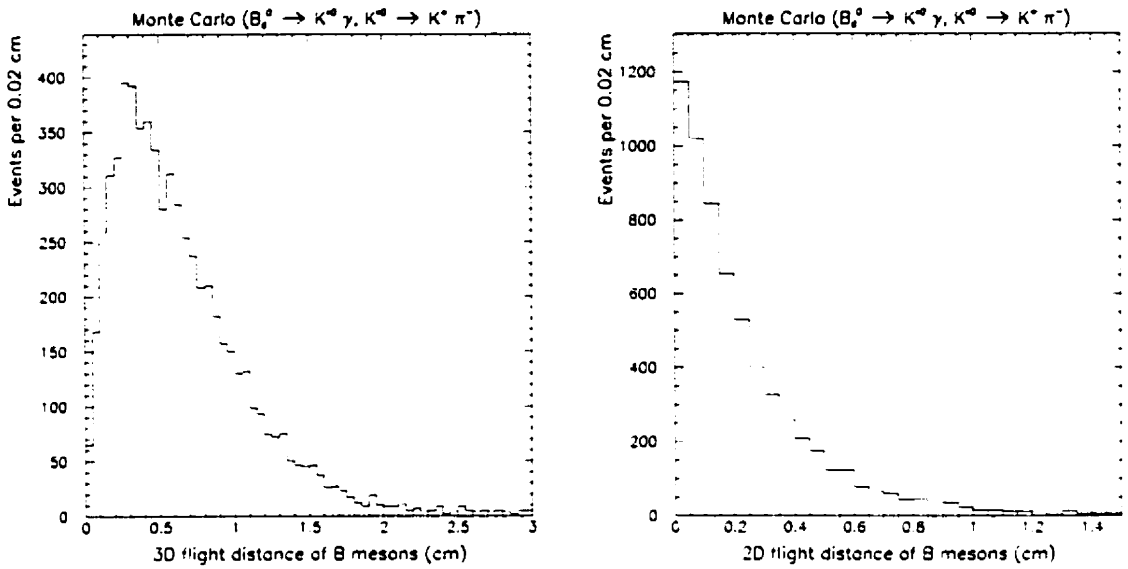

Figure 5.7: *Flight distance of simulated B mesons in the laboratory frame. The 2-dimensional distance refers to the transverse $(x-y)$ plane. The distributions are for events that satisfy the selection criteria described in Sections 5.4, 5.5 and 5.6.*

each uninterrupted data-taking period, typically several hours long. The beam-line was measured using information from the SVX detector and it did not vary more than 10 μm during the course of a single data-taking period (compare this with the flight distances of B mesons in Fig. 5.7). Using the slope and the (x, y) position at $z = 0$ from this average beam-line information, as well as the z locations of the primary vertices from the event-by-event VTX information, we calculated the x, y and z coordinates of the primary vertices in each event. The uncertainties on the x and y coordinates were fixed to $\sigma_x = \sigma_y = 25$ μm, in accordance with the observed circular beam spot size in the transverse $(x-y)$ plane. The uncertainty along the z direction was fixed to $\sigma_z = 2.5$ mm for all events, in accordance with the observed average resolution [12].

Due to the high probability for a $p\bar{p}$ interaction and the high instantaneous luminosities, the average number of $p\bar{p}$ interactions per beam crossing was expected to

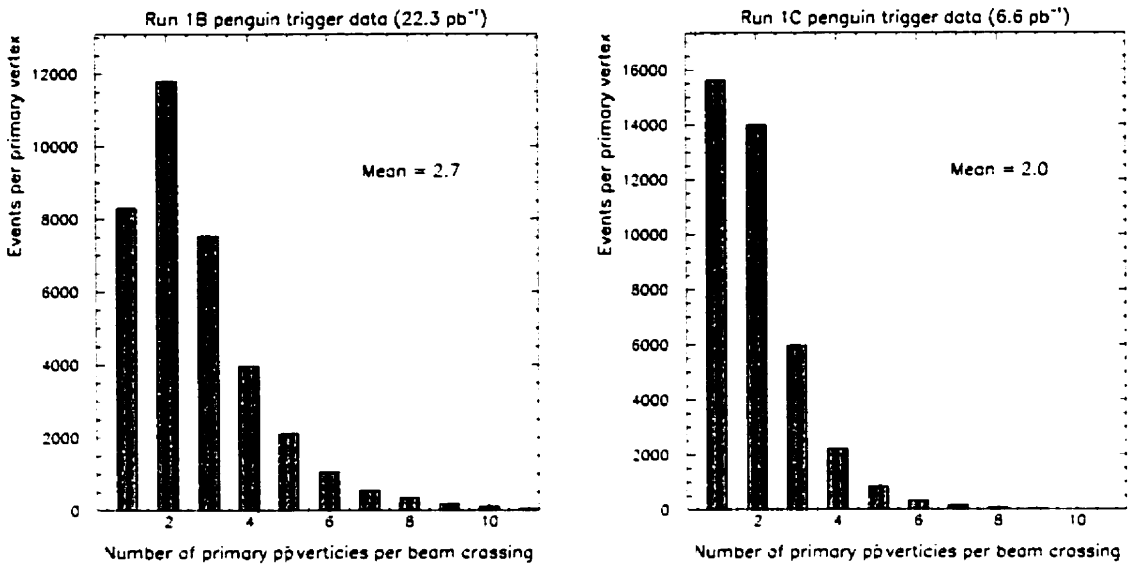

Figure 5.8: *Number of good-quality primary $p\bar{p}$ vertices per beam crossing for events in the penguin trigger data sample.*

be higher than two in Run 1B[6]. Indeed, the average number of good-quality primary vertices reconstructed in the penguin data set was 2.7 in Run 1B and 2.0 in Run 1C (see Fig. 5.8).

From all the good-quality primary vertices in an event, the one with the shortest longitudinal (z) displacement from the secondary vertex was chosen as the one that indicated the point of birth of the candidate B meson; from here on we refer to this vertex as "the primary vertex" of the event. This is a legitimate choice since the uncertainty on the flight distance of B mesons along the z direction is comparable to the primary vertex resolution along this direction and much smaller than the spacing between $p\bar{p}$ interaction points, which are distributed normally along the z axis with $\sigma \simeq 30$ cm.

Having identified the decay point of the candidate B meson with the secondary

[6]With proton and antiproton bunches crossing every 3.5 μs and the $\sim$ 800 kHz of $p\bar{p}$ inelastic collisions, due to the high instantaneous luminosities and $p\bar{p}$ interaction cross section, we expect more than 2.5 inelastic $p\bar{p}$ interactions per bunch crossing (refer to Section 2.1).

vertex, we recalculate the photon momentum vector assuming that it originated from the secondary vertex and pointed to the location of the CES cluster. We then combine the photon with the ϕ or K^{*0} candidate, this time with "correct" momenta for all the candidate daughters, and thus obtain the four-momentum of the candidate B meson.

With the four-momentum in the laboratory frame and the birth and decay points of the candidate B meson measured, we can calculate the time it took the candidate parent to decay, in its own (rest) frame. The distribution of the decay times for the candidate B mesons could reveal the presence of real B mesons among them. We call the decay times of B mesons in their rest frame "proper decay times".

Multiplying the "proper decay time" with the speed of light, we obtain the "proper decay length" of a candidate B meson, using the following recipe:

$$ct = \frac{\vec{p}_T \cdot \vec{x}_T}{p_T^2} M(B) \tag{5.1}$$

where $\vec{p}_T$ is the transverse momentum of the B meson candidate, $\vec{x}_T$ is the distance between the primary and the secondary vertices, projected on the transverse $(x-y)$ plane, and $M(B)$ is the mass of the B meson candidate, as it is calculated from its four-momentum.

In Fig. 5.9 we see the distribution of the proper decay lengths for simulated B mesons, reconstructed from their decay products using the same algorithm and the same requirements as for real data. We also see background and background-subtracted ct distributions of B meson candidates reconstructed as $B_d^0 \to J/\psi K^{*0}$ decays in Run 1B. Real B mesons manifest their presence in these semi-logarithmic plots with the appropriate linear dependence on the decay times (as expected from the exponential decay law).

The uncertainty on the reconstructed information, mainly on the secondary and primary vertices, results in B mesons which decay close to the primary vertex to have measured values of ct that are normally distributed around $ct = 0$ with a σ governed by the measurement uncertainties. In a $p\bar{p}$ event most of the particles traversing the

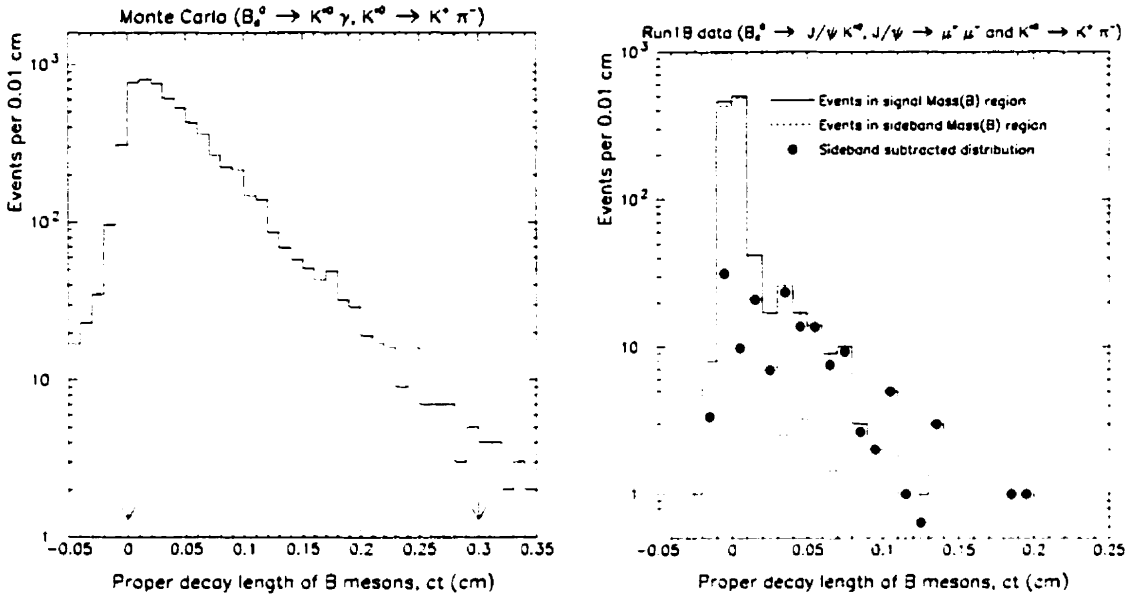

Figure 5.9: *The distribution of the proper decay length, ct, of B_d^0 mesons. Left: B_d^0 mesons in simulated $B_d^0 \to K^{*0}\gamma$, $K^{*0} \to K^+\pi^-$ decays. The arrows indicate the window within which we accept candidate B mesons. Right: Background (dashed histogram), signal plus background (solid histogram) and background subtracted (points) ct distributions for B_d^0 mesons reconstructed in the Run 1B data as $B_d^0 \to J/\psi K^{*0}$, $J/\psi \to \mu^+\mu^-$ and $K^{*0} \to K^+\pi^-$ decays. The background subtraction was performed using the events in the sidebands of the B mass region.*

detector volume are generated at the $p\bar{p}$ collision point. This means that combining two such charged particles should yield a secondary vertex which coincides with the primary $p\bar{p}$ vertex. Nevertheless, due to the uncertainties in determining the primary and secondary vertices, we usually measure a non-zero distance between the two vertices. Thus, the candidate B mesons derived from such particles will have ct values normally distributed around $ct = 0$. Requiring $ct > 0$ for the candidate B mesons, would therefore reject $\simeq 50\%$ of such background events. But since B mesons have a long lifetime ($c\tau = 468 \pm 12$ μm[4]), the $ct > 0$ requirement rejects only $\simeq 8.5\%$ of real B mesons. The $ct > 0$ requirement implies that $\vec{p}_T \cdot \vec{x}_T > 0$

(see Eq. 5.1), so it can be also thought as a request that the B momentum points less than 90^o away from the direction of the reconstructed B flight path. In order to avoid contributions from non B's we also require $ct < 0.3$ cm, since real B mesons are rarely expected to reach such high ct values (see Fig. 5.9). This requirement is satisfied by $\simeq 97.5\%$ of real B mesons.

Apart from the requirement on the decay time of the candidate B mesons, we use the fact that B mesons carry most of the energy of their parent b quarks [55]. This means that B mesons should be isolated from activity around them. We formulate the B meson isolation as the variable:

$$I_B \equiv \frac{p_T(B)}{p_T(B) + \sum_{i \notin B}^{R} p_T(i)} \tag{5.2}$$

where $p_T(B)$ is the transverse momentum of the B meson candidate and $p_T(i)$ is the transverse momentum of each charged particle i, other than those constituting the B candidate, contained within a cone of radius $R \equiv \sqrt{(\Delta\eta)^2 + (\Delta\phi)^2} = 1.0$ around the 3-momentum of the B meson candidate. In order to avoid considering irrelevant particles into the $\sum_{i \notin B}^{R} p_T(i)$, i.e. particles that were not fragmentation products of the parent b quark, we only consider charged particles that are consistent with the primary vertex: we required $|z_0^i - z_{primary}| < 5$ cm, where z_0^i is the z of the track trajectory at the point of the smallest $x - y$ distance to the (0,0) point, which is also the point of closest approach to the z axis.

In Fig. 5.10 we show the isolation variable, I_B, for candidate B mesons reconstructed as $\bar{B} \to e^- D^0 X$, $D^0 \to K^- \pi^+$ decays. Events in the sidebands of the D^0 mass peak are used as background. Their I_B distribution is used to statistically subtract the background from the signal region in the D^0 mass peak, and thus obtain a signal-only distribution. The momentum of the parent $\bar{B}$ meson is inferred from the measured $p_T(eK\pi)$ using the average correction factor of 85%, i.e., $p_T(B) = p_T(eK\pi)/0.85$ (see Fig. 5.11). Also shown are the distributions of signal events from the less populous $B_d^0 \to J/\psi K^{*0}$ and $B_u^+ \to J/\psi K^+$ decays. Statistical

subtraction of the combinatoric background is performed as before, but events in the sidebands of the B meson mass are used in this case. We impose an $I_B > 0.7$ requirement on the candidate B mesons (usually referred to as the "B isolation" requirement). This is shown in Fig. 5.10 to be $\sim$ 95% efficient in selecting real B mesons of $p_T > 15$ GeV/c, while rejecting half of the random particle combinations (background). The high energy requirements on the selected B daughter candidates, result in a small fraction of momentum carried by other particles in their vicinity. This is not the case for lower energy B mesons; e.g., for $p_T(B) > 6$ GeV/c the $I_B > 0.7$ requirement is $\sim$ 80% efficient in selecting B mesons, while rejecting $\sim$ 85% of the background [62]. Of course, requiring the "L2 isolation" on the photon at the trigger level, selects better isolated events. Consequently, the combinatoric background events have higher I_B values and the discrimination power of the $I_B > 0.7$ requirement worsens.

To summarize so far, we combine the photon, K^{*0} and ϕ candidates, selected as described in Sections 5.4 - 5.6, and form B meson candidates. We then make use of two characteristic features of B mesons that improve the signal-to-background ratio, their long lifetime and the fact that most of the energy in their vicinity is carried by them:

19. We require the proper decay length, ct, of the candidate B mesons to be positive and less than 0.3 cm (i.e. $0 < ct < 0.3$ cm).

20. We require the B candidate to carry more than 70% of the scalar p_T sum of all the tracks (including the photon) in a cone $R = \sqrt{(\Delta\eta)^2 + (\Delta\phi)^2} = 1.0$ around its 3-momentum direction:

$$I_B \equiv \frac{p_T(B)}{p_T(B) + \sum_{i \in R, i \notin B} p_T(i)} > 0.7$$

After selecting B meson candidates that meet all the requirements discussed so far, we plot their masses in Fig. 5.12. Comparing with the distributions shown

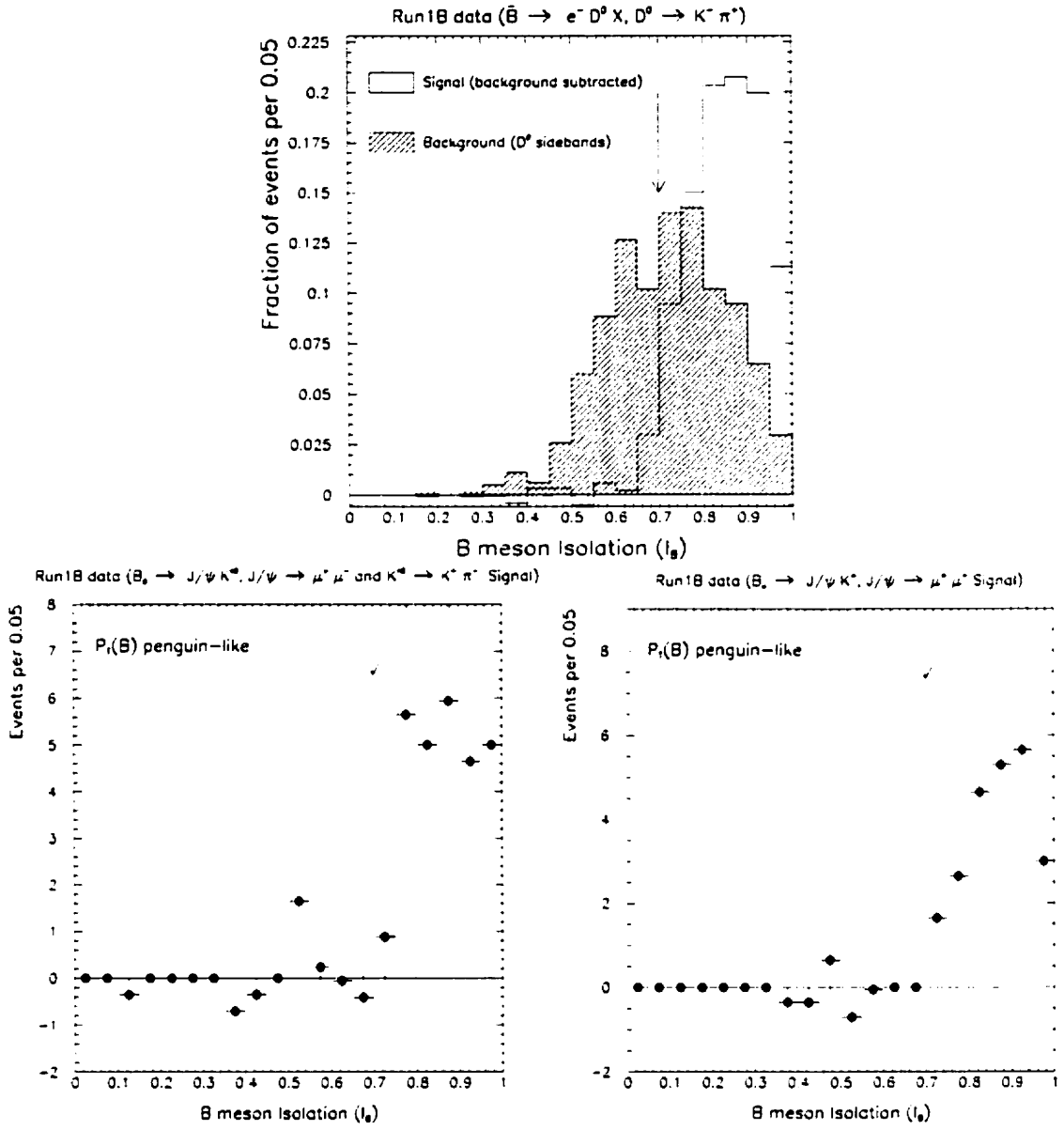

Figure 5.10: *Distribution of the isolation variable I_B for B mesons from $\bar{B} \rightarrow e^- D^0 X$, $D^0 \rightarrow K^- \pi^+$ (top), $B_d^0 \rightarrow J/\psi K^{*0}, J/\psi \rightarrow \mu^+\mu^-$ and $K^{*0} \rightarrow K^+\pi^-$ (bottom left), and $B_u^+ \rightarrow J/\psi K^+, J/\psi \rightarrow \mu^+\mu^-$ (bottom right) decays reconstructed in Run 1B data. A background subtraction was performed using events in the sidebands of the D^0 or B mass regions. The arrows indicate the point above which candidate B mesons were accepted. The momentum cuts of the daughter particles are adjusted so that the momenta of the parent B mesons have similar distributions to those anticipated for the B mesons of the penguin channels.*

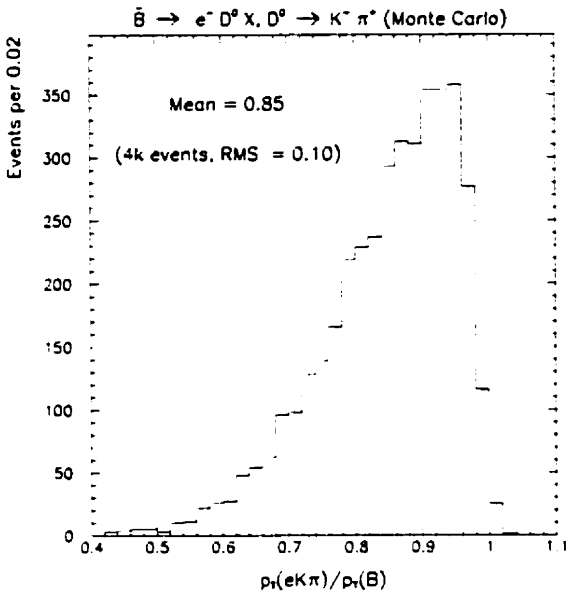

Figure 5.11: *Fraction of the parent B meson momentum carried by $eK\pi$ combinations from $\bar{B} \rightarrow e^- D^0 X$, $D^0 \rightarrow K^- \pi^+$ decays.*

in Fig. 5.6 we see that the lifetime and isolation requirements on the candidate B mesons rejected a substantial number of background events, but not enough to allow an observation of real B mesons.

The relevant $M(\gamma K\pi)$ and $M(\gamma KK)$ regions are ± 220 MeV/c^2 ($\simeq \pm 2\sigma$) windows around the B_d^0 or B_s^0 meson masses. Monte Carlo simulations of the signal processes indicate that in Run 1B we expect $\sigma(M(\gamma K\pi)) \simeq \sigma(M(\gamma KK)) \simeq 105$ MeV/c^2. As it was shown in Section 3.2, the simulation reproduces the measured resolutions of the photon energy and the track momenta. We therefore trust the mass resolutions predicted by the simulation. In Run 1C the lower average photon energy results in a slightly higher mass resolution of 110 MeV/c^2.

5.8 Additional cuts and the final data samples

As shown in Fig. 5.12, after applying the cuts listed in Sections 5.4 - 5.7, there is still no indication of the presence of B mesons among the surviving events.

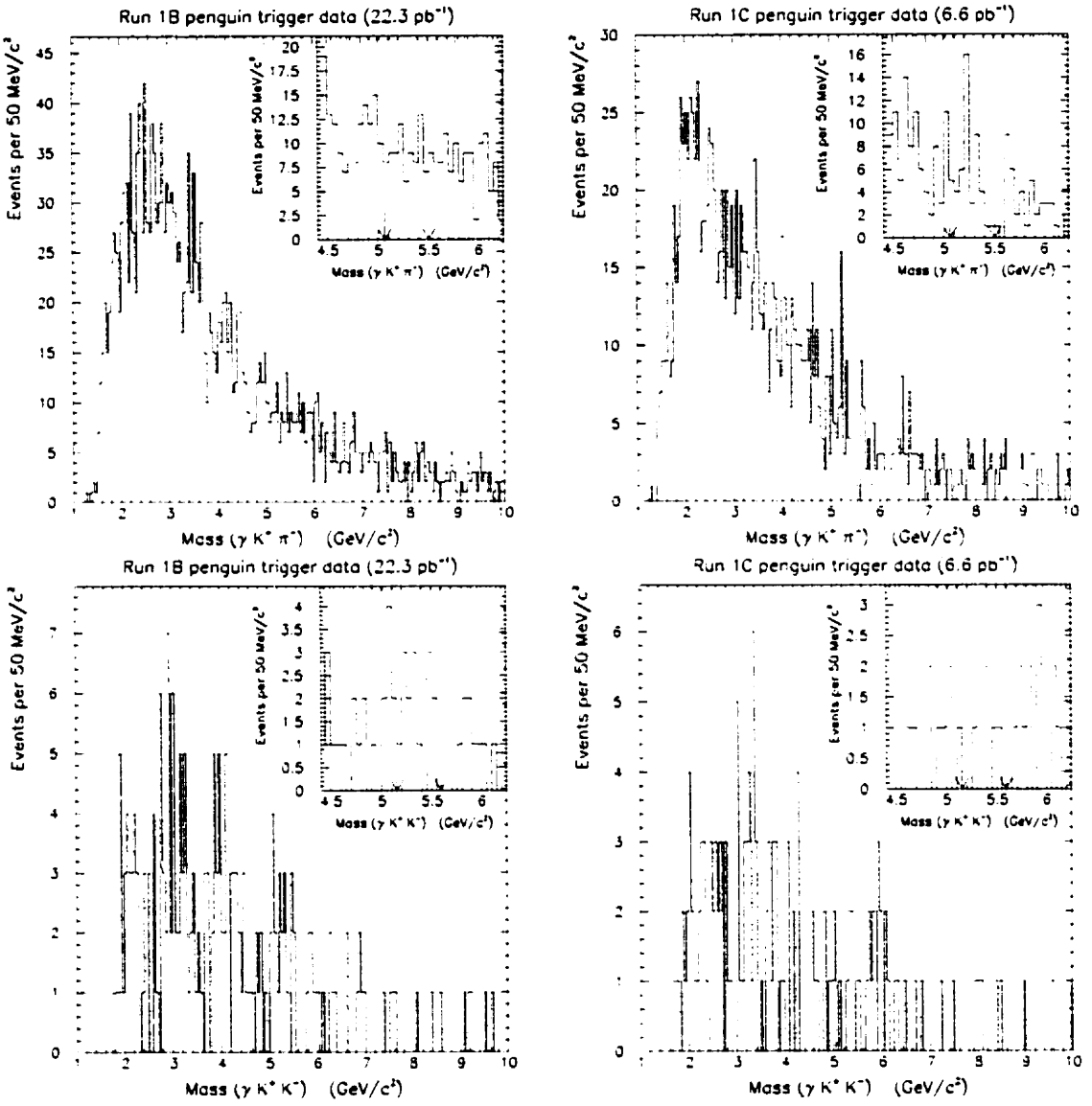

Figure 5.12: *Mass of the $\gamma K^+\pi^-$ (or $\gamma\pi^+K^-$) and γK^+K^- combinations, for photon, K^{*0} and ϕ candidates selected in the penguin trigger data set according to the criteria described in Sections 5.4 - 5.6 and with the B lifetime and isolation cuts described in the text (cuts # 19 and 20). The arrows in the inset figures indicate the search windows for penguin events. They span ± 220 MeV/c^2 ($\sim \pm 2\sigma$) around the world average B_d^0 and B_s^0 masses of* 5.2792 GeV/c^2 *and* 5.3693 GeV/c^2 *respectively [4].*

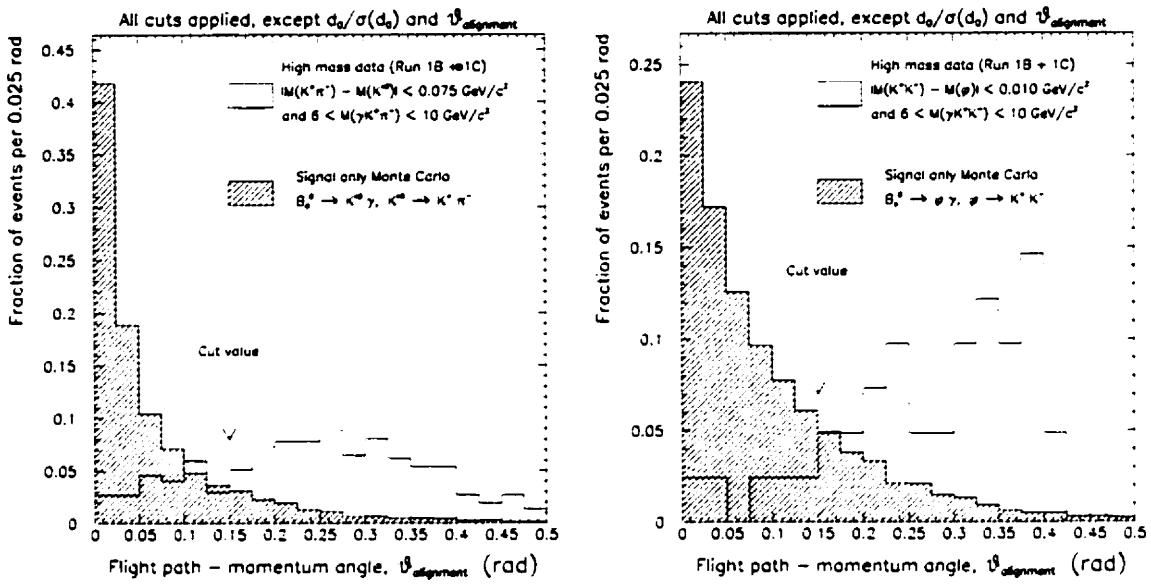

Figure 5.13: *Alignment angle, $\vartheta_{\rm alignment}$, between the momentum and the flight path of simulated B mesons (hashed histogram) and of combinatorial background combinations with $M(\gamma K^+\pi^-)$ and $M(\gamma K^+K^-)$ in the 6 to 10 GeV/c^2 region (clear histogram). The distributions shown correspond to combinations that satisfied the selection criteria described in Sections 5.4 - 5.7. The arrows indicate the points below which candidate B mesons were accepted.*

We use two more characteristic features of penguin B decays in order to improve the signal-to-background ratio. The first exploits the fact that we attempt to reconstruct B meson decays by measuring all the decay products. Once we fully reconstruct a real B meson, we should observe its momentum pointing from the primary to the secondary vertex, along the line that indicates its flight path from its creation to its decay point. We thus form an "alignment angle" between the transverse momentum, p_T, and the $x-y$ flight distance, $\vec{x_T}$, of the B meson candidate:

$$\vartheta_{\rm alignment} \equiv cos^{-1}(\frac{\vec{p}_T \cdot \vec{x}_T}{p_T \cdot x_T}) \tag{5.3}$$

Real B meson decays should yield small $\vartheta_{\rm alignment}$, but usually non-zero due to experimental resolutions, whereas the combinatorial background peaks away from

zero. In Fig. 5.13 we see the different behaviour between signal and background events. We choose to retain events with $\vartheta_{\text{alignment}} < 0.15$ rad, a requirement satisfied by 84% of $B_d^0 \to K^{*0}\gamma$, $K^{*0} \to K^+\pi^-$ events and by 74% of $B_s^0 \to \phi\gamma$, $\phi \to K^+K^-$ events.

The second criterion makes use of the long lifetime of B mesons once again, but in a different way than the lifetime cuts discussed in the previous section. It requires that the two charged daughters of the K^{*0} or ϕ decays be inconsistent with the hypothesis of originating from the primary $p\bar{p}$ vertex. Defining the "impact parameter" (d_0) of a track to be the minimum $x-y$ separation of the particle trajectory from the primary $p\bar{p}$ vertex, we ask for the impact parameter of each track to be significantly different from zero. The uncertainty on the impact parameter of a track, $\sigma(d_0)$, is calculated from the uncertainties in the track reconstruction, without taking into account the uncertainty of the primary vertex position. Simulations of the penguin channels suggest that kaons and pions from real $B_d^0 \to K^{*0}\gamma$ decays, have dramatically different $d_0/\sigma(d_0)$ distributions compared to tracks from the combinatorial background (see Fig. 5.14).

We choose the value of the cut on the minimum impact parameter significance for each track, $d_0/\sigma(d_0)$, by varying the cut value so as to obtain the maximum ratio $\epsilon^2_{signal}/\epsilon_{background}$, where ϵ_{signal} and $\epsilon_{background}$ are the fractions of signal and background events respectively which survive the cuts under study. This ratio is the appropriate figure of merit because we aim for the most significant signal, with signal significance defined as:

$$\text{Signal significance} = \frac{N_{signal}}{\sqrt{N_{signal} + N_{background}}} \tag{5.4}$$

where N_{signal} and $N_{background}$ are the number of signal and background events respectively after the application of the selection criteria. If the cuts result in N_{signal} and $N_{background}$ events, starting with N^0_{signal} and $N^0_{background}$ events respectively, we can

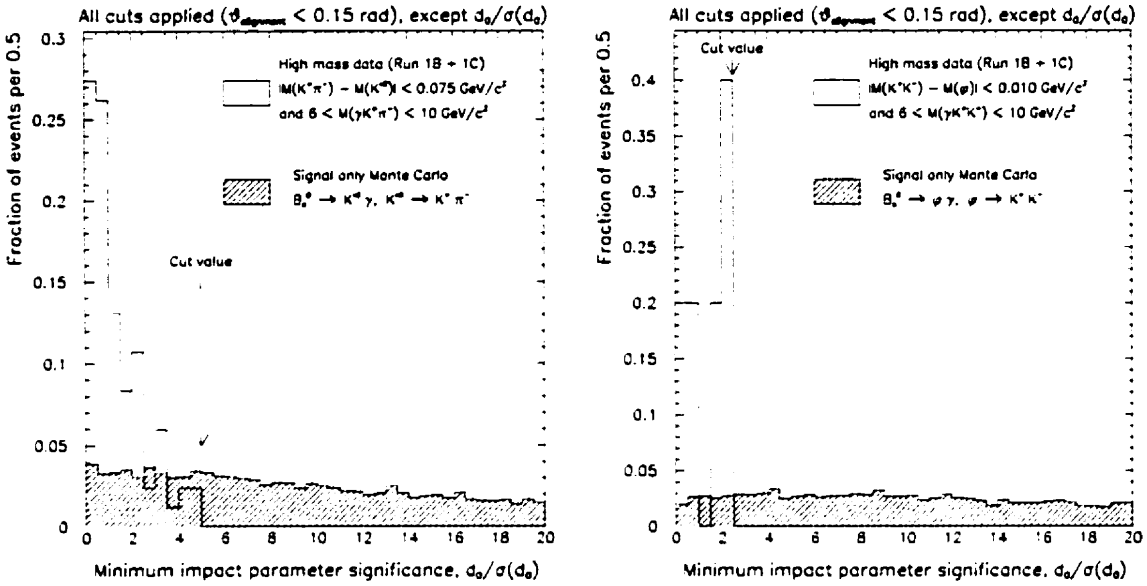

Figure 5.14: *Minimum impact parameter significance, $d_0/\sigma(d_0)$, distributions of tracks from simulated penguin B decays (hashed histogram) and from combinatorial background with $\gamma K^+\pi^-$ and γK^+K^- mass in the 6 to 10 GeV/c^2 region (clear histogram). The distributions shown correspond to combinations that satisfied the selection criteria described in Sections 5.4 - 5.7. The arrows indicate the points above which candidate B mesons were accepted.*

write:

$$N_{signal} = \epsilon_{signal} \cdot N^0_{signal}$$

$$N_{background} = \epsilon_{background} \cdot N^0_{background}$$

and consequently:

$$\begin{aligned} \text{Signal significance} &= \frac{\epsilon_{signal} \cdot N^0_{signal}}{\sqrt{\epsilon_{signal} \cdot N^0_{signal} + \epsilon_{background} \cdot N^0_{background}}} \\ &= \frac{N^0_{signal}}{\sqrt{N^0_{signal} \cdot \frac{1}{\epsilon_{signal}} + N^0_{background} \cdot \frac{\epsilon_{background}}{\epsilon^2_{signal}}}} \end{aligned} \tag{5.5}$$

Therefore, in order to achieve the maximum signal significance, we have to achieve the maximum $\epsilon^2_{signal}/\epsilon_{background}$ value.

	$B_d^0 \to K^{*0}\gamma$		$B_s^0 \to \phi\gamma$	
Cut	Run 1B	Run 1C	Run 1B	Run 1C
Proper decay length of B meson	$0 < ct < 0.3$ cm			
B meson isolation	$I_B > 0.7$			
Alignment angle	$\vartheta_{\text{alignment}} < 0.15$ rad			
Min. impact parameter significance	$d_0/\sigma(d_0) > 5.0$		$d_0/\sigma(d_0) > 2.5$	
Observed events in signal region	0	1	0	0

Table 5.1: *Chosen cuts for the $B_d^0 \to K^{*0}\gamma$ and the $B_s^0 \to \phi\gamma$ decays in Run 1B and Run 1C.*

The efficiency for the signal is calculated as the fraction of events surviving the cuts in the signal-only sample of simulated penguin decays. Depending on the penguin channel of interest, the efficiency for the background is taken to be the fraction of events in the high mass side $6 < M(\gamma K^+\pi^-) < 10$ GeV/c^2 or $6 < M(\gamma K^+K^-) < 10$ GeV/c^2, that survive the cuts. In Fig. 5.14 we see that the background distributions cut off at some point. Consequently the $\epsilon^2_{signal}/\epsilon_{background}$ value is maximum there. We thus retain $B_d^0 \to K^{*0}\gamma$, $K^{*0} \to K^+\pi^-$ and $B_s^0 \to \phi\gamma$, $\phi \to K^+K^-$ candidates with kaons and pions having $d_0/\sigma(d_0) > 5.0$ and > 2.5 respectively. These requirements are 78% and 93% efficient respectively. The narrower ϕ mass distribution compared to the K^{*0} mass resulted in a smaller number of combinatorial background in the B_s^0 channel. Therefore the need to be strict in the selection requirements was less for the B_s^0 than for the B_d^0 channel.

In summary, we apply the following cuts as well as the cuts listed in the previous sections:

21. We apply an "alignment angle" cut by requiring the angle $\vartheta_{\text{alignment}}$ between the p_T of the fully reconstructed B meson candidate and its flight path on the $x-y$ plane, to be less than 0.15 rad.

22. The two tracks should be inconsistent with the assumption that they come from the primary vertex; we require that each track has a minimum impact parameter significance, $d_0/\sigma(d_0)$, of 5.0 in the B_d^0 penguin search, or 2.5 in the B_s^0 case.

23. Finally, we define penguin candidates as these events with $\gamma K^+\pi^-$ or γK^+K^- masses within ± 220 MeV/c^2 ($\simeq 2\sigma$) from the world average B_d^0 or B_s^0 mass respectively.

In Table 5.1 we see the cuts on the characteristic quantities used to select B meson candidates. Enforcement of all the requirements discussed so far, since Section 5.4, results in the selection of one B_d^0 candidate, in Run 1C, with a photon candidate of $E_T = 18.5$ GeV, a negatively charged kaon candidate with $p_T = 2.6$ GeV/c, and a positively charged pion candidate with $p_T = 8.4$ GeV/c. The mass of the $K^-\pi^+$ combination is 0.9023 GeV/c^2, and the mass of the $\gamma K^-\pi^+$ combination is 5.309 GeV/c^2. No B_s^0 candidates were found. In Fig. 5.15 we see the mass distribution of the B candidates surviving all the selection criteria. The event display of the candidate $B_d^0 \to K^{*0}\gamma$, $K^{*0} \to K^+\pi^-$ event is shown in Fig. 5.16. The kaon and pion tracks are quite energetic and they do not curve significantly in the magnetic field. They are close to each other in ϕ and point one or two calorimeter wedges away from the photon, as the trigger requires. In the next chapter, we discuss the efficiency of the selection requirements for $B_d^0 \to K^{*0}\gamma$, $K^{*0} \to K^+\pi^-$ and $B_s^0 \to \phi\gamma$, $\phi \to K^+K^-$ decays.

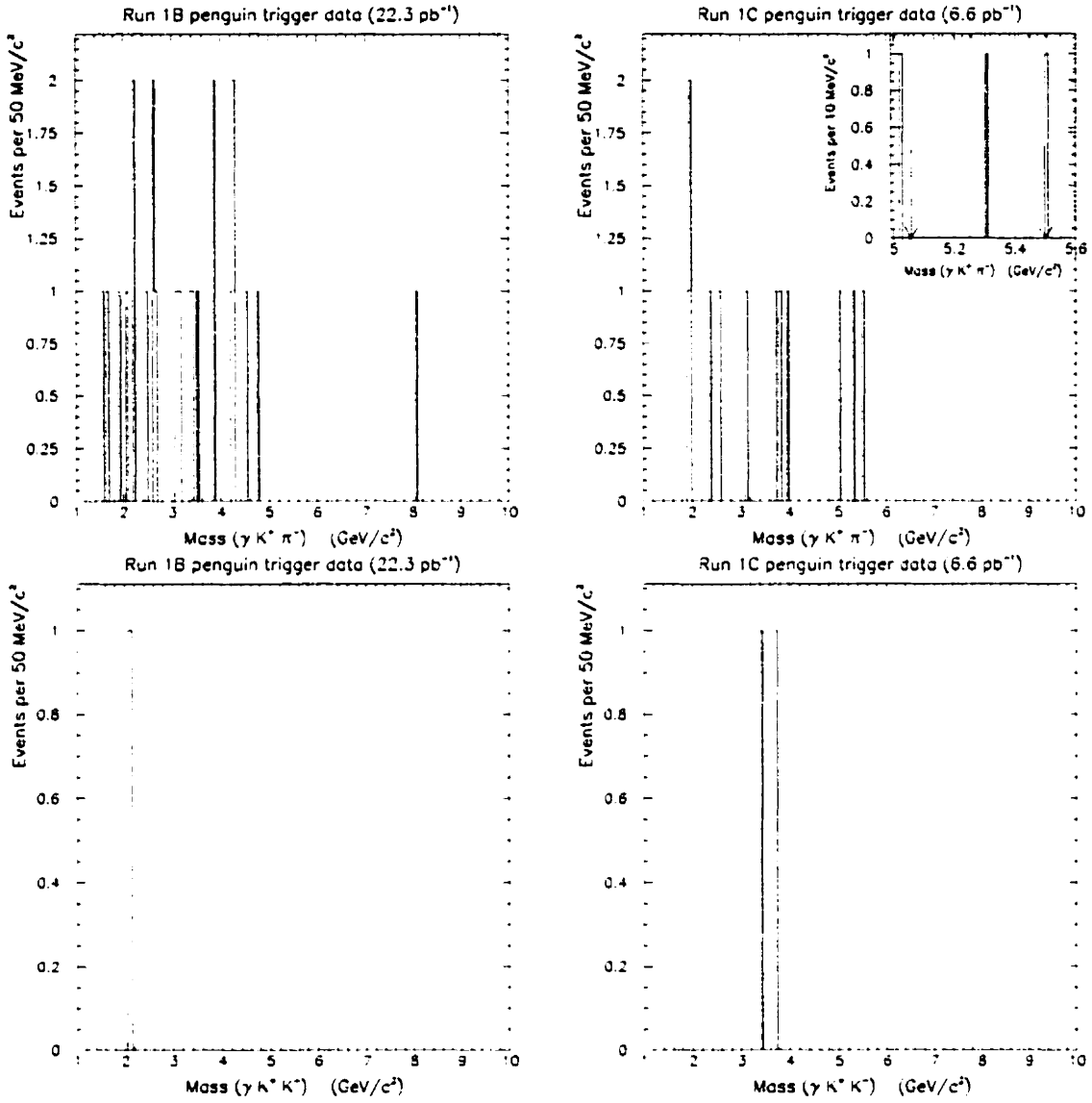

Figure 5.15: *Mass of the $\gamma K^+\pi^-$ (or $\gamma\pi^+K^-$) and γK^+K^- combinations, for photon, K^{*0}, ϕ and B candidates selected in the penguin trigger data set according to all the criteria described in Chapter 5. The arrows in the inset figures indicate the search windows for penguin events. They span ± 220 MeV/c^2 ($\sim \pm 2\sigma$) around the world average B_d^0 and B_s^0 masses of* 5.2792 GeV/c^2 *and* 5.3693 GeV/c^2 *respectively [4].*

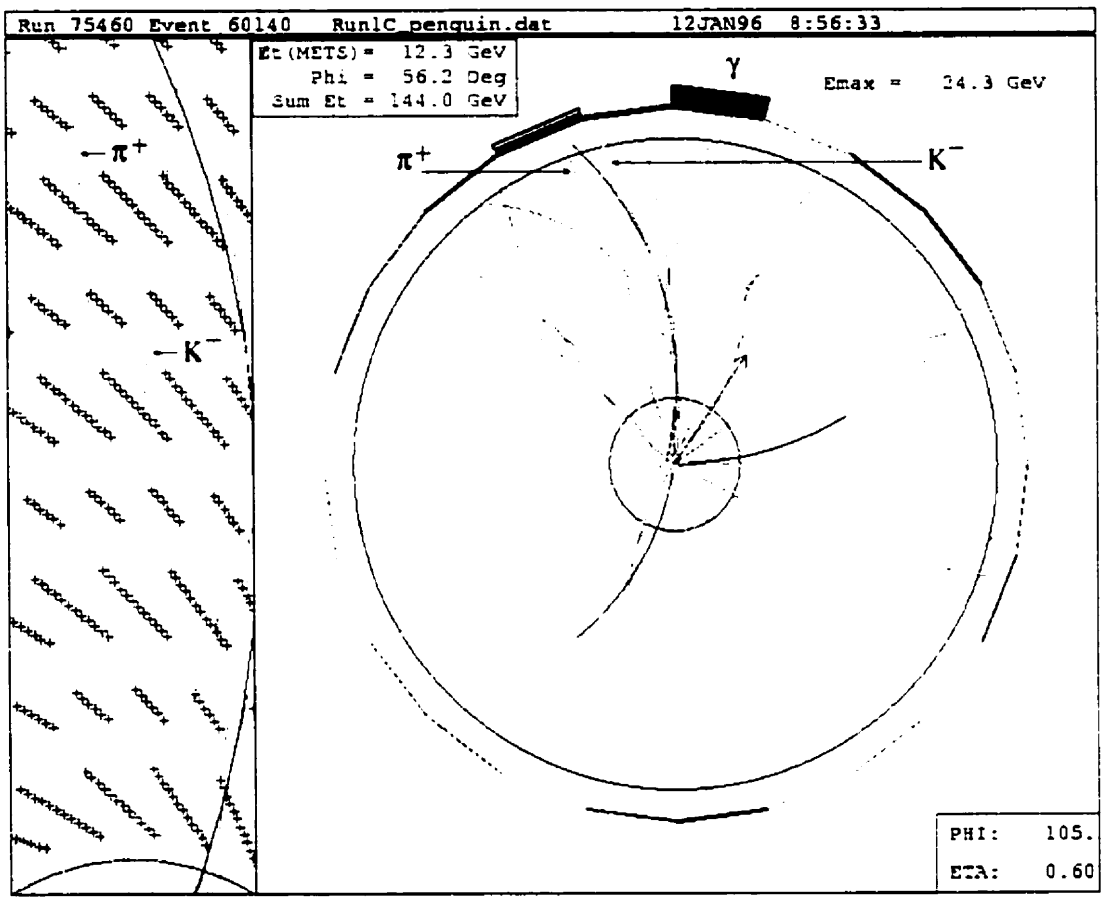

Figure 5.16: *Event display of the $B_d^0 \to K^{*0}\gamma$, $K^{*0} \to K^+\pi^-$ candidate, with the beam (z) axis being perpendicular to the page. The charged particle trajectories are shown as curved lines originating at the beam axis, crossing the inner CTC boundary (inner circle) and extending to the outer CTC boundary. The central calorimeter wedges are shown as bars spanning 15° in ϕ arranged in a cylindrical geometry outside the CTC. The magnitude and direction of the missing energy on the transverse plane ($\not\!\!E_T$), along with the total transverse energy in the event ("Sum E_T"), are shown near the top of the figure. The $\not\!\!E_T$ direction is also indicated by the arrow originating at the beam axis. At the top right corner we see the maximum energy recorded by a single calorimeter tower; it corresponds to the penguin photon candidate. At the lower right corner we see the direction of the highest energy track, which is the penguin pion candidate. A close-up view of the pion and kaon tracks is shown on the left panel of the figure. The crosses indicate the CTC wires grouped in concentric superlayers.*

Chapter 6

Efficiency Corrections

In the previous chapter we arrived at the final data sample with the application of various selection criteria which were designed to enhance the fraction of events containing penguin decays. The number of signal events observed in the final data sample, $N_{observed}$, is equal to the number of penguin events produced at the B0 collision point of the Tevatron, $N_{produced}$, scaled down by the efficiency, ϵ_{total}, of retaining these events in our final sample:

$$N_{observed} = N_{produced} \times \epsilon_{total} \tag{6.1}$$

Part of the selection inefficiency is introduced by the on-line trigger requirements, while the rest is due to the off-line data reduction procedure. The number of signal events produced is a function, among other things, of the branching fraction of the studied decay channel (see Eq. 4.1). Knowing $N_{produced}$ and the rest of the factors involved, we can extract the desired branching fraction. It is therefore essential to know the correction factor ϵ_{total} which will allow us to infer $N_{produced}$ from the number of observed signal events, $N_{observed}$, in our final data sample.

In this chapter we start by discussing the efficiencies of the various requirements imposed on the data towards the selection of the final sample of candidate penguin events. During this discussion we indicate how to evaluate these efficiencies and we

argue that the use of data, through the study of a "reference" B decay channel, is a very good alternative to Monte Carlo predictions of these efficiencies, because it takes care of detector effects, the level of activity in the vicinity of the candidate decay products, etc. We then demonstrate that the usage of Monte Carlo samples to estimate some of the efficiencies is justified by proving that we get reasonable estimates of the selection efficiencies for the reference B signal.

6.1 Selection efficiency for the penguin channels

Based on Equations 4.1 and 6.1 we can write for the number of observed $B_d^0 \to K^{*0}\gamma$, $K^{*0} \to K^+\pi^-$ candidates[1]:

$$N_{observed}(K^{*0}\gamma) = 2 \cdot \int Ldt(peng) \cdot \sigma(p\bar{p} \to B_d^0 X) \cdot \mathcal{B}(B_d^0 \to K^{*0}\gamma) \cdot \mathcal{B}(K^{*0} \to K^+\pi^-) \cdot \epsilon_{total}(K^{*0}\gamma)$$

from which we get the branching fraction of the $B_d^0 \to K^{*0}\gamma$ process:

$$\mathcal{B}(B_d^0 \to K^{*0}\gamma) = \frac{N_{observed}(K^{*0}\gamma)}{2 \cdot \int Ldt(peng) \cdot \sigma(p\bar{p} \to B_d^0 X) \cdot \mathcal{B}(K^{*0} \to K^+\pi^-) \cdot \epsilon_{total}(K^{*0}\gamma)} \quad (6.2)$$

where $\mathcal{B}(B_d^0 \to K^{*0}\gamma)$ is the branching fraction of the penguin process; $\int Ldt(peng)$ is the integrated luminosity of the penguin data sample; $\sigma(p\bar{p} \to B_d^0 X)$ is the cross section for producing a B_d^0 meson plus anything else; $\epsilon_{total}(K^{*0}\gamma)$ is the total efficiency for retaining the $B_d^0 \to K^{*0}\gamma$, $K^{*0} \to K^+\pi^-$ events which resulted from the $p\bar{p}$ collisions; and the factor of two accounts for both B_d^0 and $\bar{B}_d^0$ production, because the cross section $\sigma(p\bar{p} \to B_d^0 X)$ refers to the production of either B_d^0 or $\bar{B}_d^0$

[1]The equations and the discussion that follows applies to the $B_s^0 \to \phi\gamma$ process as well, with the obvious, and trivial, modifications. For the B_s^0 production cross section we write $\sigma(p\bar{p} \to B_s^0 X) = \frac{f_s}{f_d} \times \sigma(p\bar{p} \to B_d^0 X)$, where f_s and f_d are the fractions of the time a b quark combines with an s or a d quark to create a B_s^0 or a B_d^0 meson respectively.

mesons only, whereas in the observed candidate events, $N_{observed}(K^{*0}\gamma)$, we do not distinguish events originating from either B_d^0 or $\bar{B}_d^0$ parents. The total efficiency, $\epsilon_{total}(K^{*0}\gamma)$, can be broken down into a product of partial efficiencies, each reflecting the application of some of the selection requirements imposed on the data in the process of retaining the final sample of candidate events. We can thus write for the $B_d^0 \to K^{*0}\gamma$, $K^{*0} \to K^+\pi^-$ channel:

$$\begin{aligned}\epsilon_{total}(K^{*0}\gamma) = \quad & (6.3)\\ & \epsilon_{kinematics\&topology}(\gamma K\pi) \cdot \\ & \epsilon_{trigger\_CEM}(\gamma) \cdot \epsilon_{trigger\_XCES}(\gamma) \cdot \epsilon_{trigger\_CFT}(K,\pi) \cdot \epsilon_{trigger\_environment}(\gamma) \\ & \epsilon_{offline\_CEM}(\gamma) \cdot \epsilon_{offline\_tracking}(K,\pi) \cdot \epsilon_{offline\_track\_vertexing}(K,\pi) \cdot \\ & \epsilon_{offline\_ct}(\gamma K\pi) \cdot \epsilon_{offline\_environment}(\gamma K\pi) \cdot \\ & \epsilon_{offline\_impact}(K,\pi) \cdot \epsilon_{offline\_alignment}(\gamma K\pi) \cdot \epsilon_{offline\_mass\_cuts}(K\pi \& \gamma K\pi)\end{aligned}$$

$\underline{\epsilon_{kinematics\&topology}(\gamma K\pi)}$ is the efficiency of the kinematic and topology requirements on the products of the $B_d^0 \to K^{*0}\gamma$, $K^{*0} \to K^+\pi^-$ channel. These requirements include the selection of photon candidates with E_T above some threshold and charged particles with $p_T \gtrsim 2$ GeV/c, as well as the requirement that the tracks be close to each other ($\Delta\phi < 18^o$) and to the photon cluster in azimuthal angle (see trigger requirements I, IV, V, VI, VII and X in Section 4.2.2). Since the Monte Carlo is believed to adequately model the kinematic aspects of the decays, we obtain this efficiency using Monte Carlo events (see Chapter 3 and Section 4.3.1). The limited resolution of the detector unavoidably alters the energy distributions for the penguin decay products, but since we believe that the detector simulation correctly models these aspects of the detector behaviour (see Section 3.2), we are quite confident that the Monte Carlo approach is adequate for this point. Despite this, there is a valid argument against the use of Monte Carlo for the evaluation of this efficiency: as we see in Fig. 1.3, the theory (according to which we generate the Monte Carlo samples) does not correctly predict the momentum distribution of B mesons observed at CDF.

Reconstructing another "reference" B decay in the data can be used to get a more reliable estimate of the kinematic efficiency for the penguin decays; the B mesons in the reference signal are "born" with the same momentum spectrum as the ones which result in the penguin decays.

$\underline{\epsilon_{trigger\_CEM}(\gamma)}$ is the efficiency of the energy clustering algorithms and of the trigger requirements on the quality of the candidate photon cluster in the CEM calorimeter, namely the cuts on the fraction of energy deposited in the electromagnetic vs. the hadronic part of the central calorimeter (E_{HAD}/E_{EM}) and the profile of the energy sharing between the CEM towers (L_{SHR}) and between the strips and wires of the central strip chambers (χ^2_{strips} and χ^2_{wires}). For details refer to the trigger requirements I, VIII and IX in Section 4.2.2. The response of the detector to the penguin photon and the efficiency of the cuts on the photon quality quantities are studied by feeding Monte Carlo events through the detector simulation, whereas the energy clustering is performed by the trigger simulation (see Sections 3.2 and 3.3.1 respectively). Since the penguin photon is part of a complicated event, the values of the photon quality quantities may be altered by the presence of energy deposited in the calorimeters by other particles. In order to take into account such effects, we should ideally rely on the data itself, rather than a Monte Carlo model of the $p\bar{p}$ collision outcome. Therefore we have to use events with photon-like clusters in the CEM. Such clusters are created by photons, ultimately, and electrons. The difference in the shower development between photons and electrons is minimal and modeled in the simulation, while it is much easier to identify a pure sample of electrons, rather than photons. Using the data will also take into account any degradation of the detector performance with time and dependencies on the instantaneous luminosity.

$\underline{\epsilon_{trigger\_XCES}(\gamma)}$ is the fraction of the candidate photon clusters found at Level 2 which satisfy the XCES trigger requirements, described in Section 3.3.2. This efficiency has been parameterized as a function of the transverse energy of the candidate photon cluster (see Fig. 3.5) and it is applied to the final sample of simulated

events, after all trigger and off-line requirements, because we apply $\epsilon_{trigger\_XCES}(\gamma)$ as a correction factor after all cuts. It is found that $(94.7 \pm 1.2)\%$ of $B_d^0 \to K^{*0}\gamma$ events survive the XCES requirement in Run 1B and $(96.7 \pm 1.4)\%$ in Run 1C. For $B_s^0 \to \phi\gamma$ events $\epsilon_{trigger\_XCES}(\gamma)$ is found to be $(94.8 \pm 1.2)\%$ and $(96.7 \pm 1.4)\%$ for Run 1B and Run 1C respectively.

$\epsilon_{trigger\_CFT}(K,\pi)$ is the efficiency of the trigger requirement that both the kaon and the pion from the penguin decay be found by the CFT. This efficiency has been parameterized as a function of the transverse momentum of charged particles (see Fig. 3.6) and it is applied on the Monte Carlo tracks with the use of random numbers.

$\epsilon_{trigger\_environment}(\gamma)$ is the efficiency of the "L2 isolation" requirement, i.e. that there be no energetic track found by the CFT which points towards the same 15^o ϕ wedge as the seed wedge of the candidate photon cluster (see trigger requirement III in Section 4.2.2). This efficiency depends on the activity around the photon cluster and we prefer to use the data to describe the situation, rather than Monte Carlo. Studying this efficiency with a reference B channel using data collected in the same period as the penguin trigger data, and taking care that the B mesons in both the penguin and the reference channel have similar momentum distributions, guarantees to a great extent that the penguin and the reference B decays are embedded in a similar environment; that similarity should result in a reliable estimate of the efficiency $\epsilon_{trigger\_environment}(\gamma)$. In Section 4.3.2 we discuss the use of $\bar{B} \to e^- D^0 X$, $D^0 \to K^-\pi^+$ decays to measure the efficiency of the L2 isolation requirement for the penguin channels. The L2 isolation efficiencies for the penguin channels are shown in Table 4.1.

$\epsilon_{offline\_CEM}(\gamma)$ is the equivalent efficiency to $\epsilon_{trigger\_CEM}(\gamma)$, where this time the energies have been calculated off-line taking into account the best corrections corresponding to the relevant data-taking period[2]. The quantities used off-line to select good quality photon candidates are the same as used at the trigger level, but

[2]These corrections are not available on-line and are stored in a database for off-line use.

with stricter criteria (see requirements 1−5 in Section 5.4). In order to have a reliable estimate for the efficiencies of these requirements we select photon candidates that are contained in the well-instrumented fiducial volume of the detector (see requirements 6 and 7 in Section 5.4). For the determination of this efficiency we rely on predictions based on both Monte Carlo and data, for the reasons explained in the discussion of $\epsilon_{trigger\_CEM}(\gamma)$.

$\epsilon_{offline\_tracking}(K,\pi)$ is the fraction of the time we are able to reconstruct the track of a charged particle going through the detector volume. This efficiency has been studied as a function of the transverse momentum of charged particles satisfying the criteria 8 and 9 in Section 5.5, and it is found to be constant for $p_T > 400$ MeV/c and equal to $(92.8 \pm 2.6)\%$ [53]. The efficiency for reconstructing two oppositely charged tracks with $p_T > 400$ MeV/c was $(88.1 \pm 4.3)\%$. The performance of the silicon vertex detector is modeled well in the detector simulation, and consequently we trust the result of Monte Carlo studies to account for requirement 15 in Section 5.5. The rest of the requirements in that section are kinematic and are actually a reiteration of the corresponding trigger requirements; those too are modeled well by the Monte Carlo. Nevertheless, using tracks reconstructed in the data can take into account effects that the Monte Carlo does not take into consideration, e.g., malfunctioning detector components. As we shall see in Sections 6.3 and 6.4, we use $D^0 \to K^-\pi^+$ decays reconstructed in data collected in parallel to the penguin data to take care of such effects.

$\epsilon_{offline\_track\_vertexing}(K,\pi)$ is the fraction of kaon-pion pairs from K^{*0} decays which satisfy the "common origin/vertex" requirements, described in Section 5.6. This efficiency can be studied with Monte Carlo samples or, preferably, with a two-prong decay of a meson in the data. We use $D^0 \to K^-\pi^+$ decays as noted above.

$\epsilon_{offline\_ct}(\gamma K\pi)$ is the efficiency of the $0 < ct < 0.3$ cm requirement on the candidate B meson (see requirement 19 in Section 5.7 and the discussion therein). Since we believe the decay of B mesons to be modeled very well in the Monte Carlo

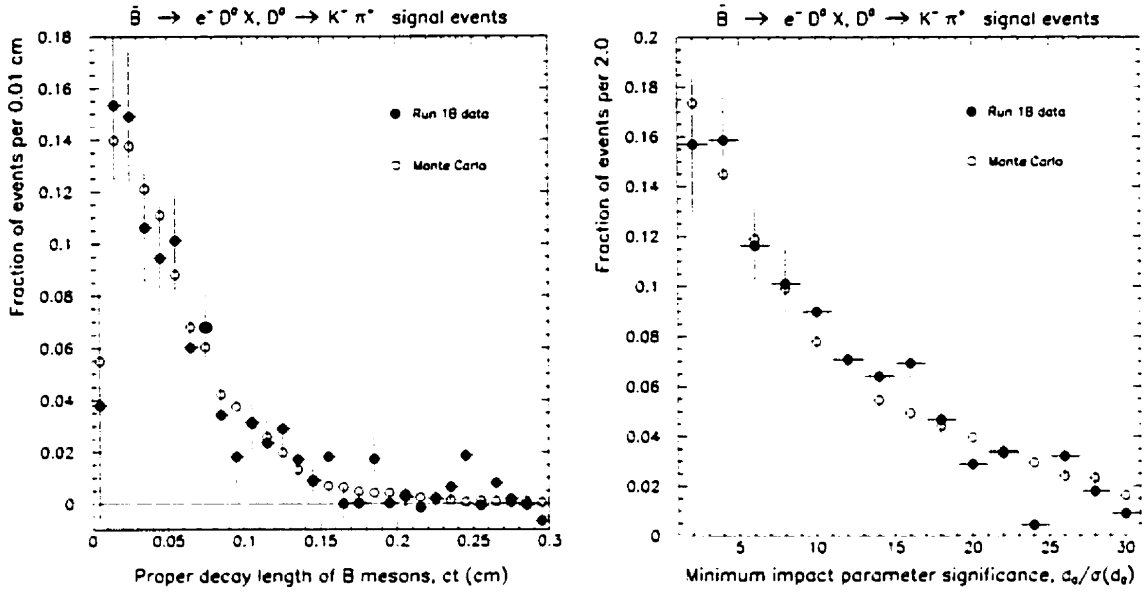

Figure 6.1: *Monte Carlo vs. data distributions of (left) proper decay length of B mesons, and (right) the minimum impact parameter significance for kaons and pions from the* $\bar{B} \to e^- D^0 X$, $D^0 \to K^- \pi^+$ *decays. The ct distributions are shown for events with kaons and pions having* $d_0/\sigma(d_0) > 1.0$, *while the* $d_0/\sigma(d_0)$ *distributions correspond to events with* $0 < ct < 0.3$ *cm.*

and the resolutions of the silicon vertex detector in the detector simulation are tuned to match those observed in the data, we rely on simulated events to estimate the efficiency of the *ct* requirements on the B mesons. We check the validity of this approach with $\bar{B} \to e^- D^0 X$, $D^0 \to K^- \pi^+$ data and conclude that indeed the Monte Carlo predicts the distribution of B meson decay lengths (see Fig. 6.1).

$\underline{\epsilon_{offline\_environment}(\gamma K \pi)}$ is the efficiency of the "B isolation" requirement, i.e. that the B meson candidate be mostly isolated from charged particles in its vicinity (see requirement 20 in Section 5.7 and the discussion therein). Since the efficiency of this requirement depends on the environment the B meson candidates are embedded in, we rely on data to estimate it. We use $\bar{B} \to e^- D^0 X$, $D^0 \to K^- \pi^+$ decays collected during the same data-taking period as the penguin data and reconstructed as described in Section 6.2. We then apply an isolation requirement on the electron,

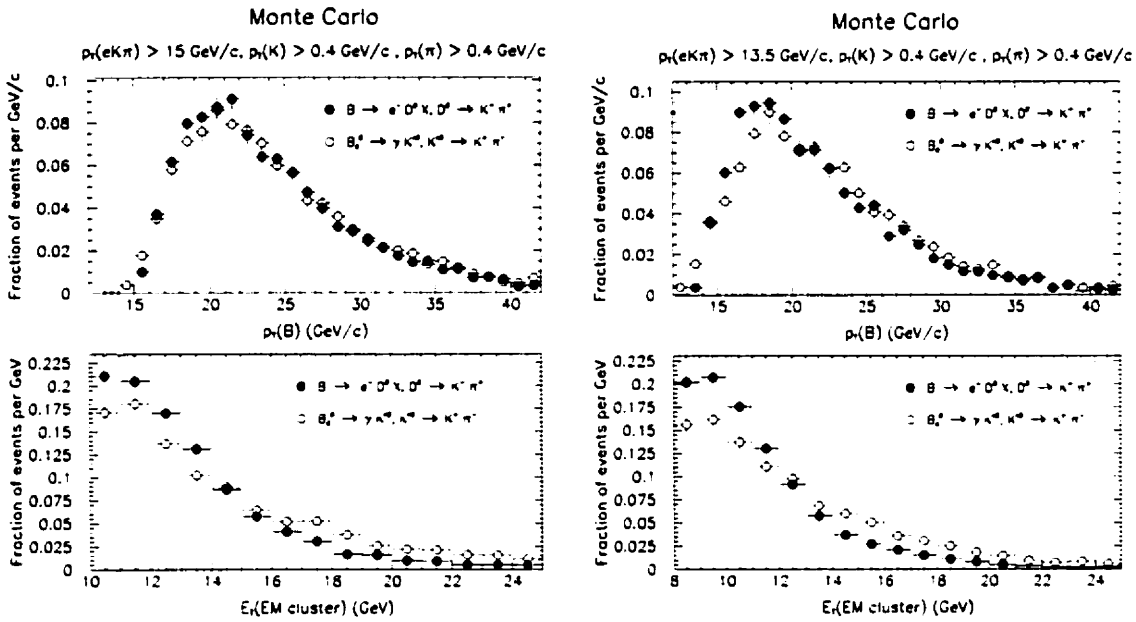

Figure 6.2: *Top: Comparison of generator level $p_T(B)$ distributions for the $B_d^0 \to K^{*0}\gamma$, $K^{*0} \to K^+\pi^-$ and $\bar{B} \to e^- D^0 X$, $D^0 \to K^-\pi^+$ channels in "Run 1B - like" (left) and "Run 1C - like" (right) Monte Carlo, after all requirements imposed on them. Bottom: Comparison of E_T (EM cluster) distributions with cuts as noted. "EM cluster" indicates either the penguin photon or the ECLB electron.*

similar to the "L2 isolation" imposed on the penguin photon (see Section 4.3.2). Requiring $p_T(eK\pi) > 15$ GeV/c (> 13.5 GeV/c) in the Run 1B (Run 1C) sample, leads to similar $p_T(B)$ spectra for the penguin and the $\bar{B} \to e^- D^0 X$, $D^0 \to K^-\pi^+$ processes, with mean values matching within 600 MeV (see Fig. 6.2 and 6.3). This matching ensures the similarity of the environments in which the B decays were embedded.

The B isolation variable is defined in terms of the p_T of the parent B meson, $p_T(B)$, but because we only have a partially reconstructed decay, we infer $p_T(B)$ from the measured $p_T(eK\pi)$ using simulated $\bar{B} \to e^- D^0 X$, $D^0 \to K^-\pi^+$ decays. In Figure 5.11 we see that $p_T(eK\pi) = 0.85 \cdot p_T(B)$ on average. We use this average correction factor to infer $p_T(B)$ from the measured $p_T(eK\pi)$ value and we require

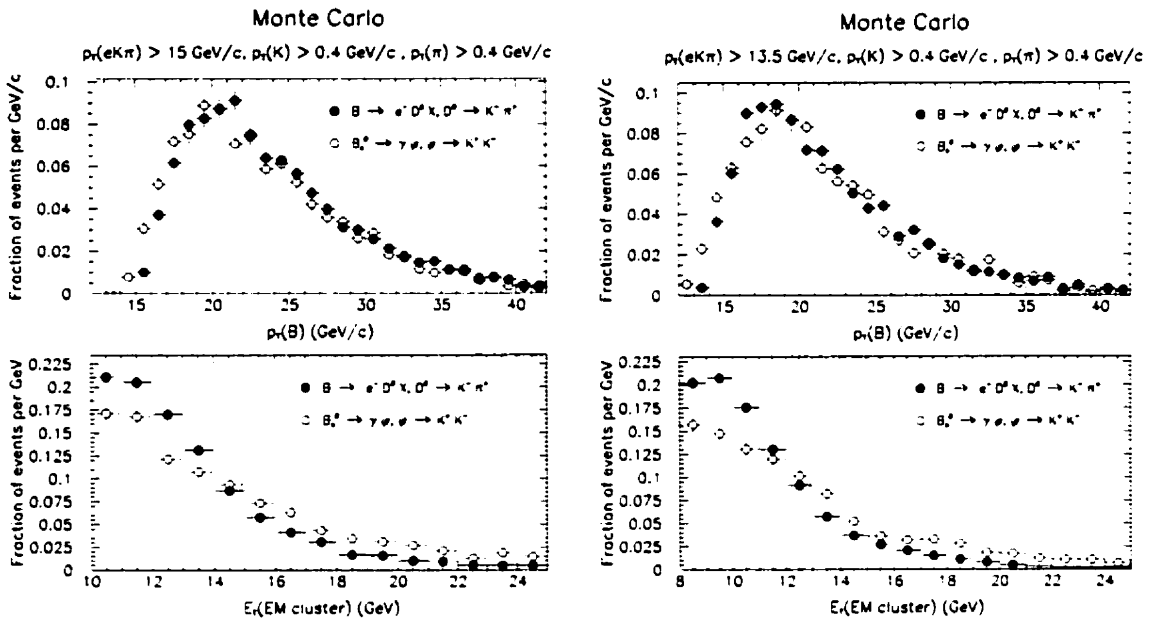

Figure 6.3: *As in the previous Figure, but for the* $B_s^0 \to \phi\gamma$, $\phi \to K^+K^-$ *and* $\bar{B} \to e^- D^0 X$, $D^0 \to K^-\pi^+$ *channels.*

$I_B > 0.7$ for the $\bar{B} \to e^- D^0 X$, $D^0 \to K^-\pi^+$ decays, as we did for the penguin decays.

We find that the efficiency of the L2 and B isolation requirements is $(59.8 \pm 7.4)\%$ in Run 1B and $(76.2 \pm 13.1)\%$ in Run 1C for $\bar{B} \to e^- D^0 X$, $D^0 \to K^-\pi^+$ decays. Differences in the b quark fragmentation processes that lead to the B_d^0 parent of the $B_d^0 \to K^{*0}\gamma$ channel, the B_s^0 parent of the $B_s^0 \to \phi\gamma$ channel, and the mostly B_u^+ parents of the $\bar{B} \to e^- D^0 X$ decays, can result in B decays embedded in different environments. Furthermore, contrary to the penguin channels, $\bar{B} \to e^- D^0 X$, $D^0 \to K^-\pi^+$ is not a fully reconstructed decay and the extra particles could result in different L2 and B isolation efficiencies compared to the penguin channels. These effects, along with the residual differences in the $p_T(B)$ spectra are corrected with the use of $p\bar{p} \to b\bar{b}$ Monte Carlo events generated with PYTHIA [54] and fed through the detector and trigger simulations. The simulation shows that the L2 and B isolation efficiencies are higher for the B_d^0 and B_s^0 penguin channels by $(4.1 \pm 2.3)\%$ and $(6.4 \pm 2.4)\%$ respectively. From the L2 and B isolation efficiencies measured with the

$\bar{B} \to e^- D^0 X$, $D^0 \to K^-\pi^+$ channel, mentioned above, we infer the ones appropriate for the penguin channels, shown in Table 6.1.

$\epsilon_{offline\_impact}(K,\pi)$ is the fraction of penguin decays that satisfy the requirement that both the daughter kaons and pions be significantly displaced from the $p\bar{p}$ collision point. As shown in Fig. 6.1, the Monte Carlo predicts the distribution of the impact parameter significance for the D^0 products of $\bar{B} \to e^- D^0 X$, $D^0 \to K^-\pi^+$ decays. Consequently, we rely on simulated events to obtain $\epsilon_{offline\_impact}(K,\pi)$.

$\epsilon_{offline\_alignment}$ is the efficiency of the requirement that the B candidate momentum form a small angle with its flight path (see requirement 22 in Section 5.8). In the estimation of $\epsilon_{offline\_alignment}$ we rely on Monte Carlo, as in the $\epsilon_{offline\_ct}(\gamma K\pi)$ and $\epsilon_{offline\_impact}(K,\pi)$ determination.

$\epsilon_{offline\_mass\_cuts}(K\pi\&\gamma K\pi)$ is the efficiency of the mass cuts imposed on the kaon-pion combinations and on the B meson candidates (see requirements 17 and 18 in Section 5.6 and requirement 23 in Section 5.8). As explained in Section 5.7, the distributions of the reconstructed masses are expected to be described well by the Monte Carlo and we thus rely on such samples of events to estimate $\epsilon_{offline\_mass\_cuts}(K\pi\&\gamma K\pi)$.

In Table 6.1 we show the total efficiencies for selecting $B^0_d \to K^{*0}\gamma$ and $B^0_s \to \phi\gamma$ decays in Run 1B (Run 1C) starting with B mesons of $p_T > 12$ (> 6) GeV/c and $|y| < 1.25$. Apart from the XCES, track reconstruction, and L2 and B isolation efficiencies, the rest have been estimated with Monte Carlo events where only the signal processes were simulated, omitting the rest of the $p\bar{p}$ collision outcome.

6.2 $\bar{B} \to e^- D^0 X$ as a reference signal

As was indicated in the discussion of the partial efficiencies that are involved in the reconstruction of the penguin decays, in some cases we ultimately rely on data. For some of these efficiencies we need events containing an energetic electromagnetic cluster in the CEM; for some we need events containing two oppositely charged

	$B_d^0 \to K^{*0}\gamma$		$B_s^0 \to \phi\gamma$	
Monte Carlo events	Run 1B	Run 1C	Run 1B	Run 1C
$\|y(B)\| < 1.25$ and $p_T(B) > 12$ GeV/c or $p_T(B) > 6$ GeV/c	737303	1942314	550968	1523628
After trigger simulation (except XCES and L2 isolation)	21716	21964	23954	24425
After off-line requirements (except track reconstruction, and B isolation)	3629	2309	3523	2208
Efficiencies (in %)				
Trigger and off-line (partial)	0.492 ± 0.008	0.119 ± 0.002	0.639 ± 0.011	0.145 ± 0.003
XCES	94.7 ± 1.2	96.7 ± 1.4	94.8 ± 1.2	96.7 ± 1.4
L2 and B isolation	62.3 ± 7.8	79.3 ± 13.7	63.6 ± 8.0	81.1 ± 14.1
Track reconstruction	88.1 ± 4.3			
Total efficiency (%)	0.256 ± 0.035	0.080 ± 0.015	0.339 ± 0.046	0.100 ± 0.018
$\int Ldt$ pb^{-1}	22.3 ± 0.9	6.6 ± 0.3	22.3 ± 0.9	6.6 ± 0.3
$2 \cdot \sigma(p\bar{p} \to BX)$ (μb)	0.622 ± 0.144	5.816 ± 1.322	$\frac{1}{3} \cdot \sigma(p\bar{p} \to B_d^0 X)$	
$\mathcal{B}(K^{*0} \to K^+\pi^-)$	2/3			
$\mathcal{B}(\phi \to K^+K^-)$			0.491 ± 0.008	
$\frac{\mathcal{B}(B_d^0 \to K^{*0}\gamma)}{\text{Number of signal events}} \times 10^5$	4.22 ± 1.15	4.88 ± 1.46		
$\frac{\mathcal{B}(B_s^0 \to \phi\gamma)}{\text{Number of signal events}} \times 10^5$			12.99 ± 3.53	15.92 ± 4.68
If: $\mathcal{B}(B_d^0 \to K^{*0}\gamma) =$ $\mathcal{B}(B_s^0 \to \phi\gamma)$	$(4.0 \pm 1.9) \times 10^{-5}$			
Then: Expected signal events	0.95 ± 0.52	0.82 ± 0.46	0.31 ± 0.17	0.25 ± 0.14

Table 6.1: *Number of penguin events expected to survive all selection requirements in Run 1B and Run 1C. Here we use* $\frac{f_s}{f_u} = \frac{1}{3}$. *The efficiencies for the* $B_d^0 \to K^{*0}\gamma$ *and the* $B_s^0 \to \phi\gamma$ *decays in Run 1B (Run 1C) are quoted starting with B mesons of* $p_T > 12$ (> 6) *GeV/c and* $|y| < 1.25$ *and applying the trigger and off-line selection requirements.*

particles that are the only daughters of a meson decay; and for some we need B mesons to study, among others, the effect of the "environment" in which the penguin decay is embedded.

We can extract information for all of these by studying the B decay channel $\bar{B} \to e^- D^0 X$, $D^0 \to K^- \pi^+$, where X indicates either an electron neutrino alone, or accompanied by one or more pions, from decays like $B \to e D^{*0} \nu, D^{*0} \to D^0 \pi$. These events end up in the collected data sample by requiring an electron-like cluster at the trigger level, while no requirements on the rest of the decay products are imposed; any channel resulting in an electron which satisfies the trigger requirements can be reconstructed using such an "inclusive electron" data set, also referred to as the ECLB, or just the electron data set.

At the second trigger level the electron-like clusters are a subset of the photon-like clusters (refer to Section 4.2.1). We can then request that the photon candidates satisfy the electron clustering algorithm. This results in equal Level 2 clustering efficiencies for photons and electrons. As far as the various quality criteria are concerned, the photon and electron candidates are treated identically. Extra requirements that are present in the penguin channels can be imposed on the $\bar{B} \to e^- D^0 X$, $D^0 \to K^- \pi^+$ channels as well, thus making the event selection for the two processes as similar as possible, apart from the fact that electron clusters have a track pointing to them while the photon clusters considered in the penguin trigger have no matching tracks.

Similarly to Eq. 6.2 we write for the number of observed $\bar{B} \to e^- D^0 X$, $D^0 \to K^- \pi^+$ candidates, $N_{observed}(eD^0X)$, and the branching fraction, $\mathcal{B}(\bar{B} \to e^- D^0 X)$, inferred from this observation:

$$N_{observed}(eD^0X) = 4 \cdot \int Ldt(eX) \cdot \sigma(p\bar{p} \to BX) \cdot \mathcal{B}(\bar{B} \to e^- D^0 X) \cdot \mathcal{B}(D^0 \to K^- \pi^+) \cdot \epsilon_{total}(eD^0X)$$

and:

$$\mathcal{B}(\bar{B} \to e^- D^0 X) = \frac{N_{observed}(eD^0X)}{4 \cdot \int Ldt(eX) \cdot \sigma(p\bar{p} \to BX) \cdot \mathcal{B}(D^0 \to K^-\pi^+) \cdot \epsilon_{total}(eD^0X)} \tag{6.4}$$

where $\int Ldt(eX)$ is the integrated luminosity of the inclusive electron data sample (at least one electron found, without dealing with the rest of the event, X); $\sigma(p\bar{p} \to BX)$ is the cross section for producing a B_d^0 or a B_u^+ meson plus anything else; $\epsilon_{total}(eD^0X)$ is the total efficiency for retaining the $\bar{B} \to e^- D^0 X$, $D^0 \to K^-\pi^+$ events which resulted from the $p\bar{p}$ collisions; and the factor of four accounts for B_d^0, $\bar{B}_d^0$, B_u^+ and B_u^- production, because the cross section $\sigma(p\bar{p} \to B_d^0 X)$ refers to the production of B_d^0 mesons only, whereas for the observed candidate events, $N_{observed}(eD^0X)$, we do not distinguish between events originating from B_d^0, $\bar{B}_d^0$, B_u^+ or B_u^- parents. The cross sections for producing B_d^0 and B_u^+ mesons are taken to be equal [4]. The efficiency for the $\bar{B} \to e^- D^0 X$ process is the weighted average of all the channels contributing to the semi-inclusive $\bar{B} \to e^- D^0 X$ process, with the weighting factors accounting for the abundances of the various contributing channels: $B \to eD^0\nu$; $B \to eD^*\nu, D^* \to D^0X$; and $B \to eD^{**}\nu, D^{**} \to D^0X$; and $B \to e(Dn\pi)_{nr}\nu, (Dn\pi)_{nr} \to D^0X$, where $(Dn\pi)_{nr}$ indicates non-resonant production of extra pions.

The advantage of using the $\bar{B} \to e^- D^0 X$ reference signal can be maximized by inferring $\mathcal{B}(B_d^0 \to K^{*0}\gamma)$ from a measurement of its ratio with the known $\mathcal{B}(\bar{B} \to e^- D^0 X)$; any common factors cancel in the ratio, while the effect of systematic uncertainties that are common to both channels is reduced. We can duly write then:

$$\frac{\mathcal{B}(B_d^0 \to K^{*0}\gamma)}{\mathcal{B}(\bar{B} \to e^- D^0 X)} = \frac{N_{observed}(K^{*0}\gamma)}{2 \cdot \int Ldt(peng) \cdot \sigma(p\bar{p} \to B_d^0 X) \cdot \mathcal{B}(K^{*0} \to K^+\pi^-) \cdot \epsilon_{total}(K^{*0}\gamma)} \cdot \left(\frac{N_{observed}(eD^0X)}{4 \cdot \int Ldt(eX) \cdot \sigma(p\bar{p} \to BX) \cdot \mathcal{B}(D^0 \to K^-\pi^+) \cdot \epsilon_{total}(eD^0X)} \right)^{-1}$$

$$= 2 \cdot \frac{N_{observed}(K^{*0}\gamma)}{N_{observed}(eD^0X)} \cdot \frac{\int Ldt(eX)}{\int Ldt(peng)} \cdot \frac{\mathcal{B}(D^0 \to K^-\pi^+)}{\mathcal{B}(K^{*0} \to K^+\pi^-)} \cdot \frac{\epsilon_{total}(eD^0X)}{\epsilon_{total}(K^{*0}\gamma)}$$

Therefore we get:

$$\mathcal{B}(B^0_d \to K^{*0}\gamma) = \tag{6.5}$$
$$N_{observed}(K^{*0}\gamma) \cdot \frac{\mathcal{B}(\bar{B} \to e^- D^0 X) \cdot \mathcal{B}(D^0 \to K^-\pi^+)}{\mathcal{B}(K^{*0} \to K^+\pi^-)} \cdot$$
$$2 \cdot \frac{1}{N_{observed}(eD^0X)} \cdot \frac{\int Ldt(eX)}{\int Ldt(peng)} \cdot \frac{\epsilon_{total}(eD^0X)}{\epsilon_{total}(K^{*0}\gamma)}$$

where the production cross section for B mesons that result in $B^0_d \to K^{*0}\gamma$ decays and for B mesons that result in $\bar{B} \to e^- D^0 X$ decays, are equal and thus cancel in the ratio; the cancellation will be exact if the momentum spectra of the parent B mesons are the same for the two processes. As demonstrated in Fig. 6.2 and 6.3, this is achieved with the application of the appropriate kinematic requirements on the decay products (see below). Keep in mind though that the production cross section for B^0_s mesons is a fraction of that for B^0_d and B^+_u mesons; $\sigma(p\bar{p} \to B^0_s X) = \frac{f_s}{f_d} \times \sigma(p\bar{p} \to B^0_d X)$. Therefore Eq. 6.5 written for the $B^0_s \to \phi\gamma$, $\phi \to K^+K^-$ decay would have a multiplicative factor of $\frac{f_d}{f_s}$ on the right hand side.

6.3 Selection criteria for $\bar{B} \to e^- D^0 X$ candidates

In this section we discuss the selection criteria imposed on the inclusive electron data in order to reconstruct $\bar{B} \to e^- D^0 X$, $D^0 \to K^-\pi^+$ candidates with similar requirements as in the penguin channels. The similarities between the two B decay channels, with each having a cluster of electromagnetic energy in the CEM and two oppositely charged kaons/pions originating from a meson, suggest that appropriate candidate-selection requirements can lead to partial efficiencies that nearly cancel in the ratio. The selection requirements described below serve exactly this purpose.

6.3.1 Selection of electron candidates

The trigger requirements on the electrons collected through the inclusive electron data stream are very similar to the ones imposed on the photons of the penguin data set (see items I, II, VII, VIII and IX in Section 4.2.2), with some necessary differences.

a) The main difference between the trigger requirements on the penguin photons and the ECLB electrons is the fact that in the electron case there should be a track which extrapolates to the CEM cluster; the trigger requires that this be a CFT track at Level 2 (refer to Fig. 3.6), which is found at Level 3 to have $p_T > 6$ GeV/c and extrapolate to the CES position of the cluster within ± 3 cm along the x and ± 10 cm along the z axes.

b) Off-line, we require that there be a three-dimensional track associated with the electromagnetic energy cluster in the CEM (tracks found in the CTC are extrapolated to the radius of the CES and if at least one of them extrapolates to the examined cluster, we have an electron candidate).

c) The electron cluster is required to have $E_T > 8$ GeV at Level 2 and $E_T > 7.5$ GeV at Level 3, in both the Run 1B and Run 1C samples.

d) Off-line the energy of the cluster is corrected in exactly the same fashion as that of the photon candidate in the penguin search (see item 2 in Section 5.4). Both the Run 1B and the Run 1C electron data were collected with a requirement of $E_T > 8$ GeV on the candidate electrons, but since only $E_T > 10$ GeV photon candidates were considered for the penguin channels in Run 1B, the minimum E_T of electron candidates for the $\bar{B} \rightarrow e^- D^0 X$ process in Run 1B was raised to 10 GeV.

e) The electron candidates are also subject to exactly the same quality criteria and the same constraints on the fiducial region of the detector as the penguin

photon candidates (see items 3 – 7 in Section 5.4 and Figure 5.2). Given the identical requirements for electron and photon clusters, we claim that equal energy electrons and photons have the same chance to satisfy them, provided they are embedded in similar environments (see the discussion on the efficiency $\epsilon_{trigger\_CEM}(\gamma)$ in Section 6.1). The similarity of the environments will be achieved by requiring that the momentum spectra of the parent B mesons be the same for the two processes and that both data sets be collected in parallel.

f) Apart from the requirements listed in Section 5.4, the penguin photon is subject to an isolation requirement at the second level of the trigger: no CFT track should be pointing at the same 15° ϕ CEM wedge as the photon cluster. In order to work with electrons that are selected with the same requirements as the penguin photons, we impose this "L2 isolation" requirement on the electrons.

6.3.2 Track criteria

g) We select tracks as described in Section 5.5 (items 8, 9, 13, 15 and the appropriate magnetic field corrections).

h) We do not require the candidate tracks to be found by the CFT, nor that they satisfy the same topological requirements as the penguin tracks (items 10, 11 and 12 in Section 5.5). Doing so would make all track criteria the same between the penguin and the $\bar{B} \to e^- D^0 X$, $D^0 \to K^- \pi^+$ processes, but it would substantially limit the number of observed $\bar{B} \to e^- D^0 X$, $D^0 \to K^- \pi^+$ events, which would increase the statistical uncertainty on the penguin branching fraction. Furthermore, the chance for a track to be found by the CFT is well modeled as a function of the track p_T (see Section 3.3.3), and we can thus take care of this part of the tracking efficiencies for the penguin samples, without using the $\bar{B} \to e^- D^0 X$, $D^0 \to K^- \pi^+$ sample. We do require though that the tracks be near the electron, by requesting that the $\eta - \phi$ separation

between the electron and the track be less than 1.0, with ϕ in radians.

i) We then require that each of the two oppositely charged tracks selected for the reconstruction of the $\bar{B} \to e^- D^0 X$, $D^0 \to K^- \pi^+$ signal have $p_T > 400$ MeV/c. Because the track reconstruction efficiency is found to be constant for $p_T > 400$ MeV/c [53], this requirement guarantees that the reconstruction efficiencies for these tracks and for the ones considered as the penguin daughters, are the same.

6.3.3 $D^0 \to K^- \pi^+$ reconstruction

j) We pair oppositely charged tracks, and we constrain them to intersect at a common point. We only retain pairs which have a confidence level for this constraint greater than 1% (refer to the discussion in Section 5.6).

k) The ambiguity of the mass assignment for each track (kaon or pion), is easily resolved in the $\bar{B} \to e^- D^0 X$, $D^0 \to K^- \pi^+$ case: the kaon has the same charge as the electron and the pion the opposite (consider the quark level diagram for these channels). In Fig. 6.4 we see the mass of the two track pairs in the case the kaon mass is assigned to the track with the same charge as the electron ("Right Sign" combinations) and in the opposite case ("Wrong Sign" combinations). We consider track combinations with masses between 1.75 and 2.0 GeV/c^2.

6.3.4 B candidate selection

l) Subsequently we add the four vectors of the two tracks and the electron and we require the mass of the three-body combination to be $M(eK\pi) < 5.0$ GeV/c^2; the un-reconstructed daughters of the $\bar{B} \to e^- D^0 X$, $D^0 \to K^- \pi^+$ decays, denoted by X, make the mass of $eK\pi$ combinations less than the world average B mass of 5.279 ± 0.002 GeV/c^2.

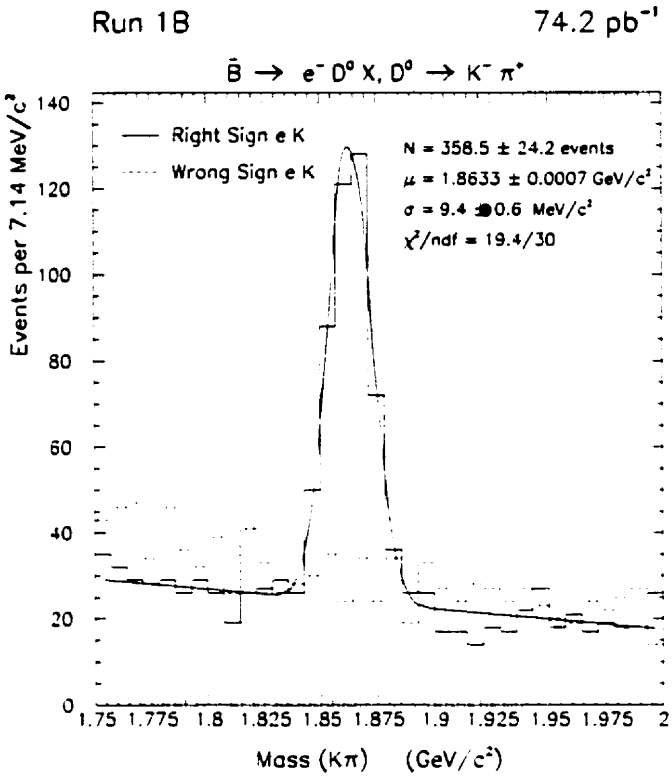

Figure 6.4: *Mass of $K\pi$ combinations in the entire Run 1B electron sample, after all selection criteria imposed on the search for $B \to eD^0X$, $D^0 \to K\pi$ decays. The "Right Sign" distribution is for same charge electrons and kaons, as should be the case if they were both products of the $\bar{B} \to e^- D^0 X$, $D^0 \to K^-\pi^+$ chain, whereas in the "Wrong Sign" distribution the kaon has opposite charge to the electron.*

m) Along the lines of the discussion in Section 5.8 we require that the B meson candidate be mostly isolated from activity around it; we retain combinations with $I_B > 0.7$, as we did for the penguin candidates. We infer $p_T(B)$ from the measured $p_T(eK\pi)$ value using the average $\frac{p_T(eK\pi)}{p_T(B)}$ value of 0.85 (refer to Fig. 5.11 and the discussion of $\epsilon_{offline\_environment}(\gamma K\pi)$ in Section 6.1).

n) We also make use of the long lifetime of B mesons to reduce combinatorial background. The $x-y$ projection of the $eK\pi$ momentum, $p_T(eK\pi)$, on the decay path of the B meson, x_T, is required to be positive, which is another

way of saying that the momentum of the $eK\pi$ system points less than 90^o away from the B flight path (i.e. $\vec{p_T}(eK\pi) \cdot \vec{x_T} > 0$). This requirement is equivalent to the $ct > 0$ requirement on the penguin candidates. We choose the primary $p\bar{p}$ vertex the same way we did for the penguin candidates, and a coarse approximation for the B decay vertex is taken to be the D^0 decay point, the two-track vertex. One could argue that this approximation is rather crude because the lifetime of D^0 mesons is a quarter of the B meson lifetime, and consequently the resolution of the detector is in principle adequate to allow the identification of the D^0 decay point as distinct from the B meson decay point. Nevertheless, data and simulated events are treated identically and it is shown that the distributions observed in the data are reproduced by the Monte Carlo (see Fig. 6.1). We also require $ct < 0.3$ cm, as in the penguin channels.

o) In addition we require the two tracks to be largely inconsistent with the assumption they come from the primary $p\bar{p}$ vertex; we require that each track have impact parameter significance, $d_0/\sigma(d_0)$, greater than 2.0. As shown in Fig. 6.1, we can reliably model the efficiency of the last two requirements using Monte Carlo samples of $\bar{B} \to e^- D^0 X$, $D^0 \to K^-\pi^+$ decays.

p) Finally, we have to make the p_T spectra of the B mesons which result in the $\bar{B} \to e^- D^0 X$, $D^0 \to K^-\pi^+$ and the penguin processes to be similar. Recall that this is a crucial condition for the cancellation of the production cross section of the parent B mesons of the penguin and the reference processes, as well as for the similarity of the environments in which the B decays were embedded[3]. As shown in Fig. 6.2 and 6.3, requiring $p_T(eK\pi) > 15$ GeV/c (> 13.5 GeV/c) in the Run 1B (Run 1C) sample, leads to similar $p_T(B)$ spectra for the penguin and the $\bar{B} \to e^- D^0 X$, $D^0 \to K^-\pi^+$ processes.

[3]Required in order to have quite similar efficiencies between the penguin and the reference channels.

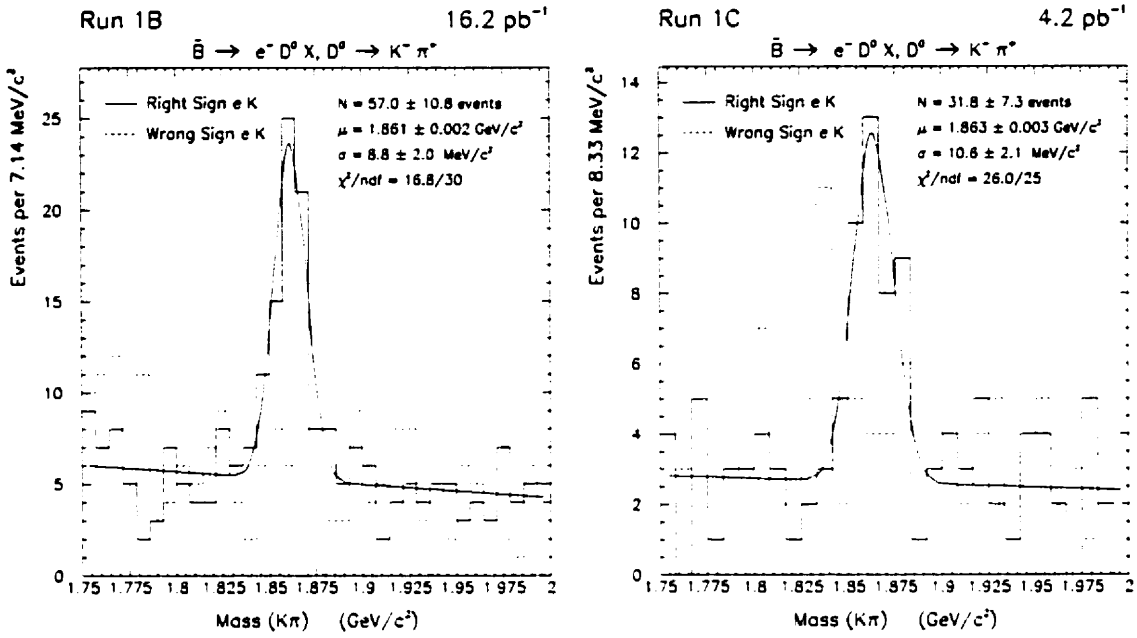

Figure 6.5: *Mass of $K\pi$ combinations, after all selection criteria imposed on the search for $B \to eD^0X$, $D^0 \to K\pi$ decays. The "Right Sign" distributions are for same charge electrons and kaons, as should be the case if they were both products of the $\bar{B} \to e^- D^0 X$, $D^0 \to K^-\pi^+$ chain, whereas in the "Wrong Sign" distributions the kaon has opposite charge to the electron.*

The masses of the selected $K\pi$ combinations are shown in Fig. 6.5. As demonstrated with a larger data sample (see Fig. 6.4), the fact that we observe $D^0 \to K\pi$ decays which are descended from B meson parents, is inferred from the difference between the "Right Sign" and "Wrong Sign" distributions; "Right Sign" distributions are for same charge electrons and kaons, as should be the case if they were both products of the $\bar{B} \to e^- D^0 X$, $D^0 \to K^-\pi^+$ chain, whereas in the "Wrong Sign" distributions the kaon has the opposite charge of the electron.

6.4 Relative efficiencies and systematic uncertainties

The efficiency $\epsilon_{total}(eD^0X)$, can be broken down into a product of partial efficiencies, each reflecting the application of some of the selection requirements imposed on the data in the process of retaining the final sample of candidate events, with some of them at the trigger level, and the rest off-line. We can write for the $\bar{B} \to e^- D^0 X$, $D^0 \to K^-\pi^+$ channel:

$$\begin{aligned}
&\epsilon_{total}(eD^0X) = \\
&\quad \epsilon_{kinematics\&topology}(eK\pi) \cdot \\
&\quad \epsilon_{trigger_CEM}(e) \cdot \epsilon_{trigger_XCES}(e) \cdot \epsilon_{trigger_CFT}(e) \cdot \epsilon_{track_CEM_matching}(e) \cdot \\
&\quad \epsilon_{offline_CEM}(e) \cdot \epsilon_{offline_tracking}(e, K, \pi) \cdot \epsilon_{offline_track_vertexing}(K, \pi) \cdot \\
&\quad \epsilon_{offline_ct}(eK\pi) \cdot \epsilon_{offline_environment}(eK\pi) \cdot \epsilon_{offline_impact}(K, \pi) \cdot \\
&\quad \epsilon_{offline_mass_cuts}(K\pi \& eK\pi)
\end{aligned} \tag{6.6}$$

where the partial efficiencies are analogous to the ones involved in the $B_d^0 \to K^{*0}\gamma$, $K^{*0} \to K^+\pi^-$ channel. It is apparent from the previous section that the penguin and $\bar{B} \to e^- D^0 X$, $D^0 \to K^-\pi^+$ candidates were selected in a fashion as similar as possible. Keep in mind though, that identical requirements do not guarantee identical efficiencies; e.g., different energy photons have different chances to meet the same E_{HAD}/E_{EM} requirement. Nevertheless, according to Eq. 6.5 only the relative efficiencies between the penguin and $\bar{B} \to e^- D^0 X$, $D^0 \to K^-\pi^+$ processes are important. Furthermore, one big advantage of the ratio of branching fractions method is that the uncertainty due to systematic effects could be substantial for each of the (penguin or $\bar{B} \to e^- D^0 X$) branching fractions, but it will be minimized in the ratio of these branching fractions, provided that both branching fractions are affected by this systematic effect. In the following paragraphs we discuss the way we determine the partial efficiencies and the uncertainties on the ratio of efficiencies due to various

systematic effects.

$\epsilon_{kinematics\&topology}(\gamma K\pi)$ and $\epsilon_{kinematics\&topology}(eK\pi)$ involve the requirements on the momenta and directions of the decay products. We rely on Monte Carlo to estimate the ratio of these efficiencies, since it models adequately these aspects of the events.

The possible discrepancy of the $p_T(B)$ spectra between theoretical predictions (input to the Monte Carlo) and the actual observations is a source of systematic uncertainty on the determination of the ratio of these fractions; a steeper $p_T(B)$ spectrum in real-life would mean lower-than-predicted chances for the decay products to satisfy the kinematic requirements. The measured B production cross section at CDF leaves room for such a discrepancy with the theoretical prediction (see Fig. 1.3). Given the different multiplicity of the reference and penguin processes, we can not assume that $\frac{\epsilon_{kinematics\&topology}(eK\pi)}{\epsilon_{kinematics\&topology}(\gamma K\pi)}$ is unaffected by such a change. We thus weight the Monte Carlo $p_T(B)$ distributions by the ratio of the measured B production cross section, $\sigma(p\bar{p} \rightarrow BX)$, over the theory prediction input in the Monte Carlo. In Fig. 6.6 we see that this ratio is $2.9 - 0.078 \cdot p_T(B)$ with $p_T(B)$ in GeV/c and we thus obtain a 2% (4%) uncertainty on the ratio of the efficiencies between the $B_d^0 \rightarrow K^{*0}\gamma$ and the $\bar{B} \rightarrow e^- D^0 X$ channels in both Run 1B (Run 1C). For the ratio of efficiencies between the $B_s^0 \rightarrow \phi\gamma$ and $\bar{B} \rightarrow e^- D^0 X$ channels the discrepancy between data and theory results in a 6% (1%) uncertainty for Run 1B (Run 1C).

Determination of efficiencies from Monte Carlo was done with a sample of $\bar{B} \rightarrow e^- D^0 X$ decays that have some nominal fractions of D^0 mesons originating from higher-spin D meson states. The uncertainty on these fractions is another source of systematic uncertainty to be considered. Depending on how far down the decay chain of the B meson the D^0 appears, the kinematics of the resulting kaon and pion are different and thus the efficiency for reconstructing the $\bar{B} \rightarrow e^- D^0 X$, $D^0 \rightarrow K^-\pi^+$ decay is different. We vary the fraction of D mesons coming from D^{**} and $(Dn\pi)_{nr}$ mesons (f^{**}), coming from D^* mesons (f^*) and coming directly from the B meson (f) from

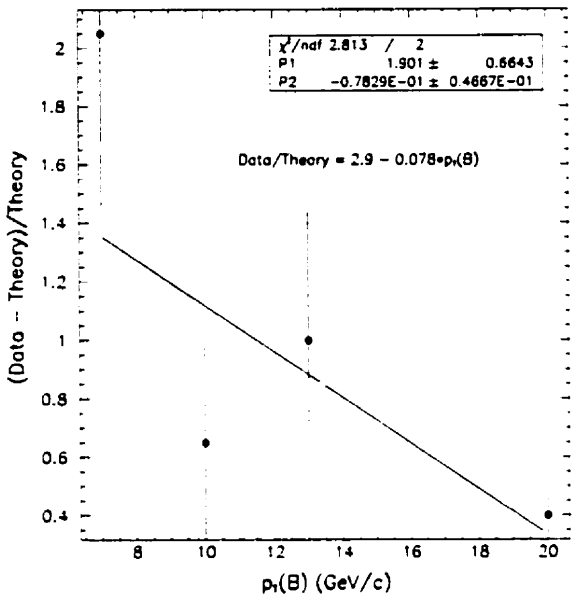

Figure 6.6: *Ratio of Data measurement vs. Monte Carlo prediction for the cross section* $\sigma(p\bar{p} \rightarrow BX)$ *according to Fig. 1.3.*

the nominal values of [4]

$(f^{**} = 0.35, f^{*} = 0.53, f = 0.12)$, to the sets:

$(f^{**} = 0.24, f^{*} = 0.62, f = 0.14)$ and

$(f^{**} = 0.47, f^{*} = 0.43, f = 0.10)$

We observe a 12% (11%) change in the ratio of efficiencies between the reference and penguin channels in Run 1B (Run 1C) which we take to be this contribution to the systematic uncertainty on the ratio of branching fractions. The relative contributions of D^{**} and $(Dn\pi)_{nr}$ states to the fraction f^{**} have been varied from the nominal 50 : 50 ratio [4] to 40 : 60 and 60 : 40. This variation contributes 1% to the aforementioned 12% and 11% uncertainties.

$\epsilon_{trigger\_CEM}(\gamma)$ and $\epsilon_{trigger\_CEM}(e)$ correspond to the requirements on the CEM cluster of the penguin photons and the ECLB electrons. We mentioned earlier that we require off-line that both the electron and the photon have passed the same cluster finding algorithm, that in Run 1B (Run 1C) the energy at the trigger level

be above 10 (8) GeV for both and that we apply the same quality criteria on the CEM clusters. Nevertheless there are differences in the E_T spectra of the photon and electron clusters, and we assign an uncertainty due to this difference, by weighting the E_T(EM cluster) distributions (see Fig. 6.2 and 6.3) with $1 + (20 - E_T)/10$ and $1 - (20 - E_T)/20$, for $10 < E_T < 20$ GeV in the Run 1B case, where E_T is given in GeV in these equations. For the Run 1C case we weight the E_T(EM cluster) distributions by $1 + (18 - E_T)/10$ and $1 - (18 - E_T)/20$ for $8 < E_T < 18$ GeV. For $E_T > 20$ (18) GeV the Run 1B (Run 1C) efficiency reaches a plateau (see Fig. 4.7) and we expect $\frac{\epsilon_{trigger\_CEM(e)}}{\epsilon_{trigger\_CEM(\gamma)}}$ to be constant. The weighting described here allows for the efficiency to vary by a factor of two (higher or lower than what is predicted by the standard simulation) for the lowest 10 GeV in the E_T(EM cluster) distributions, while no weighting is applied above that energy.

We thus estimate a systematic uncertainty of 7% (8%) on the ratio of the efficiencies $\frac{\epsilon_{trigger\_CEM(e)}}{\epsilon_{trigger\_CEM(\gamma)}}$ for the $B_d^0 \to K^{*0}\gamma$ channel in Run 1B (Run 1C). For the $B_s^0 \to \phi\gamma$ channel we obtain 8% (9%) uncertainty in Run 1B (Run 1C).

$\epsilon_{trigger\_XCES}(e)$ and $\epsilon_{trigger\_XCES}(\gamma)$ indicate the chances of ECLB electrons and penguin photons satisfying the XCES trigger requirement. The efficiency of this requirement is applied as a correction factor to the final sample of simulated events. Using the parameterization shown in Fig. 3.5 to the final Monte Carlo samples we estimate that the Run 1B XCES efficiencies are $(94.7 \pm 1.2)\%$ for the $B_d^0 \to K^{*0}\gamma$ channel, $(94.8 \pm 1.2)\%$ for the $B_s^0 \to \phi\gamma$ channel and $(94.0 \pm 1.4)\%$ for the $\bar{B} \to e^- D^0 X$ channel in Run 1B. In the Run 1C the efficiencies were $(96.7 \pm 1.4)\%$, $(96.7 \pm 1.4)\%$ and $(96.4 \pm 1.6)\%$ respectively. Therefore there is a 2% uncertainty on the ratio $\frac{\epsilon_{trigger\_XCES(e)}}{\epsilon_{trigger\_XCES(\gamma)}}$.

$\epsilon_{matching\_CEM\_track}$ indicates how often we find the electron track and match it with the electron-induced CEM cluster. We estimate this efficiency correction from the Monte Carlo electrons, presumably without taking all possible inefficiencies into account. This way we infer a greater $\mathcal{B}(B_d^0 \to K^{*0}\gamma)$ than what we should by

using the true $\epsilon_{matching\_CEM\_track}$, and we'll be arriving at a less constraining (i.e. more conservative) upper limit for this branching fraction. Therefore we accept the prediction of the Monte Carlo as adequate.

$\epsilon_{CFT}(e)$ and $\epsilon_{CFT}(K,\pi)$ are the efficiencies of the trigger requirements that the ECLB electron and the two penguin tracks are found by the CFT. These efficiencies are estimated with the use of the parameterizations shown in Fig. 3.6. For the CFT bin 4 requirement (electron case) there is an uncertainty on the efficiency of 1%. The uncertainty on the parameterizations of the CFT bin 0 requirements is 1.2% in Run 1B and 1.6% in Run 1C. Considering the CFT requirements on the two penguin tracks to be 100% correlated (due to the proximity of the tracks and the small but existing $|\eta|$ dependence of this efficiency), we assign a 3% systematic uncertainty due to the uncertainty on the CFT bin 0 and bin 4 efficiencies.

$\epsilon_{offline\_CEM}(e)$ and $\epsilon_{offline\_CEM}(\gamma)$ are the efficiencies of the quality requirements on the ECLB electrons and the penguin photons imposed off-line (E_{HAD}/E_{EM}, L_{SHR} and CES χ^2's). These requirements are identical for both channels and they should have very similar efficiencies once the E_T spectra of the CEM clusters match each other and the electrons and photons are embedded in similar environments. The different cuts on the kaon and the pion for the two channels that are used in this analysis have brought the E_T(EM cluster) distributions to an agreement within 1 GeV, but there are systematic differences. Hence we use the efficiency as it is predicted by Monte Carlo for these cuts, whereas the mismatch of the E_T(EM cluster) has already been considered as a source of systematic uncertainty in the trigger efficiency $\epsilon_{trigger\_CEM}(\gamma \text{ or } e)$ above.

$\epsilon_{offline\_tracking}(e,K,\pi)$ and $\epsilon_{offline\_tracking}(K,\pi)$ are the efficiencies to reconstruct the indicated charged products in the reference and the penguin channels. Recall that the track reconstruction efficiency is found to be constant for $p_T > 400$ MeV/c and equal to (92.8 ● 2.6)% [53]. Since we have three tracks in the $\bar{B} \to e^- D^0 X$, $D^0 \to K^-\pi^+$ channel compared to two in the penguin channels, all with $p_T > 400$

GeV/c and embedded in very similar environments around the parent B mesons, we expect $\frac{\epsilon_{offline\_tracking}(e,K,\pi)}{\epsilon_{offline\_tracking}(K,\pi)} = (92.8 \pm 2.6)\%$. As it has been mentioned before, we rely on the Monte Carlo to account for the SVX-related requirements. Residual effects present in the data cancel in the ratio of efficiencies.

$\epsilon_{offline\_track\_vertexing}(K,\pi)$ is the efficiency to reconstruct the two tracks as originating from a common secondary vertex, presumably the decay point of a D^0 or a K^{*0} meson. Given the similarities of the environments between the reference and the penguin channels and the similarities in the selection criteria imposed on the tracks, the efficiencies $\epsilon_{vertex}(K,\pi)$ should be equal and thus cancel in the ratio. We use the Monte Carlo prediction for this ratio in order to take into account any residual inequalities, but it turns out be equal to 1.0 nevertheless.

$\epsilon_{offline\_impact}(K,\pi)$ is the efficiency of the requirement that both the kaon and the pion be displaced from the primary $p\bar{p}$ vertex (impact parameter significance requirement). In Fig. 6.1 we see that the Monte Carlo predicts the distribution of the impact parameter significance for the D^0 products of $\bar{B} \to e^- D^0 X$, $D^0 \to K^-\pi^+$ decays. Consequently we rely on Monte Carlo to estimate the efficiency $\epsilon_{offline\_impact}(K,\pi)$ for the reference and the penguin channels.

$\epsilon_{offline\_ct}(eK\pi)$ and $\epsilon_{offline\_ct}(\gamma K\pi)$ are the efficiencies of the $0 < ct < 0.3$ cm requirement on the $\bar{B} \to e^- D^0 X$, $D^0 \to K^-\pi^+$ and penguin candidates respectively. We rely on Monte Carlo to estimate these efficiencies, since it is shown to reproduce features of the B decays related to their long lifetime.

The uncertainty on the lifetime of the various B meson species introduces an uncertainty on the effect of the ct and the minimum impact parameter significance requirements. By generating Monte Carlo samples with B lifetimes $\pm 1\sigma$ from the nominal values [4], we estimate the uncertainty on the ratio of branching fractions to be 4% for the $B_d^0 \to K^{*0}\gamma$ case and 6% for the $B_s^0 \to \phi\gamma$ case, in both Run 1B and Run 1C.

$\epsilon_{trigger\_environment}(\gamma)$, $\epsilon_{offline\_environment}(\gamma K\pi)$ and $\epsilon_{offline\_environment}(eK\pi)$ are the

efficiencies of (i) the trigger requirement that there be no CFT track pointing to the wedge of the photon ("L2 isolation"), and (ii) the requirement that the B system carry more than 70% of the total p_T in an $\eta - \phi$ cone of $R = 1.0$ around it ("B isolation"). For the $\bar{B} \to e^- D^0 X$, $D^0 \to K^- \pi^+$ case the efficiency $\epsilon_{offline\_environment}(eK\pi)$ includes both requirements, since neither was applied at the trigger level. Identical requirements were imposed on both processes. The p_T distributions of the parent B mesons are very similar (see Fig. 6.2 and 6.3) and this results in very similar environments around the two B mesons. We then expect the "environmental" efficiencies to be equal between the reference and the penguin processes and thus cancel in the ratio. As discussed in Section 6.1 we expect some differences between the penguin and $\bar{B} \to e^- D^0 X$, $D^0 \to K^- \pi^+$ channels. We correct for such effects with the use of $p\bar{p} \to b\bar{b}$ Monte Carlo events generated with PYTHIA [54] and fed through the detector and trigger simulations. The ratio of the L2 and B isolation efficiencies between the penguin and reference channels is then found to be (0.961 ± 0.021) and (0.940 ± 0.022) for the $B_d^0 \to K^{*0}\gamma$ and $B_s^0 \to \phi\gamma$ cases respectively. Consequently we have a 2% uncertainty on this ratio, which is accounted towards the total systematic uncertainty of the branching fraction measurement.

The $B_s^0 \to \phi\gamma$ channel is treated in the same manner as the $B_d^0 \to K^{*0}\gamma$ above, but the production cross section for B_s^0 mesons is not the same as for B_d^0 mesons; for the same $p_T(B)$ the ratio of the production cross sections is the ratio of the fragmentation probabilities for (i) a b quark to combine with an s quark and form a B_s^0 meson and (ii) a b quark to combine with a d quark to form a B_d^0 meson. This ratio is often taken to be 1/3 in the literature, which is in agreement with measured values. CDF has measured $\frac{f_s}{f_d} = 0.34 \pm 0.10 \pm 0.03$ [19] and, more recently, $\frac{f_s}{f_d} = 0.427 \pm 0.072$ [20]. The Particle Data Group quotes $\frac{f_s}{f_d} = 0.264 \pm 0.048$ [4], a value derived from the LEP experiments at CERN. The uncertainty on this ratio is a source of systematic uncertainty on the ratio of branching fractions for the $B_s^0 \to \phi\gamma$ case, but it is not mentioned in Table 6.2, were the rest of the uncertainties due to

various systematic effects are summarized.

From the information in Tables 6.1 and 6.4 and the relative off-line tracking and environment (L2 and B isolation) efficiencies, we obtain the relative efficiencies for the $\bar{B} \to e^- D^0 X$, $D^0 \to K^- \pi^+$ and the penguin channels given in Table 6.3. The dagger in this table refers to the following discussion. The Particle Data Group [4] quotes $\mathcal{B}(D^0 \to K^- \pi^+) = (3.85 \pm 0.09)\%$ and $\mathcal{B}(\bar{B} \to e^- X) = 0.1045 \pm 0.0021$. They also quote a measurement of $\frac{\mathcal{B}(\bar{B} \to e^- D^0 X)}{\mathcal{B}(\bar{B} \to e^- X)} = 0.67 \pm 0.09 \pm 0.10$ [63] and they consequently suggest $\mathcal{B}(\bar{B} \to e^- D^0 X) = (0.67 \pm 0.09 \pm 0.10) \times (0.1045 \pm 0.0021) = (7.0 \pm 1.4)\%$. They point out though that Ref. [63] used $\mathcal{B}(D^0 \to K^- \pi^+) = (4.2 \pm 0.4 \pm 0.4)\%$, which is now out-of-date. The second uncertainty on the $\frac{\mathcal{B}(\bar{B} \to e^- D^0 X)}{\mathcal{B}(\bar{B} \to e^- X)}$ measurement was due to the uncertainty on the D^0 branching fraction. As seen in Ref. [63] (Eq. 1 and Table I), the actual measurement was $\frac{\mathcal{B}(\bar{B} \to e^- D^0 X)}{\mathcal{B}(\bar{B} \to e^- X)} \times \mathcal{B}(D^0 \to K^- \pi^+) = (0.67 \pm 0.09) \times 0.042$. We use this result to obtain:

$$\mathcal{B}(\bar{B} \to e^- D^0 X) \times \mathcal{B}(D^0 \to K^- \pi^+) = \tag{6.7}$$
$$(0.67 \pm 0.09) \times 0.042 \times (0.1045 \pm 0.0021) = (294 \pm 40) \times 10^{-5}$$

6.5 Test of Monte Carlo predictions

In order to test the use of Monte Carlo for the determination of part of the efficiencies and to strengthen the case for forming ratios of branching fractions, we compare the number of $\bar{B} \to e^- D^0 X$, $D^0 \to K^- \pi^+$ events observed in the data with a prediction based on Monte Carlo $\bar{B} \to e^- D^0 X$, $D^0 \to K^- \pi^+$ events.

We generate, decay and feed through the detector and trigger simulation B_d^0, $\bar{B}_d^0$, B_u^0 and $\bar{B}_u^0$ mesons following the steps described in Chapter 3. We generated and simulated $B \to eD^0\nu$, $B \to eD^*\nu, D^* \to D^0 X$, $B \to eD^{**}\nu, D^{**} \to D^0 X$, and $B \to e(Dn\pi)_{nr}\nu, (Dn\pi)_{nr} \to D^0 X$ decays. In all cases the parent B mesons have $p_T > 12$ (> 6) GeV/c and $|y| < 1.25$ in order to avoid simulating events that have no chance of meeting the Run 1B (Run 1C) selection criteria.

	$B_d^0 \to K^{*0}\gamma$		$B_s^0 \to \phi\gamma$	
	Run 1B	Run 1C	Run 1B	Run 1C
Source of systematic uncertainty	Effect on the ratio of B's			
1) Parameterization of CFT efficiency	3%			
2) Parameterization of XCES efficiency	2%			
3) Track reconstruction efficiency	3%			
4) Differences in L2 and B isolation efficiencies	2%			
5) Differences in $E_T(e)/E_T(\gamma)$ distributions	7%	8%	8%	9%
6) Difference on $p_T(B)$ between theory and data	2%	4%	6%	1%
7) Monte Carlo statistics	2%	3%	2%	3%
8) $N_{observed}(eD^0X)$ statistics	19%	23%	19%	23%
9) Uncertainty on B lifetimes	4%		6%	
10) Fraction of D^0 mesons from other D states	12%	11%	12%	11%
11) $\mathcal{B}(\bar{B} \to e^- D^0 X) \times \mathcal{B}(D^0 \to K^-\pi^+)$	14%			
12) $\mathcal{B}(\phi \to K^+K^-)$			2%	
Total systematic uncertainty	28%	31%	30%	31%
(CDF: 1 – 8)	21%	25%	22%	25%
(external: 9 – 12)	19%	18%	20%	19%

Table 6.2: *Systematic uncertainties on the ratio of branching fractions between the penguin channels and the reference $\bar{B} \to e^- D^0 X$ channel in Run 1B and Run 1C.*

	$B_d^0 \to K^{*0}\gamma$		$B_s^0 \to \phi\gamma$	
	Run 1B	Run 1C	Run 1B	Run 1C
$\frac{\int Ldt(eX)}{\int Ldt(peng)}$	16.2/22.3	4.2/6.6	16.2/22.3	4.2/6.6
$N_{observed}(eD^0X)$ (events)	57.0 ± 10.8	31.8 ± 7.3	57.0 ± 10.8	31.8 ± 7.3
$\mathcal{B}(D^0 \to K^-\pi^+)$	$(3.85 \pm 0.09)\%$			
$\mathcal{B}(\bar{B} \to e^- D^0 X) \times \mathcal{B}(D^0 \to K^-\pi^+)$	$(294 \pm 40) \times 10^{-5}$ (†)			
$\mathcal{B}(K^{*0} \to K^+\pi^-)$	2/3			
$\mathcal{B}(\phi \to K^+K^-)$			0.491 ± 0.008	
$\frac{f_s}{f_d}$			1/3	
$\frac{\epsilon_{total}(eD^0X)}{\epsilon_{total}(penguin)}$	0.460	0.613	0.347	0.492
(CDF uncertainties: $1-7$)	± 0.042	± 0.066	± 0.040	± 0.053
(external uncertainties: $9, 10$)	± 0.058	± 0.072	± 0.046	± 0.062

Table 6.3: *Ingredients for the calculation of the branching fraction limits for the* $B_d^0 \to K^{*0}\gamma$ *and* $B_s^0 \to \phi\gamma$ *decays in the Run 1B and Run 1C samples. The uncertainties on the ratio of efficiencies are numbered according to the entries in Table 6.2. The dagger on the* $\mathcal{B}(\bar{B} \to e^- D^0 X) \times \mathcal{B}(D^0 \to K^-\pi^+)$ *value refers to the discussion at the end of Section 6.4.*

We take into account the differences in the branching fractions and selection efficiencies between these four distinct decay channels and we weight the Monte Carlo samples properly to get two representative samples of $\bar{B} \to e^- D^0 X$, $D^0 \to K^-\pi^+$ decays; one for Run 1B and one for Run 1C. For the efficiency of the XCES and CFT requirements on the electron, we use the parameterizations shown in Figures 3.5 and 3.6, for the track reconstruction efficiency we use [53] $(88.1 \pm 4.3)\% \times (92.8 \pm 2.6)\% = (81.8 \pm 4.6)\%$, whereas for the rest of the requirements we rely on the simulation as it was discussed in the previous sections. We do not apply the "environmental" requirements on the B isolation, off-line, and the CEM cluster isolation

	$\bar{B} \to e^- D^0 X$, $D^0 \to K^- \pi^+$	
	Run 1B	Run 1C
Efficiencies (in %)		
Trigger and off-line (partial)	0.256 ± 0.030	0.082 ± 0.009
XCES	94.0 ± 1.4	96.4 ± 1.6
Track reconstruction	81.8 ± 4.6	
Total efficiency (%)	0.197 ± 0.026	0.065 ± 0.008
$\int Ldt$ (pb^{-1})	16.2 ± 0.7	4.2 ± 0.2
$4 \cdot \sigma(p\bar{p} \to BX)$ (μb)	1.244 ± 0.288	11.632 ± 2.644
$\mathcal{B}(\bar{B} \to e^- D^0 X) \times \mathcal{B}(D^0 \to K^- \pi^+)$	$(294 \pm 40) \times 10^{-5}$	
Signal events after all cuts:		
Predicted by Monte Carlo	117 ± 35	93 ± 28
Observed in data	94 ± 17	41 ± 11

Table 6.4: *Predicted and observed number of $\bar{B} \to e^- D^0 X$, $D^0 \to K^- \pi^+$ events for the same data-taking period as the penguin data.*

from CFT tracks ("L2 isolation"), at the trigger level, because we base the Monte Carlo prediction on simulated events of single B decays only.

We expect 117 ± 35 $\bar{B} \to e^- D^0 X$, $D^0 \to K^- \pi^+$ events in the 16.2 ± 0.7 pb^{-1} of electron data that were collected in the same time period as the penguin data (see Table 6.4). This is consistent with the 94 ± 17 events seen in the data (see Fig. 4.8). For the entire Run 1B electron data set (74.2 ± 3.1 pb^{-1}) we expect 535 ± 162 $\bar{B} \to e^- D^0 X$, $D^0 \to K^- \pi^+$ events and we observe 507 ± 34. In Run 1C we expect 93 ± 28 $\bar{B} \to e^- D^0 X$, $D^0 \to K^- \pi^+$ events and we observe 41 ± 11 (see Fig. 4.8), a difference of 1.7 standard deviations from zero.

Along with possible non-accounted efficiencies, this discrepancy could also be due

to a difference in the shape of the B production cross section between theory (input to Monte Carlo) and data (see Fig. 1.3 and 6.6). Indeed, if in reality the B production cross section falls more rapidly with $p_T(B)$ than theory predicts, the B mesons in Monte Carlo are generated with higher momentum, on average. Consequently, the Monte Carlo prediction for the total selection efficiency is an overestimate, since the more energetic a B meson is, the higher its chances to satisfy the selection requirements are (for example, see the efficiency of the trigger requirements for $B_d^0 \to K^{*0}\gamma$ events, as a function of $p_T(B)$ in Fig. 4.7). This effect would be more apparent in Run 1C, were the lower energy threshold on the electron allows the reconstruction of lower energy B mesons.

We therefore argue that while the use of Monte Carlo for the determination of some of the efficiencies is justified to some extent (see examples in this dissertation where the Monte Carlo distributions describe the data quite well), it underestimates the number of $\bar{B} \to e^- D^0 X$, $D^0 \to K^-\pi^+$ events expected in the data, a possible hint that it does not account for some of the inefficiencies present in data. Nevertheless, in the ratio of branching fractions between $\bar{B} \to e^- D^0 X$, $D^0 \to K^-\pi^+$ and penguin decays reconstructed in the same data taking periods, many inefficiencies are common to both channels. Consequently, the Monte Carlo prediction of the ratio of efficiencies is expected to be robust. Furthermore, the B production cross section cancels in the ratio of branching fractions and thus discrepancies between theory and data have a second order effect (see Table 6.2).

Chapter 7

Branching Fraction Upper Limits

In the previous chapter we discussed the way we would infer the penguin branching fraction given a sample of selected penguin decays. We argued that the use of a similar "reference" decay could be used to get a more robust estimate of the penguin selection efficiencies. We then stated that when one forms the ratios of branching fractions between the penguin and $\bar{B} \to e^- D^0 X$, $D^0 \to K^- \pi^+$ channels, he minimizes uncertainties associated with the B meson production cross section and other common (in)efficiencies and systematic effects.

In this chapter we present the calculations of the penguin branching fractions as a function of the number of signal events in the data sample. The lack of signal in the penguin channels (see Fig. 5.15) dictates the extraction of upper limits for the penguin branching fractions.

7.1 Separate treatment of Run 1B and Run 1C data

Following the discussion in Section 6.2, we express the ratios of branching fractions between the penguin and $\bar{B} \to e^- D^0 X$, $D^0 \to K^- \pi^+$ channels as:

$$\frac{\mathcal{B}(B_d^0 \to K^{*0}\gamma)}{\mathcal{B}(\bar{B} \to e^- D^0 X)} = \tag{7.1}$$
$$= 2 \cdot \frac{N(K^{*0}\gamma)}{N(eD^0X)} \cdot \frac{\int Ldt(eX)}{\int Ldt(peng)} \cdot \frac{\mathcal{B}(D^0 \to K^-\pi^+)}{\mathcal{B}(K^{*0} \to K^+\pi^-)} \cdot \frac{\epsilon_{total}(eD^0X)}{\epsilon_{total}(K^{*0}\gamma)}$$

and

$$\frac{\mathcal{B}(B_s^0 \to \phi\gamma)}{\mathcal{B}(\bar{B} \to e^- D^0 X)} = \tag{7.2}$$
$$= 2 \cdot \frac{f_d}{f_s} \cdot \frac{N(\phi\gamma)}{N(eD^0X)} \cdot \frac{\int Ldt(eX)}{\int Ldt(peng)} \cdot \frac{\mathcal{B}(D^0 \to K^-\pi^+)}{\mathcal{B}(\phi \to K^+K^-)} \cdot \frac{\epsilon_{total}(eD^0X)}{\epsilon_{total}(\phi\gamma)}$$

where $\int Ldt$ are the integrated luminosities of the inclusive electron, "eX", and the penguin, "*peng*", data samples; ϵ_{total} are the total efficiencies for retaining the $\bar{B} \to e^- D^0 X$, $D^0 \to K^-\pi^+$ (eD^0X) and the penguin ($K^{*0}\gamma$ and $\phi\gamma$) events which resulted from the $p\bar{p}$ collisions; the factor of two accounts for $\bar{B} \to e^- D^0 X$ events produced by B_d^0, $\bar{B}_d^0$, B_u^+ and B_u^- mesons, whereas the penguin decays come from B_d^0 and $\bar{B}_d^0$ ($K^{*0}\gamma$) or B_s^0 and $\bar{B}_s^0$ ($\phi\gamma$) only; N refers to the number of candidate events satisfying all selection criteria; $\mathcal{B}$ denotes the various branching fractions, which are taken from Ref. [4], unless stated otherwise; and f_s and f_d are the fractions of the time a b quark combines with an s or a d quark to create a B_s or a B_d meson respectively. The cross sections for producing B_d^0 and B_u^+ mesons are taken to be equal, i.e. $f_d = f_u$ [4].

Using the equations above, taking the numerical values of the various ingredients from Table 6.3 and assigning the uncertainties shown in Table 6.2, we calculate the "relative" branching fractions between the penguin and $\bar{B} \to e^- D^0 X$ channels, e.g., $\frac{\mathcal{B}(B_d^0 \to K^{*0}\gamma)}{\mathcal{B}(\bar{B} \to e^- D^0 X)}$, by using $\mathcal{B}(D^0 \to K^-\pi^+) = (3.85 \pm 0.09)\%$ [4]. We also form the "absolute" penguin branching fractions, e.g., $\mathcal{B}(B_d^0 \to K^{*0}\gamma)$, by using $\mathcal{B}(\bar{B} \to e^- D^0 X) \times \mathcal{B}(D^0 \to K^-\pi^+) = (294 \pm 40) \times 10^{-5}$ (see Section 6.4). For $\frac{f_s}{f_d} = \frac{1}{3}$ we obtain:

Run 1B, $\frac{f_s}{f_d} = \frac{1}{3}$

$$\frac{\mathcal{B}(B_d^0 \to K^{*0}\gamma)}{\mathcal{B}(\bar{B} \to e^- D^0 X)} = N(K^{*0}\gamma) \times (6.67 \pm 1.69) \times 10^{-4}$$

$$\mathcal{B}(B_d^0 \to K^{*0}\gamma) = N(K^{*0}\gamma) \times (5.17 \pm 1.45) \times 10^{-5}$$

$$\frac{\mathcal{B}(B_s^0 \to \phi\gamma)}{\mathcal{B}(\bar{B} \to e^- D^0 X)} = N(\phi\gamma) \times (2.08 \pm 0.54) \times 10^{-3}$$

$$\mathcal{B}(B_s^0 \to \phi\gamma) = N(\phi\gamma) \times (1.59 \pm 0.48) \times 10^{-4} \quad (7.3)$$

Run 1C, $\frac{f_s}{f_d} = \frac{1}{3}$

$$\frac{\mathcal{B}(B_d^0 \to K^{*0}\gamma)}{\mathcal{B}(\bar{B} \to e^- D^0 X)} = N(K^{*0}\gamma) \times (1.42 \pm 0.40) \times 10^{-3}$$

$$\mathcal{B}(B_d^0 \to K^{*0}\gamma) = N(K^{*0}\gamma) \times (1.08 \pm 0.34) \times 10^{-4}$$

$$\frac{\mathcal{B}(B_s^0 \to \phi\gamma)}{\mathcal{B}(\bar{B} \to e^- D^0 X)} = N(\phi\gamma) \times (4.63 \pm 1.30) \times 10^{-3}$$

$$\mathcal{B}(B_s^0 \to \phi\gamma) = N(\phi\gamma) \times (3.54 \pm 1.10) \times 10^{-4} \quad (7.4)$$

In Tables 7.1 - 7.4 we show the "relative" and "absolute" penguin branching fractions. In the B_s case we present the calculations for three different $\frac{f_s}{f_d}$ values. The value of 1/3 is the favorite theoretical assumption in the literature. The Particle Data Group quotes $\frac{f_s}{f_d} = 0.264 \pm 0.048$ [4] and CDF reports $\frac{f_s}{f_d} = 0.427 \pm 0.072$ [20]. These latter values introduce an extra uncertainty of 18% or 17% respectively.

Since we do not have enough events in the signal region, we set upper limits for the penguin branching fractions. For the $B_d^0 \to K^{*0}\gamma$ channel in Run 1C, we set a

conservative limit by assuming that the observed event is due to signal only. We calculate the upper limit on the mean number of penguin events at a confidence level, C.L., including the total systematic uncertainty, σ, by solving the following equation numerically:

$$1 - \text{C.L.} = \sum_{n=0}^{N_{observed}} \int_0^\infty P(n;x)G(x;\mu,\sigma)dx \tag{7.5}$$

where $N_{observed}$ is the number of observed signal events; $P(n;x)$ is the Poisson probability of observing n events with mean x, and $G(x;\mu,\sigma)$ is the Gaussian probability to observe x events when the mean is μ and the standard deviation is σ. We evaluate the right hand side of this equation for each μ in increments of 0.001, starting with $\mu = 0$ events. The upper limit on the mean is the smallest μ value for which the right hand side becomes equal to, or just smaller than, the left hand side. Should the true mean be larger, the probability of observing $N_{observed}$ events or less, would have been smaller than 1 − C.L.. Following these steps we reproduce the results in Ref. [31] and [64] [1]. In the place of $N(K^{*0}\gamma)$ and $N(\phi\gamma)$ in Eq. 7.3 and 7.4, we use the calculated upper limits on the mean to obtain upper limits on the penguin branching fractions.

The resulting limits on the ratio of branching fractions between the penguin and $\bar{B} \to e^- D^0 X$ channels are tabulated in Tables 7.1 - 7.4. Limits on the absolute penguin branching fractions are also shown in these tables.

7.2 Results for combined Run 1B and Run 1C data

Using Eq. 7.2 we can write for the total number of $B_d^0 \to K^{*0}\gamma$, $K^{*0} \to K^+\pi^-$ events expected to be selected during the course of both the Run 1B and Run 1C data-taking

[1] In the latest Review of Particle Physics [4] we are presented with confidence intervals only, not upper limits.

periods:

$$N^{1B}(K^{*0}\gamma) + N^{1C}(K^{*0}\gamma) = \mathcal{B}(B^0_d \to K^{*0}\gamma) \cdot \left[N^{1B}(eD^0X) \cdot \epsilon^{1B}_{rel} + N^{1C}(eD^0X) \cdot \epsilon^{1C}_{rel} \right] \tag{7.6}$$

and we then can write for the branching fraction of the $B^0_d \to K^{*0}\gamma$ channel, and in a similar fashion for the $B^0_s \to \phi\gamma$, $\phi \to K^+K^-$ channel:

$$\mathcal{B}(B^0_d \to K^{*0}\gamma) = N^{1B+1C}(K^{*0}\gamma) \cdot \frac{1}{N^{1B}(eD^0X) \cdot \epsilon^{1B}_{rel} + N^{1C}(eD^0X) \cdot \epsilon^{1C}_{rel}} \tag{7.7}$$

where the factors ϵ_{rel} absorb the relative efficiencies, integrated luminosities and other factors in Eq. 7.2, except the number of observed candidate $\bar{B} \to e^- D^0 X$, $D^0 \to K^-\pi^+$ events. The superscripts 1B and 1C refer to Run 1B and Run 1C data taking periods, while 1B+1C refers to the entire data taking period (both Run 1B and Run 1C). When we form ratios of branching fractions between the penguins and $\bar{B} \to e^- D^0 X$ channels, we leave $\mathcal{B}(\bar{B} \to e^- D^0 X)$ out of ϵ_{rel}. In any case the numerical values of $N^{1B}(eD^0X)\cdot\epsilon^{1B}_{rel}$ and $N^{1C}(eD^0X)\cdot\epsilon^{1C}_{rel}$ are given in Tables 7.1 - 7.4. Note that the uncertainties on these two products are not uncorrelated; uncertainties $9-12$ in Table 6.2 are 100% correlated[2], while the rest are dominated by the statistics of the $\bar{B} \to e^- D^0 X$, $D^0 \to K^-\pi^+$ events and are taken to be uncorrelated.

For example, from Eq. 7.3 and 7.4 we obtain $N^{1B}(eD^0X) \cdot \epsilon^{1B}_{rel} = \frac{10^5}{5.17 \pm 1.09 \pm 0.98}$ and $N^{1C}(eD^0X) \cdot \epsilon^{1C}_{rel} = \frac{10^5}{10.82 \pm 2.71 \pm 1.95}$, where the first uncertainties are uncorrelated and the second are correlated[3]. Therefore, $N^{1B}(eD^0X) \cdot \epsilon^{1B}_{rel} + N^{1C}(eD^0X) \cdot \epsilon^{1C}_{rel} = 28585 \pm 7077$ and Eq. 7.7 yields:

$$\mathcal{B}(B^0_d \to K^{*0}\gamma) = N^{1B+1C}(K^{*0}\gamma) \times (3.50 \pm 0.87) \times 10^{-5} \tag{7.8}$$

[2]The uncertainty on $\frac{f_d}{f_s}$ is also common to both data sets.

[3]From Table 6.2 the uncorrelated uncertainty is 21% (25%) and the correlated is 19% (18%) for the $B^0_d \to K^{*0}\gamma$ channel in Run 1B (Run 1C).

With one event observed in the entire data sample and 25% uncertainty (0.87/3.50), the upper limit on the mean number of penguin events is 4.30 (5.45) at 90% (95%) confidence level. This result yields an upper limit on the branching fraction $\mathcal{B}(B_d^0 \to K^{*0}\gamma)$ of 1.5×10^{-4} at 90% C.L. and 1.9×10^{-4} at 95% C.L. Similarly we proceed in calculating upper limits for the $B_s^0 \to \phi\gamma$ channel. The results are shown in Tables 7.1 - 7.4.

Relative branching fraction	$B_d^0 \to K^{*0}\gamma$ vs. $\bar{B} \to e^- D^0 X$		
	Run 1B	Run 1C	Run 1B+1C
$\frac{1}{Nobserved} \times \frac{\mathcal{B}(B_d^0 \to K^{*0}\gamma)}{\mathcal{B}(\bar{B} \to e^- D^0 X)} \times 10^4$	6.77 ± 1.69	14.17 ± 3.97	4.58 ± 0.95
Total uncertainty	25%	28%	21%
$N_{observed}$ (events)	0	1	1
Upper Limits with 90% C.L.			
N_{mean} (events)	2.50	4.43	4.17
$\frac{\mathcal{B}(B_d^0 \to K^{*0}\gamma)}{\mathcal{B}(\bar{B} \to e^- D^0 X)}$	1.7×10^{-3}	6.3×10^{-3}	1.9×10^{-3}
Upper Limits with 95% C.L.			
N_{mean} (events)	3.34	5.68	5.20
$\frac{\mathcal{B}(B_d^0 \to K^{*0}\gamma)}{\mathcal{B}(\bar{B} \to e^- D^0 X)}$	2.3×10^{-3}	8.0×10^{-3}	2.4×10^{-3}

Absolute branching fraction	$B_d^0 \to K^{*0}\gamma$		
	Run 1B	Run 1C	Run 1B+1C
$\frac{1}{Nobserved} \times \mathcal{B}(B_d^0 \to K^{*0}\gamma) \times 10^5$	5.17 ± 1.45	10.82 ± 3.35	3.50 ± 0.87
Total uncertainty	28%	31%	25%
$N_{observed}$ (events)	0	1	1
Upper Limits with 90% C.L.			
N_{mean} (events)	2.56	4.57	4.30
$\mathcal{B}(B_d^0 \to K^{*0}\gamma)$	1.3×10^{-4}	4.9×10^{-4}	1.5×10^{-4}
Upper Limits with 95% C.L.			
N_{mean} (events)	3.46	5.97	5.45
$\mathcal{B}(B_d^0 \to K^{*0}\gamma)$	1.8×10^{-4}	6.5×10^{-4}	1.9×10^{-4}

Table 7.1: *Ratio of branching fractions* $\frac{\mathcal{B}(B_d^0 \to K^{*0}\gamma)}{\mathcal{B}(\bar{B} \to e^- D^0 X)}$ *and absolute branching fraction* $\mathcal{B}(B_d^0 \to K^{*0}\gamma)$.

Relative branching fraction	$B_s^0 \to \phi\gamma$ vs. $\bar{B} \to e^- D^0 X$		
$\frac{f_s}{f_d} = \frac{1}{3}$	Run 1B	Run 1C	Run 1B+1C
$\frac{1}{N_{observed}} \times \frac{\mathcal{B}(B_s^0 \to \phi\gamma)}{\mathcal{B}(\bar{B} \to e^- D^0 X)} \times 10^3$	2.08 ± 0.54	4.63 ± 1.30	1.44 ± 0.31
Total uncertainty	26%	28%	22%
$N_{observed}$ (events)	0	0	0
Upper Limits with 90% C.L.			
N_{mean} (events)	2.52	2.56	2.45
$\frac{\mathcal{B}(B_s^0 \to \phi\gamma)}{\mathcal{B}(\bar{B} \to e^- D^0 X)}$	5.2×10^{-3}	1.2×10^{-2}	3.5×10^{-3}
Upper Limits with 95% C.L.			
N_{mean} (events)	3.38	3.46	3.25
$\frac{\mathcal{B}(B_s^0 \to \phi\gamma)}{\mathcal{B}(\bar{B} \to e^- D^0 X)}$	7.0×10^{-3}	1.6×10^{-2}	4.7×10^{-3}

Absolute branching fraction	$B_s^0 \to \phi\gamma$		
$\frac{f_s}{f_d} = \frac{1}{3}$	Run 1B	Run 1C	Run 1B+1C
$\frac{1}{N_{observed}} \times \mathcal{B}(B_s^0 \to \phi\gamma) \times 10^4$	1.59 ± 0.48	3.54 ± 1.10	1.10 ± 0.29
Total uncertainty	30%	31%	26%
$N_{observed}$ (events)	0	0	0
Upper Limits with 90% C.L.			
N_{mean}	2.60	2.63	2.52
$\mathcal{B}(B_s^0 \to \phi\gamma)$	4.1×10^{-4}	9.3×10^{-4}	2.8×10^{-4}
Upper Limits with 95% C.L.			
N_{mean}	3.55	3.60	3.38
$\mathcal{B}(B_s^0 \to \phi\gamma)$	5.6×10^{-4}	1.3×10^{-3}	3.7×10^{-4}

Table 7.2: *Ratio of branching fractions* $\frac{\mathcal{B}(B_s^0 \to \phi\gamma)}{\mathcal{B}(\bar{B} \to e^- D^0 X)}$ *and absolute branching fraction* $\mathcal{B}(B_s^0 \to \phi\gamma)$ *using* $\frac{f_s}{f_d} = 1/3$.

Relative branching fraction	$B_s^0 \to \phi\gamma$ vs. $\bar{B} \to e^- D^0 X$		
$\frac{f_s}{f_d} = 0.264 \pm 0.048$	Run 1B	Run 1C	Run 1B+1C
$\frac{1}{N_{observed}} \times \frac{\mathcal{B}(B_s^0 \to \phi\gamma)}{\mathcal{B}(\bar{B} \to e^- D^0 X)} \times 10^3$	2.63 ± 0.84	5.85 ± 1.99	1.81 ± 0.51
Total uncertainty	32%	33%	28%
$N_{observed}$ (events)	0	0	0
Upper Limits with 90% C.L.			
N_{mean}	2.65	2.68	2.56
$\frac{\mathcal{B}(B_s^0 \to \phi\gamma)}{\mathcal{B}(\bar{B} \to e^- D^0 X)}$	7.0×10^{-3}	1.6×10^{-2}	4.6×10^{-3}
Upper Limits with 95% C.L.			
N_{mean}	3.65	3.71	3.46
$\frac{\mathcal{B}(B_s^0 \to \phi\gamma)}{\mathcal{B}(\bar{B} \to e^- D^0 X)}$	9.6×10^{-3}	2.2×10^{-2}	6.3×10^{-3}

Absolute branching fraction	$B_s^0 \to \phi\gamma$		
$\frac{f_s}{f_d} = 0.264 \pm 0.048$	Run 1B	Run 1C	Run 1B+1C
$\frac{1}{N_{observed}} \times \mathcal{B}(B_s^0 \to \phi\gamma) \times 10^4$	2.01 ± 0.70	4.47 ± 1.61	1.39 ± 0.44
Total uncertainty	35%	36%	32%
$N_{observed}$ (events)	0	0	0
Upper Limits with 90% C.L.			
N_{mean}	2.73	2.76	2.65
$\mathcal{B}(B_s^0 \to \phi\gamma)$	5.5×10^{-4}	1.2×10^{-3}	3.7×10^{-4}
Upper Limits with 95% C.L.			
N_{mean}	3.83	3.89	3.65
$\mathcal{B}(B_s^0 \to \phi\gamma)$	7.7×10^{-4}	1.7×10^{-4}	5.1×10^{-4}

Table 7.3: *Ratio of branching fractions* $\frac{\mathcal{B}(B_s^0 \to \phi\gamma)}{\mathcal{B}(\bar{B} \to e^- D^0 X)}$ *and absolute branching fraction* $\mathcal{B}(B_s^0 \to \phi\gamma)$ *using* $\frac{f_s}{f_d} = 0.264 \pm 0.048$ *[4].*

Relative branching fraction	$B_s^0 \to \phi\gamma$ vs. $\bar{B} \to e^- D^0 X$		
$\frac{f_s}{f_d} = \mathbf{0.427 \pm 0.072}$	Run 1B	Run 1C	Run 1B+1C
$\frac{1}{N_{observed}} \times \frac{\mathcal{B}(B_s^0 \to \phi\gamma)}{\mathcal{B}(\bar{B} \to e^- D^0 X)} \times 10^3$	1.62 ± 0.50	3.62 ± 1.19	1.12 ± 0.31
Total uncertainty	31%	33%	28%
$N_{observed}$ (events)	0	0	0
Upper Limits with 90% C.L.			
N_{mean} (events)	2.63	2.68	2.56
$\frac{\mathcal{B}(B_s^0 \to \phi\gamma)}{\mathcal{B}(\bar{B} \to e^- D^0 X)}$	4.3×10^{-3}	9.7×10^{-3}	2.9×10^{-3}
Upper Limits with 95% C.L.			
N_{mean} (events)	3.60	3.71	3.46
$\frac{\mathcal{B}(B_s^0 \to \phi\gamma)}{\mathcal{B}(\bar{B} \to e^- D^0 X)}$	5.8×10^{-3}	1.3×10^{-2}	3.9×10^{-3}

Absolute branching fraction	$B_s^0 \to \phi\gamma$		
$\frac{f_s}{f_d} = \mathbf{0.427 \pm 0.072}$	Run 1B	Run 1C	Run 1B+1C
$\frac{1}{N_{observed}} \times \mathcal{B}(B_s^0 \to \phi\gamma) \times 10^4$	1.24 ± 0.42	2.76 ± 0.99	0.86 ± 0.27
Total uncertainty	34%	36%	31%
$N_{observed}$ (events)	0	0	0
Upper Limits with 90% C.L.			
N_{mean}	2.70	2.76	2.63
$\mathcal{B}(B_s^0 \to \phi\gamma)$	3.3×10^{-4}	7.6×10^{-4}	2.3×10^{-4}
Upper Limits with 95% C.L.			
N_{mean}	3.77	3.89	3.60
$\mathcal{B}(B_s^0 \to \phi\gamma)$	4.7×10^{-4}	1.1×10^{-3}	3.1×10^{-4}

Table 7.4: *Ratio of branching fractions* $\frac{\mathcal{B}(B_s^0 \to \phi\gamma)}{\mathcal{B}(\bar{B} \to e^- D^0 X)}$ *and absolute branching fraction* $\mathcal{B}(B_s^0 \to \phi\gamma)$ *using* $\frac{f_s}{f_d} = 0.427 \pm 0.072$ *[20].*

Chapter 8

Summary and Outlook

Using a data sample of $\int Ldt = 28.9 \pm 1.2$ pb^{-1} of proton-antiproton collisions at $\sqrt{s} = 1.8$ TeV collected with the CDF detector at the Fermilab Tevatron collider, we searched for "penguin" radiative decays of B_d^0 and B_s^0 mesons which involve the flavor-changing neutral-current transition of a b quark into an s quark with the emission of a photon, $b \to s\gamma$. Specifically, we searched for the decays

$$B_d^0 \to K^*(892)^0\gamma$$
$$B_s^0 \to \phi(1020)\gamma$$

with the daughter mesons reconstructed via the decay modes

$$K^*(892)^0 \to K^+\pi^-$$
$$\phi(1020) \to K^+K^-$$

and the photon measured in the central ($|\eta| < 1$) electromagnetic calorimeter.

In order to collect such decays, we designed a specialized trigger which required information on all the decay products of the B meson decay chain, the first such trigger in a hadron collider environment. This "penguin" trigger collected data during the last quarter of the 1994 – 1996 data-taking period. The rapid decrease of the B production cross section with increasing B momentum makes the use of low

energy thresholds for the decay products desirable. But since $p\bar{p}$ collisions produce a plethora of particles, most of them with low energies, the energy thresholds imposed by the trigger cannot be trivial, otherwise the rate at which the trigger accepts events would reach unmanageable levels. Guided by simulations of the signal processes, we only accepted events where the candidate decay products were close to each other and we required that the transverse momenta[1] of the charged particles be above 2 GeV/c. As for the photon energy, 22.3 pb^{-1} of data were collected with a 10 GeV threshold, while in the last 6.6 pb^{-1} we were able to relax this requirement to 6 GeV.

As shown in Tables 4.1 and 6.1, the expected yield of this trigger is $\sim$ 25 $B_d^0 \to K^{*0}\gamma$ events per 100 pb^{-1}, for the 10 GeV energy threshold on the photons, with 1/5 of them surviving the off-line requirements to reject background events. After all selection criteria, we are left with one candidate $B_d^0 \to K^{*0}\gamma$ decay and no $B_s^0 \to \phi\gamma$ candidates in the entire Run 1 data sample. We then proceed to set upper limits on the branching fractions of the penguin channels. The upper limit for the $B_d^0 \to K^{*0}\gamma$ decay is consistent with the branching fraction measurement reported by the CLEO collaboration, $\mathcal{B}(B_d^0 \to K^{*0}\gamma) = (4.0 \pm 1.9) \times 10^{-5}$ [32], while the upper limit for the as yet unobserved $B_s^0 \to \phi\gamma$ decay is the most constraining one set to date [4]. Theoretical predictions for $\mathcal{B}(B_d^0 \to K^{*0}\gamma)$ are in excellent agreement with the CLEO result.

8.1 Branching Fraction Limits

We exploit the topological similarity between the $\bar{B} \to e^- D^0 X$, $D^0 \to K^-\pi^+$and the penguin decays, by forming ratios of branching fractions between the penguin and the $\bar{B} \to e^- D^0 X$ channels. Uncertainties associated with the B meson production cross section, common efficiency corrections and other systematic effects are minimal

[1] Momenta and energies of the decay products mentioned here refer to the transverse $x - y$ plane of the CDF detector.

in the ratio of branching fractions. The uncertainty on the $\bar{B} \to e^- D^0 X$ yield is the biggest contribution to the total uncertainty on the penguin branching fraction. We assume equal production rates for B_u^+ and B_d^0 mesons, while the probability of producing B_s^0 mesons relative to B_d^0 mesons, f_s/f_d, is taken to be $1/3$ [2]. The inferred upper limits on the ratios of branching fractions are

$$\frac{\mathcal{B}(B_s^0 \to \phi\gamma)}{\mathcal{B}(\bar{B} \to e^- D^0 X)} < 3.5 \times 10^{-3} \qquad \text{at 90\% C.L.}$$

$$\frac{\mathcal{B}(B_d^0 \to K^{*0}\gamma)}{\mathcal{B}(\bar{B} \to e^- D^0 X)} < 1.9 \times 10^{-3} \qquad \text{at 90\% C.L.}$$

Relative branching fraction measurements were combined with the branching fraction measurement of the $\bar{B} \to e^- D^0 X$, $D^0 \to K^- \pi^+$ decay chain, $\mathcal{B}(\bar{B} \to e^- D^0 X) \times \mathcal{B}(D^0 \to K^- \pi^+) = (294 \pm 40) \times 10^{-5}$ (see end of Section 6.4), to extract the following absolute branching fraction limits

$$\mathcal{B}(B_s^0 \to \phi\gamma) < 2.8 \times 10^{-4} \qquad \text{at 90\% C.L.}$$
$$\mathcal{B}(B_d^0 \to K^{*0}\gamma) < 1.5 \times 10^{-4} \qquad \text{at 90\% C.L.}$$

8.2 Future prospects

For the data-taking period to commence in the year 2000 (Run 2), the Fermilab accelerator complex is being upgraded with the "Main Injector" which will replace the Main Ring in providing the Tevatron with proton and antiproton beams. The center-of-mass energy of the colliding beams will be $\sqrt{s} = 2$ TeV, the instantaneous luminosity will reach 2×10^{32} cm^{-2} sec^{-1}, with beams colliding every 396 ns, compared to 3.5 μs in Run 1, and the Tevatron is expected to provide an integrated luminosity of $\int Ldt = 2$ fb^{-1} in Run 2. The CDF detector is also being rebuilt into

[2] In Chapter 7 we present results for two other f_s/f_d values, one from LEP experiments and one from CDF.

an upgraded "CDF II" detector [65] in order to cope with these changes and explore the wealth of new data. Key upgrades for B physics include: (i) the extended coverage of the silicon trackers to $|\eta| \leq 2$, thus covering almost all the luminous $p\bar{p}$ collision region, compared to the 60% coverage provided by the silicon tracker in Run 1, (ii) the three-dimensional information provided by the silicon trackers, compared to the two-dimensional in Run 1, and (iii) the ability of the data acquisition system to handle bunch crossings every 132 ns [3] and of the trigger to use tracking information at Level 1, impact parameter information for tracks at Level 2, and to handle 300 Hz of data at Level 3. We thus anticipate significant increases to the trigger bandwidth and to the signal-to-background ratio at the trigger level for tracks originating from b decays. Consequently, we expect to lower the photon energy threshold to 5 GeV and the track momentum requirement to 1.5 GeV and collect ~ 135 $B_d^0 \to K^{*0}\gamma$ events per 100 pb^{-1}, or ~ 2700 per 2 fb^{-1}, with a similar trigger to the one implemented in Run 1. Additional off-line requirements will improve the signal-to-background ratio and still leave a significant number of $B_d^0 \to K^{*0}\gamma$ events observed, allowing for a precise measurement of this branching fraction.

As soon as $\mathcal{B}(B_d^0 \to K^{*0}\gamma)$ is measured, it will be interesting to study the decay $B_d^0 \to \rho^0\gamma$, where the ρ meson can be reconstructed from its decay into two charged pions. The theoretical prediction of $\mathcal{B}(B_d^0 \to \rho^0\gamma) \sim 10^{-6}$ [34] puts this decay within reach for Run 2. The ratio of branching fractions $\frac{\mathcal{B}(B_d^0 \to \rho^0\gamma)}{\mathcal{B}(B_d^0 \to K^{*0}\gamma)}$ is proportional to the ratio $|\frac{V_{td}}{V_{ts}}|^2$, with the proportionality constant being model dependent. A measurement of $|\frac{V_{td}}{V_{ts}}|$ constrains one side of the CP unitarity triangle. $B_d^0 \to \rho^0\gamma, \rho^0 \to \pi^+\pi^-$ decays with one pion misidentified as a kaon, results in $K\pi$ and $\gamma K\pi$ mass distributions resembling the corresponding distributions from $B_d^0 \to K^{*0}\gamma$ decays. Therefore, these decay modes cannot be separated on a event-by-event basis, but the relative contributions of these channels should be extracted statistically. This task will be

[3] Originally the Tevatron will operate with proton-antiproton bunches crossing every 396 ns, but there are plans for crossings every 132 ns.

facilitated by the particle identification system (from dE/dx information from the new drift chamber) which is going to provide separation between kaon and pions at the 1σ level in the momentum range of interest. Discrimination against backgrounds from higher multiplicity penguin decays, $B_d^0 \to K^{*}\pi^0$ and $B_d^0 \to \rho^0\pi^0$ decays, where the π^0 is detected as a single electromagnetic cluster of energy in the calorimeter, has been studied with Monte Carlo and such backgrounds are shown to be manageable [56]..

Information on $|\frac{V_{td}}{V_{ts}}|$ can also be obtained from the ratio of branching fractions $\frac{\mathcal{B}(B_s^0 \to K^{*0}\gamma)}{\mathcal{B}(B_s^0 \to \phi\gamma)}$. The size of the B_s^0 penguin sample is expected to be 1/3 to 1/2 the size of the B_d^0 penguin sample, for decays where the same CKM matrix element is involved (e.g., $B_s^0 \to \phi\gamma$ and $B_d^0 \to K^{*0}\gamma$ decays, which involve V_{ts} in $b \to t \to s$ transitions). The mass resolution of the reconstructed B meson is dominated by the resolution on the photon energy measured in the calorimeter; it was $\sim$ 100 MeV/c^2 for the $E_T > 10$ GeV photons in Run 1. Since the mass difference between B_d^0 and B_s^0 mesons is $\sim$ 90 MeV/c^2, event-by-event separation of $B_d^0 \to K^{*0}\gamma$ from $B_s^0 \to K^{*0}\gamma$ events will not be possible. But photons can also be measured from their conversion to electron-positron pairs. The loss of signal yield due to the $\sim$ 5% probability for a photon to convert in the material before the drift chamber, will be offset by a lower energy threshold. The B mass resolution will then be almost 5 times better. Furthermore, separation of photons from π^0 will be almost twenty times better, allowing a cleaner separation between electromagnetic and hadronic penguin decays. Comparison of the $|\frac{V_{td}}{V_{ts}}|$ results from B_d^0 and B_s^0 penguin decays, and B_s^0 and B_d^0 mixing, will help constrain theoretical uncertainties, mainly due to low-energy (i.e. "long-distance") final state interactions which lead to $b \to d$ transitions without the involvement of virtual t quarks in the CKM-suppressed $b \to t \to d$ transitions.

Appendix A

The CDF Collaboration

T. Affolder,[21] H. Akimoto,[42] A. Akopian,[35] M. G. Albrow,[10] P. Amaral,[7] S. R. Amendolia,[31] D. Amidei,[24] J. Antos,[1] G. Apollinari,[35] T. Arisawa,[42] T. Asakawa,[40] W. Ashmanskas,[7] M. Atac,[10] P. Azzi-Bacchetta,[29] N. Bacchetta,[29] M. W. Bailey,[26] S. Bailey,[14] P. de Barbaro,[34] A. Barbaro-Galtieri,[21] V. E. Barnes,[33] B. A. Barnett,[17] M. Barone,[12] G. Bauer,[22] F. Bedeschi,[31] S. Belforte,[39] G. Bellettini,[31] J. Bellinger,[43] D. Benjamin,[9] J. Bensinger,[4] A. Beretvas,[10] J. P. Berge,[10] J. Berryhill,[7] S. Bertolucci,[12] B. Bevensee,[30] A. Bhatti,[35] C. Bigongiari,[31] M. Binkley,[10] D. Bisello,[29] R. E. Blair,[2] C. Blocker,[4] K. Bloom,[24] B. Blumenfeld,[17] B. S. Blusk,[34] A. Bocci,[31] A. Bodek,[34] W. Bokhari,[30] G. Bolla,[33] Y. Bonushkin,[5] D. Bortoletto,[33] J. Boudreau,[32] A. Brandl,[26] S. van den Brink,[17] C. Bromberg,[25] N. Bruner,[26] E. Buckley-Geer,[10] J. Budagov,[8] H. S. Budd,[34] K. Burkett,[14] G. Busetto,[29] A. Byon-Wagner,[10] K. L. Byrum,[2] M. Campbell,[24] A. Caner,[31] W. Carithers,[21] J. Carlson,[24] D. Carlsmith,[43] J. Cassada,[34] A. Castro,[29] D. Cauz,[39] A. Cerri,[31] P. S. Chang,[1] P. T. Chang,[1] J. Chapman,[24] C. Chen,[30] Y. C. Chen,[1] M. -T. Cheng,[1] M. Chertok,[37] G. Chiarelli,[31] I. Chirikov-Zorin,[8] G. Chlachidze,[8] F. Chlebana,[10] L. Christofek,[16] M. L. Chu,[1] S. Cihangir,[10] C. I. Ciobanu,[27] A. G. Clark,[13] M. Cobal,[31] E. Cocca,[31] A. Connolly,[21] J. Conway,[36] J. Cooper,[10] M. Cordelli,[12]

J. Guimaraes da Costa,[24] D. Costanzo,[31] J. Cranshaw,[38] D. Cronin-Hennessy,[9] R. Cropp,[23] R. Culbertson,[7] D. Dagenhart,[41] F. DeJongh,[10] S. Dell'Agnello,[12] M. Dell'Orso,[31] R. Demina,[10] L. Demortier,[35] M. Deninno,[3] P. F. Derwent,[10] T. Devlin,[36] J. R. Dittmann,[10] S. Donati,[31] J. Done,[37] T. Dorigo,[14] N. Eddy,[16] K. Einsweiler,[21] J. E. Elias,[10] E. Engels, Jr.,[32] W. Erdmann,[10] D. Errede,[16] S. Errede,[16] Q. Fan,[34] R. G. Feild,[44] C. Ferretti,[31] I. Fiori,[3] B. Flaugher,[10] G. W. Foster,[10] M. Franklin,[14] J. Freeman,[10] J. Friedman,[22] Y. Fukui,[20] S. Gadomski,[23] S. Galeotti,[31] M. Gallinaro,[35] T. Gao,[30] M. Garcia-Sciveres,[21] A. F. Garfinkel,[33] P. Gatti,[29] C. Gay,[44] S. Geer,[10] D. W. Gerdes,[24] P. Giannetti,[31] P. Giromini,[12] V. Glagolev,[8] M. Gold,[26] J. Goldstein,[10] A. Gordon,[14] A. T. Goshaw,[9] Y. Gotra,[32] K. Goulianos,[35] H. Grassmann,[39] C. Green,[33] L. Groer,[36] C. Grosso-Pilcher,[7] M. Guenther,[33] G. Guillian,[24] R. S. Guo,[1] C. Haber,[21] E. Hafen,[22] S. R. Hahn,[10] C. Hall,[14] T. Handa,[15] R. Handler,[43] W. Hao,[38] F. Happacher,[12] K. Hara,[40] A. D. Hardman,[33] R. M. Harris,[10] F. Hartmann,[18] K. Hatakeyama,[35] J. Hauser,[5] J. Heinrich,[30] A. Heiss,[18] B. Hinrichsen,[23] K. D. Hoffman,[33] C. Holck,[30] R. Hollebeek,[30] L. Holloway,[16] R. Hughes,[27] J. Huston,[25] J. Huth,[14] H. Ikeda,[40] M. Incagli,[31] J. Incandela,[10] G. Introzzi,[31] J. Iwai,[42] Y. Iwata,[15] E. James,[24] H. Jensen,[10] M. Jones,[30] U. Joshi,[10] H. Kambara,[13] T. Kamon,[37] T. Kaneko,[40] K. Karr,[41] H. Kasha,[44] Y. Kato,[28] T. A. Keaffaber,[33] K. Kelley,[22] M. Kelly,[24] R. D. Kennedy,[10] R. Kephart,[10] D. Khazins,[9] T. Kikuchi,[40] M. Kirk,[4] B. J. Kim,[19] H. S. Kim,[23] S. H. Kim,[40] Y. K. Kim,[21] L. Kirsch,[4] S. Klimenko,[11] D. Knoblauch,[18] P. Koehn,[27] A. Köngeter,[18] K. Kondo,[42] J. Konigsberg,[11] K. Kordas,[23] A. Korytov,[11] E. Kovacs,[2] J. Kroll,[30] M. Kruse,[34] S. E. Kuhlmann,[2] K. Kurino,[15] T. Kuwabara,[40] A. T. Laasanen,[33] N. Lai,[7] S. Lami,[35] S. Lammel,[10] J. I. Lamoureux,[4] M. Lancaster,[21] G. Latino,[31] T. LeCompte,[2] A. M. Lee IV,[9] S. Leone,[31] J. D. Lewis,[10] M. Lindgren,[5] T. M. Liss,[16] J. B. Liu,[34] Y. C. Liu,[1] N. Lockyer,[30] M. Loreti,[29] D. Lucchesi,[29] P. Lukens,[10] S. Lusin,[43] J. Lys,[21] R. Madrak,[14] K. Maeshima,[10] P. Maksimovic,[14] L. Malferrari,[3] M. Mangano,[31] M. Mariotti,[29] G. Martignon,[29] A. Martin,[44]

J. A. J. Matthews,[26] P. Mazzanti,[3] K. S. McFarland,[34] P. McIntyre,[37] E. McKigney,[30] M. Menguzzato,[29] A. Menzione,[31] E. Meschi,[31] C. Mesropian,[35] C. Miao,[24] T. Miao,[10] R. Miller,[25] J. S. Miller,[24] H. Minato,[40] S. Miscetti,[12] M. Mishina,[20] N. Moggi,[31] E. Moore,[26] R. Moore,[24] Y. Morita,[20] A. Mukherjee,[10] T. Muller,[18] A. Munar,[31] P. Murat,[31] S. Murgia,[25] M. Musy,[39] J. Nachtman,[5] S. Nahn,[44] H. Nakada,[40] T. Nakaya,[7] I. Nakano,[15] C. Nelson,[10] D. Neuberger,[18] C. Newman-Holmes,[10] C.-Y. P. Ngan,[22] P. Nicolaidi,[39] H. Niu,[4] L. Nodulman,[2] A. Nomerotski,[11] S. H. Oh,[9] T. Ohmoto,[15] T. Ohsugi,[15] R. Oishi,[40] T. Okusawa,[28] J. Olsen,[43] C. Pagliarone,[31] F. Palmonari,[31] R. Paoletti,[31] V. Papadimitriou,[38] S. P. Pappas,[44] A. Parri,[12] D. Partos,[4] J. Patrick,[10] G. Pauletta,[39] M. Paulini,[21] A. Perazzo,[31] L. Pescara,[29] T. J. Phillips,[9] G. Piacentino,[31] K. T. Pitts,[10] R. Plunkett,[10] A. Pompos,[33] L. Pondrom,[43] G. Pope,[32] F. Prokoshin,[8] J. Proudfoot,[2] F. Ptohos,[12] G. Punzi,[31] K. Ragan,[23] D. Reher,[21] A. Ribon,[29] F. Rimondi,[3] L. Ristori,[31] W. J. Robertson,[9] A. Robinson,[23] T. Rodrigo,[6] S. Rolli,[41] L. Rosenson,[22] R. Roser,[10] R. Rossin,[29] W. K. Sakumoto,[34] D. Saltzberg,[5] A. Sansoni,[12] L. Santi,[39] H. Sato,[40] P. Savard,[23] P. Schlabach,[10] E. E. Schmidt,[10] M. P. Schmidt,[44] M. Schmitt,[14] L. Scodellaro,[29] A. Scott,[5] A. Scribano,[31] S. Segler,[10] S. Seidel,[26] Y. Seiya,[40] A. Semenov,[8] F. Semeria,[3] T. Shah,[22] M. D. Shapiro,[21] P. F. Shepard,[32] T. Shibayama,[40] M. Shimojima,[40] M. Shochet,[7] J. Siegrist,[21] G. Signorelli,[31] A. Sill,[38] P. Sinervo,[23] P. Singh,[16] A. J. Slaughter,[44] K. Sliwa,[41] C. Smith,[17] F. D. Snider,[10] A. Solodsky,[35] J. Spalding,[10] T. Speer,[13] P. Sphicas,[22] F. Spinella,[31] M. Spiropulu,[14] L. Spiegel,[10] L. Stanco,[29] J. Steele,[43] A. Stefanini,[31] J. Strologas,[16] F. Strumia, [13] D. Stuart,[10] K. Sumorok,[22] T. Suzuki,[40] R. Takashima,[15] K. Takikawa,[40] M. Tanaka,[40] T. Takano,[28] B. Tannenbaum,[5] W. Taylor,[23] M. Tecchio,[24] P. K. Teng,[1] K. Terashi,[40] S. Tether,[22] D. Theriot,[10] R. Thurman-Keup,[2] P. Tipton,[34] S. Tkaczyk,[10] K. Tollefson,[34] A. Tollestrup,[10] H. Toyoda,[28] W. Trischuk,[23] J. F. de Troconiz,[14] S. Truitt,[24] J. Tseng,[22] N. Turini,[31] F. Ukegawa,[40] J. Valls,[36] S. Vejcik III,[10] G. Velev,[31] R. Vidal,[10] R. Vilar,[6] I. Vologouev,[21] D. Vucinic,[22] R. G. Wagner,[2]

R. L. Wagner,[10] J. Wahl,[7] N. B. Wallace,[36] A. M. Walsh,[36] C. Wang,[9] C. H. Wang,[1] M. J. Wang,[1] T. Watanabe,[40] T. Watts,[36] R. Webb,[37] H. Wenzel,[18] W. C. Wester III,[10] A. B. Wicklund,[2] E. Wicklund,[10] H. H. Williams,[30] P. Wilson,[10] B. L. Winer,[27] D. Winn,[24] S. Wolbers,[10] D. Wolinski,[24] J. Wolinski,[25] S. Worm,[26] X. Wu,[13] J. Wyss,[31] A. Yagil,[10] W. Yao,[21] G. P. Yeh,[10] P. Yeh,[1] J. Yoh,[10] C. Yosef,[25] T. Yoshida,[28] I. Yu,[19] S. Yu,[30] A. Zanetti,[39] F. Zetti,[21] and S. Zucchelli[3]

(CDF Collaboration)

[1] *Institute of Physics, Academia Sinica, Taipei, Taiwan 11529, Republic of China*

[2] *Argonne National Laboratory, Argonne, Illinois 60439*

[3] *Istituto Nazionale di Fisica Nucleare, University of Bologna, I-40127 Bologna, Italy*

[4] *Brandeis University, Waltham, Massachusetts 02254*

[5] *University of California at Los Angeles, Los Angeles, California 90024*

[6] *Instituto de Fisica de Cantabria, University of Cantabria, 39005 Santander, Spain*

[7] *Enrico Fermi Institute, University of Chicago, Chicago, Illinois 60637*

[8] *Joint Institute for Nuclear Research, RU-141980 Dubna, Russia*

[9] *Duke University, Durham, North Carolina 27708*

[10] *Fermi National Accelerator Laboratory, Batavia, Illinois 60510*

[11] *University of Florida, Gainesville, Florida 32611*

[12] *Laboratori Nazionali di Frascati, Istituto Nazionale di Fisica Nucleare, I-00044 Frascati, Italy*

[13] *University of Geneva, CH-1211 Geneva 4, Switzerland*

[14] *Harvard University, Cambridge, Massachusetts 02138*

[15] *Hiroshima University, Higashi-Hiroshima 724, Japan*

[16] *University of Illinois, Urbana, Illinois 61801*

[17] *The Johns Hopkins University, Baltimore, Maryland 21218*

[18] *Institut für Experimentelle Kernphysik, Universität Karlsruhe, 76128 Karlsruhe, Germany*

[19] *Korean Hadron Collider Laboratory: Kyungpook National University, Taegu 702-701; Seoul National University, Seoul 151-742; and SungKyunKwan University, Suwon 440-746; Korea*

[20] *High Energy Accelerator Research Organization (KEK), Tsukuba, Ibaraki 305, Japan*

[21] *Ernest Orlando Lawrence Berkeley National Laboratory, Berkeley, California 94720*

[22] *Massachusetts Institute of Technology, Cambridge, Massachusetts 02139*

[23] *Institute of Particle Physics: McGill University, Montreal H3A 2T8; and University of Toronto, Toronto M5S 1A7; Canada*

[24] *University of Michigan, Ann Arbor, Michigan 48109*

[25] *Michigan State University, East Lansing, Michigan 48824*

[26] *University of New Mexico, Albuquerque, New Mexico 87131*

[27] *The Ohio State University, Columbus, Ohio 43210*

[28] *Osaka City University, Osaka 588, Japan*

[29] *Universita di Padova, Istituto Nazionale di Fisica Nucleare, Sezione di Padova, I-35131 Padova, Italy*

[30] *University of Pennsylvania, Philadelphia, Pennsylvania 19104*

[31] *Istituto Nazionale di Fisica Nucleare, University and Scuola Normale Superiore of Pisa, I-56100 Pisa, Italy*

[32] *University of Pittsburgh, Pittsburgh, Pennsylvania 15260*

[33] *Purdue University, West Lafayette, Indiana 47907*

[34] *University of Rochester, Rochester, New York 14627*

[35] *Rockefeller University, New York, New York 10021*

[36] *Rutgers University, Piscataway, New Jersey 08855*

[37] *Texas A&M University, College Station, Texas 77843*

[38] *Texas Tech University, Lubbock, Texas 79409*

[39] *Istituto Nazionale di Fisica Nucleare, University of Trieste/ Udine, Italy*

[40] *University of Tsukuba, Tsukuba, Ibaraki 305, Japan*

[41] *Tufts University, Medford, Massachusetts 02155*

[42] *Waseda University, Tokyo 169, Japan*

[43] *University of Wisconsin, Madison, Wisconsin 53706*

[44] *Yale University, New Haven, Connecticut 06520*

Appendix B

Glossary

B isolation The fact that a B meson carries most of the b quark momentum after its fragmentation.

Calorimeter tower The smallest calorimeter unit read out by the same electronic channel. In the central detector region ($|\eta| < 1$), it spans 0.1×15^0 in $\eta - \phi$ space.

CDF Collider Detector at Fermilab.

CEM Central electromagnetic calorimeter.

CES Central strip chambers.

CFT Central track-finder processor used at the trigger level.

CHA Central hadronic calorimeter.

CTC Central drift chamber.

ECLB The inclusive electron data stream, collected with a trigger which required an electron with transverse energy above 8 GeV.

Event The amount of information the CDF detector collects to describe the result of a single beam crossing.

KSGB The "penguin" data stream, collected with the specialized trigger looking for a high energy photon and two oppositely charged energetic tracks nearby.

Level 1, etc. See *L1, L2, L3.*

L1, L2, L3 First, second and third level trigger system.

L2 isolation The penguin trigger requirement that there be no high energy track pointing at the same ϕ as the penguin photon.

MC See *Monte Carlo*

Monte Carlo Computer programs which use random numbers to simulate physics processes, like proton-antiproton collisions, and/or the response of the detector to the passage of particles through its volume.

Prescaling A specific trigger component is said to be prescaled by a factor x, when this component is considered for the overall trigger decision only one out of x times that this trigger component's conditions were actually satisfied.

η, **pseudorapidity** It is defined as $\eta = -\ln[\tan(\theta/2)]$, where θ is the polar angle with respect to the proton-antiproton beam axis (z axis).

Seed tower The calorimeter tower containing the highest energy deposition amongst a group of contiguous calorimeter towers.

SVX Silicon vertex detector.

Transverse The transverse to the proton-antiproton beam axis component of a vector quantity, e.g., momentum. We also talk about transverse energy by considering the energy as a vector which originates at the proton-antiproton collision point, points to the energy deposition in the calorimeters and has a magnitude equal to that energy deposition.

Vertex The *primary vertex* is the point of the proton-antiproton collision, and the *secondary vertex* is the B meson's decay point.

XCES The trigger level requirement that there be substantial energy deposition in the strip chambers embedded in the CEM.

Bibliography

[1] C. Quigg. "Elementary Particles and Forces". *In "Particles and Forces: At the Heart of the Matter. Readings from Scientific American"*, pages 3–17, 1990. Edited by R. A. Carrigan, Jr. and W. P. Trower. Published by W. H. Freeman and Company.

[2] Frank Wilczek. "Quantum Field Theory". *Rev. Mod. Phys.*, **71 (2)**:S85–S95, 1999.

[3] Gordon L. Kane. "Modern elementary particle physics: the fundamental particles and forces?". 1993. Published by Addison-Wesley Pub., Reading, Mass.

[4] C. Caso et al. (Particle Data Group). "Review of Particle Physics". *The European Physical Journal*, **C3**:1–794, 1998.

[5] S. L. Glashow, J. Iliopoulos, and L. Maiani. "Weak Interactions with Lepton-Hadron Symmetry". *Phys. Rev.*, **D2**:1285–1292, 1970.

[6] S. W. Herb et al. "Observation of a dimuon resonance at 9.5 GeV in 400-GeV proton-nucleus collisions". *Phys. Rev. Lett.*, **39**:252–255, 1977.

[7] C. Berger et al. (PLUTO Collaboration). "Observation of a narrow resonance formed in e^+e^- annihilation at 9.46 GeV". *Phys. Lett.*, **B76**:243–245, 1978.

[8] C. W. Darden et al. (DASP Collaboration). "Observation of a narrow resonance at 9.46 GeV in electron-positron annihilations". *Phys. Lett.*, **B76**:246–251, 1978.

[9] J. K. Bienlein et al. "Observation of a narrow resonance at 10.02 GeV in electron-positron annihilations". *Phys. Lett.*, **B76**:360–363, 1978.

[10] C. W. Darden et al. (DASP Collaboration). "Evidence for a narrow resonance at 10.01-GeV in electron-positron annihilations". *Phys. Lett.*, **B76**:364–368, 1978.

[11] K. Ueno et al. "Evidence for the Υ'' and a search for new narrow resonances". *Phys. Rev. Lett.*, **42**:486–489, 1979.

[12] Manfred Paulini. "B lifetimes, mixing and CP violation at CDF". *Int. J. Mod. Phys.*, **A10**:1990–2990, 1999. hep-ex/9903002.

[13] Michelangelo L. Mangano. "Two lectures on heavy quark production in hadronic collisions". *CERN publication*, CERN-TH/97-328 and hep-ph/9711337, 1997. Presented at the International School of Physics "E. Fermi", Course CXXXVIII, *Heavy flavour physics: a probe of nature's grand design.*

[14] P. Nason, S. Dawson, and R. K. Ellis. "The total cross section for the production of heavy quarks in hadronic collisions". *Nucl. Phys.*, **B303**:607–633, 1988.

[15] A. D. Martin, W. J. Stirling, and R. G. Roberts. "New information on parton distributions". *Phys. Rev.*, **D47**:867–882, 1993.

[16] P. Nason, S. Dawson, and R. K. Ellis. "The one particle inclusive differential cross section for heavy quark production in hadronic collisions". *Nucl. Phys.*, **B327**:49–92, 1989. *Erratum, ibid.* **B335**:260, 1990.

[17] C. Peterson, D. Schlatter, I. Schmitt, and P. M. Zerwas. "Scaling violations in inclusive e^+e^- annihilation spectra". *Phys. Rev.*, **D27**:105–111, 1983.

[18] J. Chrin. "Upon the determination of heavy quark fragmentation functions in e^+e^- annihilation". *Z. Phys.*, **C36**:163–171, 1987. This value encompasses more recent measurements, including G. Alexander et al. (OPAL Collaboration), *Phys. Lett.* **B364**: 93-106, 1995 and D. Buskulic et al. (ALEPH Collaboration), *Phys. Lett.* **B357**:699-714, 1995.

[19] F. Abe et al. (CDF Collaboration). "Ratios of bottom meson branching fractions involving J/ψ mesons and determination of b quark fragmentation fractions". *Phys. Rev.*, **D54**:6596–6609, 1996.

[20] F. Abe et al. (CDF Collaboration). "Measurement of b quark fragmentation fractions in $p\bar{p}$ collisions at $\sqrt{s}$ = 1.8 TeV". *Submitted to Phys. Rev. Lett.*, FERMILAB-Pub-99/243-E, 1999. hep-ex/9909011.

[21] A. Ali. "Flavour Changing Neutral Current processes in B decays". *Nucl. Phys. Proc. Suppl.*, **59**:86–100, 1997. hep-ph/9702312.

[22] M. Gronau and D. London. "New physics in CP asymmetries and rare B decays". *Phys. Rev.*, **D55**:2845–2861, 1997.

[23] A. J. Buras. "Rare decays, CP violation and QCD". *Acta Phys. Polon.*, **B26**:755–788, 1995. hep-ph/9503262.

[24] A. J. Buras. "CP violation and rare decays of K and B mesons". *Lectures given at the "14th Lake Louise Winter Institude"*, Feb. 14 - 20, 1999. hep-ph/9905437.

[25] A. Ali. "Flavour Changing Neutral Current processes and CKM phenomenology". *Published in the "Proceedings of the First APCTP Workshop Pacific Particle Physics Phenomenology"*, Seoul National University, Seoul, South Korea, Oct. 31 - Nov. 2, 1997. hep-ph/9801270.

[26] J. Chay, H. Georgi, and B. Grinstein. "Lepton energy distributions in heavy meson decays from QCD.". *Phys. Lett.*, **B247**:399–405, 1990.

[27] D. Boutigny et al. (BaBar Collaboration). "The BaBar Physics Book". *SLAC report*, SLAC-R-504, 1998. SLAC, unpublished.

[28] G. Eigen. "Measurements of $B \to X_s\gamma$ and study of $B \to X_s\ell^+\ell^-$". *hep-ph/9901005*, 1999.

[29] R. Barate et al. (ALEPH Collaboration). "A measurement of the inclusive $b \to s\gamma$ branching ratio". *Phys. Lett.*, **B429**:169–187, 1999.

[30] K. Lingel, T. Skwarnicki, and J. G. Smith. "Penguin decays of B mesons". *Annu. Rev. Nucl. Part. Sci.*, **48**:253–306, 1998.

[31] R. M. Barnett et al. (Particle Data Group). "Review of Particle Physics". *Phys. Rev.*, **D54**:1–720, 1996.

[32] R. Ammar et al. (CLEO Collaboration). "Evidence for penguins: First observation of $B \to K^*(892)\gamma$". *Phys. Rev. Lett.*, **71**:674–678, 1993.

[33] N. G. Deshpande, P. Lo, and J. Trampetic. "Prediction of $B \to K^*\gamma$ as a Test of the Standard Model". *Phys. Rev. Lett.*, **59**:183–185, 1987.

[34] J. M. Soares. "Constraints on $|V_{td}|$ from radiative decays of the B mesons". *Phys. Rev.*, **D49**:283–288, 1994. This is a reference for the previous generation of the device. The replacement for the Run 1 (1992-1996) data-taking period has more modules, each with a shorter drift length, but otherwise similar.

[35] A. Ali. "Theory of rare B decays". *Published in the "Proceedings of the Seventh International Symposium on Heavy Flavor Physics"*, University of California Santa Barbara, California, July 7 - 11, 1997. hep-ph/9709507.

[36] L. M. Lederman. "The Tevatron". *Scientific American*, pages 48–55, March 1991.

[37] F. Abe et al. (CDF Collaboration). "Measurement of Antiproton-Proton Total Cross Section at $\sqrt{s} = 546$ and 1800 GeV". *Phys. Rev.*, **D50**:5550–5561, 1994.

[38] F. Abe et al. (CDF Collaboration). "Measurement of $\sigma B(W \to e\nu)$ and $\sigma B(Z^0 \to e^+e^-)$ in $p\bar{p}$ collisions at $\sqrt{s} = 1.8$ TeV". *Phys. Rev. Lett.*, **76**:3070–3075, 1996.

[39] F. Abe et al. (CDF Collaboration). "The CDF detector: An overview". *Nucl. Instr. and Meth.*, **A271**:387–403, 1988.

[40] D. Amidei et al. "The Silicon Vertex Detector of the Collider Detector at Fermilab". *Nucl. Instr. and Meth.*, **A350**:73–130, 1994.

[41] P. Azzi et al. "SVX', the New CDF Silicon Vertex Ditector". *Nucl. Instr. and Meth.*, **A360**:137–140, 1995.

[42] F. Snider et al. "The CDF Vertex Time Projection Chamber System". *Nucl. Instr. and Meth.*, **A268**:75–91, 1988.

[43] F. Bedeschi et al. "Design and Construction of the CDF Central Tracking Chamber". *Nucl. Instr. and Meth.*, **A268**:50–74, 1988.

[44] L. Balka et al. "The CDF Central Electromagnetic Calorimeter". *Nucl. Instr. and Meth.*, **A267**:272–279, 1988.

[45] D. Amidei et al. "A two level FASTBUS based trigger system for CDF". *Nucl. Instr. and Meth.*, **A269**:51–62, 1988.

[46] F. Abe et al. (CDF Collaboration). "Evidence for top quark production in $p\bar{p}$ collisions at $\sqrt{s} = 1.8$ TeV". *Phys. Rev.*, **D50**:2966–3026, 1994.

[47] G. W. Foster et al. "A fast hardware track-finder for the CDF central tracking chamber". *Nucl. Instr. and Meth.*, **A269**:93–100, 1988.

[48] F. Abe et al. (CDF Collaboration). "Measurement of the B meson differential cross section $d\sigma/dp_T$ in $p\bar{p}$ collisions at $\sqrt{s} = 1.8$ TeV". *Phys. Rev. Lett.*, **75**:1451–1455, 1995.

[49] P. Avery, K. Read, and G. Trahern. "QQ: A Monte Carlo generator". *Internal Software Note*, CSN-212, 1985. Cornell University, unpublished.

[50] W. J. Taylor, K. Byrum, and P. K. Sinervo. "Run 1B Level 2 CEM_8_CFT_7_5 and XCES electron trigger efficiencies". *Internal Note*, CDF-Note 4691, 1998. CDF, unpublished.

[51] K. Kordas, K. Ragan, and F. DeJongh. "Search for electromagnetic penguins in Run1B and Run1C". *Internal Note*, CDF-Note 5113 (version 2.0), 1999. CDF, unpublished.

[52] F. Abe et al. (CDF Collaboration). "Measurement of the bottom-quark production cross section using semileptonic decay electrons in $p\bar{p}$ collisions at $\sqrt{s} = 1.8$ TeV". *Phys. Rev. Lett.*, **71**:500–504, 1993.

[53] F. Abe et al. (CDF Collaboration). "Observation of $B^+ \to \psi(2S)K^+$ and $B^0 \to \psi(2S)K^*(892)^0$ decays and measurements of B-meson branching fractions into J/ψ and $\psi(2S)$ final states". *Phys. Rev.*, **D58**:072001, 1998.

[54] H-U. Bengtsson and T. Sjöstrand. "The Lund Monte Carlo for Hadronic Processes (PYTHIA)". *CERN Report*, CERN-Th.6488, 1992. CERN, unpublished.

[55] J. D. Bjorken. "Properties of Hadron Distributions in Reactions Containing Very Heavy Quarks". *Phys. Rev.*, **D17**:171–173, 1978.

[56] F. DeJongh and M. Shapiro. "A proposal for observing radiative B decays at CDF". *Internal Note*, CDF-Note 2570, 1994. CDF, unpublished.

[57] F. Abe et al. (CDF Collaboration). "Prompt photon cross section measurement in $p\bar{p}$ collisions at $\sqrt{s} = 1.8$ TeV". *Phys. Rev.*, **D48**:2998–3025, 1993.

[58] K. Yasuoka et al. "Response maps of the CDF central electromagnetic calorimeter with electrons". *Nucl. Instr. and Meth.*, **A267**:315–329, 1988.

[59] R. G. Wagner et al. "Cosmic ray test of the CDF central calorimeters". *Nucl. Instr. and Meth.*, **A267**:330–350, 1988.

[60] F. Abe et al. (CDF Collaboration). "Observation of $\Lambda_b \to J/\psi\Lambda$ at the Fermilab Proton-Antiproton Collider". *Phys. Rev.*, **D55**:1142–1152, 1997.

[61] F. Abe et al. (CDF Collaboration). "Measurement of the W Boson Mass". *Phys. Rev.*, **D52**:4784–4827, 1995.

[62] F. Abe et al. (CDF Collaboration). "Search for the decays $B_d^0 \to \mu^+\mu^-$ and $B_s^0 \to \mu^+\mu^-$ in $p\bar{p}$ collisions at $\sqrt{s} = 1.8$ TeV". *Phys. Rev.*, **D57**:R3811– R3816, 1998.

[63] R. Fulton et al. (CLEO Collaboration). "Exclusive and inclusive semileptonic decays of B mesons to D mesons". *Phys. Rev.*, **D43**:651–663, 1991.

[64] R. D. Cousins and V. Highland. "Incorporating systematic uncertainties into an upper limit". *Nucl. Instr. and Meth.*, **A320**:331–335, 1992.

[65] R. Blair et al. (CDF II Collaboration). "The CDF II Detector: Technical Design Report". *Fermilab Publication*, FERMILAB-Pub-96/390-E, 1996. Fermi National Accelerator Laboratory, unpublished.